A validated methodology to estimate the reliability and safety of suspension bridge cables

Arturo Montoya

Submitted in partial fulfillment of the
Requirements for the degree
of Doctor of Philosophy
in the Graduate School of Arts and Sciences

COLUMBIA UNIVERSITY

2012

Abstract

A validated methodology to estimate the reliability and safety of suspension bridge cables

Arturo Montoya

The safety of suspension bridges depends on its main cables which are constructed of thousands of high strength steel wires radially clamped together at certain locations along the cable. After many years of service, these cables are showing signs of serious distress with many wires corroded and even broken inside. A new methodology to determine the reliability and safety of this structure is suggested in this research work. A three dimensional random field simulation is used to determine the remaining tensile strength in the cable. The key idea is to determine how an individual wire break affects the load transfer to the surrounding wires. This local damage eventually causes a global reduction in the load carrying capacity of the cable, up to a complete failure. A Monte Carlo technique is used to generate realizations of the wires' strength within a finite element model. Among the major contributions of the thesis is a novel technique for modeling the contact-friction mechanism between thousands of wires that account for load recovery in broken wires due to friction induced by radial clamps. The idea is to place elasto-plastic springs at the contact points between wires. These springs have varying parameters depending on their proximity to the clamping loads and are assigned according to the Boussinesq's solution to a point load in half space. While traditional contact algorithms have difficulties converging on this problem, this technique converges in few iterations. Moreover, parallelization of the problem enables

a full stochastic analysis to determine the effect of corrosion uncertainty on the cable's failure load. This method represents a dramatic improvement compared to the current inspection methods that are unreliable and expensive.

Contents

List of Figures

List of Tables

Acknowledgements

I would like to express my deep and sincere gratitude to my advisors, Raimondo Betti, George Deodatis, and Haim Waisman, for their guidance and encouragement throughout the course of my Ph.D. My interaction with each of them, at different stages of my research, refined my work. It was truly a pleasure to work with them and have their advice for my career decisions.

I am also very grateful to Professor I.C Noyan who provided the experimental tests necessary for the validation of my model and participated in valuable discussions at early stages of this research.

I am very grateful to Professor Kysar for his willingness to form part of the defense committee.

My appreciation also goes to Prof. Meyer, Prof. Culligan, Prof. Testa, Prof. Ling, and Prof. Smyth for providing me a strong knowledge foundation to perform this research.

I gratefully acknowledge the support of the National Science Foundation under grant No. CMMI-0928129.

Finally, I would like to express my love and great gratitude to my parents, siblings, grandmother, and the rest of my extensive Honduran family for believing in me and constantly showing me their unconditional love, support, and encouragement to pursue my dreams.

To my parents, Carlos Montoya and America Rodriguez, who are the inspiration of my life.

Chapter 1

Introduction

1.1 Research scope and Objectives

Suspension bridge structures support the roadway by suspending it from two (or more) main cables, anchored at either side of the bridge. These cables, made of thousands of small-diameter high-strength steel wires, are subjected to large tension forces that are then transferred to the towers and to the anchorages as shown in Figure 1.1. The load transfer from the horizontal deck to the main cables is done through vertical cables (much smaller in diameter, called suspenders) that are connected to the main cables through radial clamps, separated from each other by some given distance. This type of bridge structure is considered reliable and has been used to bridge very long gaps at many places around the globe [10].

However, due to environmental degradation, aging, and intense operating loads, these steel wires tend to deteriorate and break, reducing the life expectancy of the bridge. It has been determined that the most important factors responsible for this deterioration are corrosion and hydrogen embrittlement of the wires [4]. Moreover, Betti et al. [6] define the corrosion of the wires as a complex phenomenon since uniform and/or localized corrosion (pitting), and undamaged conditions can be present along the wire in no particular order. Shi et al. [54] consider the deterioration process as highly uncertain, since it is possible to find wires in pristine conditions and broken wires within the same cable cross-section. Furthermore, specific corrosion trends have been observed by Suzumura and Nakamura [43] along the cross-section of a cable, where wires closer to the sides and bottom sectors of the main cable were significantly more corroded than wires in the upper and center sectors, due to water entrapment in these areas, leading to more humid (e.g. aggressive) conditions.

(a)

(b)

(c)

Figure 1.1: An example of a suspension bridge and its main cables: (a) The George Washington Bridge: connects Manhattan to New Jersey, having a total length of 1450 m. The cables are made of 26,474 parallel steel wires, each of about 5 mm in diameter. (b) Close up at the radial clamps present along the cable span, and (c) a full scale laboratory model (built at Columbia University) showing the packing of parallel wire strands.

Nonetheless, it is very difficult to inspect and assess the condition of such cables due to the way they are built. Today the biggest challenge suspension bridge owner authorities face is to estimate the current and remaining strength/safety of a main cable in order to help them decide whether it is necessary to provide inmmediate maintenance and/or rehabilitation (or even replacement) of such cables. This work aims at the development of a new methodology that estimates the reliability of suspension bridge cables by generating a finite element (FE) model that accounts for load redistribution between wires, improves the quantification of uncertainty variables, and addresses the incorporation of sensing technologies to the method. Aktan et. al [3] state that a proper calibrated and validated FE model serves as an invaluable baseline for future conditions evaluations especially if a bridge exhibits distress signs following aging and deterioration.

It has been concluded [42, 25] that friction induced in the cable due to the presence of radial clamps and pretensioned wrapping along the cable span, guarantees that even if a wire breaks somewhere within the cable, it can partially or fully recover the tension load. Therefore, a considerable effort was placed on this work to understand and model the load transfer mechanism between wires in a main cable, so that an accurate assessment of the cable's remaining strength can be predicted. In particular, understanding the inter-friction mechanisms of broken wires, the load transfer between wires and the critical recovery length, also known as clamping length (the length from the fractured end at which the wire will regain its load carrying capacity), are significantly important issues in bridge design, evaluation, and maintenance.

Several models were proposed in the literature to study development lengths in parallel wires. Chen [12] and Costello [13] proposed an analytical method in which they estimated an effective development length based on the contact loads between the wires, Coulomb type friction, and Saint-Venant's principle. Raoof [33] extended this theoretical model to include the transition between the full-slip to no-slip friction

along the middle wire based on orthotropic sheet theory. Gjelsvikf [19] proposed a theoretical model for estimating the recovering length in a parallel wire strand where he showed that this length depends on pretensioned cable wrapping or clamping bands. Raoof [34], and Raoof [35] modified Gjelsvik's model to include different contact force estimates and transition of shear forces from no-slip to full-slip. Utting [49, 50] studied experimentally and analytically the response of helical wire strands, and showed that under axial loads, away from the strand boundaries there is no slipping between wires. This has been corroborated by a finite element model of Nawrocki [29] who later studied the energy dissipation due to friction [24]. Huang [23, 22] studied the effects of friction and interwire slip on the mechanical properties of axially loaded strands and investigated the frictional energy losses.

This research employs the finite element method to study the load transfer and recovery length in parallel high-strength steel wires commonly found in main cables of suspension bridges. To analyze the contact mechanics, a seven wire strand, with one inner wire and six outer wires, is studied: this can be viewed as the fundamental cell-unit of a main cable. The outer wires are axially pulled while the middle wire, slightly shorter than the outer wires, is left unloaded. The strand is radially tightened at several locations and the load is transferred to the inner wire through friction. The numerical model developed in this study relies on the experimental results provided by Noyan et. al. [31]: in this study, longitudinal strain within three parallel wires is measured at the center points by a neutron diffraction technique, showing that most of the load in the inner wire is recovered.

In this work we propose two simplified contact models that capture the load transfer and recovery length due to friction avoiding a full contact model. Full contact models solve a constrained optimization problem which is computationally expensive, slow and may not converge at all (if many contact points are considered) [53]. In our approach, elasto-perfectly plastic springs, with varying properties (stiffness or yielding

force), are placed at the contact points between objects. The idea is to determine the springs varying properties by considering the analytical Boussinesq solutions of a point force applied on a half space [47]. Specifically, Model I assumes that the springs are stiffer in the vicinity of the load and their stiffness decays away from the load (with a similar yielding assigned to all springs), and Model II assumes that the springs have the highest yielding in the vicinity of the load which decay when moving further away (holding the elastic constants fixed to the same value for all springs). We show that both models recover Coulomb friction law, agree well with the experimental results and are fast to converge. It is also interesting to note that when the springs are chosen to have similar properties (disregarding Boussinesq distribution), the proposed model recovers the well-known shear lag model, first introduced by Volkersen [51] and further developed by many researchers, e.g. [20, 14, 28, 27, 44]. This model is shown to be only applicable for weak and continuous contact loads.

The model is extended to the many parallel wire case and acccounts for random wire breaks. Hence, the model is generalized to take into account the re-distribution of the load among different layers of neighboring wires in the vicinity of a break, and the partial regaining of the carrying capability of the broken wire. More specifically, the model considers the friction decay along the cross section of the cable (from the outer wires to the inner wires), i.e. an outer broken wire, closer to the cable clamp, will be able to regain the load over a shorter distance than an inner wire which is further away from the compacting action of the clamp.

A suspension bridge is exposed to uncertain loading conditions that vary with time, traffic, and weather conditions [30]. In this analysis, a displacement controlled loading is used to tension the wires to a given load. During this loading process, and due to corrosion, individual wires snap at random locations and at a random sequence causing the load to be distributed between neighboring wires. We emphasize that a full contact model for many wires is unfeasible as it requires extensive computational

time and may not converge at all. Thus, this study predicts the load that will drive a main suspension bridge cable to failure due to corrosion in its wires.

The yield strength of aging wires is considered to be highly uncertain; thus, estimating the remaining strength of a suspension bridge cable is considered a stochastic mechanics problem. Bocchini and Dedoatis [7] emphasize that the only universal method to solve accurately any kind of stochastic mechanics problem is the Monte Carlo Simulation. The drawback of the Monte Carlo Simulation is the computational cost, thus the method is implemented on a parallel computer architecture to overcome the limitations in terms of storage and memory of serial machines.

Furthermore, a special effort has been made to introduce a general approach for estimating the yield strength of each wire of the suspension bridge cable along a prescribed length. This new method accounts for the spatial correlation of the cable strength, which occurs both within the cross-section (over different wires) and along the length of the cable. The strength of the cable is simulated as a 3D stochastic field by the spectral representation method. The probabilistic characteristics of the field are determined from data obtained from the Williamsburg bridge investigation and subsequent experimentation [42]. The yield strength of each wire along the length is interpolated from the cable's strength field. Moreover, the generation of the field is expedited by using the Fast Fourier Transform (FFT) technique, making the overall simulation computationally efficient.

The methodology to estimatate the cable's failure load is completed by incorporating the strength variation of the wires in the finite element model. The state of the axial stress is determined adaptively and a check to determine if it exceeds the yield strength of the elements is performed. As the cable is loaded, the sections of the wires that reach their yield strength will break. As the element breaks, the user friction model is activated as the spring elements start transferring load between wires. When such a break happens in one wire, the load in all other wires (depending on

their proximity to the broken wire) will automatically be adjusted and hence may enter a yield stress state which will lead to their failure, i.e. the domino effect. Due to the spatial correlation in the strength of the wires, localized clustering of broken wires are observed. The objective is to estimate the statistics of the failure load of the cable. This is accomplished through the Monte Carlo Simulation by generating a number of realizations of the cable's strength within the FE model and obtaining the failure load for each realization. Then the statistics are estimated by ensemble averaging and fitting the best distribution to the data.

As state of the art technology in the health monitoring field becomes available, it should be incorporated to the proposed methodology in order to provide authorities with very accurate means to determine the safety and maintenace of supension bridge cables. Sensors for corrosion monitoring have become available both in direct and indirect approaches. Direct sensors provide the corrosion rate of the wires and indirect sensors indicate the environmental conditions inside a cable, such as temperature and relative humidity which are related to the corrosion rate of the wires. The recorded data from the sensors will help predict the cable's reliability both at the current time and the future. The evolution of the reliability/strength of the cable with time is expected to be a deteriorating one.

1.2 Literature Review on Current Standard Approaches

The current standard approaches to determine the strength of the cable involve removing wires from an actual cable and subsequent experimentation. The characteristics of the field are obtained from the experimental data and the strength of each wire of the cable is estimated based on probabilistic approaches. It is emphasized that no previous methodology has incorporated a stochastic finite element analysis to determine the

strength of the cable. In detail, the extraction and testing of wires procedure involves the following steps: (1) select a number of wires within the cable's cross-section that provides a representative pool of all sectors of the cable; (2) cut and remove the wires from the cable (usually the removed wires are 6-12 m (20-40 ft) long to obtain data of the wire's strength along the length) (3) cut each wire in a series of segments of unit length (this is usually a length of approximately 30.48 cm (1 ft)) ; (4) test each one of the unit-length segments for strength.

Then, calculating the strength of the cable consists on the following procedure: (1) determine the probability distribution of the strength of the unit-length wire segments, (2) calculate the strength of a wire of prescribed length based on the probability distribution of the strength of the unit length segments; and (3) establish the strength of the entire cable's cross section made of a prescribed number of parallel wires. The prescribed length is usually linked to the recovery length of the wires.

There are essentially five basic methods to determine the strength of the cable. These methods vary on how the strength of a wire consisting of n unit-length segments is estimated. All of the variations assume that the strength of a wire is the minimum of the n strengths of the n unit-length segments, this assumption is known as the weakest link model. The idea behind it is that the wires are most likely to fail at their weakest point; thus, determining the overall strength of that wire. Four of these methods treat the strength of each segment as independent, which means that the corresponding n strengths are uncorrelated. Although this assumption of independence is very good for brittle and quasibrittle materials, it is not good for ductile materials like steel. The variations used by the methods are the following: (1) using the exact extreme value distribution (EVD) of the smallest value (denoted by Exact EVD); (2) using the Type I asymptotic distribution of the smallest value (denoted by Type I EVD); (3) using the Type III asymptotic distribution of the smallest value, also known as the Weibull distribution and denoted by Type III EVD; and (4) using Monte Carlo

simulations reflecting the extreme value distribution (simulating independent and identically distributed random variables and denoted by IID R.V.). The (5) fifth approach contradicts the other four methods by accounting for the spatial correlation of the strength along the length of a wire and simulating the strength of wire as a one dimensional non-Gaussian random field. This approach also considers a Monte Carlo Simulation to obtain the statistics of the strength of the cable.

1.2.1 Exact Extreme Value Distribution

After determining the initial distribution, the probability distribution of the random variable modeling the strength of unit-length wire segments, the distribution of the strength of a wire of prescribed length can be easily established using the exact extreme value distribution (EVD) of the smallest value, (refer to [5] and [2]). Various distributions have been suggested for the initial distribution including the normal, the lognormal, and the beta. Although the normal (Gaussian or bell curve) is not an appropriate choice from the theoretical point of view (as it allows the strength of a unit-length wire segment to assume negative values, something that is physically impossible), it often provides reasonably good estimates when compared to distributions that assume only non-negative values, as it has been found to match laboratory results of strengths of unit-length wire segments quite closely. The left tail of the normal becomes negligibly thin for negative values of the strength. To be rigorous from the theoretical point of view, it is recommended to use a distribution that assumes only non-negative values e.g., lognormal and beta.

1.2.2 Type I Exact Value Distribution

The Type I asymptotic distribution of the smallest value is obtained when the initial distribution is of exponential type to the left and the number of unit-length segments n becomes large (refer to [5] and [2]). This distribution has the same theoretical

problem as the exact EVD used in combination with the normal distribution as initial distribution. Despite this theoretical problem, the Type I asymptotic distribution of the smallest value has been found to provide reasonably good estimates for the strength of a wire of prescribed length.

1.2.3 Weibull Distribution

The Type III asymptotic distribution of the smallest value, also known as the Weibull distribution, is obtained when the initial distribution is limited to the left (usual value assumed for the lower limit is zero) and the number of unit-length segments n becomes large e.g., (refer to [5] and [2]). This distribution apparently does not have the theoretical problem of the Type I EVD mentioned above, and for this reason it should be preferred over the Type I.

1.2.4 Simulation of Independent and Identically Distributed Random Variables

This Monte Carlo based approach is essentially equivalent to numerically computing the results of the Exact EVD approach several times and obtaining the statistics of all the realizations performed. This approach involves the following steps: (1) model the wire of prescribed length as n uncorrelated random variables each describing the strength of a unit-length wire segment; (2) generate n unit-length wire segment strengths from a prescribed initial distribution e.g., lognormal, beta; (3) determine the smallest strength out of the n generated strengths (this is the strength of the wire of prescribed length); and (4) repeat steps 2 and 3 a large number of times (e.g. 1,000-100,000) to establish the statistics of the strength of a wire of prescribed length.

In general, the IID R.V. approach is more expensive computationally than either one of the three EVD variations. The aforementioned standard approach was introduced in

the technical report by Steinman et al. [42] as part of the cable investigation program of the Williamsburg Bridge in New York City. Steinman et al. assumed a Gaussian distribution for the strength of 1-ft-long wire segments (initial distribution) and then used the IID R.V. approach. Matteo et al. [25] used the same initial distribution from the Steinman et al. report, introduced the Type I EVD approach, and compared it to the IID R.V. approach. In 1997, Haight et al. [36] studied the cable safety factors against failure for the main cables of four suspension bridges using the Type I EVD approach. In 1998, Perry [32] suggested using the Type III EVD model for the reliability analysis of the Williamsburg Bridge cables . In 2003, Camo [11] suggested a Gaussian distribution-based simulation technique.

1.2.5 Wire Strength as a Random Field

Shi et. al [54] introduced a general methodology for estimating the strength of suspension bridge cables, accounting for the spatial correlation of wire strength along its length. The main difference compared to previous approaches is that the strength of a wire of length equal to n unit-length segments is modeled as one dimensional random field (or equivalently as n correlated random variables). More details of this approach are provided in Chapter 4 as the proposed methodology in this dissertation can be considered as an extension of this method.

1.3 Outline of the Dissertation

The dissertation is organized in the following way. Chapter 2 introduces the spring model used to account for frictional behavior throughout the examples provided in this research work. The model is validated by matching the results provided by an experimental test performed on a seven wire strand to consider load recovery on a broken wire. Chapter 3 develops the finite element model that is used to drive

a simulated main cable composed of 9061 wires to failure. The chapter illustrates how the model accounts for random wire breaks and load recovery in broken wires. Numerical examples were performed for various sized wire strands, since it is easier to track the random wire break sequence and the redistribution of the stresses between neighboring wires on a smaller number of wires. This chapter also illustrates the parallel implementation of the model required to expedite the solution. The numerical examples provided valuable observations to finalize the model for 9,061 wires. Memory and speed limitations indicated that one dimensional truss elements were essential to facilitate a full stochastic analysis of the problem. In Chapter 4, a three dimensional random field that simulates the varying strength capacity in the cable is proposed in order to account for the spatial correlation of the cable's strength, which occurs both within the cross section (over different wires) and along the length of the cable. Data from wires that were removed from the Williamsburg Bridge is used to develop the power spectrum needed to generate the sample realizations according to the Spectral Representation Method for three dimensional stochastic fields. Chapter 5 includes the Monte Carlo run for the simulated main cable, showing the failure mechanism for a suspension bridge cable and providing the statistics of the cable's failure load. Chapter 6 concludes this dissertation providing the major results and offers recommendations to improve the model and ideas for future research.

Chapter 2

Proposed Contact Friction Model

2.1 Chapter Summary

A simplified semi-analytical contact-friction approach is proposed to study the load transfer between tightened parallel steel wires, commonly used in suspension bridge main cables. The approach is based on placing elasto-perfectly plastic spring elements at the contact region between the objects. These springs have varying stiffness (Model I) or yielding (Model II) depending on their proximity to the clamping loads. Closer to this force, their stiffness or yielding is the highest and it decays when moving further away from the clamp. This decayed behavior is assigned according to Boussinesq's well known solution to a point load (applied on a half space). Both models converge quickly compared to a full contact model, and recover Coulomb friction law on a 2D benchmark problem. Moreover, when the same properties are chosen for all springs (disregarding Boussinesq solutions), the models reduce to the classical shear-lag model, which for high clamping (point) loads gives inaccurate results.

The spring models are validated experimentally on a seven wire tightened strand. In this case study, the outer wires are axially pulled, while the middle wire, slightly shorter than the outer wires, experiences no direct applied axial load. However, since the strand is radially fastened at several locations, the axial load is transferred to the inner wire by inter friction mechanism between the wires. The strains at the center points of the outer and inner wires are measured via neutron diffraction, for different clamping loads, showing that the inner wire is capable of recovering most of the load.

2.2 Theoretical Contact Models

2.2.1 Coulomb's Friction

Coulomb's model is the classical friction law widely used in engineering, e.g. [53]. This law is given by the following inequality :

$$F_T \leq \mu F_N \tag{2.1}$$

where μ is the friction coefficient (an empirical property of the contacting materials), F_N is the normal (contact) applied force and F_T is the resulting tangential force due to friction in a direction that is opposite to the motion that the object would experience in the absence of friction. The law assumes that once F_T is above a certain limit then the contacting surfaces no longer stick together but move with a relative displacement u_T. Hence, the inequality in Eq. (2.1) represents two conditions: Stick and Slip. Stick occurs when $F_T < \mu F_N$ and the relative displacement is $u_T = 0$, while slip occurs when $F_T = \mu F_N$ and the relative displacement is $u_T \neq 0$.

2.2.2 Shear Lag Model

The shear lag model was developed for predicting stress transfer between two perfectly bonded linear elastic materials. A rich literature is available on the shear lag model, e.g. the work on cemented joints [20], fibrous materials [14] and thin film composites [27, 28]. The main assumption of the shear lag model is that there exists a small interface layer, of some thickness η, in between the two objects which transfers stresses through shear. This interface layer is assumed to be linear elastic and isotropic, with a shear modulus of G_0, as depicted in Figure 2.1. From direct equilibrium considerations, the shear stress τ_0 in the intermediate layer at an arbitrary location x, can be written

as

$$\tau_0(x) = \frac{G_0}{\eta}[u_1(x) - u_2(x)] = \frac{G_0}{\eta}[\![u(x)]\!] \tag{2.2}$$

where $[\![u(x)]\!]$ is the relative displacement (displacement jump) between the two elements.

An approximate solution to the resulting stress σ_x^1 in the x-direction (as illustrated in Figure 2.1), given in [27, 28] is

$$\sigma_x^1(x) \cong \sigma_0^1 \left[1 - \frac{\cosh(\beta x)}{\cosh(\beta L)}\right] \tag{2.3}$$

where σ_0^1 is a constant given in [27, 28], and β is given by

$$\beta = \sqrt{\frac{G_0}{\eta}\left(\frac{1-\nu_1^2}{E_1}\right) \times \left[\frac{1}{t_1} + \frac{\alpha}{t_2} + \frac{3(t_2+t_1)^2}{t_2^3 + \frac{t_1^3}{\alpha}}\right]} \tag{2.4}$$

and α is the ratio

$$\alpha = \frac{E_2}{E_1}\left(\frac{1-\nu_1^2}{1-\nu_2^2}\right) \tag{2.5}$$

where E and ν are the Young's modulus and Poisson's ration of the two materials, respectively, while t_1 and t_2 are the thicknesses of the two materials.

2.2.3 Boussinesq's Solution to a Point Load

The shear lag model does not account for the normal forces (e.g. induced by the radial clamps in the seven wire experiment or by the wire compaction). On the other hand, Boussinesq's solution to a point load applied on a half space [48, 47] provides a theoretical way to incorporate these normal forces into a numerical model.

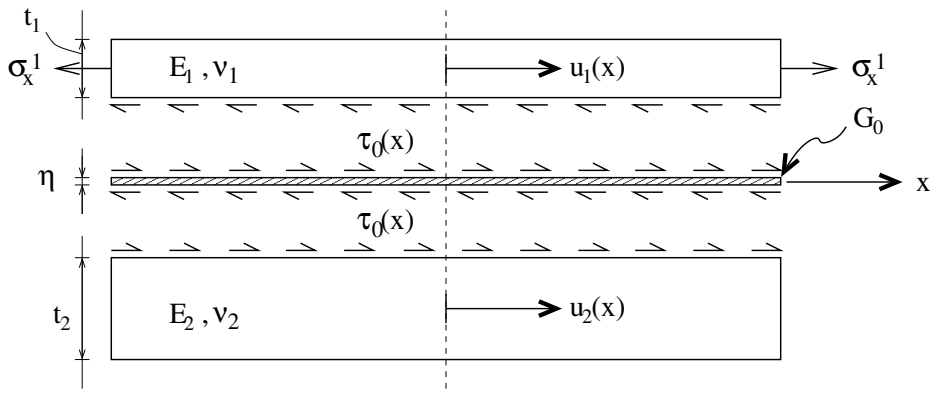

Figure 2.1: The Shear lag model assuming a fictitious interface layer that transfers shear stresses

Boussinesq's solution is given by

$$\sigma_z = \frac{-3P}{2\pi z^2}\left(\frac{1}{1+(r/z)^2}\right)^{5/2} \tag{2.6}$$

where P is the applied load, r is the distance in the x-y plane from the force and z is the depth at which the stress is computed. Figure 2.2 illustrates Boussinesq's stress distribution in the z-direction. It can be seen in Figure 2.2(b) how the stress decays away from the force. The normal stress in either x or y directions (here denoted by k), perpendicular to the normal force, is given by

$$\sigma_k = \frac{-P}{2\pi r^2}\left[\frac{3k^2 z}{r^3} - (1-2\nu)\left(\frac{z}{r} - \frac{r}{r+z} + \frac{k^2(2r+z)}{r(r+z)^2}\right)\right] \tag{2.7}$$

2.3 Simplified Numerical Techniques: Spring Models for Frictional Behavior

The proposed approach is based on placing elasto-perfectly plastic spring elements at the contact regions between the objects. These springs have varying stiffness (Model I)

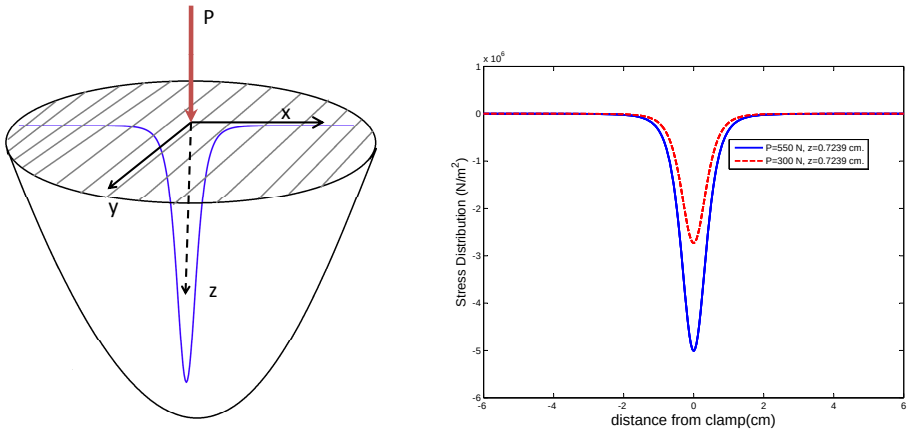

(a) (b)

Figure 2.2: Boussinesq's problem. (a) point force on a surface and stress decay away from the force. (b) Stress distribution in the z-direction due to point forces with different magnitudes.

or yielding force (Model II) depending on their proximity to the contact loads. Closer to the force, their stiffness or yielding is the highest and it decays when moving away from the contact points. This decaying behavior is obtained by Boussinesq's solution to a point load applied on a half space (see Section 2.2.3). Both models converge quickly compared to a full contact model, and recover Coulomb friction law on a 2D benchmark problem shown at the end of this section. Moreover, when the same properties are chosen for all springs (disregarding Boussinesq solutions), we show that the contact model reduces to the classical shear-lag model, which for high normal loads gives inaccurate results.

2.3.1 Linear Constant-Springs Model

The shear lag model described in Section 2.2.2 provides a simple way to model the friction between wires by introducing an artificial layer which only sustains shear stresses. A "shear force" F_τ is obtained by multiplying Eq. (2.2) by the thickness η

such that

$$F_\tau(x) = \eta\tau_0(x) = G_0[u_1(x) - u_2(x)] = G_0[\![u(x)]\!] \tag{2.8}$$

In principle, this equation is exactly equivalent to a linear spring law given by

$$F_\tau(x) = K[u_1(x) - u_2(x)] = K[\![u(x)]\!] \tag{2.9}$$

where K is the spring constant which does not change as a function of x. Hence the shear lag model is equivalent to employing springs with constant parameters. Figure 2.3(a) illustrates the shear lag model behavior as compared with the Coulomb's friction law. Note that the shear lag model is quite different from Coulomb's friction law.

2.3.2 Model I: Elasto-perfectly Plastic Springs Model with Similar Yielding and Varying Spring Constants

The shear lag model can be enhanced by considering an elasto-perfectly plastic spring behavior. Here, the springs deform elastically up to a certain value of the force after which they simply continue to deform plastically. The plastic deformation of the spring models the slip mechanism of Coulomb friction. To account for the attenuating pressure imposed by the contact forces, the spring constants are assumed to be a function of their position with respect to the location of the applied force. In other words, springs that are closer to the clamping force are modeled by a larger elastic stiffness than springs further away. Moreover, this model assumes that all springs have a similar yielding force. An illustration of this model is shown in Figure 2.3(b). The elastic stiffness of the springs varies as a function of the longitudinal coordinate according to Boussinesq's solution shown in Figure 2.2(b), with K_1 representing the closest spring to the force and K_4 the farthest. Boussinesq's solution can be used to

distribute the values of the spring stiffnesses in between the objects in contact (in the longitudinal direction). By indicating with x the distance between the point of application of the clamping force and the location where the spring is placed, the stiffness of a spring at a distance x from the normal force can be expressed as:

$$K = K_0 \frac{\sigma(x)}{\sigma(0)} \tag{2.10}$$

where K_0 is the stiffness of the spring under the force while $\sigma(0)$ and $\sigma(x)$ represent the stresses under the force and at some distance x, respectively.

2.3.3 Model II: Elasto-perfectly Plastic Springs Model with Similar Stiffness and Varying Yielding

A second model based on elastic-perfectly plastic springs is considered. In this model, it is assumed that the predefined yielding force of the springs varies while keeping the elastic spring modulus constant for all the springs. Thus, springs that are closer to the clamping force have higher yielding than springs that are further away. Similar to Model I, the yielding force varies with the Boussinesq distribution shown in Figure 2.2(b). An illustration of this model is shown in Figure 2.3(c). By indicating with x the distance between the point of application of the contact force and the location where the spring is placed, the yielding force of a spring at a distance x from the radial clamp can be expressed as:

$$F_T(x) = F_T(0) \frac{\sigma(x)}{\sigma(0)} \tag{2.11}$$

where $F_T(0)$ is the yielding force of the spring under the force while $\sigma(0)$ and $\sigma(x)$ represent the stresses under the force and at some distance x, respectively.

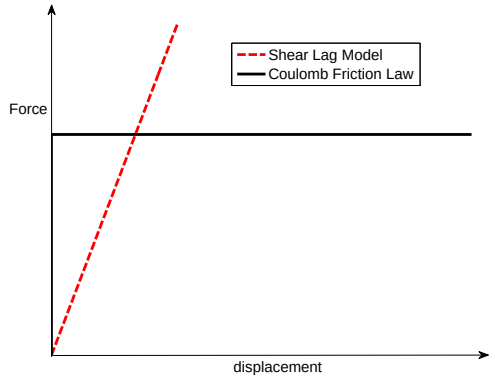

(a)

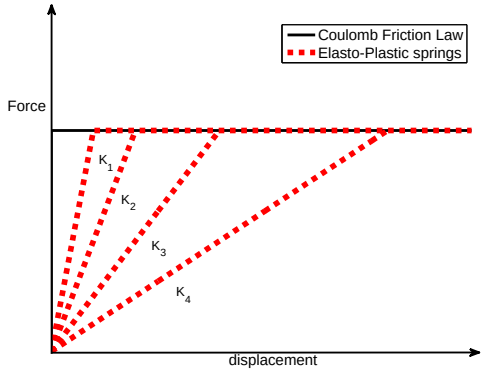

(b)

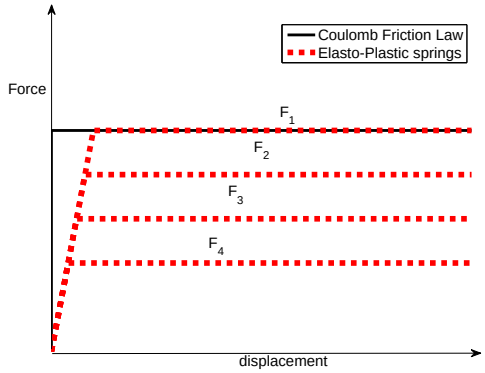

(c)

Figure 2.3: Spring Models. (a) Shear Lag (linear spring) model as compared to Coulomb friction law, (b) Model I: elasto-perfectly plastic springs with varying spring constants as compared to Coulomb friction law ,(c), Model II: elasto-perfectly plastic springs with similar elastic behavior but different yielding forces as compared to Coulomb friction law

2.3.4 Comparison Between the Models on a 2D Benchmark Problem

To validate the spring models as compared to the actual friction law (a full scale contact simulation), two steel plates in contact with each other were analyzed. The 2D model consists of two 10 cm long steel plates with a width of 0.7239 cm (3 wire-radii); the left end of both plates is fixed and the bottom edge of the lower plate is only free to deform along the longitudinal x-direction. A tension pressure of 60 MPa is applied to the upper plate on the right boundary and a concentrated (clamping) load is applied in the center, 5 cm from the ends, as illustrated in Figure 2.4. The finite element model implemented in Abaqus consists of 909 nodes and 800 elements. The elements are plane stress, 4 noded quadrilaterals. Three different cases were considered by adjusting the concentrated load in order to get different levels of recoveries in the lower plate. The full contact model was run by assuming a friction coefficient parameter μ of 0.4 and the spring stiffness parameters, which were calibrated with the friction results for each model, are illustrated in Table 3.1. Figure 2.5 shows the results obtained for each clamping case for the three spring models as compared to the full contact analysis, and Figure 3.11 shows the shear force at the springs as compared to the force obtained from the full contact model. Note that all spring models can be calibrated to capture the final load regain level at the end of the plate. However, the linear spring model does not predict well the overall behavior: the stress distribution along the plate and the shear forces do not agree with the full contact model. On the other hand, the other spring models I and II are in excellent agreement with the contact model except for the left boundary in Figure 3.11 which introduces some numerical artifacts in the full contact model. It is also interesting to point out that a kink is observed in Figure 2.5(b) for all models at the location of the clamp. This behavior can be explained by plotting Boussinesq equation in the longitudinal direction given by Eq. (2.7) and illustrated in Figure 2.7. It can be seen that a concentrated force introduces

stress in the direction perpendicular to the force with the same characteristics to the stress behavior observed in Figure 2.5(b). The magnitude of the spike depends on the magnitude of the force.

While a full contact model is more accurate, it is computationally more expensive to use and the contact algorithm may not converge, in particular when many contact points are considered. The computational justification for the elasto-perfectly plastic spring models are given in Table 2.2, where we report the number of iterations required by each method to converge for the 2D benchmark problem as the contact forces increase in magnitude. The iteration is terminated when the force residual is less than 5×10^{-3} or if the number of iteration exceed 16.

It is clear that the full contact model only converges when the normal forces are less than a certain magnitude ($4500N$ in the example) while the spring models converge for any force with almost the same number of iterations. For these models the number of iterations will be determined by the number of springs entering the plastic region.

To summarize, using distributed elasto-plastic springs gives an attractive and computationally efficient way to model friction and load transfer, in particular for the seven wire problem studied in the next Section. This advantage becomes even more evident when considering a problem with many contact points such as a full scale main cable. It is also important to emphasize that although the 2D benchmark problem presented in this Section is not exactly equivalent to the 3D circular surfaces problem (presented in Section 2.5), in both cases the contact is due to a point load and occurs along a line. Hence the simplicity of the 2D problem provides a way to validate the general contact methodology.

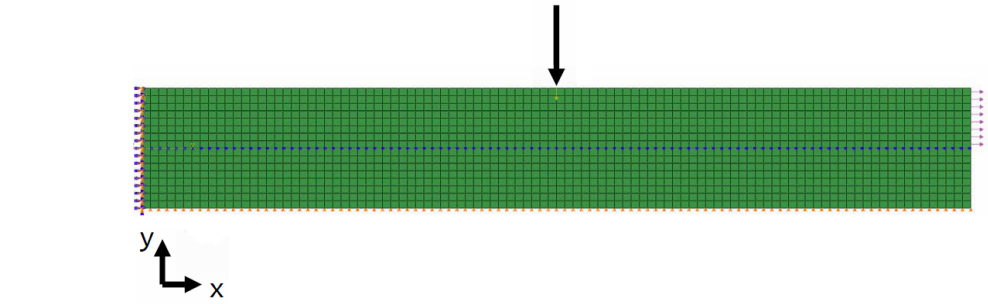

(a)

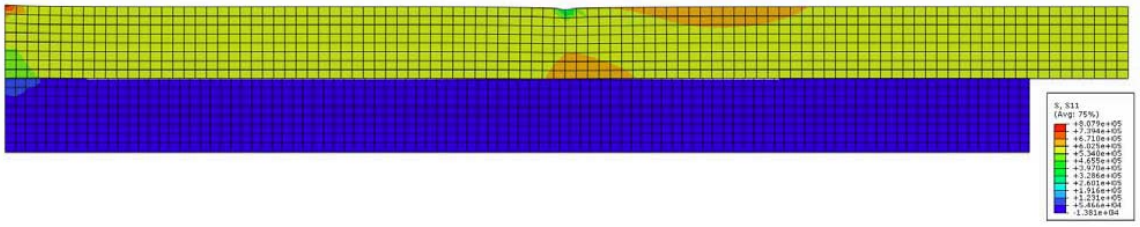

(b)

Figure 2.4: Example problem employed in the analysis (a) problem definition: an upper plate is in tension and frictional contact with another plate due to a point force. Fixed b.c. are applied on the left end and rollers on the lower plate edge. For the Spring Models, springs (shown as blue dots) are placed at the contact points along the length of the plates.(b) Stress and deformed shape in the horizontal direction

Table 2.1: Parameters of the Spring Models for the 2D Plate Analysis.

Spring Model	**Parameters**[1]	**Clamping Forces**		
		550 N	1500 N	3000 N
Shear Lag Model	K	200	650	1900
Spring Model I	K_{max}	2000	6500	25000
	K_{min}	9	29	114
	$K_{average}$	213	693	2666
	F_T	25	65	140
Spring Model II	$F_{T,max}$	25	65	140
	$F_{T,min}$	0.11	0.29	0.63
	$F_{T,average}$	2.66	6.93	14.93
	$K_{elastic}$	2000	6500	25000

[1]The stiffness K is given in units of [KN/m] and the yielding force F_T in [N]

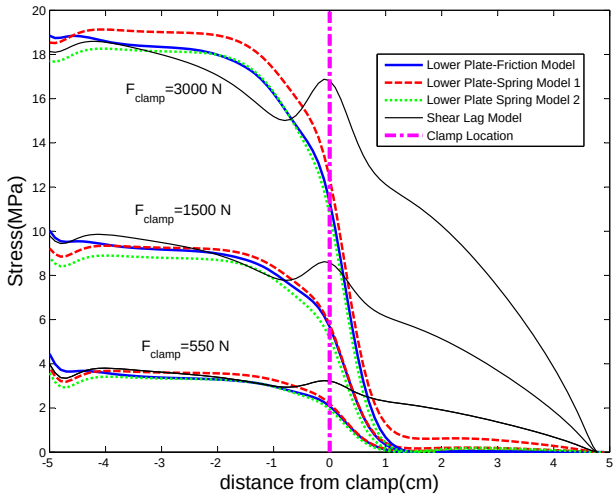

(a)

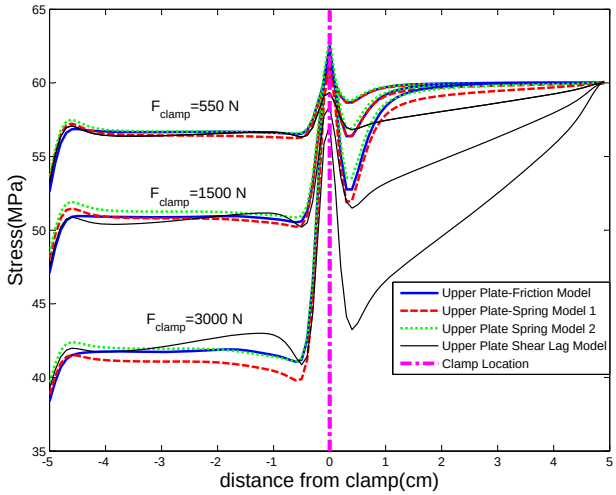

(b)

Figure 2.5: Stress curves comparing the contact obtained from friction and the springs models (a) Stress in the lower plate in the x-direction for three different clamping forces (b) Stress in the upper plate in the x-direction for three different clamping forces.

2.4 Modeling the Load Transfer and Recovery Length in Parallel Wires

The spring models developed in the previous Section are validated experimentally on a seven wire tightened strand, subjected to a tensile load. In this case study, the outer

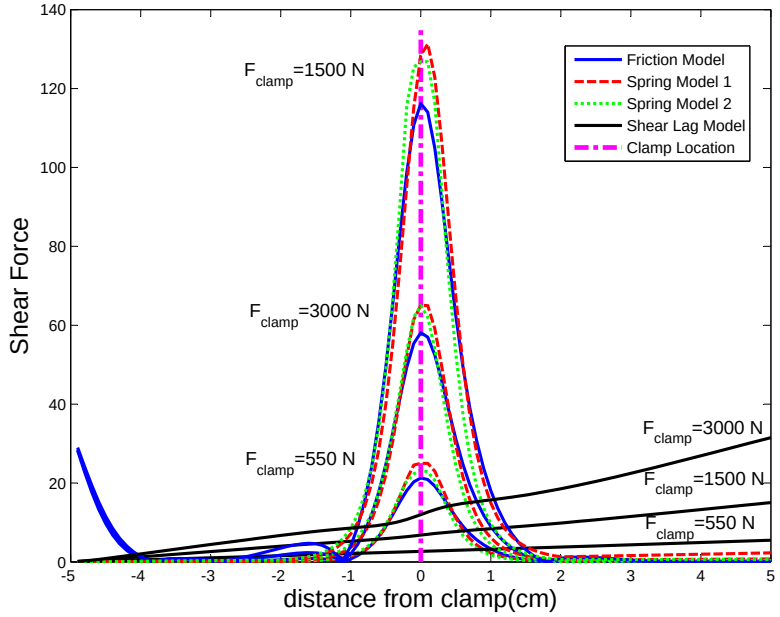

Figure 2.6: Shear forces in the spring models compared to the forces from the full contact model

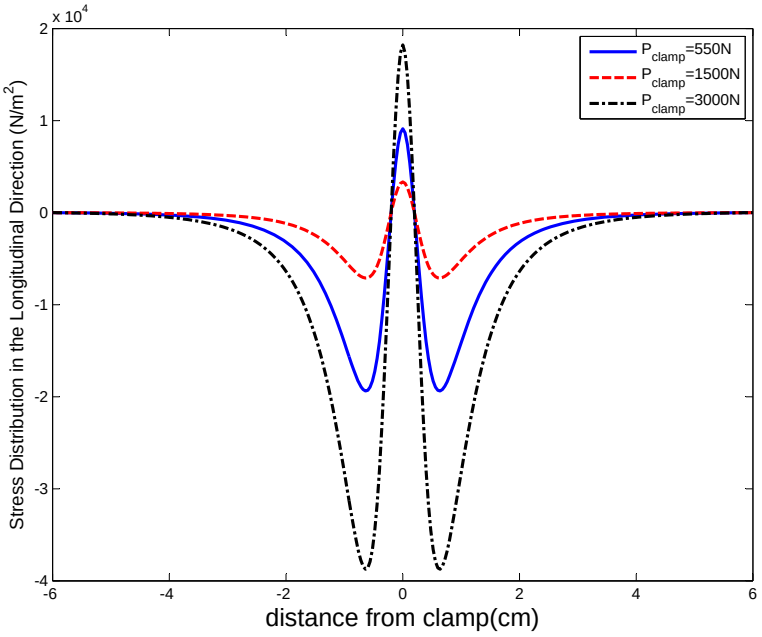

Figure 2.7: Longitudinal Stress distribution provided by Eq. (2.7) due to a force in the normal direction.

wires are axially pulled, while the middle wire, slightly shorter than the outer wires, is axially unloaded. However, since the strand is radially tightened at several locations,

Table 2.2: Number of iterations to converge on the two plate contact problem for different models

Model	Contact Force (N)	Number of Iterations
Full Contact Model	$550 \leq F_N \leq 4500$	3
	$F_N \geq 4500$	Not converging
Spring Model I	$550 \leq F_N \leq 4500$	1
	$F_N \geq 4500$	2
Spring Model II	$550 \leq F_N \leq 4500$	2
	$F_N \geq 4500$	2

the axial load is transferred to the inner wire by inter friction mechanism between the wires. The experimental and numerical details are given in the following subsections.

2.4.1 Experimental Details

The experimental system consisted of a standard seven wires strand, socketed at both ends with a total clear length of 31 cm and clamped in this condition using standard wire clamps as shown in Figure 2.8. The outer six wires were centered at the vertices of a regular hexagon. The seventh core wire, located at the center of the hexagon, was 10 mm shorter than the outer wires and terminated before the end sockets. One radial band was placed 2.5 cm away from each fixed end. The experiments were conducted on the following three configurations: (1) tightly clamped, (2) loosely clamped, and (3) unclamped. In the tightly clamped case, the strand was tightened to above 135 N-m while, in the loosely clamped configuration, the strand was tightened to 14 N-m. In the unclamped case, one clamp was removed while other one was moved into the center of the bundle and clamped finger-tight. The sample was then mounted on an Instron hydraulic tensile tester and loaded in-situ on the SMARTS neutron diffractometer at the LUJAN center of Los Alamos National Laboratory. The Instron controller monitored the applied load, the cross-head displacement and the macroscopic strain

in one of the bottom wires of the bundle through an attached extensometer. At each load level, the longitudinal and transverse atomic lattice strains ϵ_{xx} and ϵ_{yy} ,within the three central wires (Far, Center and Near) at the bundle mid-length were measured using a 2mm $\times$ 2mm neutron beam. More details on the experimental setting are provided by Noyan et.al.[31].

Figure 2.8: Experimental setup of the seven wire parallel strand. More images on the experimental setting are provided by Noyan et.al. [31].

2.4.2 Theoretical Considerations and Definition of a Load Regain Parameter

A general simplified one dimensional equilibrium analysis (considering the center line of the wires) can reveal the relation between the longitudinal strain of the outer wires and the strain in the inner one (see Figure 2.9 for illustration). Here, the total force carried by the wires at the cross-section a-a (defined at some x=$\frac{L}{2} - \delta$ where $0 \leq \delta \leq s$ and s is some distance between the end section of the center wire and the cross-head) is

$$F_{a-a} = \sigma^{out} \sum_{out} A = E\epsilon^{out}_{a-a} 6A \tag{2.12}$$

where A is the area of the single wire and the superscript "out" is used to indicate outer wires. At any other cross section, for instance b-b (defined between $0 \leq x \leq x_c$

where x_c indicates the location of the radial band), the forces are shared between all wires

$$F_{b-b} = \sigma^{out} \sum_{out} A + \sigma^{in} \sum_{in} A = E\epsilon_{b-b}^{out} 6A + E\epsilon_{b-b}^{in} A \tag{2.13}$$

where the superscript "in" is used to denote the inner wire. The force carried by the wires (or the strain sustained by the wires) depends on the bonding and slipping mechanism. In general, the internal (interface) force (shown in Figure 2.10) can be defined as either due to friction or to bonding:

$$\bar{f}^{int} = (1-\beta) \cdot f^{friction}(P,\mu) + \beta \cdot f^{bonding}(F) \qquad \beta = 0, 1 \tag{2.14}$$

where $f^{friction}$ is the friction component and can be considered a function of the contact force P and the friction coefficient μ (which is a material parameter) while the bonding component, $f^{bonding}$, is only a function of the applied load F. The contact mechanism parameter β (0 or 1) is introduced to describe the contact mechanism that generates the internal force. The following cases are possible: (i) $\beta = 1$ represents the case of pure bonding (e.g. welding, glue or chemical reaction), and (ii) β=0 indicates the case of pure friction due to an applied radial load P such that

$$\bar{f}^{int} = \begin{cases} f_{\beta=0}^{friction}(P,\mu) & \text{if} \quad \beta = 0 \qquad \text{pure friction} \\ f_{\beta=1}^{bonding}(F) & \text{if} \quad \beta = 1 \qquad \text{pure bonding} \end{cases} \tag{2.15}$$

Note that the highest friction force (assuming perfect pure friction and perfect pure bonding) must satisfy the condition that

$$f_{\beta=0}^{friction} \leq f_{\beta=1}^{bonding} \tag{2.16}$$

since the friction mechanism is expressed as:

$$f_{\beta=0}^{friction} = \begin{cases} F & \text{if} \quad F < \mu P \\ \mu P & \text{if} \quad F > \mu P \end{cases} \tag{2.17}$$

Figure 2.10 illustrates the friction force obtained by application of the tension load F. At this point, it is important to define a load (strain) regain parameter χ ($0 \leq \chi \leq 1$) to denote the level of strain that is regained by the central wire at $x = 0$. In other words, this parameter defines whether the entire load has been converted to friction and applied to the center wire or a part of it has been lost due to slip (e.g. converted into heat and/or sound and dissipated). By this definition, full strain regain occurs when $\chi = 1$ (the red region in Figure 2.10) and the central wire regains its full load at the center. On the other hand, partial strain regain occurs when the external force increases while the friction force has reached its limit, i.e. μP. This implies that the load regain parameter must satisfy the condition $\frac{\mu P}{F} \leq \chi \leq 1$, with the pure slip case $\chi = 0$ corresponding to the condition:

$$lim_{F \to \infty} \ \chi = 0 \tag{2.18}$$

By this definition, the actual interface force f^{int} between an outer wire and the inner one can be expressed by

$$f^{int} = \chi \cdot \bar{f}^{int} \tag{2.19}$$

From direct force equilibrium of the seven wire strands shown in Figure 2.11, one gets:

$$F_{b-b}^{in} = 6f^{int} \tag{2.20}$$

$$F_{b-b}^{out} = \frac{F}{6} - f^{int} \tag{2.21}$$

$$F_{b-b} = 6F_{b-b}^{out} + F_{b-b}^{in} = 6\left(\frac{F}{6} - f^{int}\right) + 6f^{int} = F = F_{a-a} \tag{2.22}$$

where F_{b-b}^{in} and F_{b-b}^{out} are values of the internal forces in the inner and outer wires, respectively, at the b-b cross-section. The number "6" at the right side of Eq. 2.20 indicates that there are 6 contact lines applied to the center wire due to the wires packing. Thus, in a general scenario, considering only the right half of the cable ($0 \leq x \leq \frac{L}{2}$-s), one can obtain the following relation between the axial strains of the inner and outer wires at a location x and those at one of the ends:

$$\epsilon^{in}(x) = 6\epsilon_{a-a}^{out} - 6\epsilon^{out}(x) \tag{2.23}$$

where $\epsilon^{in}(x)$ must be a nonlinear function which ends at zero (due to the free end) and begins at a value that is close to ϵ_{b-b}^{out}, depending on whether full or partial regain of stress in the wire is obtained. Mathematically it is written as

$$\begin{cases} \epsilon^{in}(x=0) = \chi \cdot \epsilon^{out}(x=0) = \chi \cdot \epsilon_{b-b}^{out} \\ \epsilon^{in}(x=\frac{L}{2} - s) = 0 \end{cases} \tag{2.24}$$

Figure 2.12 illustrates several possibilities for partial regain of strain and recovery lengths (rate of regain) in the inner wire. It is noteworthy that Figure 2.12 is not analogous to the shear lag model (where the plateau region occurs) at the center but corresponds to the full contact model with different clamping forces (where the plateau region may initiate farther from the center). All the curves are shown to regain 85% of the load, but they are differentiated by the rate of regain. The rate of regain is in

direct correlation with the clamping force (up to a certain limit).

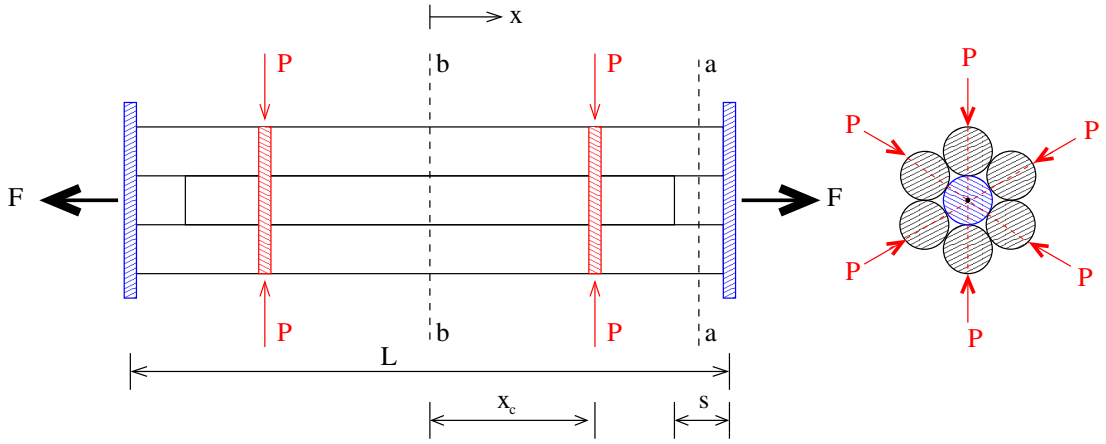

Figure 2.9: Two dimensional simplification of the seven wire problem

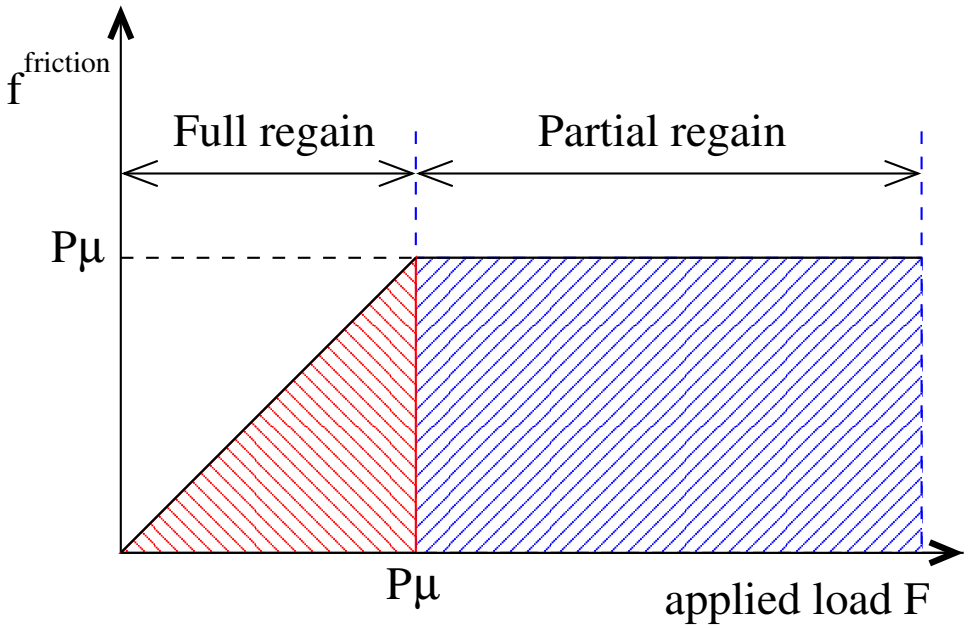

Figure 2.10: Friction force obtained due to applied tension load F. Triangular area showing full strain regain $\chi = 1$ and rectangular area showing partial strain regain $0 \leq \chi \leq 1$ of the middle wire

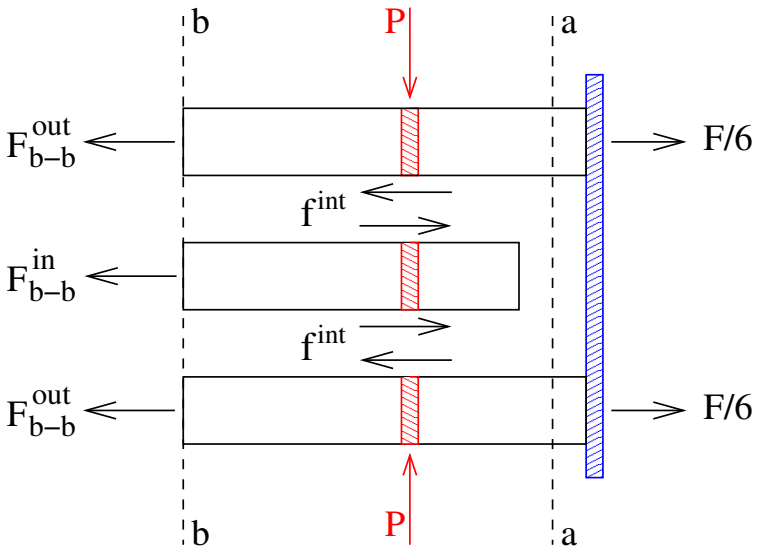

Figure 2.11: Two dimensional force diagram showing the friction mechanism in the wires

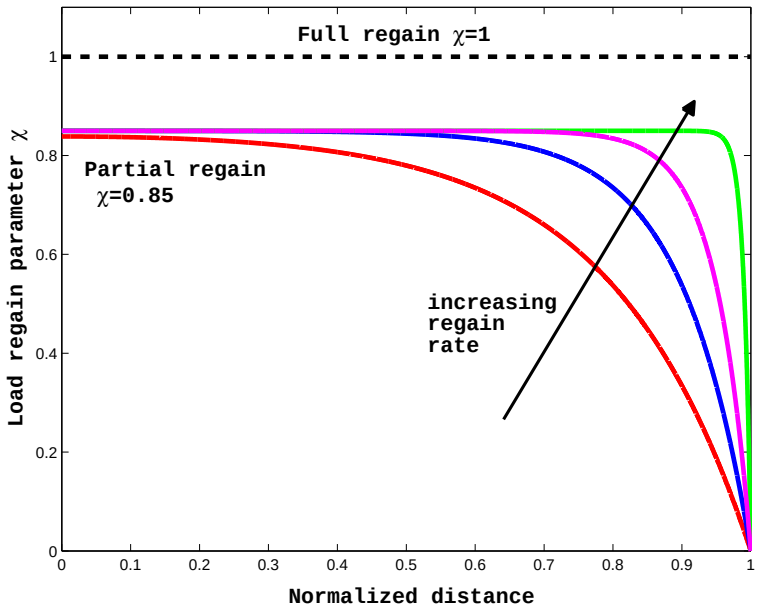

Figure 2.12: Various recovery lengths and strain regain rates in the inner wire corresponding to different friction loads and $\chi = 0.85$.

2.5 Numerical Results: Modeling the Seven Wire Problem

The seven wire model is implemented in ABAQUS [21] to study the load transfer mechanism in wires due to friction induced by the radial clamps. The problem is modeled assuming symmetric boundary conditions and the radial clamps are modeled as point forces at the contact points. Figure 2.13 illustrates the finite element mesh, boundary conditions and the point forces. The outer wire's length (assuming half a model) is 15.5 cm and the inner wire is 14.5 cm long. Hexagonal (brick) elements with a total of 9,460 elements and 11,322 nodes were used. The contact points between the outer wires and the inner are modeled by placing springs at the overlapping nodes (see Section 2.3). To insure in plane contact between all wires, stiff springs with a 10^{11} N/m stiffness constant are placed along the y and z directions and elasto-perfectly plastic springs are used in the x-direction. The results are first presented for the tightly clamped case (strong radial bands), then for loosely clamped case, and finally for the "finger" clamped (unclamped) case.

2.5.1 Tightly, Loosely and Finger Clamped Case Studies

The tightly clamped case illustrates the behavior of the seven wire strand when the radial forces are very large: in this case, the central wire, although not being pulled directly, carries almost 94% of the load carried by the outer wires. The loosely clamped case illustrates the behavior of the seven wire strand when the radial bands are only weakly tight, and the finger clamped case corresponds to an unclamped case. While the unclamped case is not physically clamped, some load is still transferred to the center wire due to the natural curvature of the wire (in their initial condition, the wires are slightly bent). Thus, since during the test the wires are straightened, the tendency to return to the original curvature induces some weak contact forces.

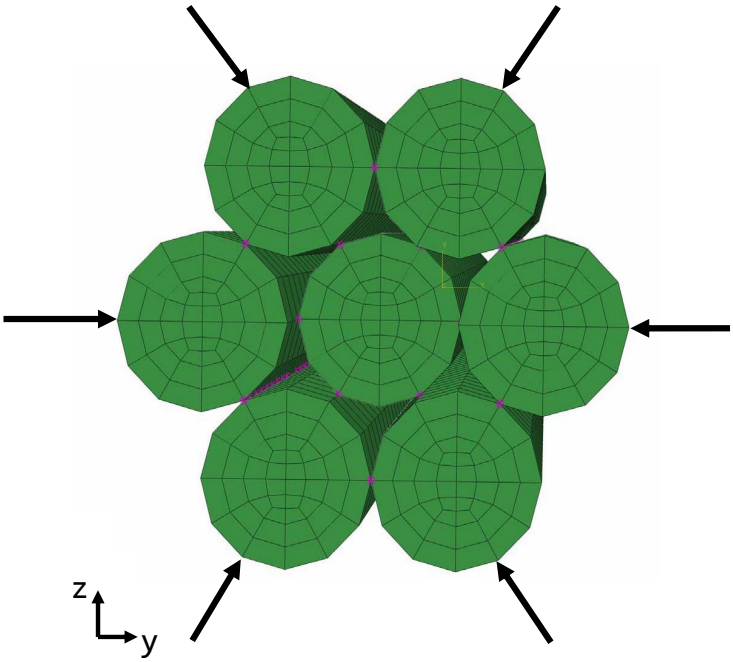

Figure 2.13: Finite element model for the seven wire problem. Tightening bands modeled as point forces and the contact points are modeled as springs shown in pink

Table 2.3 reports the parameter values that were calibrated to match the experimental results for each of the three models illustrated in Figure 3.1. Table 2.4 compares the experimental results given in Noyan et.al. [31] with those obtained from the three spring models, modeled by FEA, for the strains at the center point of the inner wire and at the outer wire. Figures 2.14, 2.15 and 2.17 show the longitudinal stress in the outer wires and the regained stress in the inner wires due to the tightly, loosly and finger clamped cases. The levels of stress regained in the inner wire reduces with the reduction of the applied radial forces in the clamps. As expected, the stress curves for the shear lag model are maximized only at the center of the wire, while the stress curves for Spring Model I and II regain the load near the clamp. This indicates that the rate of regain is inaccurate for the shear lag model in the tightly and loosely clamped cases. Nevertheless, in the finger clamped case the friction force is obtained due to the curvature of the wire and thus the contact is distributed along the entire

length. For that reason and due to the small load regains obtained, the simpler linear constant springs model is the more accurate and better corresponds to the physical problem. We also note the kink in the vicinity of the clamp as it was observed for the 2D plates, which could be explained by the predicted behavior in Boussinesq's analytical solution (see Figure 2.7).

Figure 2.16 shows a comparison between shear forces at the springs along one of the contact points between the inner and outer fire for each of the three models at 240 MPa. The shear forces of Spring Models I and II have a Boussinesq-like distribution, while the Shear Lag model shows a complectly different behavior with a maximum force obtained at the right end of the wire. The magnitude for the shear forces in the tightly clamped case (Figure 2.16(a)) is slightly higher than the magnitude of the shear forces in the loosely clamped case (Figure 2.16(b)). However the sum of the shear transferred in the six contact points between the inner and outer wire represents a 10% difference in the load regain of the center wire.

Table 2.3: Parameters of the Spring Models for the 3D Plate Analysis

Sprin Model	**Parameters**[1]	**Clamping Forces**		
		Tightly Clamped	Loosely Clamped	Unclamped Case
Shear Lag Model	K	1500	680	170
Spring Model I	K_{max}	9000	4500	-
	K_{min}	41	21	-
	$K_{average}$	1237.5	619	-
	F_T	250	125	-
Spring Model II	$F_{T,max}$	250	125	-
	$F_{T,min}$	1.15	0.57	-
	$F_{T,average}$	34.4	17.2	-
	$K_{elastic}$	9000	4500	-

[1]The stiffness K is given in units of [KN/m] and the yielding force F_T in [N]

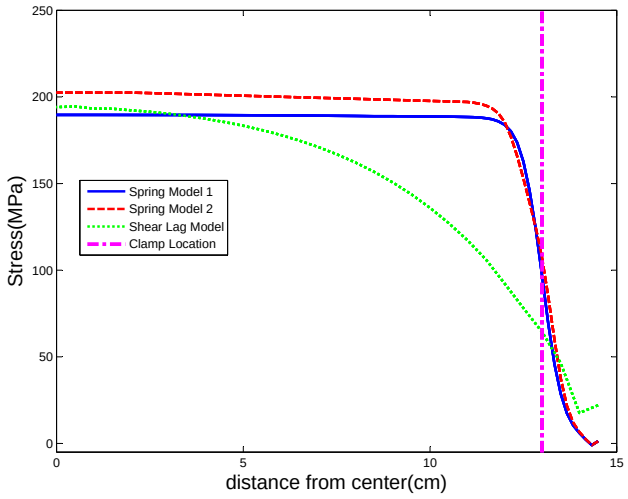

(a)

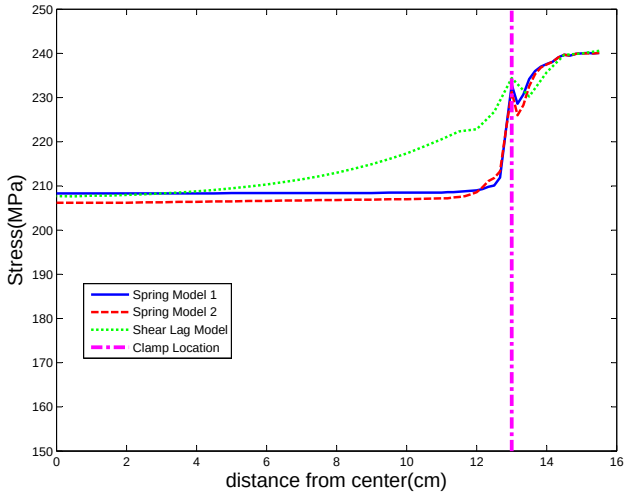

(b)

Figure 2.14: Stress results in the (a) center wire (b) outer wire obtained from FEA results provided by the spring models for a seven wire problem with a tight clamp. The stiffness parameters employed for each analysis are provided in Table 2.3.

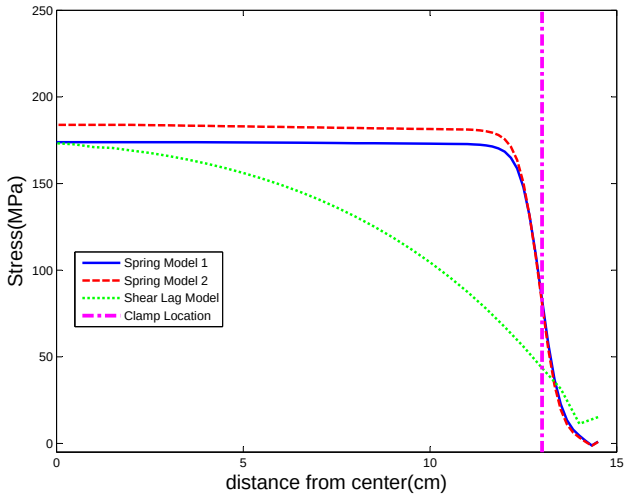

(a)

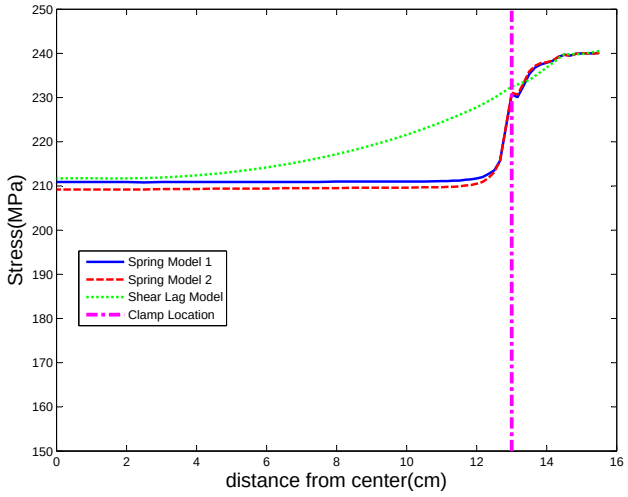

(b)

Figure 2.15: Stress results in the (a) center wire (b) outer wire obtained from FEA results provided by the spring models for a seven wire problem with a loose clamp. The stiffness parameters employed for each analysis are provided in Table 2.3.

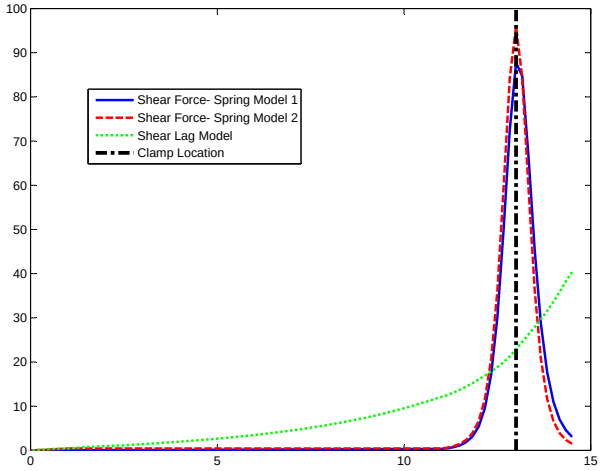

(a)

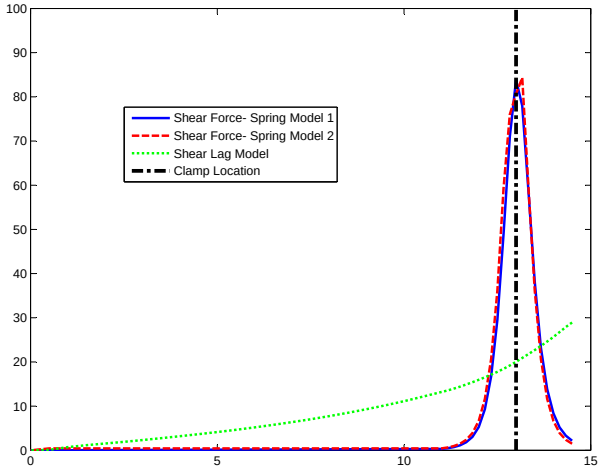

(b)

Figure 2.16: Shear force (force at the springs) for the FEA results for each of the springs models in a (a) tightly and (b) loosely clamped case.

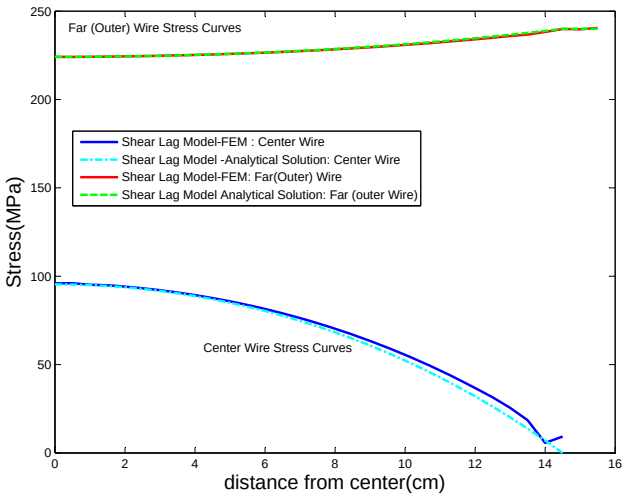

Figure 2.17: Stress results in the center wire and outer wire obtained from FEA results provided by the spring models for a seven wire problem for the unclamped case. The stiffness employed for the analysis is provided in Table 2.3.

Table 2.4: Comparison of the load regain parameter χ in the tightly clamped case, between experimental data and FEA springs models

			Spring Models		
Clamping Magnitude		**Experimental**	**Shear Lag**	**Model I**	**Model II**
Tightly Clamped	Center wire (slope)	4.70	4.10	3.98	4.26
	Far wire (slope)	5.00	4.35	4.36	4.31
	Load regain χ	0.94	0.94	0.91	0.99
Loosely Clamped	Center wire (slope)	3.98	3.73	3.66	3.63
	Far wire (slope)	4.82	4.43	4.41	4.41
	Load regain χ	0.83	0.84	0.83	0.82
Unclamped	Center wire (slope)	2.00	2.10	-	-
	Far wire (slope)	4.47	4.67	-	-
	Load regain χ	0.45	0.45	-	-

2.5.2 Discussion of the Proposed Friction Models

For the tightly clamped case, the elasto-perfectly plastic spring Model I, with similar yielding but varying stiffness constants, provide results that are in very good agreement with the experimental data and shows that the load regain parameter of the inner wire is 91% while the experiments have shown a value of 94%. It is interesting to note that, in this case (see Figure 2.14), the stress (and strain) in the central wire reaches a constant value at a very small distance away from the clamp: this suggests that the recovery length (sometimes called development length, [19]) is quite small, or alternatively the rate of regain is very high, indicating that the central wire regains 94% of the load quickly over a relative small distance from the clamp.

For the loosely clamped case, both elasto-perfectly plastic spring Models I and II, provide results which are in very good agreement with those obtained from experiments. For instance, Model I predicts a load regain of 82% while the experimental measures show a value of 84%. For the unclamped case, the shear lag (linear spring model) approach provides excellent results showing a load regain of 44% identical to the one obtained from the experiments.

Overall, it can be concluded that the proposed elasto-plastic spring elements recovers quite well Coulomb's friction law and accurately predicts the actual load transfer mechanism between wires, in close agreement with the experimental data. Both models I and II behave very similar on this problem as well as the 2D benchmark problem in Section 2.3.4. Numerical and experimental work (e.g. measuring the strain along the center wire and considering larger wire strands) would be needed for more detailed comparison. On the other hand, the shear lag model can be employed for "unclamped" cases which indicates that the load is transferred due to the natural curvature of the wires (being slightly bent).

Chapter 3

FE model with Random Wire Breaks

3.1 Chapter Summary

In this chapter, the finite element model that will predict the breaking load of a cable by incorporating random wire breaks induced by corrosion is developed. The contact model introduced in Chapter 2 is extended to the many parallel wire case. Hence, the model is generalized to take into account the re-distribution of the load among different layers of neighboring wires in the vicinity of a break, and the partial regaining of the carrying capability of the broken wire. More specifically, the model considers the friction decay along the cross section of the cable (from the outer wires to the inner wires), i.e. an outer broken wire, closer to the cable clamp, will be able to regain the load over a shorter distance than an inner wire which is further away from the compacting action of the clamp. The model is validated on 2D and 3D simpler problems by comparing the behavior to a reference solution obtained from a full contact analysis.

A study on various sized wire strands, breaking at a random wire sequence and at different locations, show the redistribution of the stresses between neighboring wires and the overall nonlinear load-loss response of the system. Furthermore, to overcome the storage and speed limitations of serial computers, the method is implemented on a parallel computer architecture and the number of linear/nonlinear iterations, CPU time and parallel scalability are reported. Finally, the model is simplified for the multi-scale case(more than 9000 wires) in order to facilitate a full stochastic analysis of the problem.

3.2 A Spring Model for Frictional Behavior

The method described in this chapter extends the method proposed in Chapter 2 to many wires compacted together by the clamping action of cable bands. From this chapter on, we will only refer to Model II, since the elasto-perfectly plastic spring

elements at the contact lines between the wires represent the stick-slip behavior more accurately. The stick behavior is characterized by the linear elastic stiffness K, and the slip part by the perfect plasticity, where the yielding force F_T represents the maximum transferred shear forces. In this spring model, the yielding force decays when moving along the length of the wire away from the clamp, as illustrated in Figure 3.1. This behavior is related to the decay in the compaction pressure generated by the clamp and is obtained *apriori* by an analytical solution to a point load applied on a half space (Flamant's solution in 2D and Boussinesq's solution in 3D). In Figure 3.1, $F_{T,1}$ represents the yielding point of the closest spring to the force and $F_{T,4}$ the farthest.

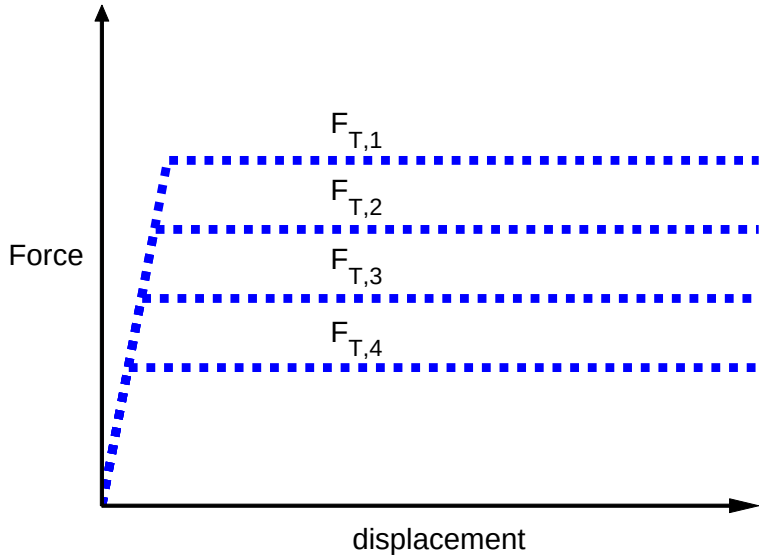

Figure 3.1: Elasto-perfectly plastic spring model with varying yielding forces. The elastic part represents the sticking behavior and the plastic part the slipping behavior.

3.2.1 Multi-wire Case

For strands composed of many wires, the steel clamps which enforce contact between wires are strongly tightened to enhance the friction between outer and inner wires. We assume that all outer wires are in contact with the steel band, i.e. a radial force is exerted on the strand at the outer points of contact. In the 7 wires case (a core strand

shown in Figure 3.2(a)),the yielding force of the springs is assumed to vary along the length of the wires at the contact points, i.e. the yielding force is only a function of x. However, to account for friction in multi-wire cases (as shown in Figures 3.2(b) and 3.2(c)), where the depth from the clamps is important, the yielding force of the sprigs are adjusted to decay along x and d, where $d = \sqrt{y^2 + z^2}$ is defined as the radial distance from the clamp in the cross-sectional plane $y - z$.

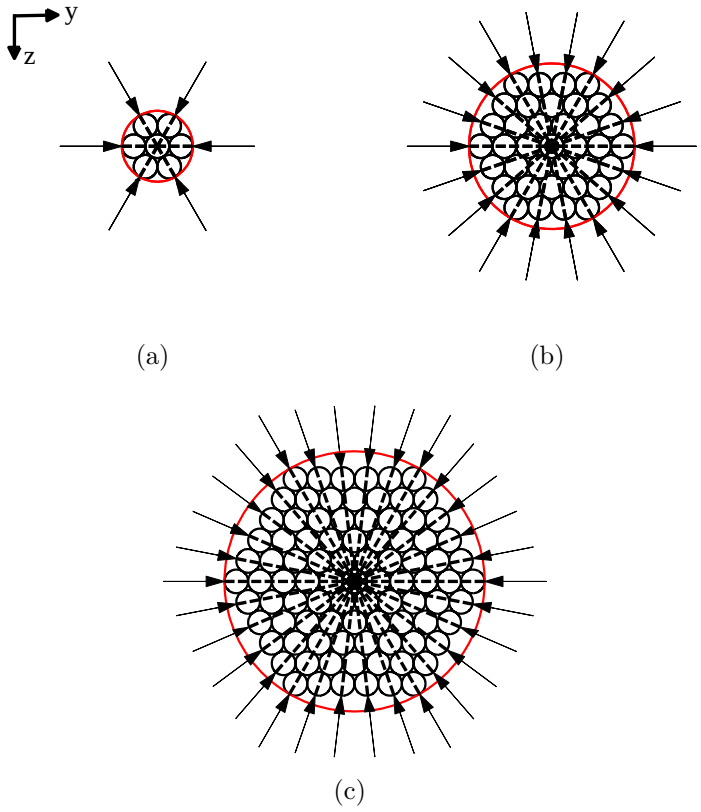

Figure 3.2: Radial bands inducing contact, (a) 7 wire core strand, (b) 37 wire strand, and (c) 91 wire strand.

In this work, the frictional decaying behavior in the $y - z$ plane is obtained from Boussinesq's solution [8, 47, 48], which is given by

$$\sigma_z = \frac{3P}{2\pi z^2}\left(\frac{1}{1 + (r/z)^2}\right)^{5/2} \tag{3.1}$$

where P is the applied load, r is the distance in the $x-y$ plane from the force, i.e. $r=\sqrt{x^2+y^2}$, and z is the depth at which the stress is computed. Figure 3.3 shows how the stress distribution varies at three different depths from the surface where the normal force is applied. Note that the maximum magnitude of the stress varies depending on the depth, i.e. being much greater at a depth closer to the force and decaying when moving away in $x-y$ plane.

Each clamping load contributes to the compaction stress at the interface layer of the wires. In order to capture the effect of each clamp, the axes are re-oriented for each clamping force and the stress is found at the contact interfaces between the wires according to the Boussinesq solution. Then the contribution from each point load is accounted for by superposition to determine the total compaction stress at each contact interface. The decay in the compaction stress along the depth of the strand is observed in strands composed of many wires, in which the greatest compaction stresses are at the wires near the clamping forces and the clamp influence decays as one moves toward the center of the strand. Once the compaction stress in the cable is known, the yielding force of a spring at a radial distance d from the clamp's ring in the y-z plane and a longitudinal distance x from the clamp can be directly computed to obtain consistent nodal forces without the need for calibration. An illustration of the normalized yielding spring force magnitudes is shown in Figure 3.4 for the 7-wire, 37-wire, and 91-wire strands.

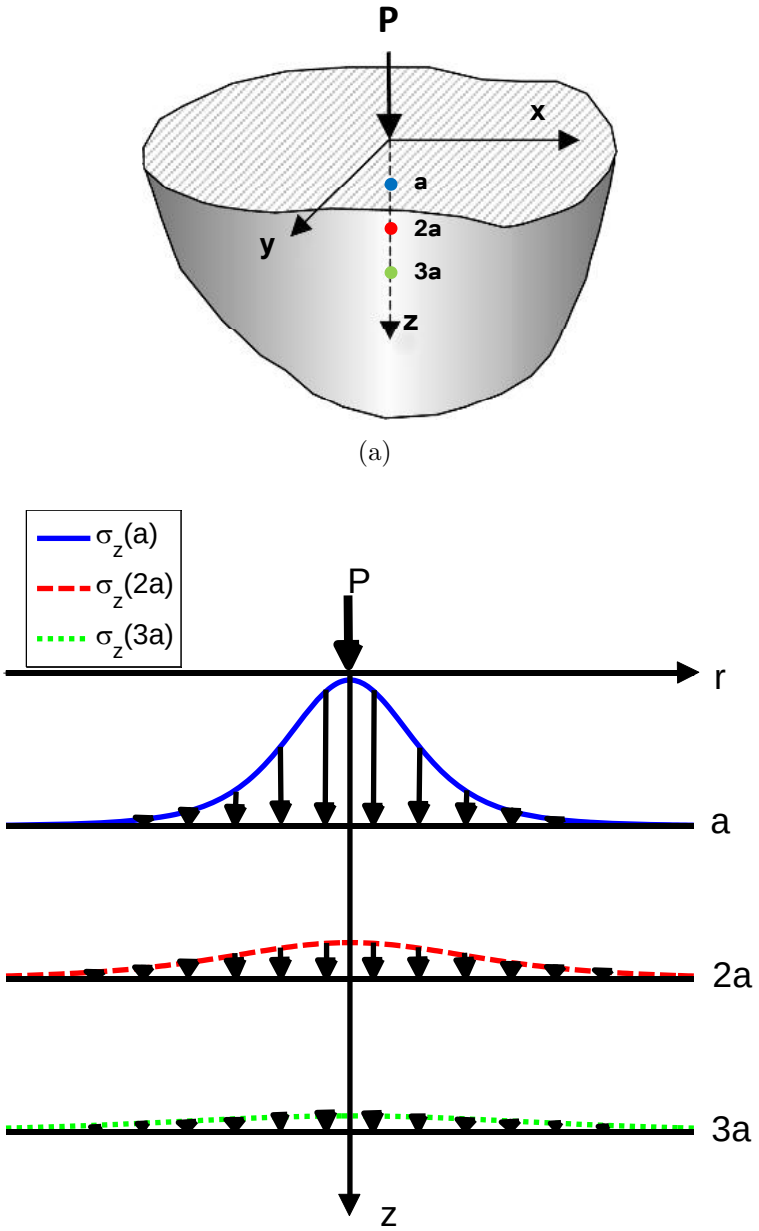

Figure 3.3: Boussinesq's problem (a) point force on a semi-infinite surface and three different depths (b) the stress distribution at these three different depths as a function of r, where $r=\sqrt{x^2+y^2}$

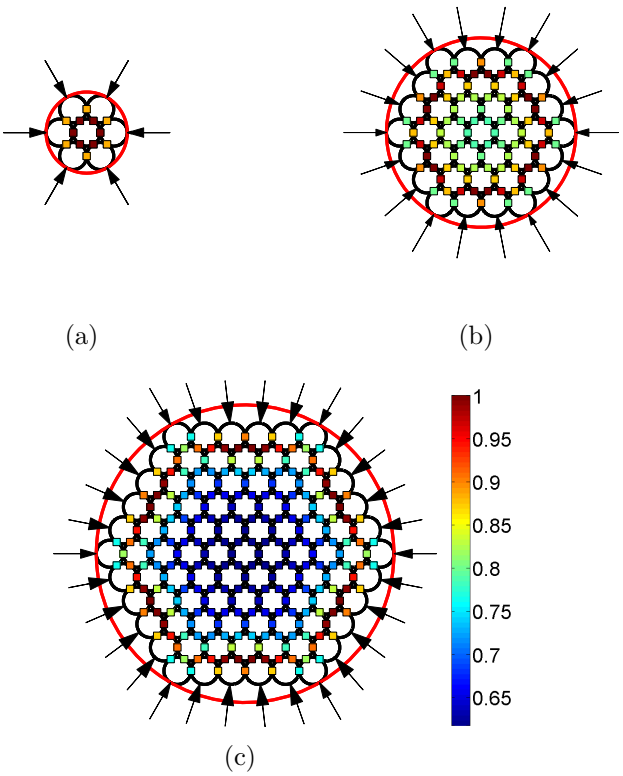

Figure 3.4: Normalized yielding forces at the springs in the cross-section at x=0 m for (a) 7 wire core strand, (b) 37 wire strand, and (c) 91 wire strand. The colored squares at the contact interfaces illustrate the yielding force magnitude of the spring.

Figure 3.5 shows the elasto-plastic springs for different contact points along the cable's cross-section composed of 37 wires. Three sets of springs located at radial distances a, $2a$, and $3a$ are shown. The locations are labeled as , $\square$, Δ, and O, respectively. The contact points in the set have the same d, but a different longitudinal distance x from the clamp. The spring with the maximum yielding force in each set is the one closest to the clamp at $x = 0$. The spring with the maximum yielding force among the three sets is the one located at $x = 0$ and a radial distance $d = a$. However, the yielding force of the rest of the springs at $d = a$ decays faster than the springs in the other sets since the compaction stress has a higher peak at the clamp ($x = 0$), but decays rapidly in the longitudinal direction. The yielding forces in the set at $d = 3a$ decay slower than the other two sets as the compaction stress spreads over a longer distance for interior wires as observed in Figure 3.5(c).

3.3 Spring Model Validation

In this section, we validate the proposed springs model in two and three dimensions by comparing the behavior to a reference solution obtained from a full contact analysis. A key point in these validation studies is that the spring yielding parameters are directly evaluated by analytical means and no calibration of parameters is needed. The experimental validation of this model was performed by Waisman et al. [52] by comparing the results of the model to experimental tests conducted by Noyan et al. [31] in a seven wire cracked short strand.

3.3.1 Spring Model Validation in 2D

The load distribution and dissipation in space of a point load applied on half space for a semi infinite body can be approximated through Flamant's [18, 37] analytical

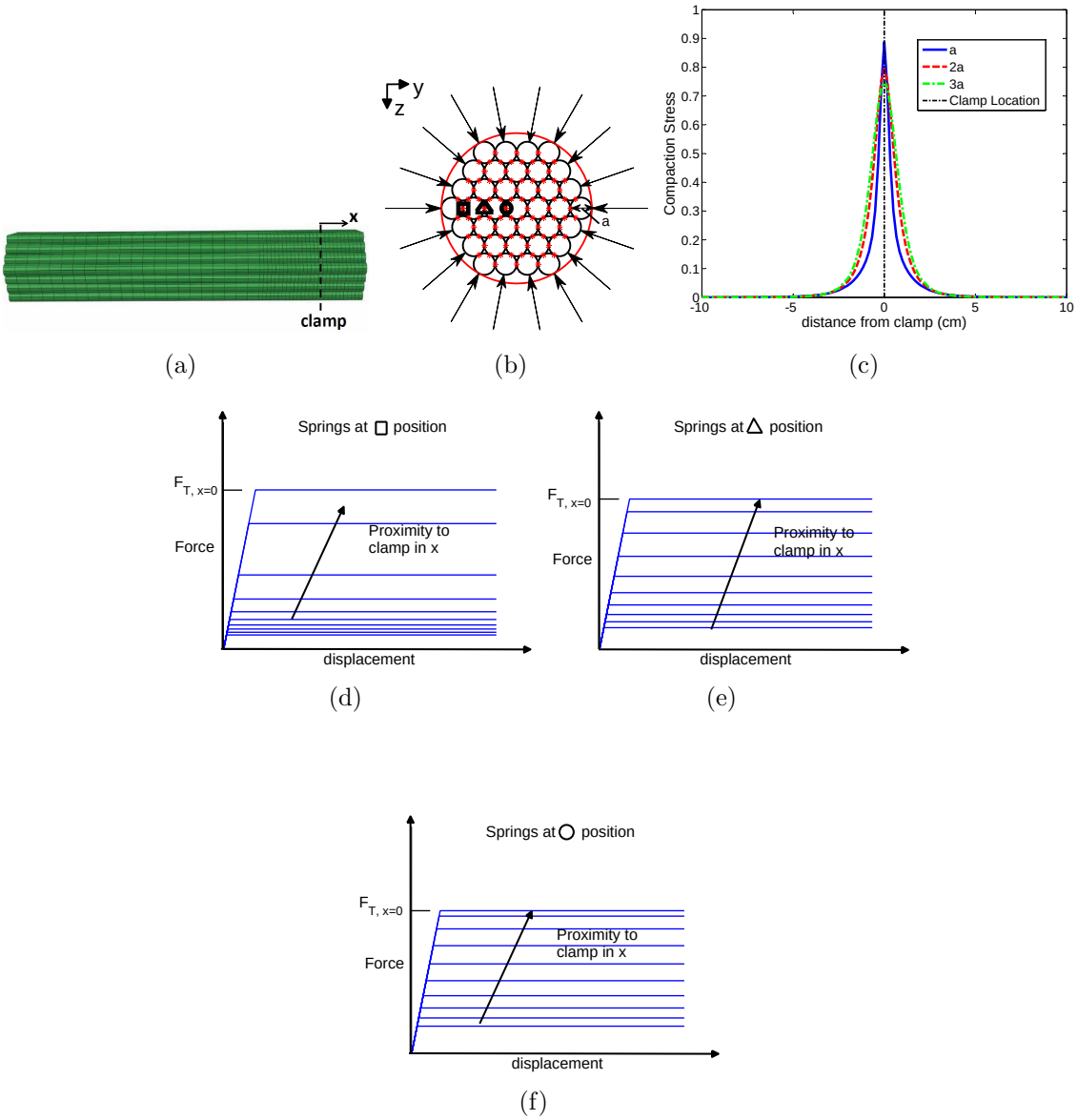

Figure 3.5: Varying elasto-plastic springs placed in a 37 wire strand. (a) coordinate system along the wires, (b) cross-section of the strand showing the springs at the contact points, (c) compaction stress as function of depth. Subfigures (d) to (f) illustrate the decaying spring behavior as function of depth (for □, Δ, and O locations shown in subfigure (b)).

solution. By this solution, the stress in the y-direction is given by,

$$\sigma_y = \frac{-2Py^3}{\pi(x^2+y^2)^2} \tag{3.2}$$

where P is the normal applied load, y is the depth, and x the longitudinal distance from the applied load at which the stress is computed. Invoking Coulomb's law, the tangential force F_T is related to the normal applied load by

$$F_T = \mu P \tag{3.3}$$

where, μ is the coefficient of friction (material and surface parameter). Thus at some depth t_1 under the applied load, the frictional force F_T can be approximated by direct integration of Flamant's solution, i.e.

$$F_T(t_1) = \mu \cdot \int_{-L}^{L} \sigma_y(x, t_1) dx \tag{3.4}$$

where, L is the distance in the longitudinal direction from the applied load to either end of the space being considered. By substituting Eq. (3.2) into Eq. (3.4), we obtain the yielding force in the spring model at t_1 as,

$$F_T(t_1) = \mu \cdot \int_{-L}^{L} \frac{-2Py^3}{\pi(x^2 + t_1^2)^2} dx = \mu P \cdot \frac{2}{\pi} \left(\frac{t_1 L}{t_1^2 + L^2} + tan^{-1} \left(\frac{L}{t_1} \right) \right) = \mu P \cdot \gamma(t_1) \tag{3.5}$$

In Eq. (3.5) the parameter γ is introduced to determine the percentage of the load that has been dissipated in the system. Note that directly under the load at $t_1 = 0$, γ is singular. However at an ϵ, a very small distance away from the origin ($\epsilon \ll 1$), $\lim_{t_1 \to \epsilon} \gamma \to 1$ and $\lim_{t_1 \to \infty} \gamma \to 0$. The case of $\gamma = 1$ corresponds to the Coulomb's Law. The function γ is plotted in Figure 3.6 as a function of t_1 and L. Note also that γ can be considered analogous to the influence factor used in foundation design to predict the stress at a depth z below the foundation [15].

Employing Flamant's solution, the discretized yielding forces at the springs can be

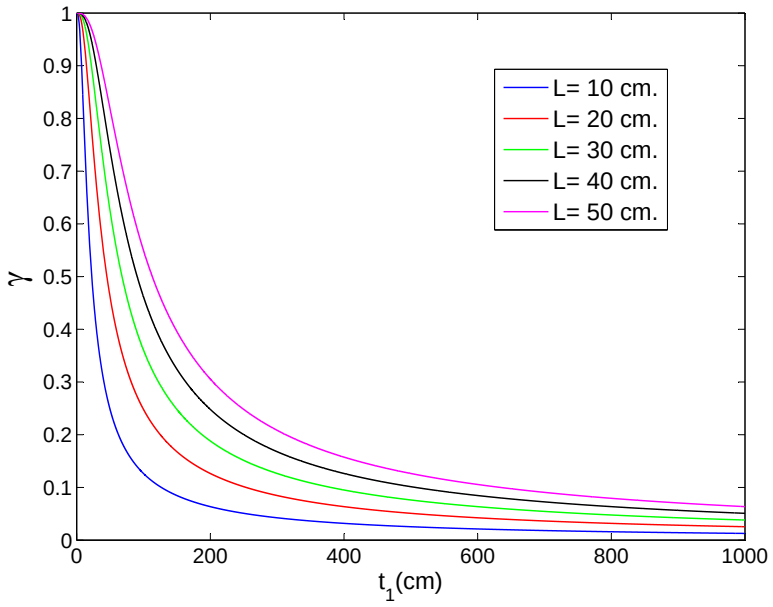

Figure 3.6: The dissipation parameter, γ, as a function of the length and thickness of the top plate.

obtained by standard FEM interpolation, i.e:

$$F_T^e(t_1) = \mu \cdot \int_{-L_e}^{L_e} \mathbf{N}^T \cdot \frac{-2Pt_1^3}{\pi(x^2 + t_1^2)^2} dx \tag{3.6}$$

where the 1D shape functions for a bar element $\mathbf{N}$ are used to obtain consistent nodal forces in the springs and L_e is half the length of the element.

To validate the spring's model, consider a simple 2D Model, consisting of two 10 cm long steel plates, with one normal point force (P= 3000 N) at the center of the top plate as shown in Figure 3.7. The left end of both steel plates are fixed and roller boundary conditions are applied to the bottom edge of the lower wire, i.e., it is only free to move in the x-direction. An axial traction of 100 MPa is applied to the upper plate. Three different cases are considered by increasing the depth of the top plate in order to obtain different levels of load recovery on the lower plate, which has a fixed thickness of 0.4826 cm. The solution provided by the Spring Model is compared to a reference solution obtained with a full contact algorithm, and a Coulomb friction

coefficient parameter of $\mu = 0.4$. The full contact model is the contact algorithm implemented in Abaqus which employs Lagrange multipliers to enforce the contact and searches for contact regions between the two surfaces [21]. In the spring model, the elastic stiffness K was set to a value of 30×10^8 $[N/m]$ to enforce the sticking conditions in the model and the yielding forces of the springs are obtained using Equation 3.6.

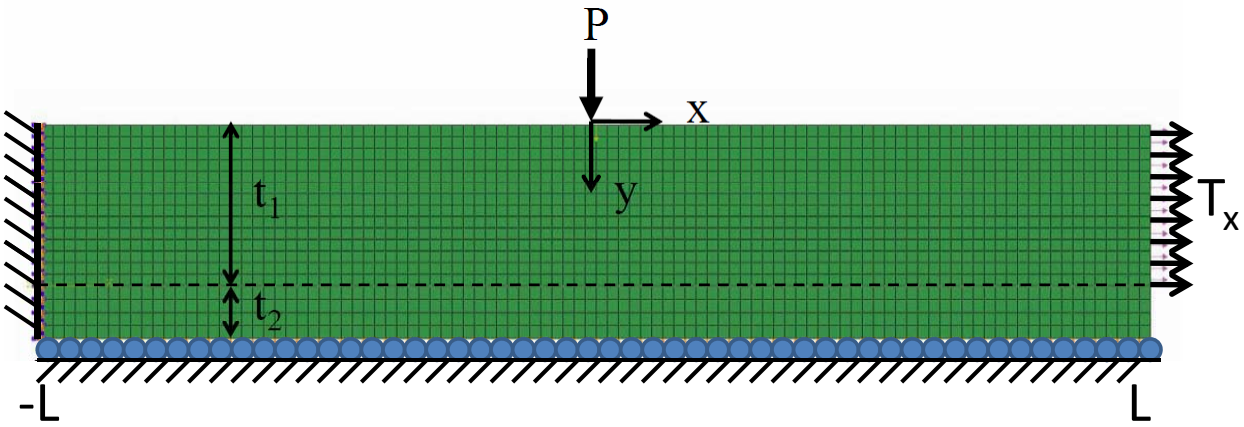

Figure 3.7: An example problem of two plates in frictional contact used for validation of the Spring Model.

The dissipation parameter γ obtained analytically by Eq. (3.5), for three different depths is reported in Table 3.1 and compared to the FEM results using the full friction model in Abaqus and the Spring Model proposed in this chapter. The results provided by the full friction model employed in Abaqus are in good agreement with the analytical results, which provides the yielding parameters for the spring model.

Table 3.1: Parameters for spring model used for the verification study in 2D with two steel plates, where a =0.4826 [cm], P =3000 [N] and $F_T = \mu P \gamma(t_1)$ [N]

t_1: **Top Plate Thickness**	$\gamma_{analytical}$	γ_{abaqus}	γ_{model}	$F_{T,analytical}$	$F_{T,abaqus}$	$F_{T,model}$
a	1	1	1	1200	1200	1200
$3a$	0.99	0.98	0.99	1188	1176	1188
$5a$	0.96	0.92	0.94	1152	1104	1128

It can be observed from Figure 3.8 that both models show a similar behavior, i.e, the plate closer to the applied load regains load over a shorter distance than a plate at a farther depth. As the depth increases, the level of recovery decreases due to load dissipation at the interface between the plates. While the Coulomb model is more accurate than the spring model, it is also significantly more computationally expensive as observed in Table 3.2. Moreover when the applied contact load is very high or alternatively when the depth is closer to the surface, the contact algorithm implemented in Abaqus may diverge. Thus the spring model provides an accurate and robust contact algorithm for such problems.

Table 3.2: Computational Performance for the Friction Models in 2D

Model	**Depth**	**Iterations**	**CPU Time(s)**
Coulomb	a	32	3.0
Model	3a	10	2.0
	5a	6	1.7
Spring	a	3	0.4
Model	3a	3	0.7
	5a	3	1.2

3.3.2 Spring Model Validation in 3D

In three dimensional problems, the compaction stress along the wires generated by the contact load can be approximated by Boussinesq's solution to a point load applied on a half space of a semi-infinite solid, which is given by Eq. (3.10). The concentrated load dissipates in a 3D space. The frictional force at a some radial distance from the clamp, $d = \sqrt{y^2 + z^2}$ is found by the same formulation as in 2D (see Section 3.3.1) with Boussinesq's solution integrated along a line, which yields

$$\begin{aligned} F_T(y,z) &= \mu \cdot \int_{-L}^{L} \sigma_z(x,y,z)dx = \mu \cdot \int_{-L}^{L} \frac{3P}{2\pi z^2}\left(\frac{1}{1+(r/z)^2}\right)^{5/2} dx \\ &= \mu P \cdot \left(\frac{Lz^3\left(2L^2+3y^2+3z^2\right)}{\pi(y^2+z^2)^2(L^2+y^2+z^2)^{3/2}}\right) = \mu P \cdot \gamma(y,z) \end{aligned} \tag{3.7}$$

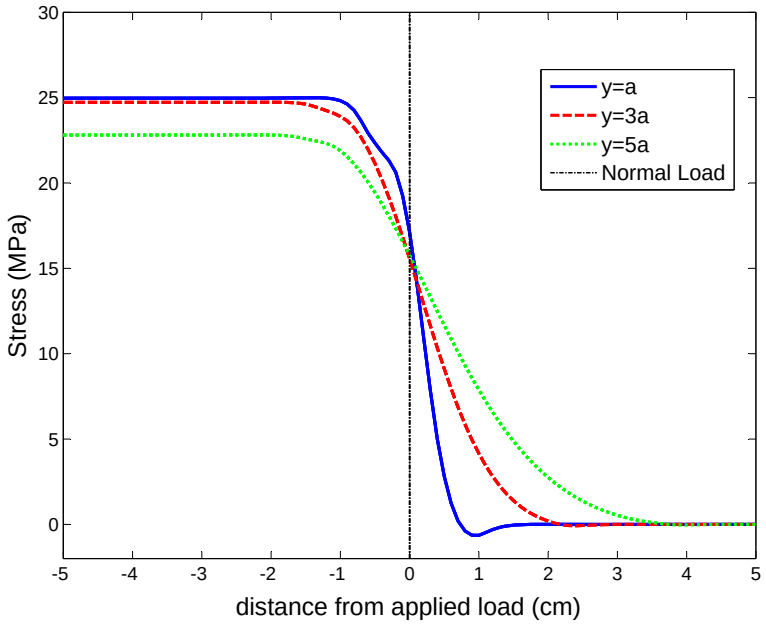

(a)

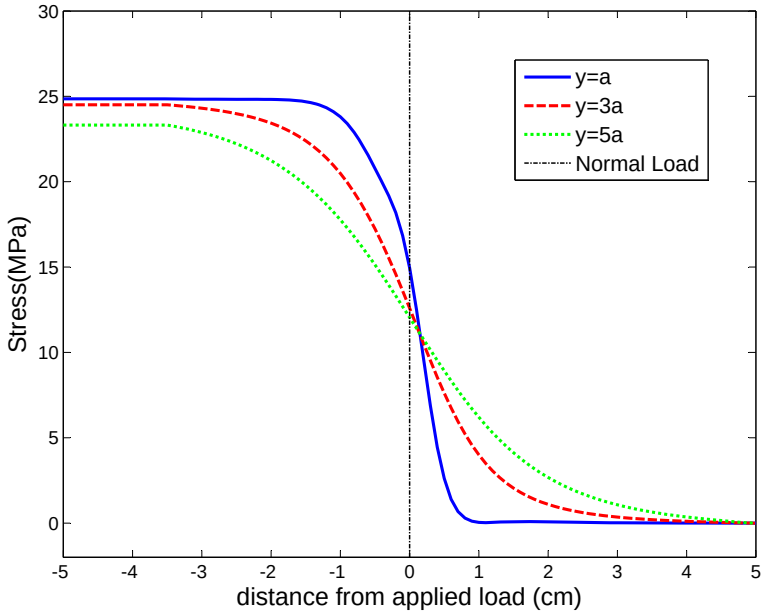

(b)

Figure 3.8: Stress curves showing the stress transfer in the lower plate due to friction at three different depths using the (a) Coulomb Model and the (b) Spring Model, where a= 0.4826 cm.

where, L is the distance in the longitudinal direction from the applied load to either end of the solid being considered. Note that the dissipation parameter γ is now a

function of y and z and similar to the 2D case, the stresses at the origin are singular [8, 16]. In very close proximity to the load, due to the high stresses in that region, γ is slightly greater than 1. This occurs at $y = 0$ and $z \leq 0.635$ cm. Nevertheless, γ tends to zero as the depth approaches infinity $\lim_{z\to\infty} \gamma(z) = 0$. The variation of γ in space is illustrated in Figure 3.9. At the top surface ,where the load is applied ($z = 0$), γ must be equal to zero when y is not equal to zero. As the depth increases, γ increases since the load is dissipated over a wider space with increasing depth. However, it eventually reaches a peak and then starts vanishing as the distance becomes infinitely far from the origin.

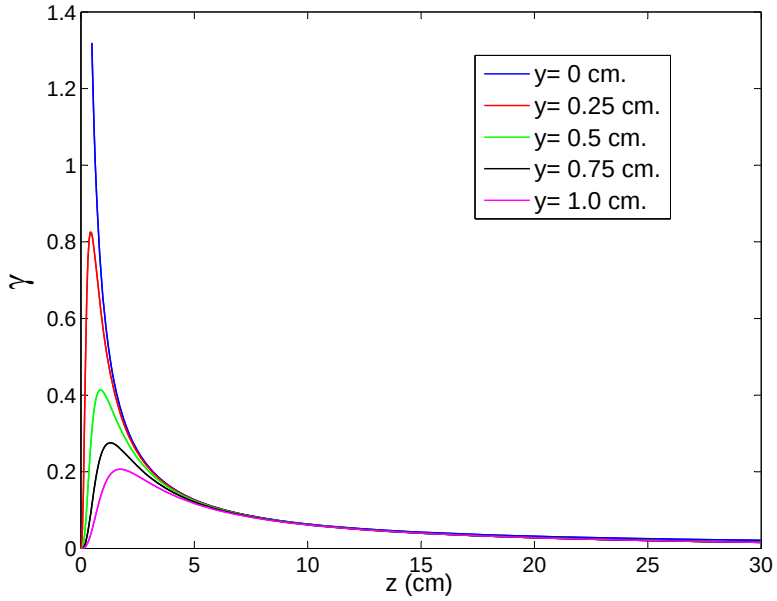

Figure 3.9: The dissipation parameter, γ, as a function of y and z.

To validate the model, consider an example problem that consists of two steel wires 20 cm long with a radius of 0.2413 cm. The left end of both wires is fixed and the bottom edge of the lower wire is only free to move in the longitudinal x-direction. An axial traction of 120 MPa is applied to the upper wire on the right end and a concentrated load is applied at the center (10 cm from the ends) as shown in Figure 3.10. The reference solution, obtained by modeling the problem in Abaqus, consists of 2074 nodes and 1440 eight node hexagonal (brick) elements. Three different

cases are considered by increasing the magnitude of the concentrated load in order to get different levels of recoveries in the lower wire. The full contact analysis is obtained by assuming a Coulomb friction coefficient parameter of $\mu = 0.4$ and iterating until converges. The solution with the spring model is obtained by determining the yielding force in the spring elements and defining the elastic stiffness K to a value of 30×10^8 $[N/m]$. We emphasize that the yielding forces at the spring elements in the interface layer are approximated by integrating the compaction stress along the length of the wire (x-direction) using standard FEM, i.e. no calibration is required.

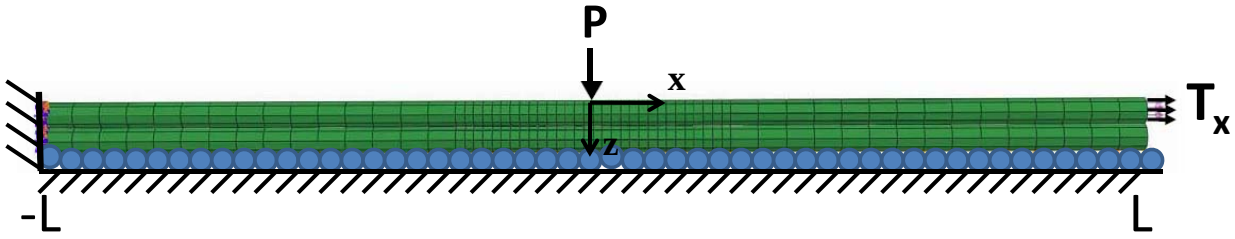

Figure 3.10: An example problem of two wires in frictional contact used for validation of the Spring Model with a full contact model.

The dissipation parameter for the two 20-cm wires in which the interface is at $y = 0$ and $z = 0.4826$ cm (diameter of the wire) is 1.32 as observed in Figure 3.9 and Table 3.3. Figure 3.11 shows the shear force at the springs as compared to the force obtained from the full contact model. The shear force distribution along the wire shows a Boussinesq-like behavior in all the models [8, 48, 47] and a proper estimation of the sum of the yielding forces along the length of the wire. Thus, the full friction model in Abaqus also exhibits the singularity effects of a point load at very close proximity to the clamp. The kink observed in Figure 3.12 (b) for all models at the location of the clamp is due to the fact that concentrated force introduces stress in the direction perpendicular to the force as predicted by Timoshenko and Goodier [47]. In general, the semi-analytical elasto-perfectly plastic spring model is in excellent agreement with the full contact model except for the left boundary in Figure 3.11 which exhibits some numerical artifacts in the full contact model. The spring model

has a slightly better computational performance as observed in Table 3.4.

Table 3.3: Parameters for spring models used for the two-wire verification study, where P =1000 [N] and $F_T = \mu P \gamma(y,z)$ [N]

Applied load	$\gamma_{analytical}$	γ_{abaqus}	γ_{model}	$F_{T,analytical}$	$F_{T,abaqus}$	$F_{T,model}$
P	1.32	1.25	1.32	528	501	528
$1.5P$	1.32	1.25	1.31	792	753	786
$2P$	1.32	1.25	1.30	1056	1000	1040

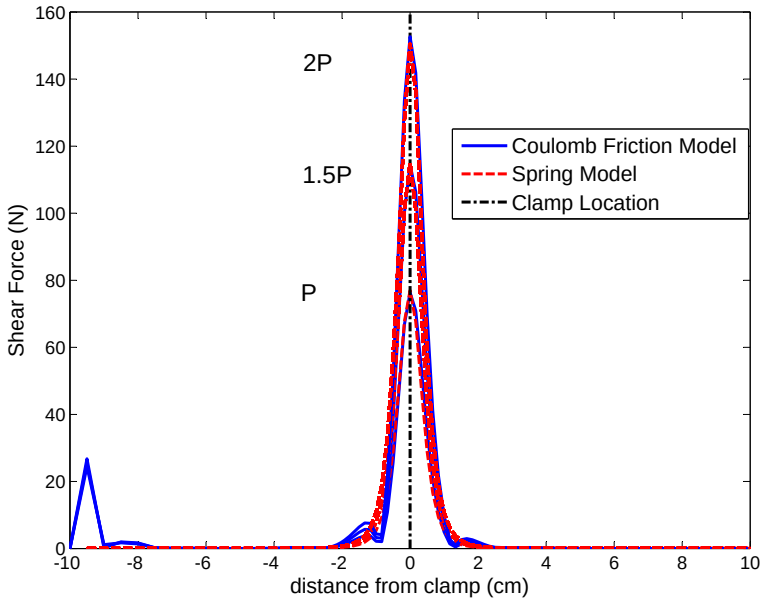

Figure 3.11: Shear forces in the spring models compared to the friction forces from the full contact model

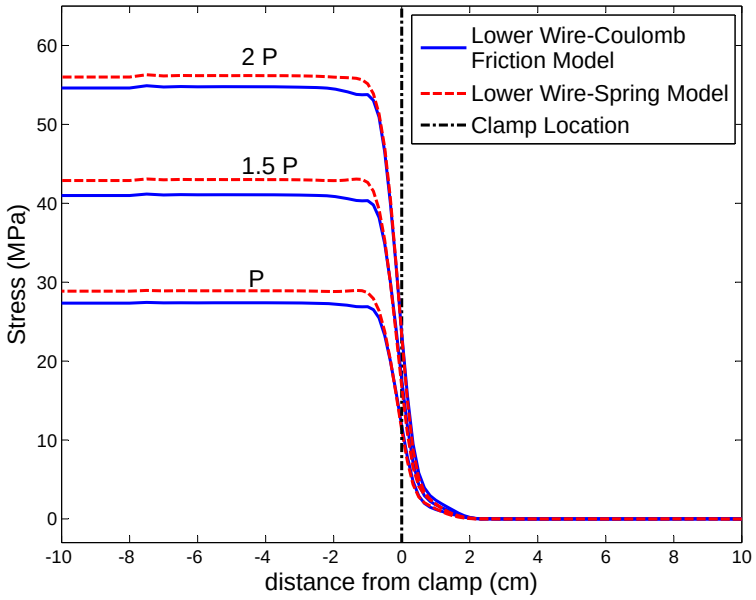

(a)

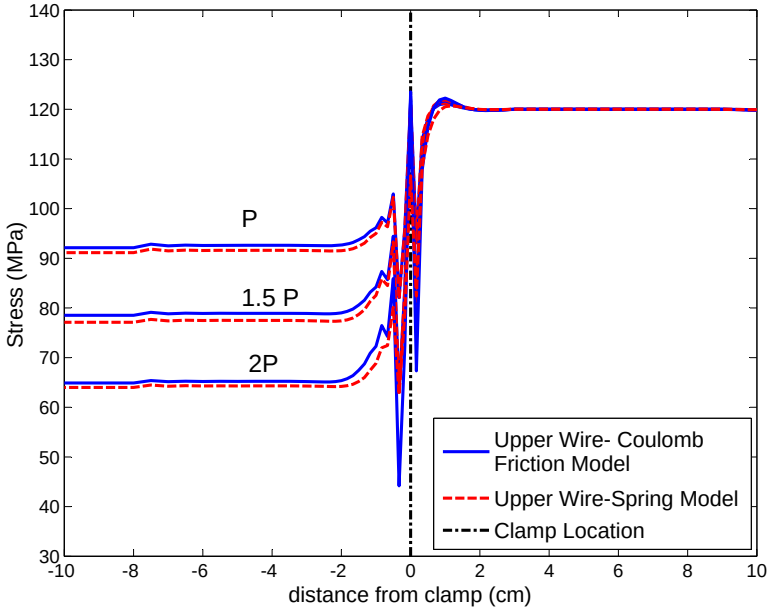

(b)

Figure 3.12: Stress curves showing the stress transfer between the (a) lower and (b) upper wire due to friction, for three different clamping forces, where P=1000 [N]

Table 3.4: Computational Performance for the Friction Models in 3D: Two Wires Example

Model	**Clamping Force**	**Iterations**	**CPU Time(s)**
Coulomb	P	6	1.7
Model	1.5P	6	1.7
	2P	6	1.8
Spring	P	3	1.2
Model	1.5P	3	1.2
	2P	3	1.2

3.3.3 Spring Model Validation on a Seven Wire Strand

Finally, we validate the model on a seven wire strand for which clamping loads are applied at the center of the strand in the radial direction at the perimeter of the strand. All seven wires are fixed at the left end as illustrated in Figure 3.13, while only the outer wires are subjected to an axial tension of 100 MPa at the right end. The inner wire (simulating a broken wire) is not directly loaded, however it recovers partial load due to friction induced by the radial clamp. Each clamping load contributes to the compaction stress at the interface layer of the wires. Due to symmetry, the inner-outer and outer-outer contact interfaces exhibit the same compaction stress as shown in Figure 3.13. The inner-outer interfaces have a slightly higher compaction stress due to their closer proximity to the clamping loads.

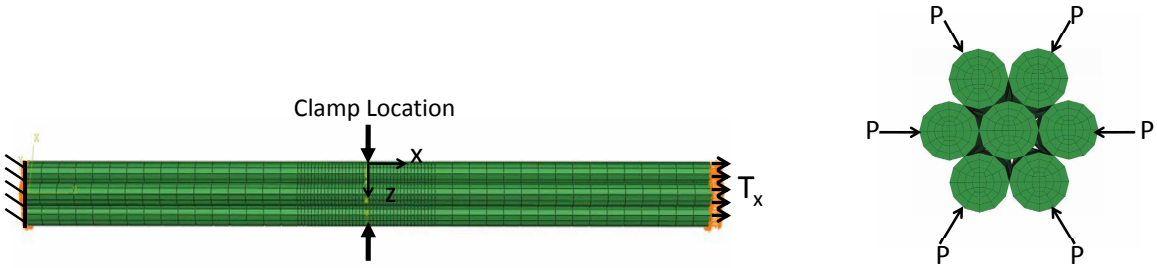

(a) (b)

Figure 3.13: An example problem of seven wires in frictional contact used for validation of the Spring Model with a full contact model.

The results of the spring model for three different clamping forces are compared to the Coulomb friction model (implemented in Abaqus) in Figures 3.15 and 3.16, showing excellent agreement. However, the computational effort, number of iterations and CPU time, for the full friction model increases dramatically for the seven wire case as observed in Table 3.5. As the clamping force increases in magnitude (e.g. in case of tightly clamped radial forces) the number of nonlinear iterations increases and the algorithm may not converge. Moreover, we emphasize that for the many wires problem, (i.e. when many contact points need to be resolved as considered in this

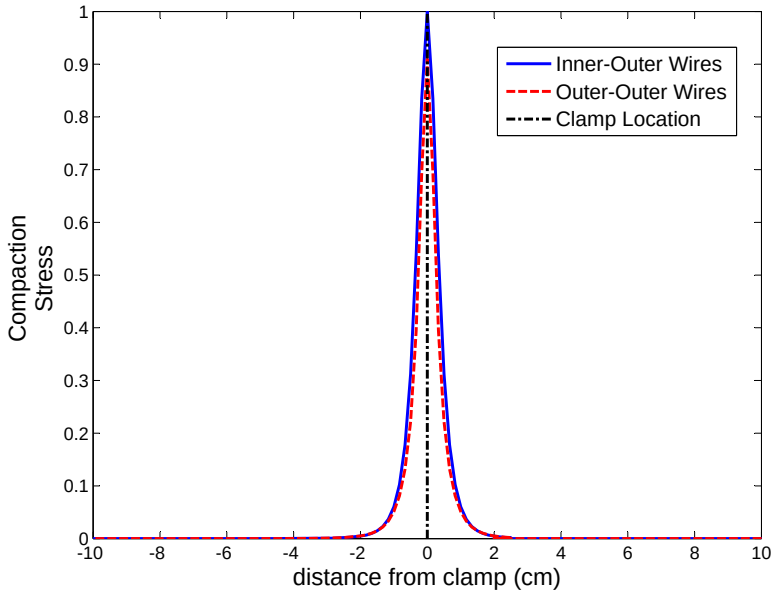

Figure 3.14: Compaction Stress at the Interfaces computed analytically (in a relative scale) between the inner-outer wires, and outer-outer wires.

Table 3.5: Computational Performance for the Friction Models in 3D: Seven Wire Example

Model	**Clamping Force**	**Iterations**	**CPU Time(s)**
Coulomb	P	121	857
Model	1.5P	131	952
	2P	152	1091
Spring	P	4	31
Model	1.5P	4	31
	2P	4	31

analysis) the algorithm implemented in Abaqus does not converge at all.

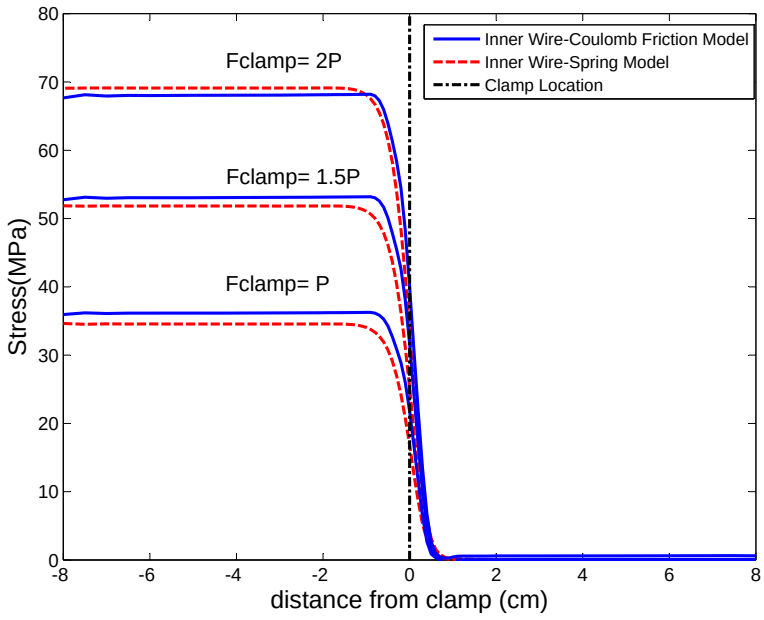

(a)

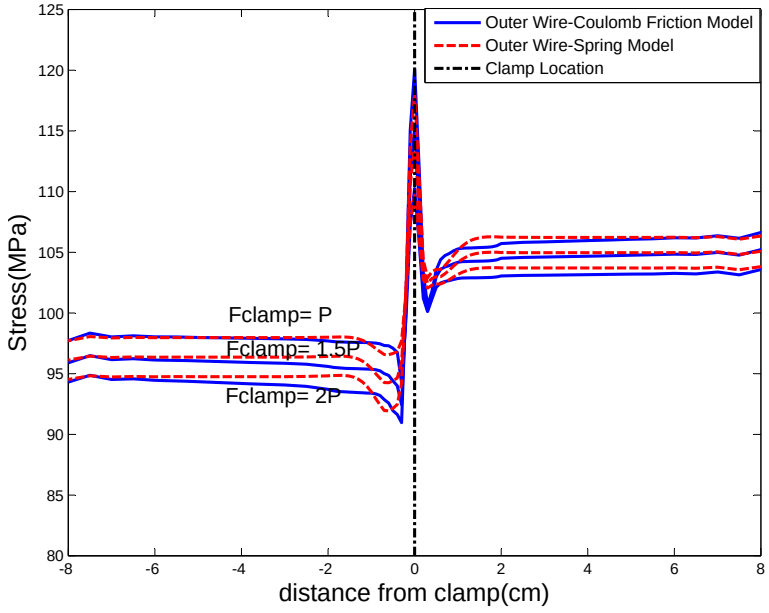

(b)

Figure 3.15: Stress curves showing the stress transfer between the (a) center and (b) outer wires of a seven wire strand due to friction, for three different clamping forces.

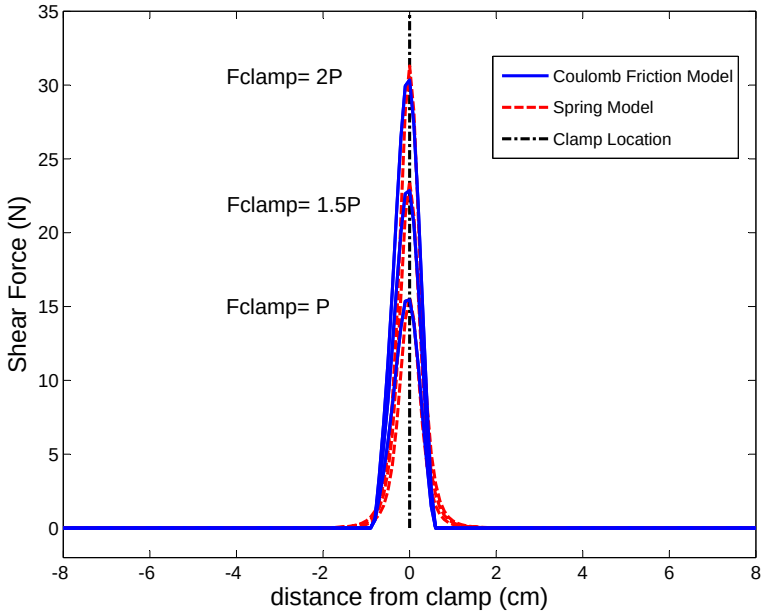

Figure 3.16: Shear forces in the spring models along one of the contact lines compared to the friction forces from the full contact model

3.4 Implementation and Verification of Wire Fracture

The corrosion experienced by wires of suspension bridge cables decreases the area of the wires considerably, leading to wire breaks at random locations and in an arbitrary sequence. Having a 3D model that adjusts the mesh based on the area reduction due to corrosion would be very troublesome and would increase the computational cost excessively. Consequently, for computational purposes, it is preferred to associate the area reduction to a wire's Critical Failure Stress, which varies randomly (but smoothly) along the length of each individual wire as observed in Figure 3.17(a). The Critical Failure Stress is considered a material property and is input by the user before the simulation begins. The algorithm is implemented as a user material model in FEAP [45] and it is illustrated in Figure 3.17(b). The state of the axial stress is determined adaptively and a check to determine if it exceeds the Critical Failure Stress (CFS) of the elements is performed. As the cable is loaded, the sections of the wires that reach their Critical Failure Stress will break. This break is reflected in the model by eliminating the stiffness of the individual wire element, the so called element deletion technique [17]. As the element breaks, the user friction model is activated as the spring elements start tranferring load between wires. We emphasize that when such a break happens in one wire, the load in all other wires (depending on their proximity to the broken wire) will automatically be adjusted and hence may enter a critical stress state which will lead to their failure, i.e. the domino effect.

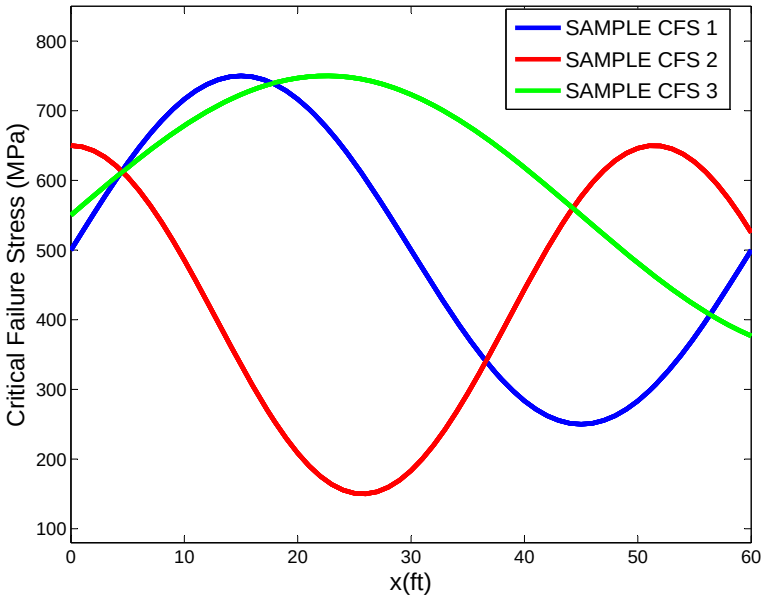

(a)

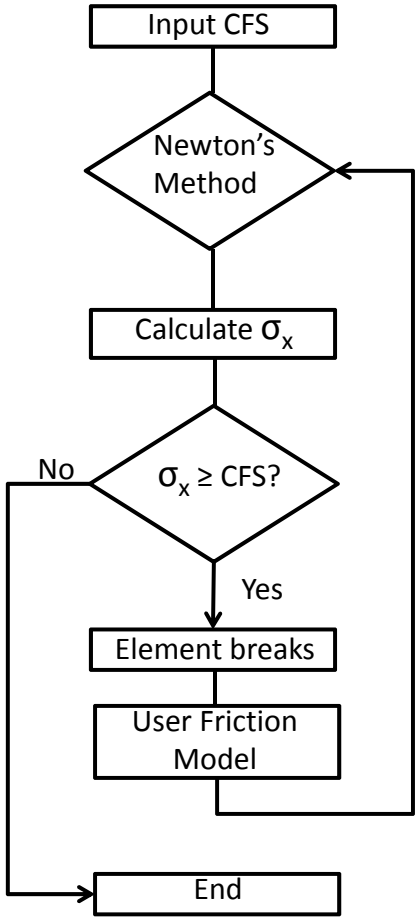

(b)

Figure 3.17: Crtical Failure Stress along three sample wires employed in the model to employ corrosion randomness. (b) Algortihm flow, implemented in FEAP, to account for wire breaks and load recovery.

3.5 Numerical Examples of Wire Breaks at Random Sequence and Location

In this section a sequence of wire breaks is simulated in strands composed of several wires. The numerical tests are conducted on parallel wires of the same length with a similar setup as the tightly clamped case for a seven wire strand experimentally tested by Noyan et al. [31] and modeled in [52]. The experimental system consisted of a standard seven wire strand, socketed at both ends with a total clear length of 31 cm. and clamped in this condition using standard wire clamps as observed in Figure 3.18. The problem is modeled assuming symmetric boundary conditions and the radial clamps are modeled as point forces at the contact points. The wire's length (assuming half a model) is 15.5 cm. and the clamp is placed at 13 cm. from the center.

(a)

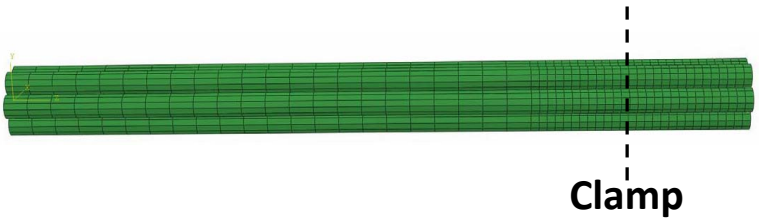

(b)

Figure 3.18: Experimental Setup of the Seven Wire Case (b) FEM mesh composed of brick elements and a radial clamp at 13 cm from the center for the seven wire case.

The model is implemented in FEAP [45] for strands with 7, 19, 37, 91, and 127

wires. Hexagonal (brick) elements with three degrees of freedom per node are used. Each wire consisted of 2550 nodes and 2156 elements. Table 3.6 summarizes the mesh details for the cases studied. It can clearly be seen that the number of equations quickly increases with the number of wires considered. Note that the 91 and 127 wire strands cannot be solved on a single processing unit (due to insufficient memory) and hence parallel implementation is necessary and will be discussed in Section 3.5.2. The wires are loaded axially using a displacement control loading.

Table 3.6: Number of wires, nodes, elements and equations used in the FEM Model

Wires	**Nodes**	**Elements**	**Springs**	**Number of Equations**
7	17,850	15,092	600	53,5550
19	48,450	40,964	2,100	145,350
37	94,350	79,772	4,500	283,050
91	232,050	196,196	12,000	696,150
127	323,850	273,812	17,100	971,550

For these tests, it is assumed that the wires had localized corrosion at some random points along the length of the cable with random severity (magnitude). The Critical Failure Stress values, which defines the severity of the corrosion, and its location (where pitting corrosion occurs) were obtained by generating random values. For these studies, we assumed that the maximum tensile strength of a wire is $\sigma_{max}^{wire} = 600\ MPa$. Thus we set the random failure stresses of each wire along its length to a uniform distribution between 50 $MPa \leq \sigma_{cr}^{wires} \leq 600\ MPa$ (except for the seven wire case). We allow each wire to only break once and some wires would not break at all (only in the seven wire case all wires break).The strands were displaced up to 0.195 mm, which is the displacement corresponding to a noncorroded case in which the wires are loaded at 250 *MPa*.

We apply an initial step of 0.03894 mm, equivalent to 50 *MPa*, right below the region of interest which is when the wires start breaking. Then we apply ninety-nine equal loading increments for 7 and 19 wire strands ($\Delta u = 0.00157mm$), and only nine

equal loading increments ($\Delta u = 0.0173mm$) for larger strands. Such a reduction in the number of loading increments for larger strands is due to obvious computational reasons. Hence, more accurate response may be obtained for smaller wire strands. A discussion on the axial stress at individual wires and their redistribution after wire breaks is provided for the smaller strands (seven and nineteen wires) in Section 3.5.1. The overall system response in terms of the reduction in the load carrying capacity is shown for all strands in Section 3.6. The springs parameters used were those obtained for a tightly clamped case for a seven wire strand experimentally tested by Noyan et al. [31] and modeled in [52], in which $K_{max} = 9000\ [KN/m]$ and $F_T(x = 0) = 250\ [N]$. Furthermore, the clamping forces were kept the same for all wire strand cases, i.e. the outer wires that make contact with the clamp ring feel the same force.

3.5.1 Implementation on Seven and Nineteen Wire Cases

Seven Wire Case

The distribution of Critical Failure Stress values along the length of the wires is obtained through a random number generator following a uniform probability distribution between $50\ MPa \leq \sigma_{cr}^{wires} \leq 250\ MPa$ in order to allow all the wires to break under the maximum load. Table 3.7 provides the values of the Critical Failure Stress for every single wire of the seven wire strand. Note that this value only provides the input failure stress but it does not give the sequence by which the wires break. This can only be obtained in "real time" during the load increments as the load in the wires is re-distributed after every break, leading to wire breaks in an unknown order. Summary of true sequence breaks is given in Table 3.7. The axial stress in the wires at different loading increments is shown in Figures 3.19-3.23. For clarity of these figures, we only plot the wires with the minimum and maximum stress and all wires that have snapped.

At the first loading step (Figure 3.19), none of the wires have exceeded the Critical

Failure Stress, i.e. none of the wires break and hence all carry the same load. The response of the strand is compared to a linear line which represents the response of the linear elastic wires in perfect conditions (no corrosion) as observed in Figure 3.19(a). At the current loading, both curves show the same response since none of the wires have broken. As the wires start to break, the response of the curve which takes into account the effect of corrosion starts deviating from the perfect condition curve. The small bump observed at the location of the clamp is due to the fact that concentrated forces increase the stress in the longitudinal direction, as predicted by Boussinesq, being more severe in the wires that make contact with the clamp. Once wire # 7 fails (the first wire to break), as shown in Figure 3.20, the load is distributed between other wires, and in particular the neighboring wires [# 1, # 2, and # 6] take most of the burden. Note that this leads to non-symmetry in the load transferred to different wires.

Clearly, as the wire breaks within a close proximity to the right of the clamp, wire # 7 immediately recovers part of the load due to friction (crossing the clamp from right to left) relieving the stress in wires # 1, # 2, and # 6. Wires # 4, # 5,and # 3, which are farther away from the broken wire, end up carrying slightly more load at the center of the wire as some load from wires #1, #2, and #6 is transferred to them due to friction between these wires. Friction occurs between these wires due to differential stress, i.e. since individual wires carry different loads, they deform differently, creating shear stresses which result in stress transfer between the wires close to the clamp.

The second break corresponds to the failure of wire #6 at the left of the clamp as observed in Figure 3.21), recovering stress once it crosses the clamp (from left to right). Due to this break, wire #5 carries more load than the rest of the wires to the left of the clamp. Wire #2 takes most of the load left by wire #7 at the right of the clamp since wire #6 is broken and can only regain partial load.

In the next step, shown in Figure 3.22, wire #1 breaks to the right of the clamp

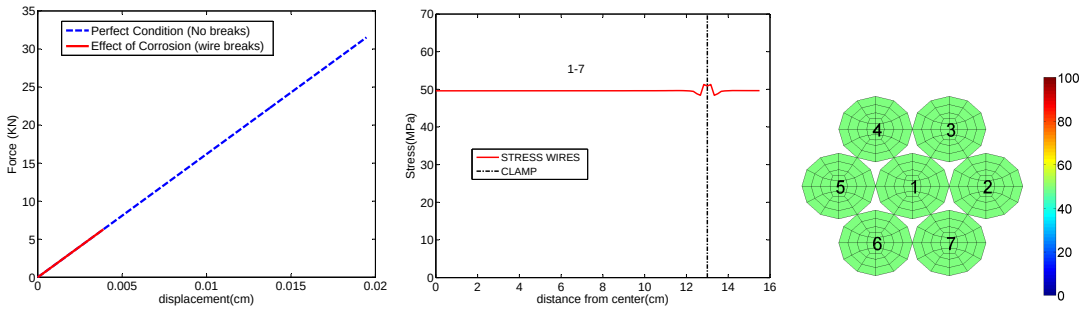

(a) (b) (c)

Figure 3.19: Seven Wire Case. (a) Force-displacement curve of the corroded strand compared to the perfect condition case (no breaks). Axial stress after loading increment 1 (b) along the length of the wires (c) at the cross section of the wire at either the right or left end of the wire. Note that none of the wires break, i.e. all carry similar stress levels.

recovering stress to the left of the clamp. It recovers more stress than wire #7 since it breaks farther to the right of the clamp and makes contact with more wires, thus having more length for frictional interaction. Wire #2 carries more load near the right end since it has two broken wires next to it.

As the strand continues to be loaded (Figure 3.23), all wires eventually break. Nevertheless, the system continues to carry an axial load only due to the frictional forces induced by the clamp. Table 3.7 shows the breaking sequence of the wires. Notice that the breaking sequence does not happen at the same order of the distribution of the Critical Failure Stress, which is due to the fact that, as wires break, the remaining wires redistribute the stresses among themselves not uniformly, depending on the location of the break and of the broken wire with respect to the other wires. Therefore, a wire with a higher failure stress may reach its critical stress before a wire with lower critical stress.

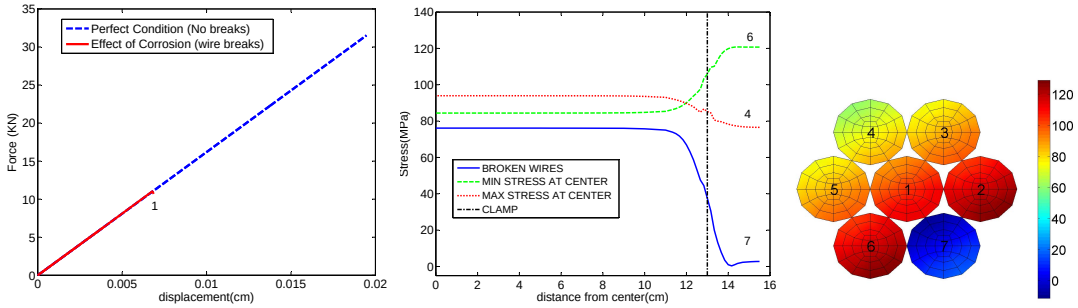

(a) (b) (c)

Figure 3.20: Seven Wire Case behavior after the first wire breaks*

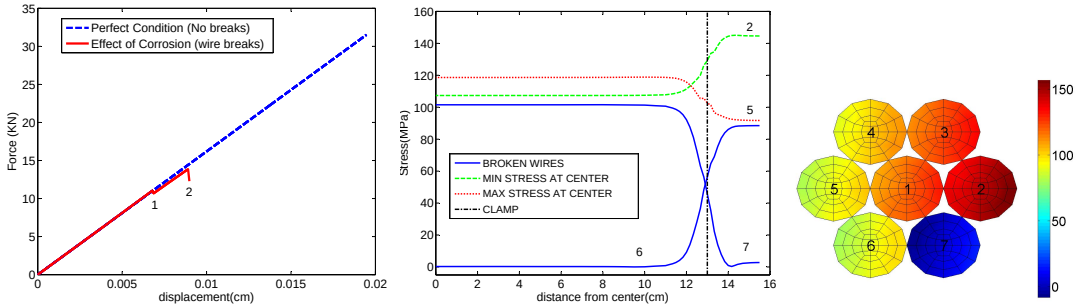

(a) (b) (c)

Figure 3.21: Seven Wire Case behavior after the second wire breaks*

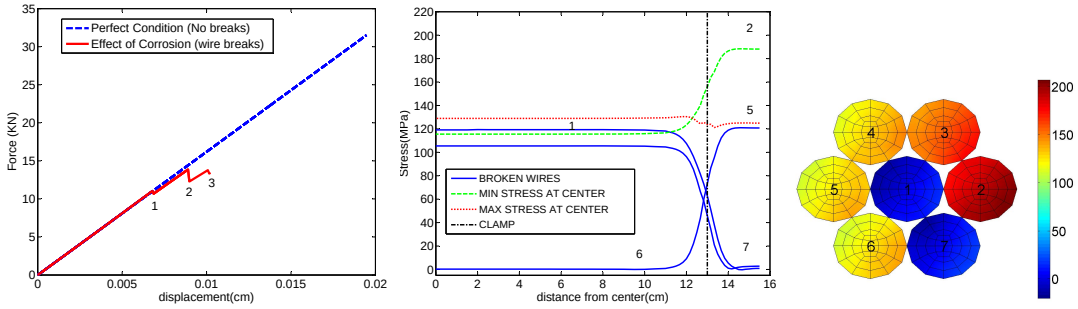

(a) (b) (c)

Figure 3.22: Seven Wire Case behavior after the third wire breaks*

*(a) Force-displacement curve of the corroded strand compared to the perfect condition case (no breaks). Axial stress (b) along the length of the wires for selected wires and (c) on the cross section of the strand at the right end.

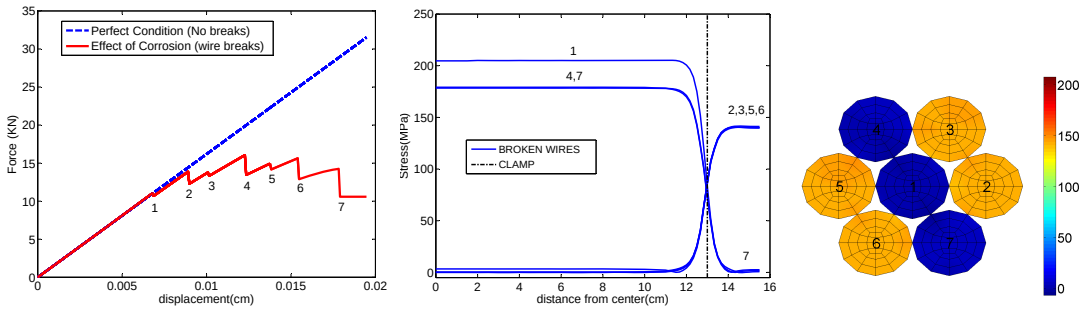

(a) (b) (c)

Figure 3.23: Seven Wire Case behavior after all wires break.

*(a) Force-displacement curve of the corroded strand compared to the perfect condition case (no breaks). Axial stress (b) along the length of the wires for selected wires and (c) on the cross section of the strand at the right end.

Table 3.7: Critical Failure Stress (CFS) and actual breaking sequence of the 7 wire case

Wire Number	**CFS values in [MPa]**	**Initial CFS Order**	**Actual Breaking Sequence**
1	154	3	3
2	185	5	6
3	233	7	7
4	199	6	5
5	162	4	4
6	110	2	2
7	92	1	1

Nineteen Wire Case

As in the previous case, the distribution of the Critical Failure Stress along the length of the wire is obtained through a random number generator with a uniform probability distribution between 50 $MPa \leq \sigma_{cr}^{wires} \leq 600\ MPa$. Contrary to the seven wire case, not all the wires are driven to failure. Table 3.8 illustrates the value of the Critical Failure Stress for every single wire of the 19 wire strand. The axial stress in the wires at different loading increments is shown in Figures 3.24 to 3.26. It can be observed that the patterns in re-distribution of stresses among the wires due to broken wires are similar to those mentioned in Section 3.5.1 for the seven wire case. However, the length on which broken wires recover load varies as they are farther away from the clamping force and the compaction stress decays over a longer distance for interior contact interfaces. The sequence of breaks in "real time" for the 19 wire case is given in Table 3.8.

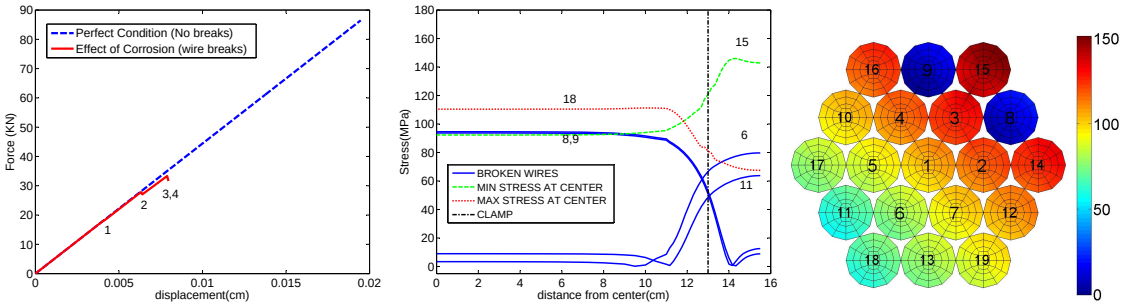

(a) (b) (c)

Figure 3.24: 19 Wire Case behavior after 4 wires break*

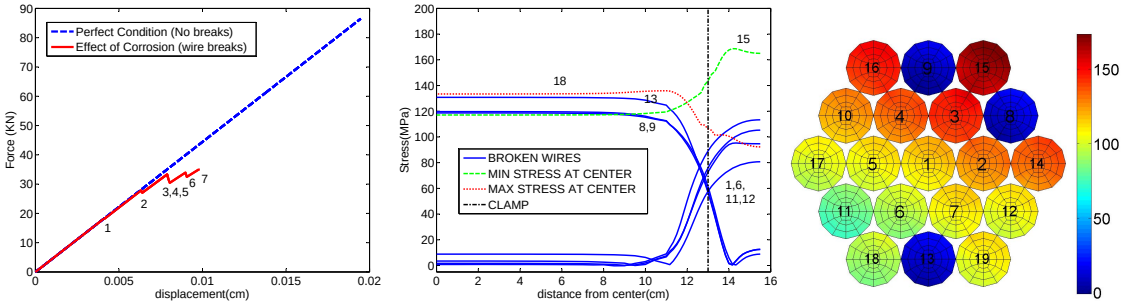

(a) (b) (c)

Figure 3.25: 19 Wire Case behavior after 7 wires break*

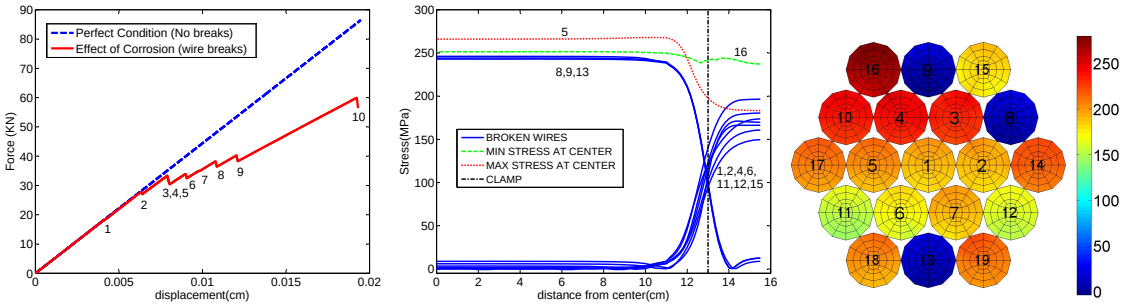

(a) (b) (c)

Figure 3.26: 19 Wire Case behavior after 10 wires break*

* (a) Force-displacement curve of the corroded strand compared to the perfect condition case (no breaks). Stresses (b) along the length of the wire for selected wires and (c) on the cross section of the strand at the right end.

Table 3.8: Critical Failure Stress (CFS) and actual breaking sequence of the 19 wire case. NB stands for not broken, which indicates that the wire did not break under the applied loading.

Wire Number	**CFS values in [MPa]**	**Initial CFS Order**	**Actual Breaking Sequence**
1	150	5	5
2	153	9	8
3	318	11	NB
4	268	10	10
5	420	13	NB
6	82	2	2
7	433	15	NB
8	121	7	4
9	54	1	1
10	448	17	NB
11	109	4	3
12	119	6	6
13	104	3	7
14	437	16	NB
15	151	8	9
16	553	18	NB
17	357	12	NB
18	594	19	NB
19	426	14	NB

Table 3.8 corroborates that the breaking sequence and the Critical Failure Stress are not in the same order. Due to the redistribution of the load among neighboring wires, it may happen, as previously suggested, that wires with higher Critical Failure Stress reach this limit before other wires with lower Critical Failure Stress.

3.5.2 Many Wire Strand - Implementation on a Parallel Computer

The computing speed and memory requirements of single processor machines impose severe limitations on the size and time it takes to solve these problems. For instance, an analysis of 127 wire strand (the size of a typical prefabricated strand in suspension bridges) requires approximately 1 million equations for a reasonable accuracy; however, it cannot be solved serially due to a lack of memory. Hence implementation on a parallel machine is essential for real life applications.

To overcome these limitations, the method is implemented in Parallel Finite Element Analysis Program (ParFEAP) [46] and compiled using MPI on a SiCortex parallel machine SC1458, containing 243 nodes. Each node has one chip and there are six 64-bit processors per chip, i.e. 1458 processors are available. FEAP interfaces with the PETSc library to employ its linear solvers package and with METIS and ParMETIS libraries to partition each mesh for parallel solution. Feap is compiled using PETSc v3.0.0-p11, BLAS/LAPACK v.3.1.1, ARPACK 2001, and Sicortex MPI which is based on the MPICH2 software from Argonne National Laboratory.

Two sets of tests are performed to evaluate the efficiency of the parallel implementation, where the problems are solved at 4, 64, 128, 256 and 512 processors. Figure 3.27 shows a sample partition for the 127 wires into 64 processors. The ghost nodes, the overlapping nodes between processors, are either along the longitudinal direction of a wire or at the edges of the wire when there is a transition between processors. We use the MINRES linear solver with a block Jacobi preconditioner, where 1 block per processor is chosen, and each block is solved with an ILU(0) smoother. The tolerance of both the linear and the nonlinear solver (a standard Newton method) is set to a relative tolerance of 1.0E−05.

The first test (reported in Table 3.9) includes the case that none of the wires break, hence only linear systems are solved every increment. We consider wire strands that

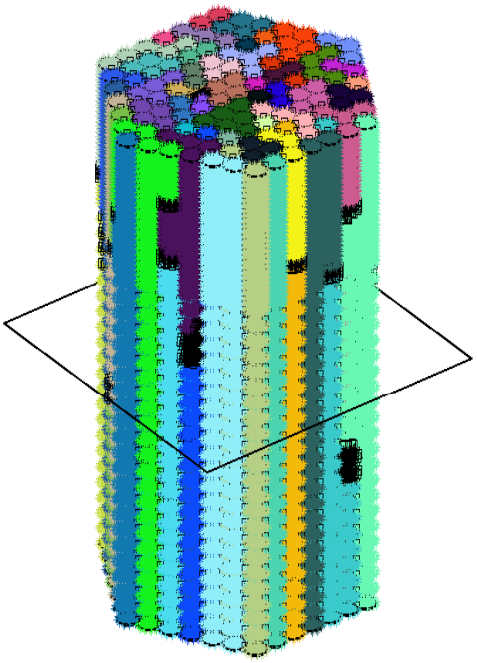

(a)

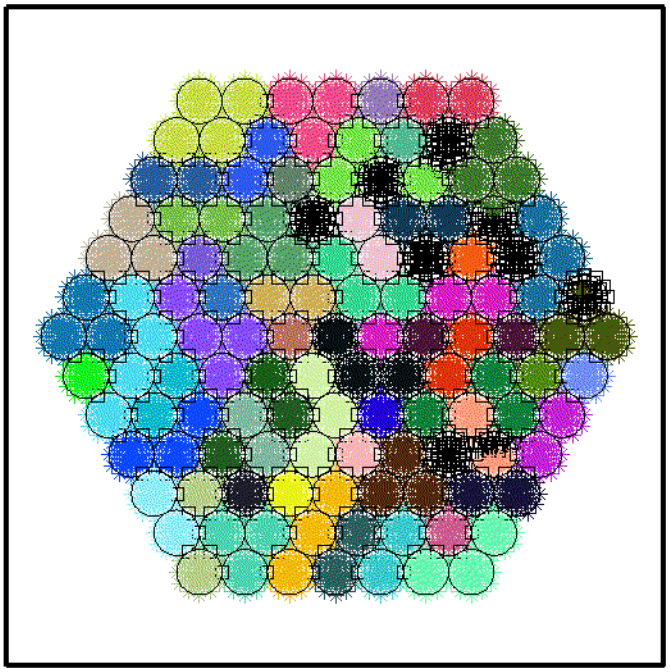

(b)

Figure 3.27: Partition of the 127 wires mesh into 64 processors for parallel solution. The colored sections contain the nodes assigned to each processor and the symbol □ represents ghost nodes. The mesh partition in (a) 3D view and (b) in the 2-D plane shown in (a) are shown.

consist of 19, 37, 91, 127 wires and report the CPU time and the number of linear solves it takes until convergence, for one loading increment. As expected, the computational demand increases with the number of wires and the largest wire strands cannot be solved on 4 processors. Also, while for 91 and 127 wire strands, employing more processors decreases the CPU time, it is not the case for the 19 and 37 wires solved on 512 processors. In this case the communication between processors is more expensive than the linear solves, suggesting that the problem is too small to be analyzed with 512 processors.

Next, we investigate the parallel scalability of the implementation, shown in Figure 3.28, where only the first increment of the loading is considered (one linear solve), i.e. there are no wire breaks which induce nonlinearity. The relative parallel speedup of the system is defined as [41]:

$$S(p) = \frac{T(min_p, n_p)}{T(p, n_p)} = \frac{T(64, n_p)}{T(p, n_p)} \tag{3.8}$$

where $T(min_p, n_p)$ is the time to solve a problem of size n_p using the minimum number of processors (min_p) that can handle the job. $T(p, n_p)$ is the time to solve a problem of size n_p when using p processors. The minimum number of processors for the 91 and 127 wire problems was 64 as shown in Eq. (3.8). The speedup is compared to the maximum linear speedup proposed by the SiCortex machine manufacturer. The parallel scalability improves as the size of the problem increases as shown in Figure 3.28, where the 127 wire case shows a slightly better performance than the 91 wire case.

The second test (reported in Table 3.10) includes random wire breaks, hence nonlinear iterations are performed as some of the contact-friction springs enter the plastic regime. We consider wire strands that consist of 91 and 127 wires and report

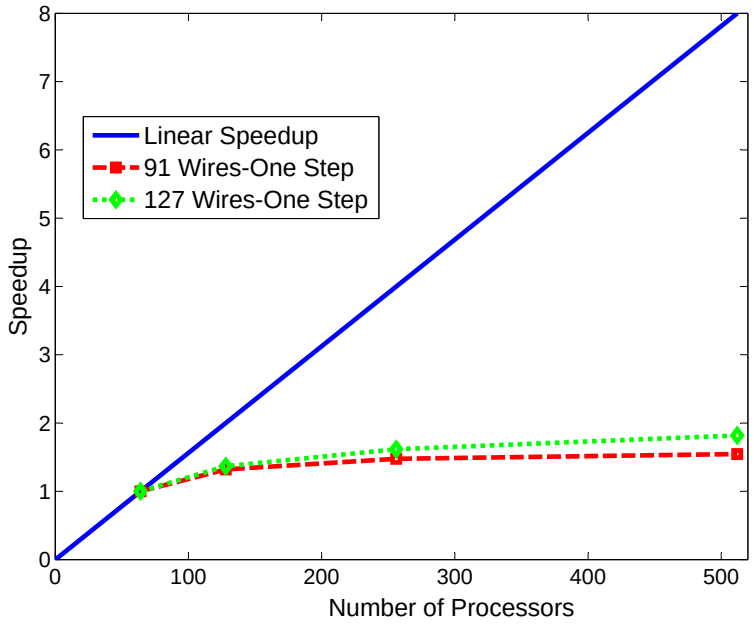

Figure 3.28: Speedup for the parallel runs

the CPU time and the number of nonlinear solves it takes until convergence after 10 loading increments has been achieved. It is obvious that the CPU time has now increased tremendously compared to the intact (non breaking) case in Table 3.9 as more linear solves are now performed due to the nonlinearity. However, the parallel implementation significantly lowers the CPU time and speeds computations.

Table 3.9: Parallel performance (CPU time (s) and number of linear iterations) for one loading increment - no breaks

No. of Wires	**No. of Equations**	**No. of Processors**									
		4		**64**		**128**		**256**		**512**	
		CPU	Iters.	CPU	Iters.	CPU	Iters.	CPU	Iters.	CPU	Iters.
19	145,350	130.01	88	26.57	91	28.30	91	26.77	97	29.81	107
37	283,050	372.80	96	64.73	93	58.67	95	55.64	98	67.06	105
91	696,150	-	-	232.30	99	176.00	97	157.54	100	150.40	102
127	971,550	-	-	395.19	100	289.08	100	244.46	102	217.46	98

Table 3.10: Parallel performance (CPU time (s) and number of nonlinear iterations) for ten loading increment - many wires break

No. of Wires	**No. of Equations**	**No. of Processors**							
		64		**128**		**256**		**512**	
		CPU	Nonlinear Iters.	CPU	Nonlinear Iters.	CPU	Nonlinear Iters.	CPU	Nonlinear Iters.
91	696,150	1570.32	62	836.07	65	537.67	64	370.07	62
127	971,550	2993.19	71	1632.02	71	886.34	67	613.48	68

3.6 Discussion of the Numerical Examples

Many factors contribute to the load transfer between wires as they start to break. When a wire breaks, its immediate neighbors pick up most of the load carried by that wire (depending on the location of the break), with the remaining part of the load being redistributed to more distant wires. However, due to the friction induced by the clamp, the broken wire itself will regain part of the stress, along a so-called recovery length. The tightness of the clamp, location of the break from the clamp, and number of surrounding unbroken wires are key factors in the level of partial load regains. The rate of recovery depends on the proximity of the broken wire to the clamp, since at interior contact interfaces the compaction stress spreads over a longer distance from the clamp. It is also interesting to note that once the broken wire regains back some of its load carrying capacity, the load will again be redistributed more uniformly between all neighboring wires. Furthermore, the sequence by which wires break in a strand is essentially unknown *apriori* even though the initial Critical Failure Stress (a material property randomly set by the user to model corrosion uncertainty effects) is set as an input parameter to the simulation. The true sequence is obtained in "real time" during the loading increments and depends on how the stresses are being distributed between wires. The overall load carrying capacity of the strand (viewed here as a system) determines whether or not the strand is able to carry the applied tension load. We also note that the response of the system becomes nonlinear, as individual wires start to break, and the overall stiffness of the system decreases. This behavior is illustrated by a force-displacement curve in Figure 3.29, and obtained with an incremental loading. The linear straight lines in the Figure 3.29 show the system's perfect (intact) response in case that none of the wires break due to corrosion. However, as evidenced by the force-displacement curves, when wires in the strands start breaking, the response of the system deteriorates and becomes nonlinear. These nonlinear curves were smoothed out by a least square fit of the simulation results to

show the overall reduction in the load carrying capability of the strand. Moreover, due to computational limitations only ten increments are applied which means that several wires may break in one step and hence a smooth curve can capture this trend.

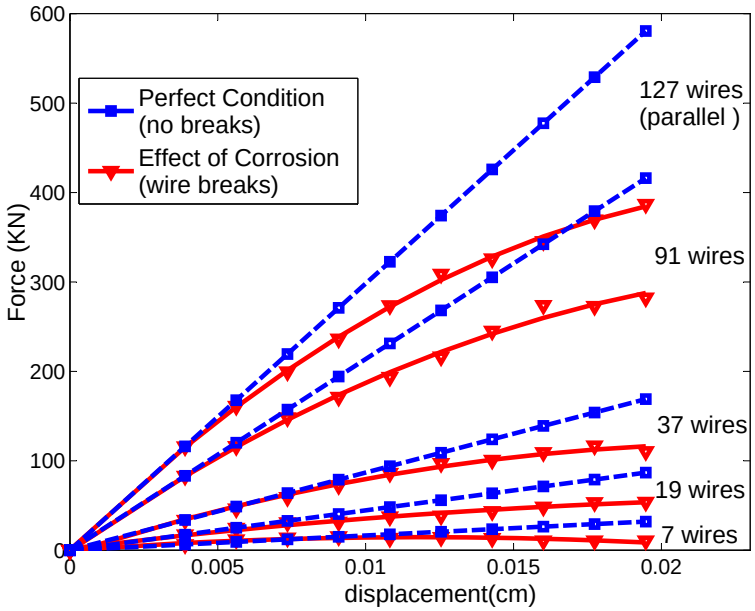

Figure 3.29: Force-displacement curves showing the reduction in the load carrying capacity of different wire strands. Ten displacement increments are employed.

Nevertheless, to better resolve and obtain a more accurate response, the simulations for 7 and 19 wires were repeated using 100 smaller loading increments, as shown in Figure 3.30. It can be seen that the true behavior is that of a "zig-zag" curve since the wires themselves are linear elastic but the contact behavior is nonlinear. It is also interesting to point out that in the seven wire case, all wires are eventually driven to failure and the system begins to exhibit softening. The residual capacity as a fraction of the elastic limit of the intact cable is reported in Table 3.11. Notice that for the case in which many wires break, the residual capacity is about 70% for the strands with more than seven wires and 38% for the seven wire case in which all the wires were broken. Although all wires are broken in the seven wire case, the wire strand continues to carry an axial load only due to friction forces induced by the clamp.

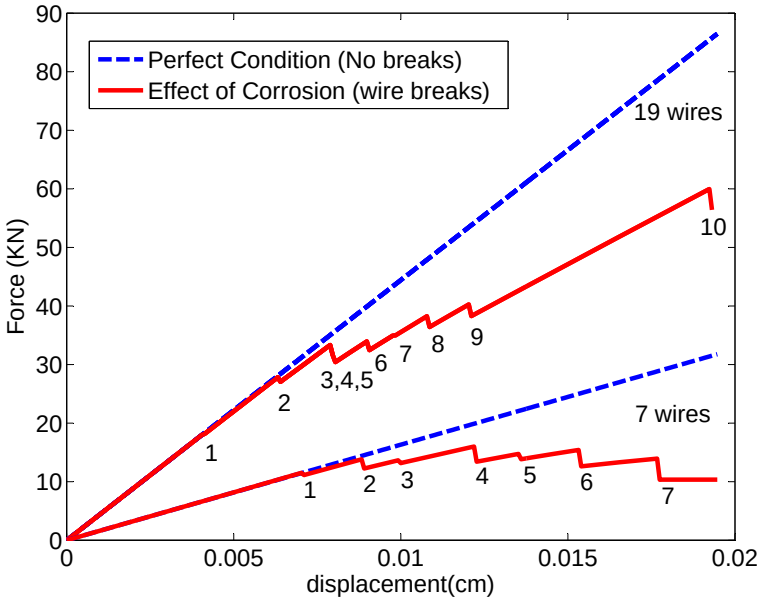

Figure 3.30: Force-displacement curves showing the reduction in the load carrying capacity of 7 and 19 wire strands. One hundred displacement increments are employed and a "zig-zag" response is observed.

Table 3.11: Residual capacity as a fraction of the elastic limit of the intact cable

Wires	**Residual Capacity**(%)
7	38
19	67
37	65
91	72
127	67

3.7 Multi-scale Model for Main Cables

The main span of a suspension brige cable can vary from 100 m to 1991 m, the length of the current longest central span in the world. However modeling the actual length of the cable implies a high computational effort that can be reduced by considering the recovery length of a broken wire within a cable. A study was performed by the firms of Steinman, Gronquist, and Birdsall [42] on the Williamsburg bridge to determine the recovery (or clamping) length of a broken wire. The inspectors indicated that a cable band provides the necessary friction so that a broken wire can regain about 80% of its load carrying capacity. Thus, two successive cable bands will provide nearly full recovery from a wire. If the effect of the undisturbed wrapping wire is added, it was concluded that only one band would be needed on each side of a break, making the overall clamping length 6.1 m (20 ft), the typical distance between cable bands.

It was recommended to include three cable bands when modeling a main cable. In this manner, despite of the location of the break, the broken wire will obtain full recovery at least at one of the ends of the simulated cable. Thus, the prescribed length of interest has been defined as 18.288 m length (60 ft), typically three successive clamping lengths. Although the wires are arched, the prescribed length allows us to model the wires as parallel and provides a good estimation of the ultimate strength of the cable at any point along the full length of the cable. Three clamps having a width of 20 cm are placed over the length, spaced at 6.096 m from each other as shown in Figure 3.31. The cable is pulled at both ends, since corrosion variation along the wires in a main cable is not symmetric and symmetric boundary conditions may not be assumed. In order to obtain the breaking load of a cable, the load is increased slowly, having wires break a few at a time according to their current deterioration. This simulation is equivalent to having the cable removed from a bridge and pulling it slowly in a giant uniaxial testing machine. The simulated cable has a diameter of 24.37 cm, composed of 9061 wires with a diameter of 0.4826 cm each as shown in

Figure 3.32. (Note that a change in the axis orientation for the multi-scale model was performed in order to match the orientation defined by Shi et. al [54] as will be illustrated in Chapter 4).

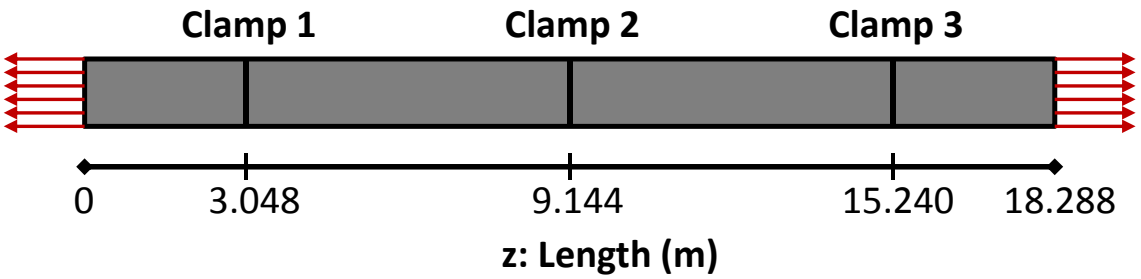

Figure 3.31: The main cable model has a prescribed length of 18.288 m (60ft). Three clamps having a width of 20 cm are placed spaced at 6.096 m (20 ft) from each other. The cable is loaded at both ends.

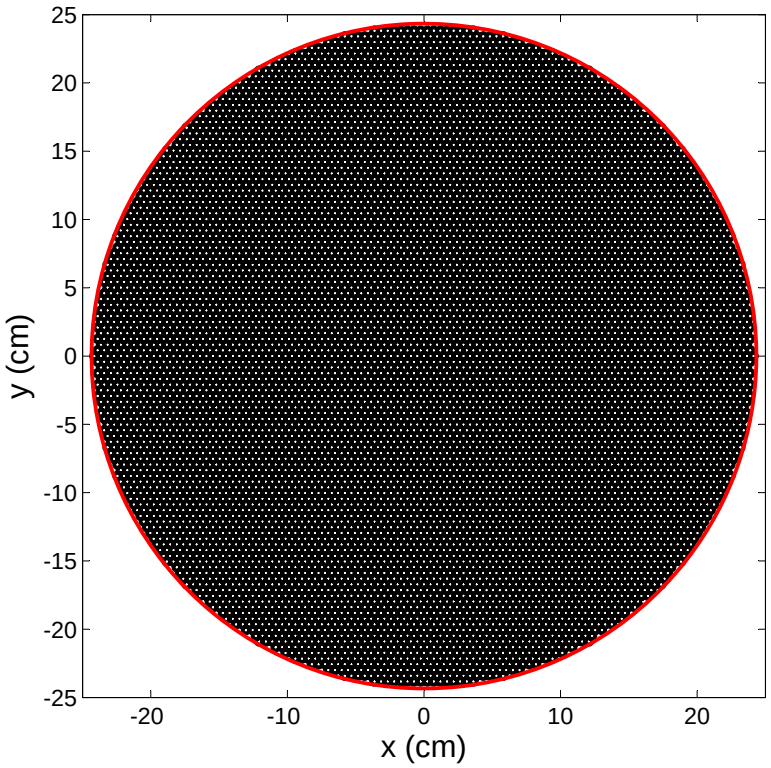

Figure 3.32: Cable's cross section, composed of 9061 wires with a dimameter of 0.4826 cm each.

3.7.1 Frictional Interaction Between Wires

Elasto plastic spring elements ,described in Section 3.3.2, are used to account for the frictional interaction between wires, where the tangential spring parameters can be obtained from Equation 3.7. For the main cable case, a band width of 20 cm is assumed; thus a distributed force per unit length (N/cm) is used to account for the clamping action as shown in Figure 3.33. The contact force between wires is obtained by adding the contribution of equivalent clamping forces placed at the nodes defined in the mesh. The normal force of the 9061 wire case was found by assuming a distributed force of 1N/cm at each of the 342 outer wires. If a higher clamping load is assumed, it will be linearly propotional to this solution. Figure 3.34 show the contact force due to a concentrated force of 5 N acting in each of the outer wires and using a mesh spacing of 1 cm. The contact force is shown at the cross section where the concentrated force is applied, showing that the outer wires have a higher contact force at this location due to their proximity to an applied external load. However, in a multiscale model, the details of the frictional decay in the micro scale becomes trivial, since in order to account for the exact distribution many nodes will be needed in the clamp region. The total contact force between wires is the relevant parameter in the macro-scale, because it will determine the load that can be recovered by a broken wire in a clamp. The frictional springs are defined in the nodes of the 20 cm clamp region and a node at 2.5 cm from the ends of the clamp. Boussinesq solution specifies that the pressure force decays to zero very fast when moving away from the clamp in the longitudinal direction. Therefore, the clamping effect is considered a local phenomenon that appears only within the clamp and very close to the tips. The cable bands are considered independent and each cable band will generate the same compaction pressure. Figure 3.35 shows the total contact force at the 26,838 contact points between wires. It is observed that the total contact force is higher in the center-most region of the cable than the region near the perimeter of the cable. Since

the force is in the radial direction, the contribution of all the clamping forces is higher towards the center of the cable. For instance, the wires in the bottom perimeter of the cable feel the effect of the clamping forces near the bottom edge, but the clamping forces in the top perimeter are too distant to provide significant compaction to those wires.

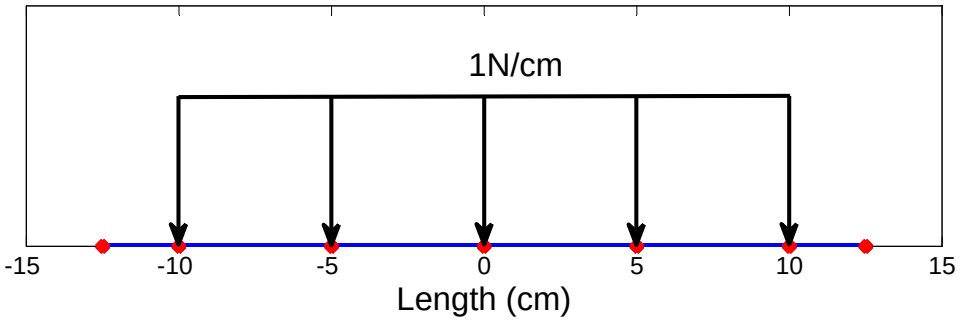

Figure 3.33: Distributed clamping force within the 20 cm clamp.

In order to account for different clamping magnitudes, the distributed clamping force must be adjusted. The calibration of the the distributed clamping force is performed according to the total radial contact force caused by the clamp-cable interaction as specified by the Manual of Bridge Engineering [1]. As the screwed rods are tensioned, the band will be pulled into tight contact with the cable's perimeter. If N pairs of screwed rods are tensioned to a load P, the total tension force applied to each quadrant of the band is PN. Frictional losses due to small circumferential movement between the band the cable wires will tend to reduce the tension in the band to a minimum value of:

$$F_{Nlosses} = NPe^{\frac{-\pi\mu}{2}} \tag{3.9}$$

where μ is the coefficient of friction between the wires and the cable band, 0.2 is usually recommended. The effective total radial contact force will therefore be:

$$F_{Nband} = \frac{4NP}{\mu}[1 - e^{\frac{-\pi\mu}{2}}] \tag{3.10}$$

A reduction of 70 % of the nominal value is recommended to allow for the relaxation of screwed rod tension. The effective total radial contact force provided by the cable band can be distributed at the outer wires in order to determine the distribution of the contact force in the cross section. The conclusions provided by the Williamsburg Inspection [42] did not specify frictional variation within the cross section as only a few wires were tested to reach the recovery length conclusions. Since the tests to determine the load recovery were most likely performed with the outer wires due to accessibility, the contact points in this region are calibrated to obtain recovery lengths of 6 m, (one cable band), and 12 m (two cable bands).

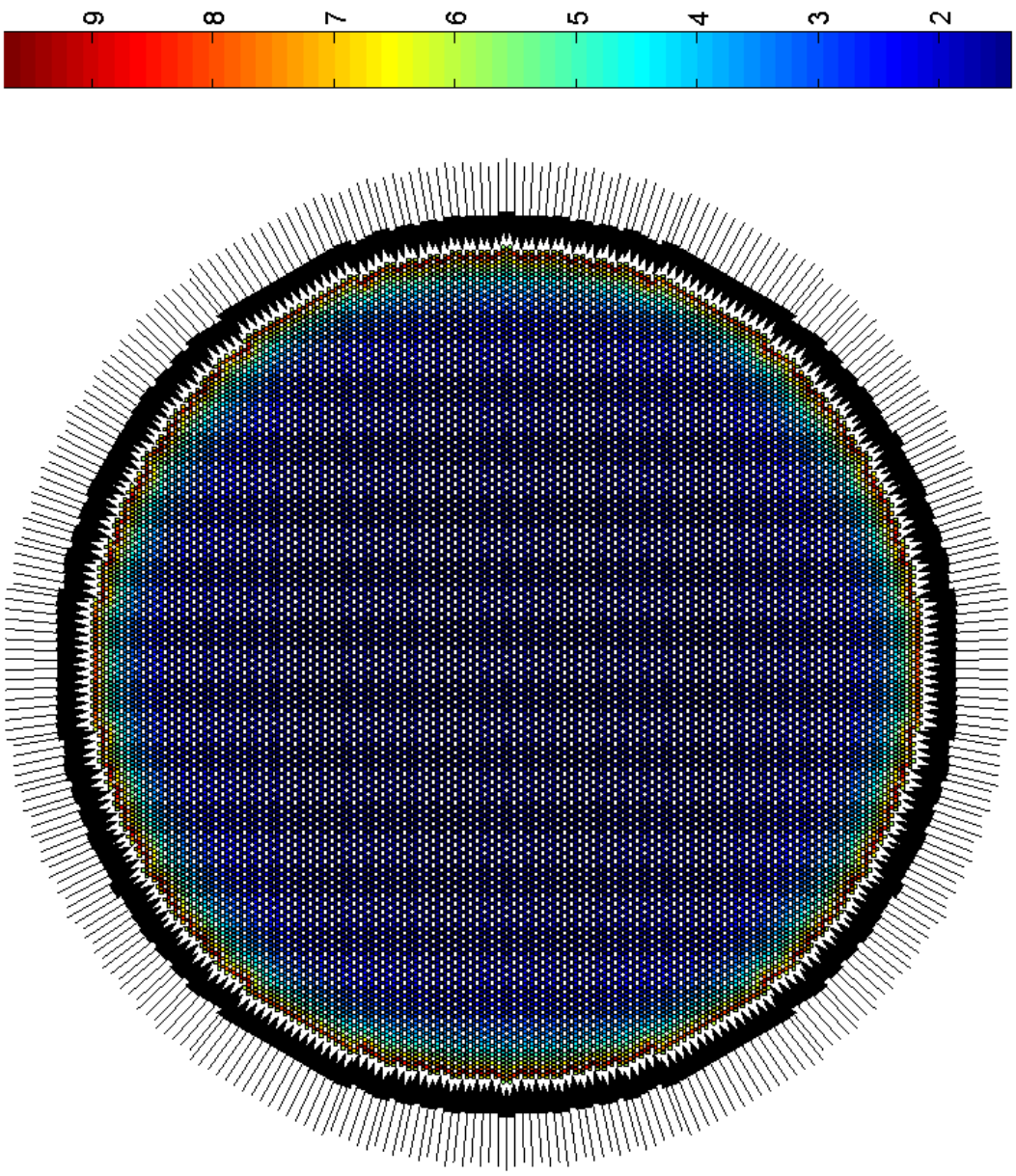

Figure 3.34: Contact force (N) for the 9061 wire case, having 26,838 contact points between wires, at the location of the clamp. A clamping force of 5N is assumed to act in each of the 342 outer wires. A mesh spacing of 1 cm is used to obtain the consistent contact forces; L_e= 1 cm. Due to the number of contact points (26,838) and the limitations on the size of the figure, it is not easy to distinguish the exact distribution in the above figure. However, the trend that the compaction force near the perimeter of the cross section is higher than the center region at the location of the clamp is observed.

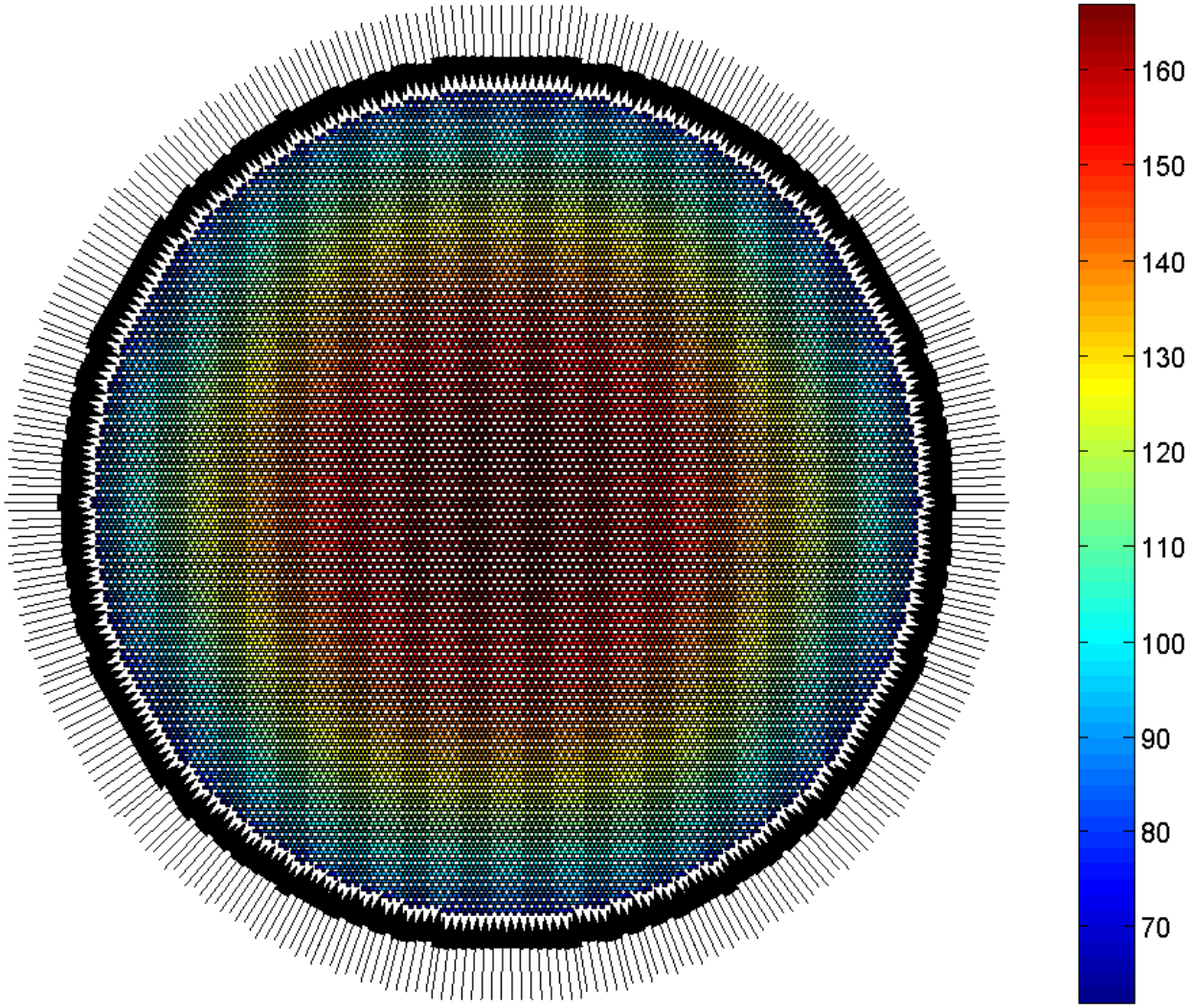

Figure 3.35: Total Contact force (N) for the 9061 wire case, having 26,838 contact points between wires. A clamping force of 1N/cm is assumed to act in each of the 342 outer wires. Due to the number of contact points (26,838) and the limitations on the size of the figure, it is not easy to distinguish the exact distribution in the above figure. However, the trend that the total compaction force near the perimeter of the cross section is lower than the center region is observed. The consistent contact forces are obtained by integrating the resulting compaction stresses 0.3048 m (1ft) away from the center of the clamp, L=0.6096 m (2ft).

3.7.2 Mesh Description

Although brick elements provide more complete results, accounting for the stresses occurring in different directions, their computational effort is considerably high as observed for the 127 wire case 15.5 cm long (an extremely small length compared to the presrcibed length of 18.288 m), requiring almost one million equations. In order to facilitate a full stochastic analysis of the problem and reduce the resulting computational effort to manageable levels, the elements used to model the wires of a main cable are truss elements. It has been determined that the axial stress in each wire is the main stress component and these elements will predict it with sufficient accuracy. One dimensional truss elements consist of 2 nodes and 1 degree of freedom per node, significantly reducing the computational effort associated with brick elements. Although the problem is a three-dimensional one, for computational purposes the problem is in 1D, since the element connectivity matrix is enough to account for the elements that are in contact. This approach eliminates the degrees of freedom and coordinates in the cross-sectional direction. A sample truss system, composed of 127 wires for clarity purposes, is illustrated in Figure 3.36.

The mesh is finer in the clamp region as shown in Figure 3.37 and becomes coarser when moving away from the clamp. A total of 59 nodes and 58 elements per wire are required. The center element between two successive clamps is selected as a possible breaking point, where in order for breakage to occur, the stress has to exceed the critical failure stress of the element. This critical failure stress is the minimum strength of all the elements between the two successive clamps, but the breaking point is placed at the midpoint between clamps since the wires can only recover load at the clamp and thus the exact location of the breaking position becomes irrelevant. This method also reduces memory storage and avoids checks at every element that increase the CPU time considerably.

The size of the problem associated with the 9061 wire case is described in Table 3.12.

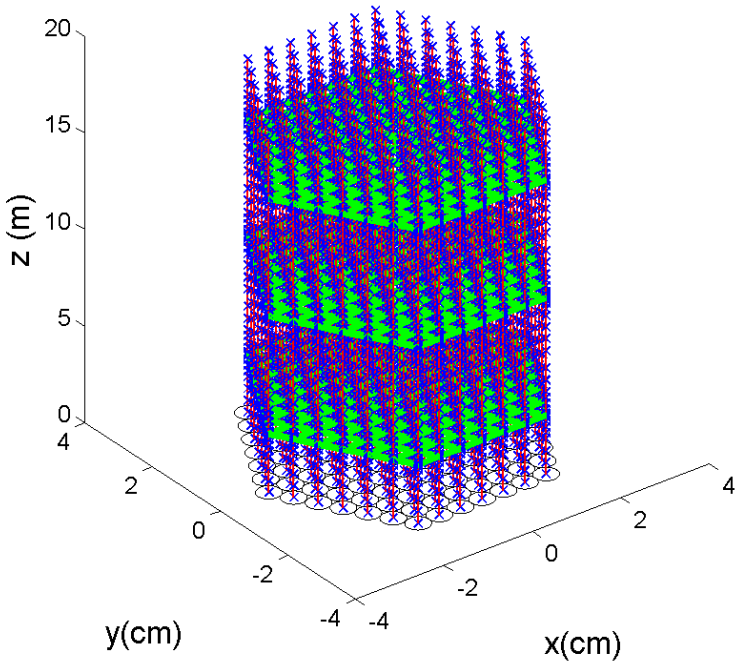

Figure 3.36: One dimensional truss elements in a three dimensional space; the connectivity matrix accounts for the wires that are in contact. Spring elements are placed at the contact nodes near the clamp.

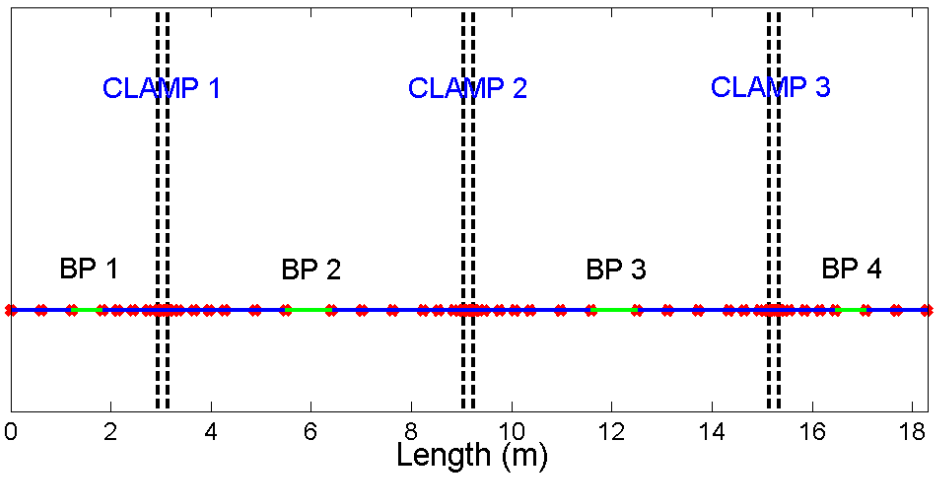

Figure 3.37: Indivual mesh of a wire modeled with 1-D truss elements. BP stands for breaking points where a check is performed to determine if the current axial stress exceeds the Critical Failure Stress.

Table 3.12: Size of the problem associated with the 9,061-wires cable

FEM Paramaters	**One Wire**	**Entire Cable (9061 wires)**
Nodes	59	534,599
Truss Elements	58	525,538
Spring Elements	-	563,598
TOTAL Elements	-	1,089,136

3.7.3 Sample Run for the Multi-scale Model

As the computational effort is high, the problem is parallelized in order to speed the computation. The problem was solved using the parallel version of the Finite Element Analysis Program (FEAP) on a SiCortex machine. The problem was split into 100 processors (refer to Figure 3.38), with an average number of 5,247 nodes per processor. The Conjugate Gradient (CG) linear solver with a block Jacobi preconditioner is employed to solve the problem.

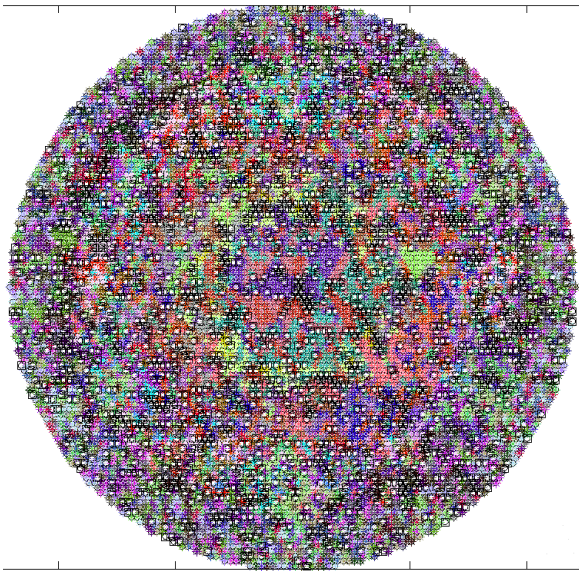

Figure 3.38: Partition of the 9,061 wires mesh into 100 processors for parallel solution over the cross-section. The 100 different colors correspond to the 100 processors. The colored sections contain the nodes assigned to each processor and the symbol □ represent the ghost nodes.

3.7.4 Monte Carlo Simulation

A Monte Carlo simulation approach is used to estimate the cable's safety. In order to obtain an idea of the computational time associated with a Monte Carlo simulation, the problem was run with an uncorrelated (white noise) random corrosion pattern (which does not simulate actual conditions of a cable). The randomness associated with corrosion was generated using a standard pseudo-random number generator. A different random number to represent the critical failure stress (CFS) was generated for each of the four breaking points in each wire for a total of 1,000 realizations. The cable was loaded using the displacement controlled method for ten steps: the wires started breaking as they exceed their CFS at different load levels as observed in Figure 3.39. Broken wires recovered load as they crossed the clamps. The computational time for the 9,061 wires was recorded and the approximate CPU time for 10,000 and 100,000 realizations (shown in Table 3.13) is extrapolated based on the recorded results for 1,000 realizations. As the problem is run on a Sicortex machine that contains 1,458 processors and whose processors' memories are independent of each other, we can have several FEAP executables running at the same time. Thus, the CPU time when running 5 FEAP executables is approximated in Table 3.13 as well.

Table 3.13: CPU time for Monte Carlo simulations using FEAP

Number of Realizations	**100 Processors (1 FEAP Executable)**	**500 Processors (5 FEAP Executable)**
1,000	9 hrs. (measured)	1 hr 48 min (approximated)
10,000	90 hrs(4 days) (extrapolated)	18 hrs (extrapolated)
100,000	900 hrs (38 days) (extrapolated)	180 hrs (8 days) (extrapolated)

The resulting force-displacement curves in Figure 3.40 for the 1,000 realizations show a slight increase in scattering as the load is increased. However, this level of scattering is considered generally small. As the simulated random pattern for the

corrosion (white noise) does not reflect realistic conditions at this stage, the number of realizations needed for a realistic random corrosion pattern cannot be predicted at this point with accuracy. Furthermore, the amount of scatter for the realistic random corrosion pattern is expected to be different too. An accurate simulation of the strength variation induced by corrosion is proposed in the next chapter.

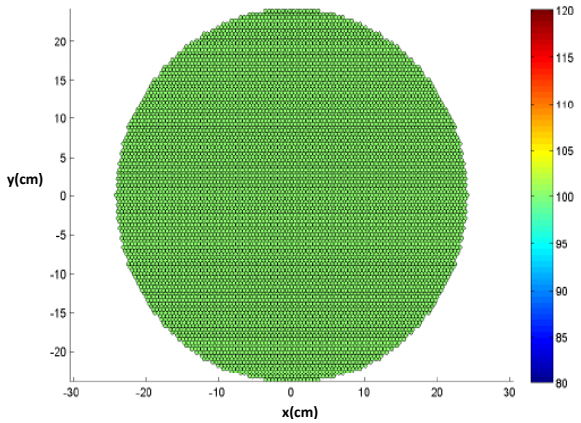

(a)

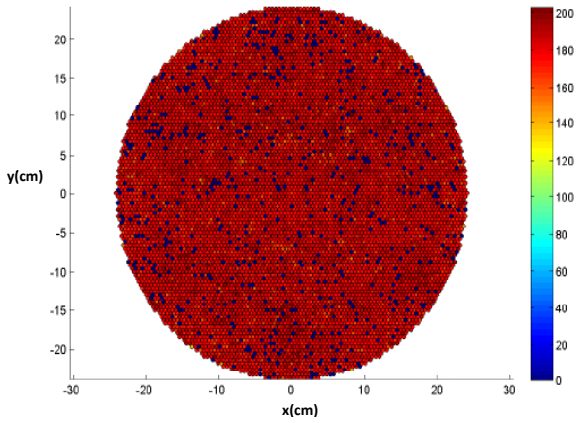

(b)

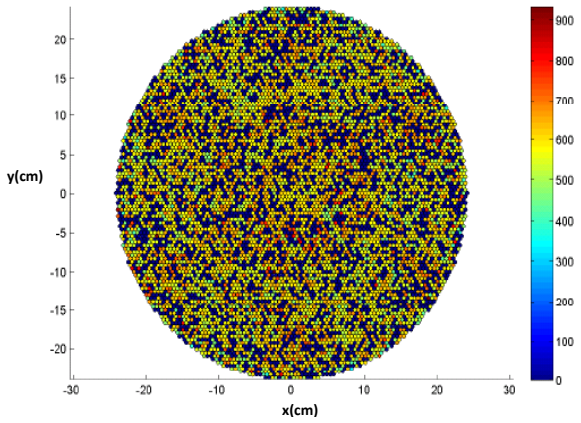

(c)

Figure 3.39: Sample Stresses [MPa] at different loading steps for the 9,061-wires case at the left end (x=0 m) of the cable. It should be pointed out that the scales for the three plots are not the same.

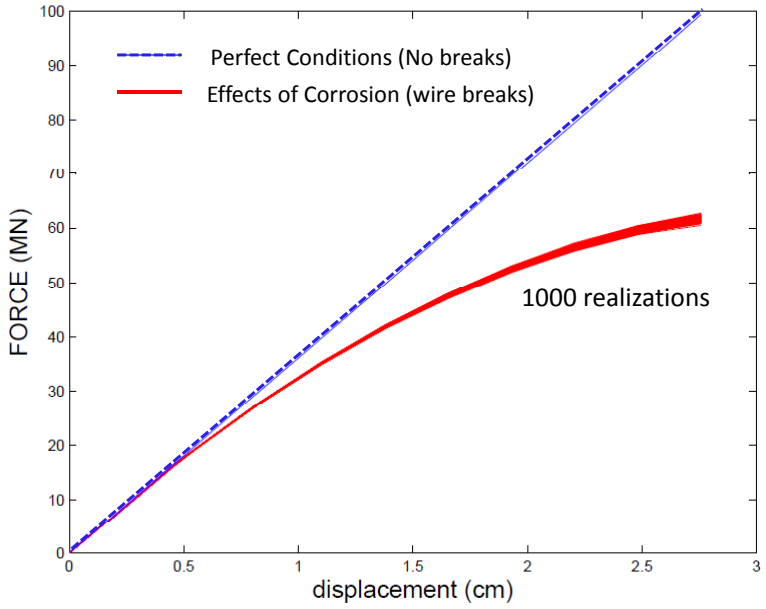

Figure 3.40: Force-displacement curves for the 9,061-wires case for each of the 1,000 realizations of corrosion compared to the perfect conditions (representing no breaks).

Chapter 4

Modeling Strength Variation in Main Cables

4.1 Chapter Summary

In this chapter, it is proposed to treat the strength of the entire cable as a three dimensional stochastic field in order to account for the spatial correlation of the cable's strength. This correlation occurs both within the cross section (over different wires) and along the length of the cable. The probabilistic characteristics of the field are obtained from data available from a Williamsburg bridge investigation program, which included the removal of 32 wires from the cable and subsequent experimentation. The method can be considered an extension of treating the strength of the wire as one dimensional random field; thus an overview of this approach is provided in this chapter. Moreover, potential drawbacks of considering the strength of the wires within the cable's cross section as independent and uncorrelated are addressed. The strength of the cable is simulated by the Spectral Representation Method in three dimensions and its prescribed power spectrum is obtained from the field data of the Williamsburg Bridge. The simulation algorithm for the Gaussian field is dramatically improved with the application of the Fast Fourier Transform technique.

4.2 Williamsburg Bridge Investigation Program

The Williamsburg Bridge is an essential transportation network of New York City, which crosses New York City's East River and connects the Lower East side of Manhattan to Brooklyn. It was opened for service on December 19, 1903 and its main span is of 488 m (600 ft). The bridge has a total of four main cables, two at each side, each composed of 7696 ungalvanized steel wires, whose diameter is of 0.49 cm (0.192 in). Due to the severe deterioration observed from visual inspections, a thorough assessment to determine the existing strength of the main suspension cables was performed in 1988. The investigation was conducted by the engineering firms of Steinman, Gronquist, and Birdsall in association with Columbia University. The

investigation included opening one of the main cables at eight (8) equally spaced radial positions. The grooves positions are shown in Figure 4.1 and labeled from A-E. The wires were visually inspected at these locations, where approximately only 15% of all the main cable wires could be observed. A total of fifteen (15) broken wires were found during the inspection, three (3) in the B groove opening and twelve (12) on the bottom surface. The wires were assigned a corrosion grade based on the visual inspections; however in order to provide more in-depth observations, wires were taken to the laboratory for testing [42].

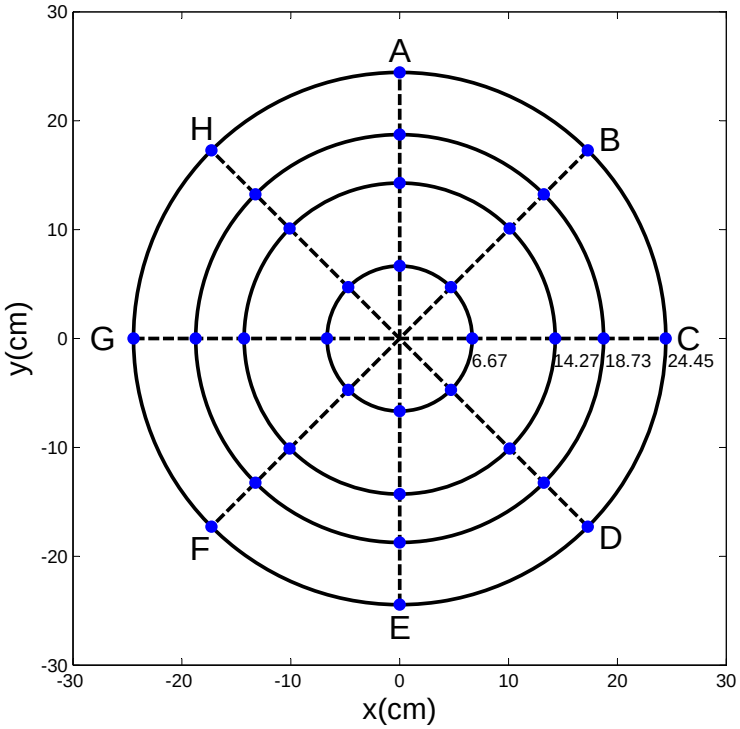

Figure 4.1: Williamsburg Bridge Investigation. The groove openings are labeled from A-H and the dots represent the wire sample locations within a cable cross section.

Thirty two (32) wires from four different radii and the eight grove openings were removed in order to get a representative pool of all the sections of the cable as observed in Figure 4.1. The lengths of these 32 sample wires range from about 6.85 m to 11 m (22.5 ft to 36 ft). The wires were taken to the Carleton Laboratory at Columbia University, where each of these 32 wires was cut into 46 cm (18 in) long segments. As

15 cm (6 in) of each wire segment were inside the grisps of the tensile test machine, the effective length of each wire segment was presumed to be 30.48 cm (or 1ft, 1 ft = 30.48 cm.). Ten or eleven such wire segments from each of the 32 sample wires were selected for a total of 330 segments. The sequence of these 10 or 11 wire segments from each wire was also recorded. The tensile strength of each wire segment was then obtained through laboratory tension testing.

4.3 One Dimensional Random Field Based Approach for Strength Evaluation of Suspension Bridge Cables

The innovation of the modeled proposed by Shi et.al. [54] is that it models the strength of each wire as a random field over a prescribed length of the cable, accounting for the spatial correlation of the wire strength along its length (z-direction). This method is a dramatic improvement to previous methodologies that treated the strength of consecutive wire segments as uncorrelated. In such methods, the n random variables modeling the strength of n successive unit-length segments along the wire of a prescribed length are independent. This assumption is not considered appropriate for ductile materials like steel and can generate significant errors when estimating the strength of suspension bridge cables. Shi et.al. [54] showed the capabilities of the methodology through an application involving the experimental data set of the Williamsburg Bridge Inspection referred in section 4.2.

4.3.1 Probabilistic Characteristics of the Tensile Strength of the Tested Wires

The mean and standard deviation of the tensile strength of the 330 wire segments tested from the wires extracted from the Williamsburg Bridge are:

$$\mu_{330} = 1,495\ MPa\ [216,476\ psi] \tag{4.1}$$

$$\sigma_{330} = 88\ MPa\ [12,682\ psi] \tag{4.2}$$

The wire strengths z_i for each of the 330 wire segments are standardized to zero mean and unit standard deviation, according to the following equation:

$$\bar{z}_i = \frac{z_i - \mu_{330}}{\sigma_{330}} \tag{4.3}$$

The criteria used to fit the data was the quality of the fit at the left tail of the probability density function(PDF) since it ultimately controls the smallest value of the strength over a prescribed length of a wire segment. The probability distribution that provided the best fit for the data was a beta function, with the following PDF

$$f(\bar{z}) = \frac{(\bar{z} - \bar{l_a})^{\alpha-1}(\bar{l_b} - \bar{z})^{\beta-1}}{Beta[\alpha,\beta](\bar{l_b} - \bar{l_a})^{\alpha+\beta-1}} \tag{4.4}$$

with $\bar{z} \in [\bar{l_a}, \bar{l_b}]$ and with corresponding cumulative distribution function (CDF)

$$f(\bar{z}) = \int_{\bar{l_a}}^{\bar{z}} f(u)du \tag{4.5}$$

where $\bar{l_a}$ and $\bar{l_b}$ are the lower and upper bounds of the beta distribution; α and β are shape parameters, and Beta[α, β] stands for the beta function. These four parameters were estimated using least squares in conjunction with the method of moments as

$$\bar{l_a} = -9.75,\ \bar{l_b} = 2.25,\ \alpha = 17.01,\ \beta = 3.93 \tag{4.6}$$

Figure 4.2 and Figure 4.3 display the CDF and PDF, respectively. The standardized empirical CDF is compared to the fitted theoretical beta CDF. The PDF is compared to the standardized Gaussian PDF. It can be observed that the beta distribution is relatively mildly skewed from the Gaussian distribution.

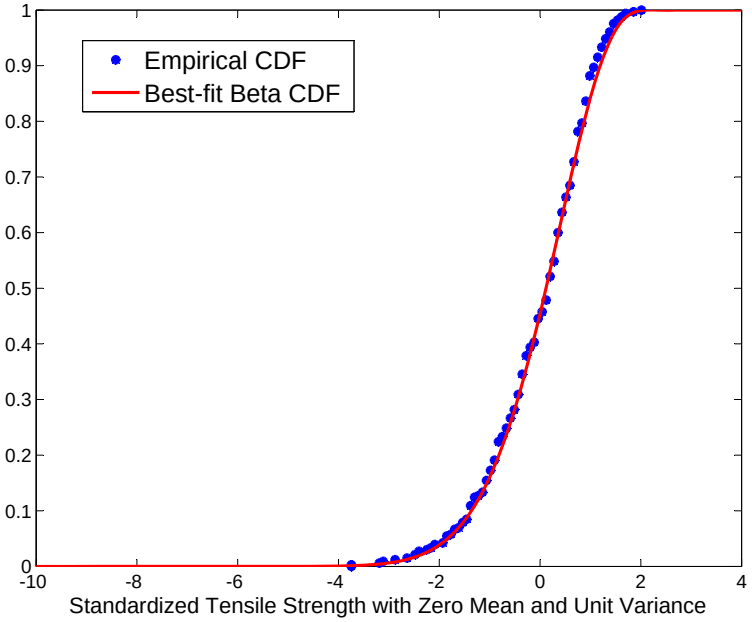

Figure 4.2: Empirical CDF obtained from standardized experimental data versus best-fit beta CDF

Since the sequence of the wires segments was also kept, the correlation structure from the tensile strengths of sample wires was obtained. Shi et.al. [54] found that the function that provided the minimum error when compared to the empirical autocorrelation function is the following

$$R_{\tilde{z}}(\xi) = e^{(-\xi/714)^2} \tag{4.7}$$

Figure 4.4 indicates that the correlation is strong for segments that are even 3

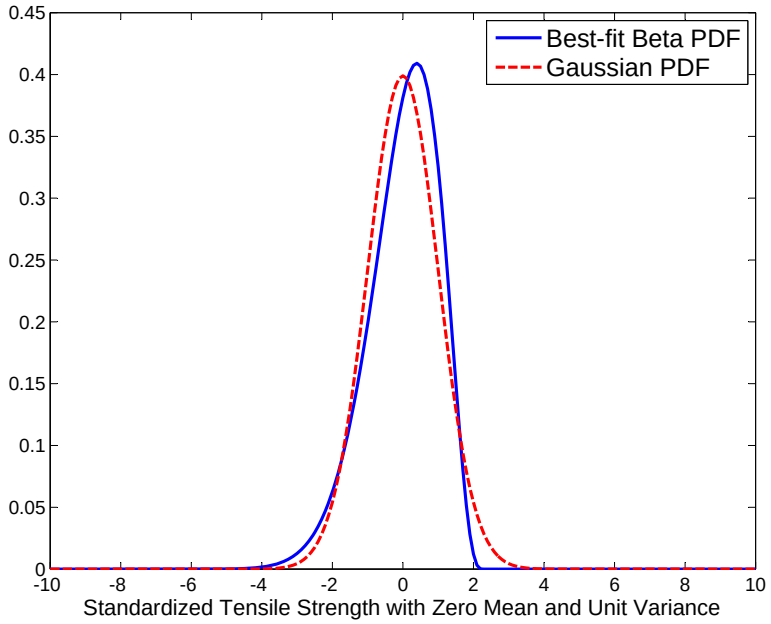

Figure 4.3: Best-fit beta PDF versus corresponding standardized Gaussian PDF

m (10 ft) apart from each other, corroborating that the assumption of treating the strength of the segments as uncorrelated is not appropriate. The Spectral Density Function (SDF) (or power spectrum) of a Stationary Random Process is defined by the Fourier Transformation of the autocorrelation as:

$$S_{xx}(k) = \frac{1}{2\pi}\int_{-\infty}^{\infty} R_{xx}(\xi)e^{-i\kappa\xi}d\xi \tag{4.8}$$

Thus, the corresponding SDF can be computed analytically from the autocorrelation function in Equation 4.4 as

$$S_{\bar{z}}(\kappa) = 79.3e^{-3060\kappa^2} \tag{4.9}$$

Figure 4.5 illustrates the theoretical SDF according to Equation 4.9. The upper cut off frequency is specified as 0.012 rad/cm since the spectrum goes to zero at this point.

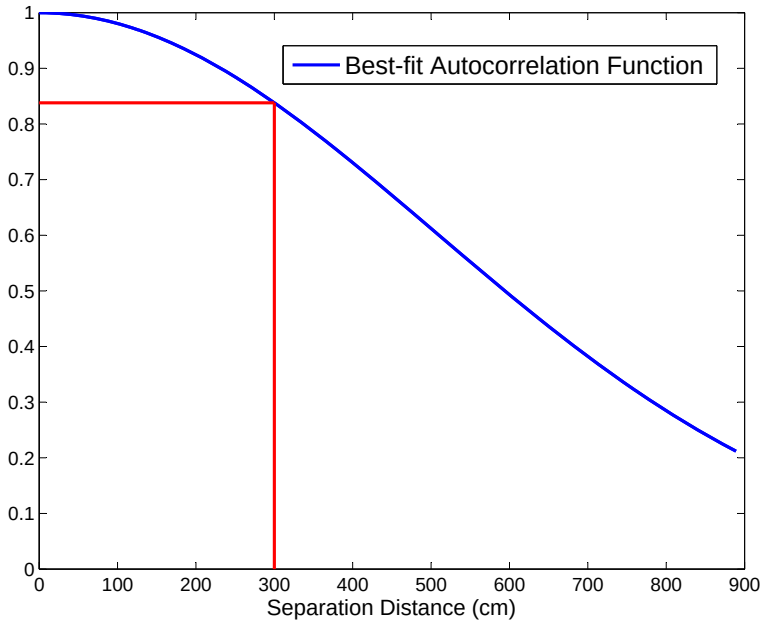

Figure 4.4: Autocorrelation function in the z-direction proposed by Shi. et. al (2007).

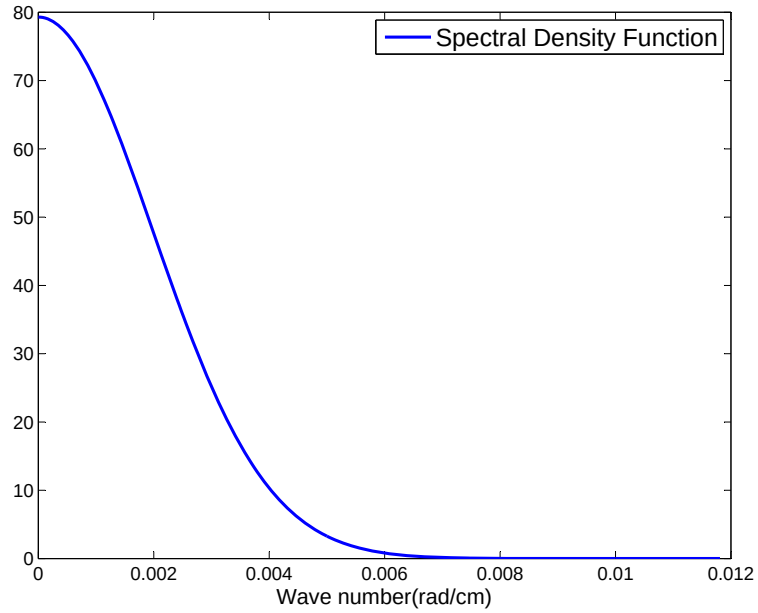

Figure 4.5: Theoretical spectral density function corresponding to the autocorrelation function.

4.3.2 Simulation Methodology for the Strength of the Wires

As the process deviates slightly from Gaussian, the strength of the wires was simulated as a non-Gaussian random field in order to be strict from a theoretical point of view.

The method used was based on the Spectral Representation Method (SRM) and the concept of translation field. SRM is employed for the simulation of Gaussian stochastic processes [39]. The one dimensional (1D), uni-variate(1-V) formulation of the SRM produces sample realizations of the process according to a prescribed SDF, $S_g(\kappa)$. The simulation formula is given by:

$$g(x) = \sqrt{2} \sum_{j=0}^{N-1} * \sqrt{2 S_g(\kappa_j) \Delta\kappa} \cos(\kappa_j x + \phi_j) \tag{4.10}$$

where,

$$\Delta k = \frac{k_u}{N} \tag{4.11}$$

$$k_j = j\Delta k, \;\; j = 0, 1, ..., N-1 \tag{4.12}$$

and,

$$S_g(\kappa_0 = 0) = 0 \tag{4.13}$$

κ_u is the uppercutoff wave number beyond which the SDF, $S_g(\kappa)$, can be assumed to be zero for either mathematical or physical reasons. N is the number of points in the wave number domain between zero and κ_u. ϕ_j are independent random phase angles uniformly distributed in [0 , 2π]. The ergodicity property requires the conditions specified in Equation 4.13. An ergodic process is a stationary random process from which it is possible to estimate the mean autocorrelation function from just one sufficiently long sample function. The generated sample functions are periodic with period:

$$L = \frac{2\pi}{\Delta\kappa} \tag{4.14}$$

By means of the SRM, a realization of the homogeneous Gaussian stochastic field can be obtained. Then, the non-Gaussian stochastic field is obtained by mapping an underlying Gaussian field to the desired marginal probability distribution function [7]. The non-Gaussian sample function $f(x)$ is defined as:

$$f(x) = F^{-1} \cdot \Phi[g(x)] = h[g(x)] \tag{4.15}$$

The function h is a monotonically increasing function and can be computed analytically or numerically. F represents the CDF of the arbritrary non-Gaussian field and Φ the CDF of the standardize Gaussian field.

The simulation algorithm for the Gaussian field is dramatically improved with the application of the Fast Fourier Transform technique (FFT). Thus, Equation 4.16 can be rewritten in the following form:

$$g(\kappa\Delta x) = Re\left\{\sqrt{2}\sum_{j=0}^{M-1} * \sqrt{2S_g(\kappa_j)\Delta\kappa} * exp(i\phi_j)exp[i(j\Delta\kappa)(\kappa\Delta x)]\right\} \tag{4.16}$$

where Re· represents the real part of the complex expression enclosed in the curly braces and M is the number of points in the field (space) domain. For optimum efficiency, M has to be a power of 2.

$$M = 2^{\mu} \tag{4.17}$$

with the restriction,

$$\Delta x \leq \frac{2\pi}{2\kappa_u} \tag{4.18}$$

This restriction is automatically satisfied when M $\geq$ 2N. When using FFT, the M generated points in the time domain constitute always exactly one period. A typical sample function of the standardized beta field $\bar{z}$ over a length of 18.3 m (60 ft) is displayed in Figure 4.6. The prescribed length was selected according to the study performed by Steinman [42] and Matteo et.al. [25], referred in Chapter 3. Thus, it was assumed that a broken wire is not contributing to the load carrying capacity of the main suspension cable for only three panel lengths. A wire segment subjected to axial tensile forces will fail at the weakest point along its length; therefore the tensile strength of a generated wire segment was defined as the smallest value of the strength along its length. In Figure 4.6, the strength of a wire segment is indicated by a dot.

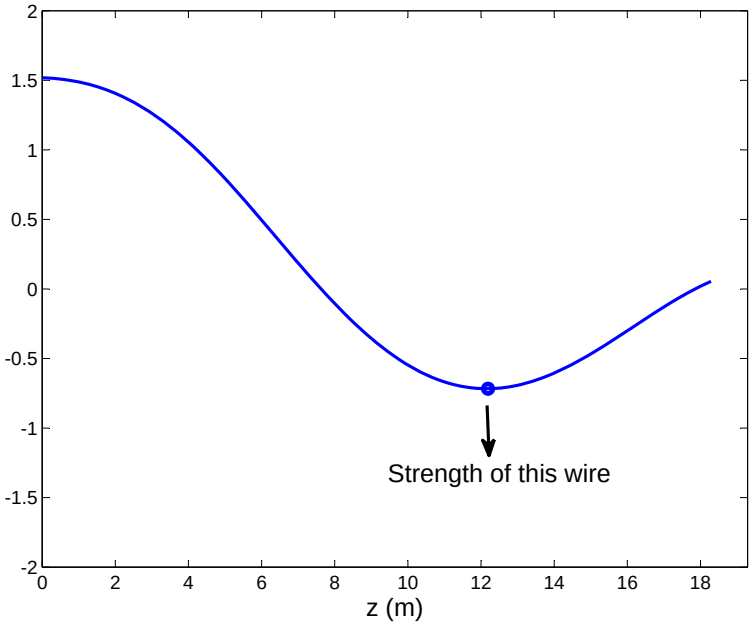

Figure 4.6: Typical sample function of standardized field $\bar{z}$ modeling wire strength, plotted over the effective clamping length 18.3 m (60 ft).

4.3.3 Mean Strength Variation Surface

By plotting the individual mean strengths at the 32 wire sampling locations, as shown in Figure 4.7, a strong dependency of the strength with the y-coordinate (top-bottom

in the cross-section of the cable) was observed. This behavior is caused by water accumulation in lower sections of the cable, increasing the corrosion rate for these wires. Consequently, the following variation was adopted for the mean strength along the y coordinate

$$\mu(x, y) = 1493 + 2.8 * y \; (MPa) \tag{4.19}$$

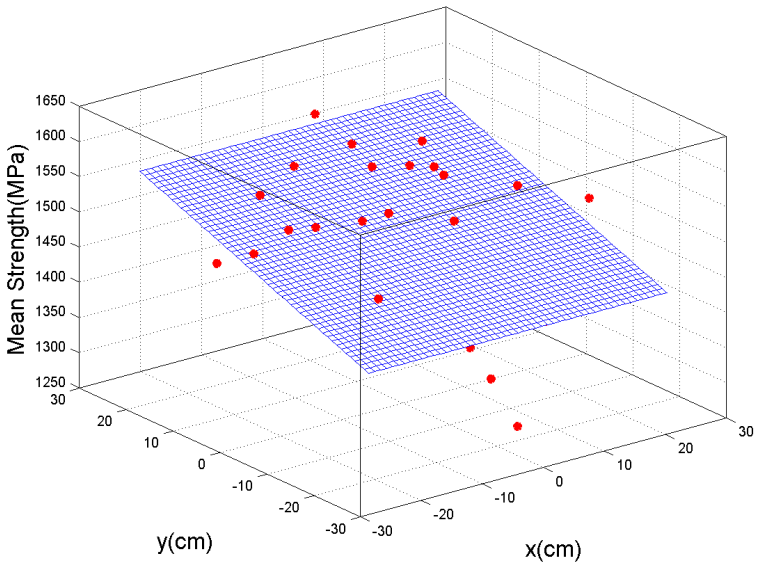

Figure 4.7: Mean strength variation plane along the cable cross section (dots represent individual mean strengths at the 32 wire sampling locations)

Eventually, the actual tensile strength $Z_{(i)}$ of a wire of prescribed length [denoted by (i)] and situated at location (x_i, y_i) within the cable's cross-section, is computed as

$$Z_{(i)} = \mu(x_i, y_i) + \sigma_{330} * \bar{Z_{(i)}} \tag{4.20}$$

where, $\bar{Z_{(i)}}$ is the corresponding minimum standardized strength of the wire of prescribed length. The tensile strength $Z_{(i)}$, expressed in terms of units stress, is converted

to units of force (N) by multiplying it times the wire's cross sectional area, A,

$$X_{(i)} = Z_{(i)} * A \tag{4.21}$$

For the Williamsburg bridge, the nominal area of the wire's cross section is 0.19 cm^2 . The strength Y of the entire cable consisting of 7,696 wires is a random variable that can be estimated by simply adding up the 7,696 individual wire strengths $X_{(i)}$,

$$Y = \sum_{i=1}^{7,696} X_{(i)} \tag{4.22}$$

The ultimate objective is to estimate the statistics of the strength Y of the cable. This can be accomplished through The Monte Carlos Simulation by generating a number of realizations Y and then estimating its statistics by ensemble averaging.

4.3.4 Drawbacks of the One Dimensional Random Field-Based Approach

The 1-D Random Field-Based approach provides more accurate results when compared to previous methodologies that treated the strength of the wire segments as uncorrelated. However, it does not account for the correlation in the wire strength within the cable's cross section. The method assumes that the strength of the 18.3 m. (60 ft.) wires within the cable's cross section are independent and uncorrelated. Contour plots developed by Steinman [42] show the spatial correlation of the the wire strength within the cable's cross section. It is expected that at short distances within the cable's cross section, wires will be strongly correlated. However, when treating wires' strength as independent, the weak points of two adjacent wires do not necessarily occur at locations close to each other. Figure 4.8 illustrates two random fields for the strength of two wires with weak points considerably far apart from each

other. The current approach is disregarding homogeneous-like corrosion among small sections within the cross section of the cable, which is very likely to happen and can have drastic effects on the overall strength of the cable.

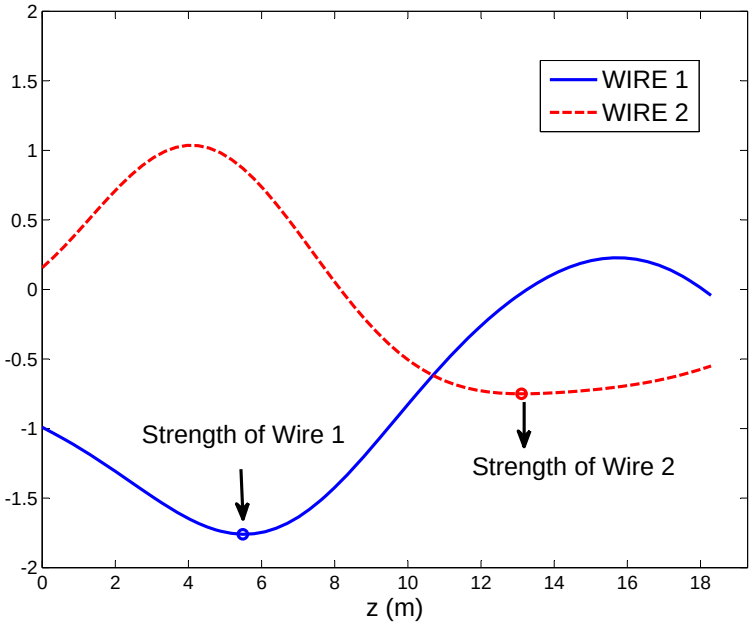

Figure 4.8: Two random fields modeling the strength of two adjacent 18.3 m (60 ft) wires . The weak points are about 7 m apart from each other.

4.4 Visualization of the Field Data

In order to visualize the pool of data that was obtained from the Williamsburg Bridge within the cable's cross section, Steinman et. al [42] provided contour plots including the minimum values of the 32 removed wires and interpolating for the rest of the points within the cross-section of the cable. In order to obtain a more realistic scenario, we have plotted the data at the locations where the segments were taken before testing and interpolating for the rest of the points within the cross-section. The data for 24 different locations was available; Figures 4.9 to 4.16 illustrates the strength variation in the cross-section at locations that are about 1 m (3 ft) apart. along the length. The dots represent the strength of the 32 wire samples that were obtained from the tensile strength tests and the rest of the field is obtained by performing a cubic interpolation based on the 32 available points in the cross-section. The figures at the right illustrate the field data on a mesh view and the figures at the left are the contour plots for the same data. Broken wires found in the segments are illustrated with an x in the contour plots.

By observing the patterns in the data, it can be concluded that the strength of the cable is clearly a function of three dimensions, since a clear correlation is observed in the cross-section of the cable. The strength of the cable clearly decreases from top to the bottom of the cable throughout the entire length. The center portion is the only sector where some variation from that trend is observed. The strength in the center sector seems to be more consistent throughout the length of the wire. However, the top and the bottom sectors have considerable variations in the maximum and the minimum values shown, as observed from Figures 4.9 to 4.16. These observations argree witth the patterns described by Suzumura and Nakamura [43].

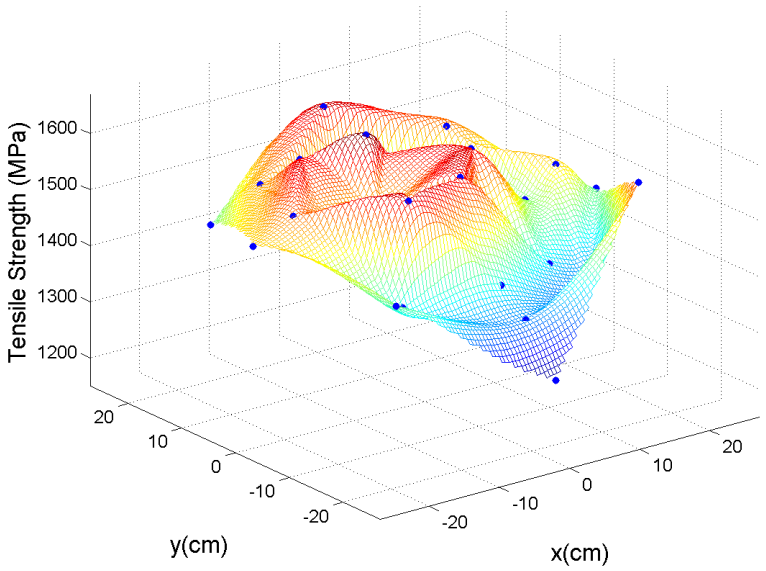

(a)

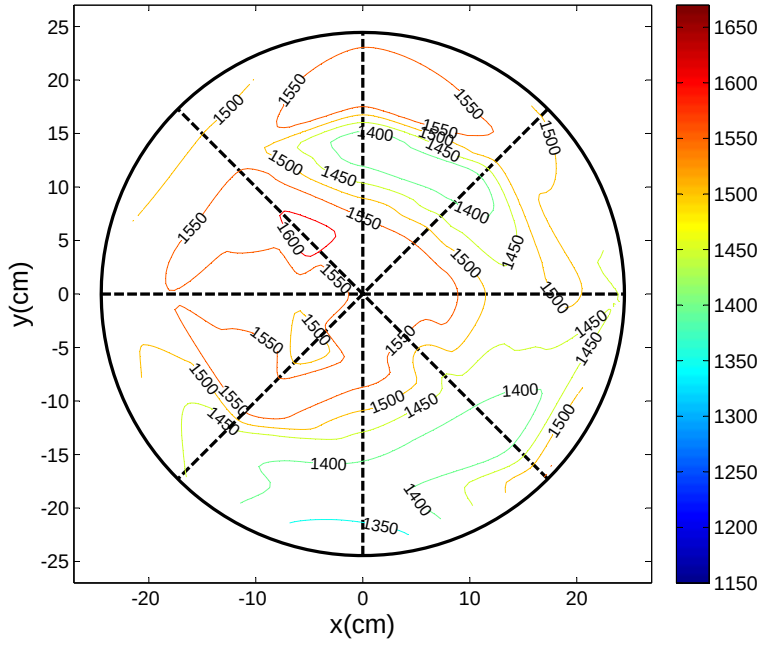

(b)

Figure 4.9: Tensile strength field data from the Williamsburg Bridge at segment 0.46-0.91 m.

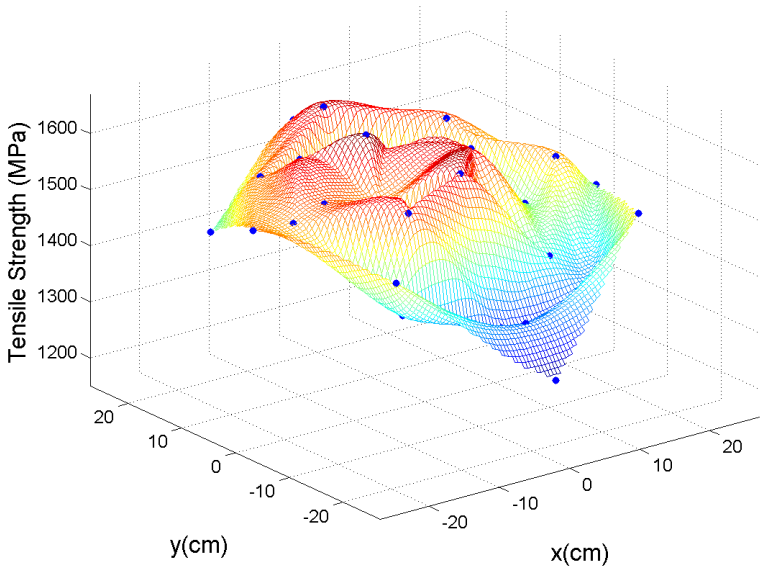

(a)

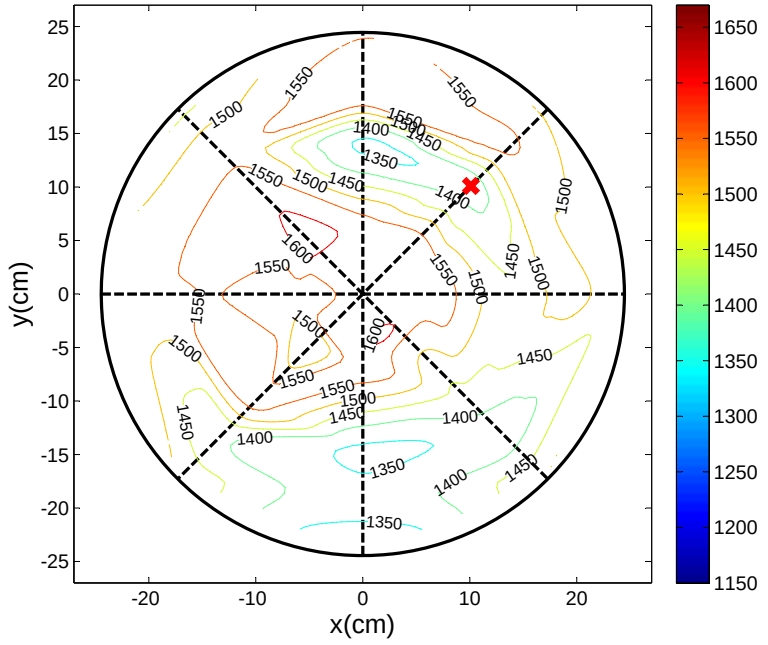

(b)

Figure 4.10: Tensile strength field data from the Williamsburg Bridge at segment 1.83-2.29 m. Broken wires are indicated with an x.

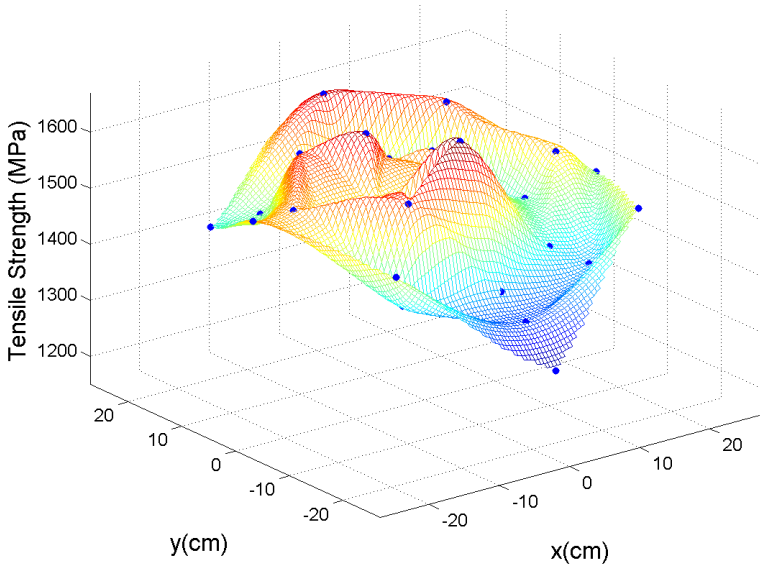

(a)

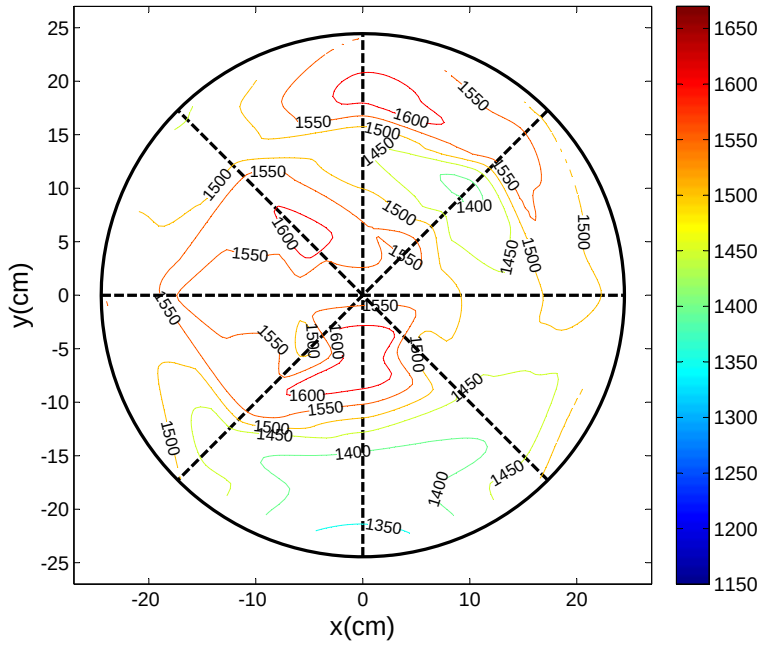

(b)

Figure 4.11: Tensile strength field data from the Williamsburg Bridge at segment 3.20-3.66 m.

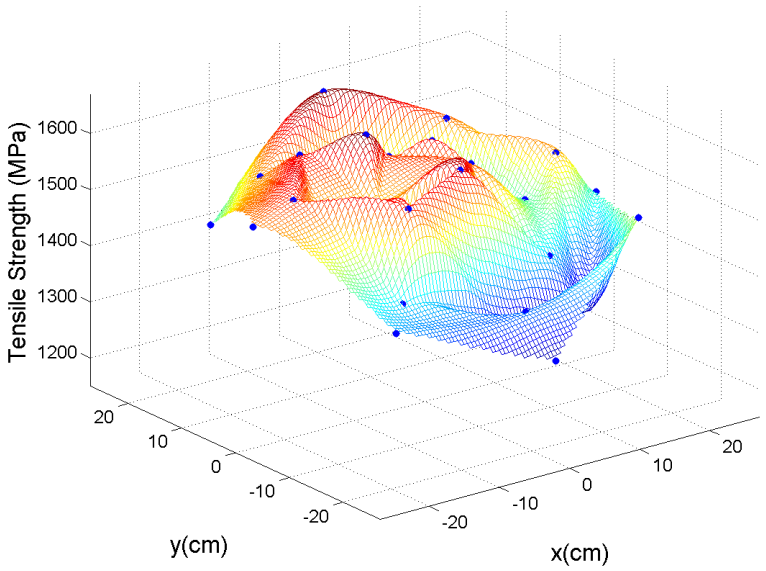

(a)

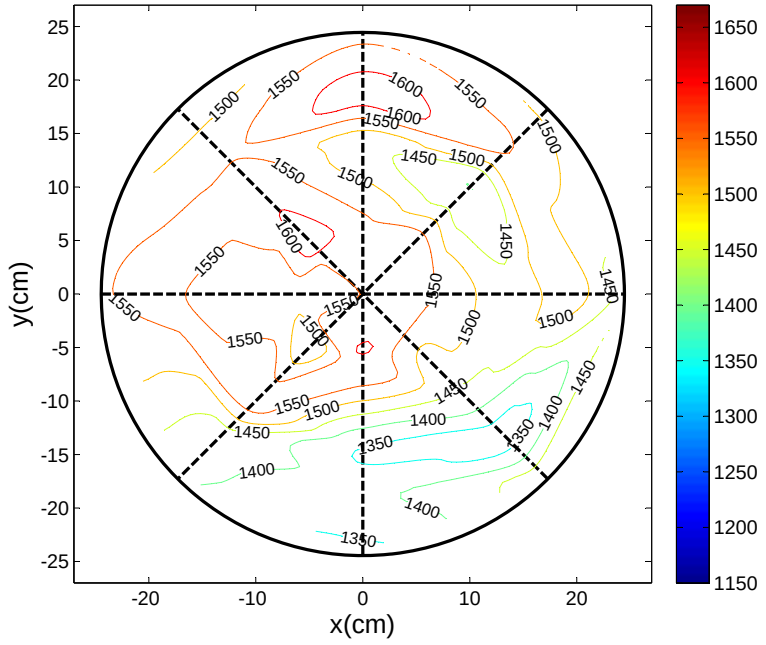

(b)

Figure 4.12: Tensile strength field data from the Williamsburg Bridge at segment 4.57-5.03 m.

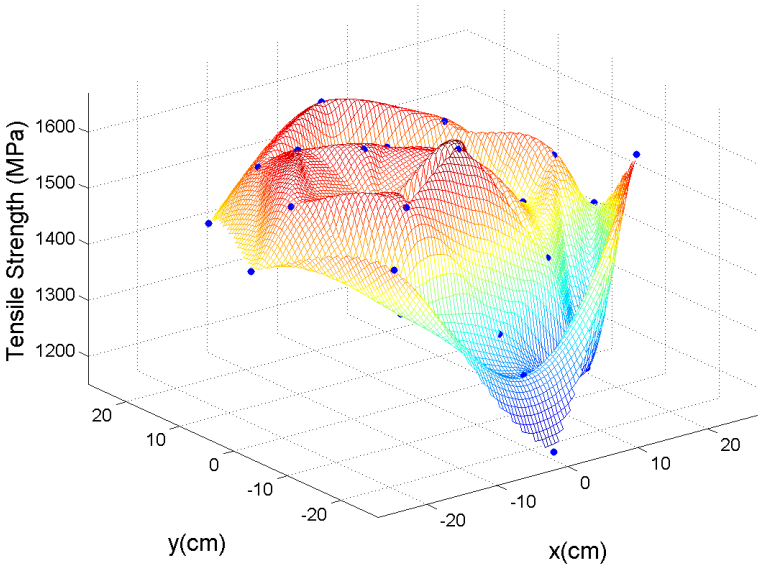

(a)

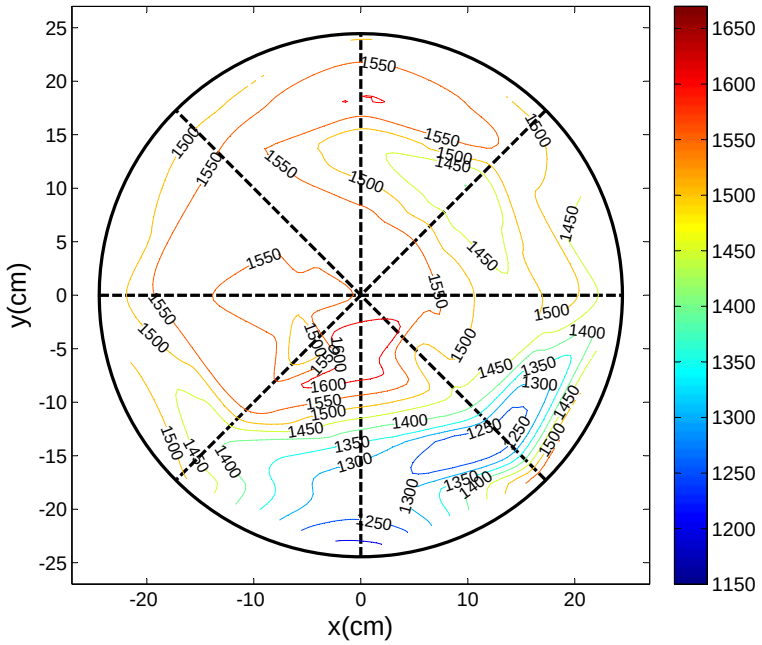

(b)

Figure 4.13: Tensile strength field data from the Williamsburg Bridge at segment 5.94-6.4 m.

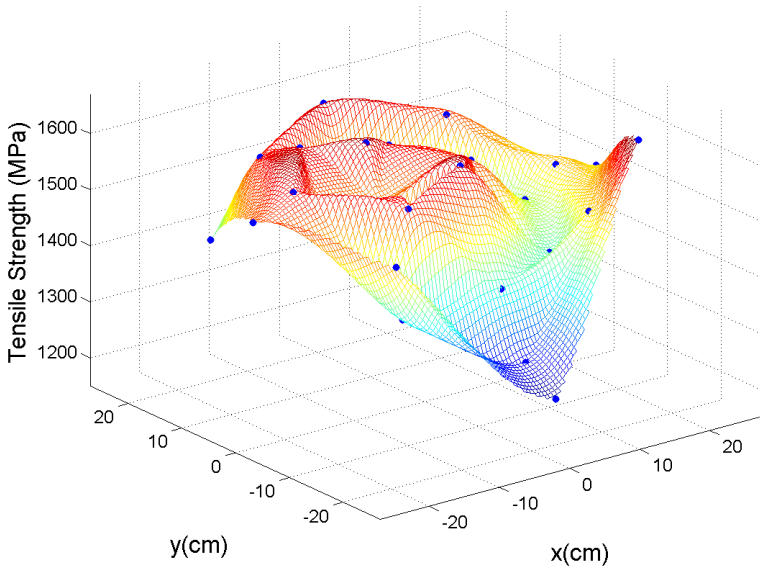

(a)

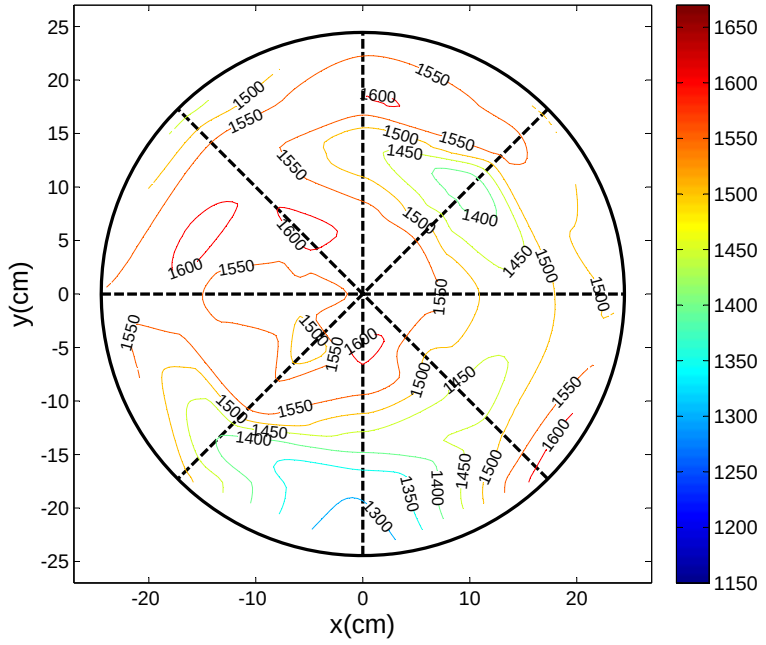

(b)

Figure 4.14: Tensile strength field data from the Williamsburg Bridge at segment 7.32-7.77 m.

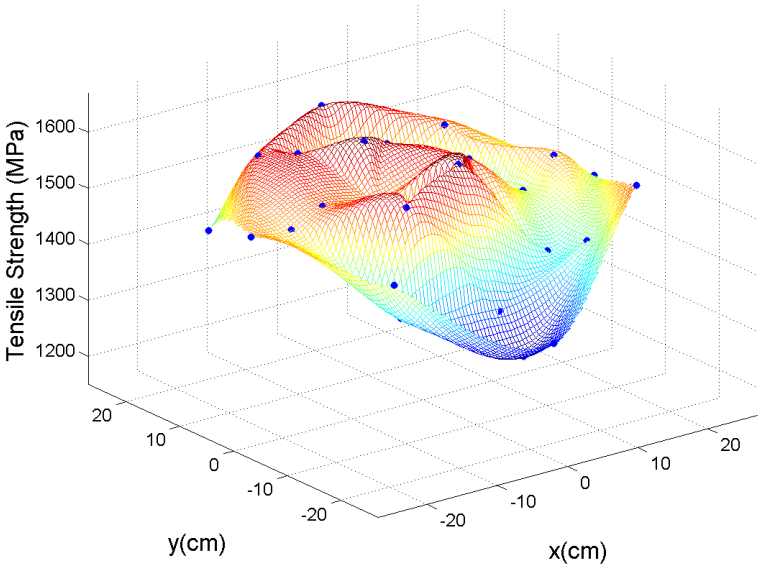

(a)

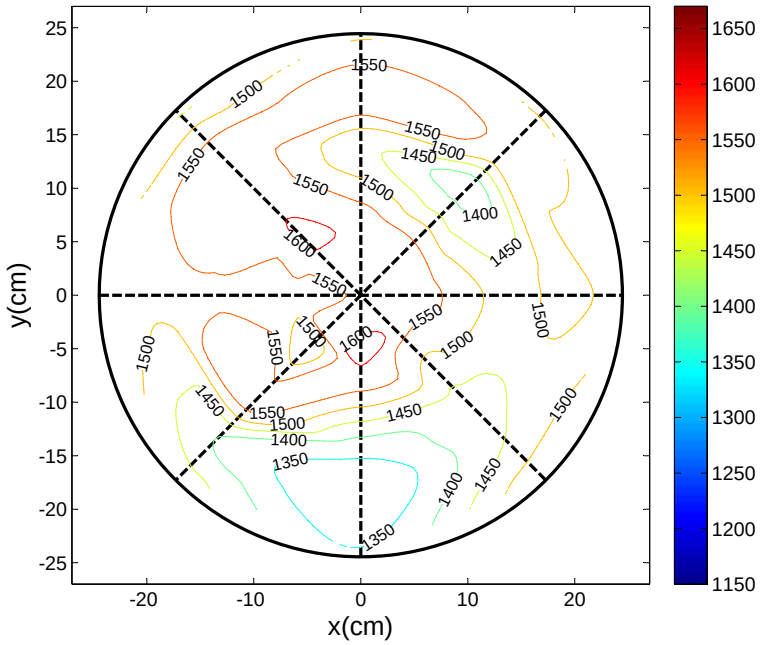

(b)

Figure 4.15: Tensile strength field data from the Williamsburg Bridge at segment 8.69-9.14 m. Broken wires are indicated with an x.

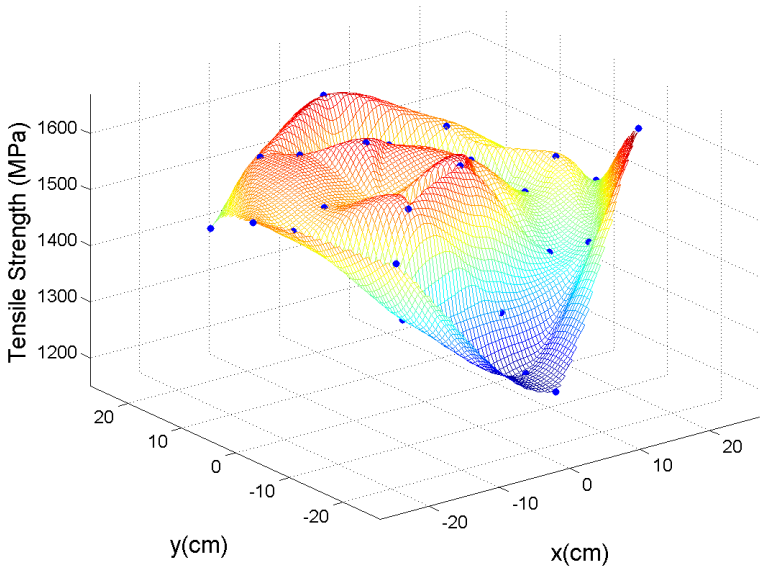

(a)

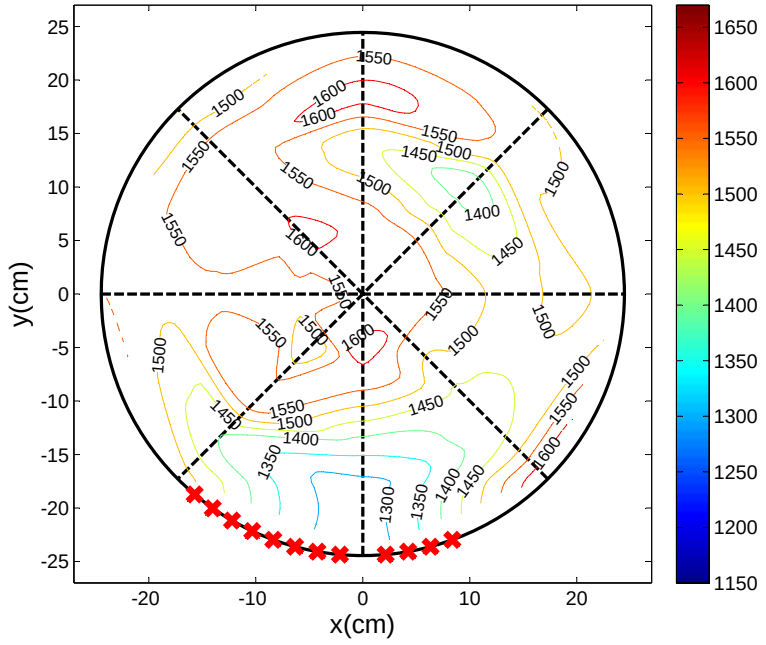

(b)

Figure 4.16: Tensile strength field data from the Williamsburg Bridge at segment 10.06-10.52 m. Broken wires are indicated with an x.

4.5 Spectral Density Function of the Cable's Cross-Section

Since it is assumed that the strength variation inside the cable is an ergodic process; by definition, the power spectrum S(κ_1, κ_2) corresponding to the cross-section of the cable (x-y plane), can be obtained from one sufficiently long sample function as

$$Sxy(k_1, k_2) = \frac{\int_0^x \int_0^y f(x,y) e^{ik_1 x} e^{ik_2 y} dxdy}{(2\pi)^2 (A)} \tag{4.23}$$

where $f(x, y)$ is the field data obtained in Section 4.4 by performing an interpolation based on the 32 available points in the cross-section at each segment along the length and A is the cross sectional area of the field. Since, there are 24 different segments along the length, Equation 4.23 can be used to obtain the spectral density function along each of the 24 segments. Finally, the spectral density can be estimated by averaging the spectrums obtained from each segment. Nonetheless, since there is some dependence of the strength with the y coordinate, a preferable approach is to capture the variation of the field from the mean strength variation plane within the cable's cross section. The plane with the mean strength was obtained by performing an ensemble average of the strength of the 24 segments along the length and having the maximum and mininum points of the ensemble be those of the plane. Thus, the mean plane is defined by the following equation at each point (x_i,y_i) of the grid

$$\mu_{pl}(x_i, y_i) = 1450.8 + 6.81 * y_i \; MPa \tag{4.24}$$

where the slope of the plane (6.81) is in units of [MPa/cm]. The standard deviation

of the ensemble average is defined as

$$\sigma_{grid} = 72.35\ MPa \tag{4.25}$$

The plane is shown in Figure 4.17 against a typical field of one of the segments along the cross section, where part of the field lies above and another part below the plane. The strength (s) for each of the grid points within the cross sections is standardized to zero mean and unit standard deviation.

$$\bar{s}_i(x_i, y_i) = \frac{s_i - \mu_{pl}(x_i, y_i)}{\sigma_{grid}} \tag{4.26}$$

Finally, the spectral density function (SDF) S(κ_1, κ_2) is obtained according to Equation 4.23 for each of the 24 segments. The ensemble average of the standardized strength at the 24 different points along the length is shown in Figure 4.18 and considered as the SDF of the cable's cross section. The upper limits can be defined as:

$$\kappa_{1_u} = \kappa_{2_u} = 1.18\ rad/cm \tag{4.27}$$

since the spectrum cleary goes to zero at those points.

4.5.1 Simulation of Strength Variation in the Cable's Cross-Section

By making use of the Spectral Density function, S(κ_1, κ_2), the strength variation within the cable's cross-section can be simulated using the Spectral Representation Method (SRM) for two-dimenisonal Gaussian stochastic fields. Although the distribution of the tensile strength data deviates slightly from Gaussian, it has been concluded that making use of a normal distribution will provide reasonable good estimates [54]. Several researchers have used a Gaussian distribution to make their strength

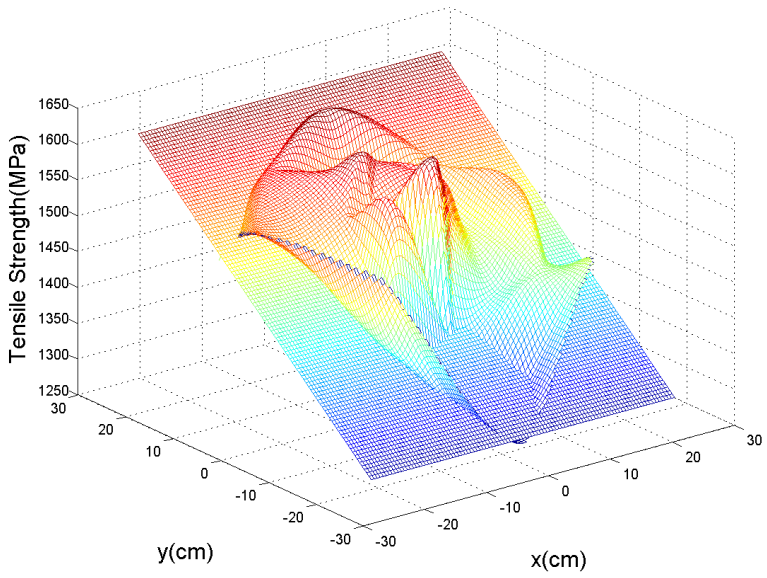

Figure 4.17: A typical field of one of the segments along the cross-section and the plane indicating the mean strength varying as a function of the y coordinate.

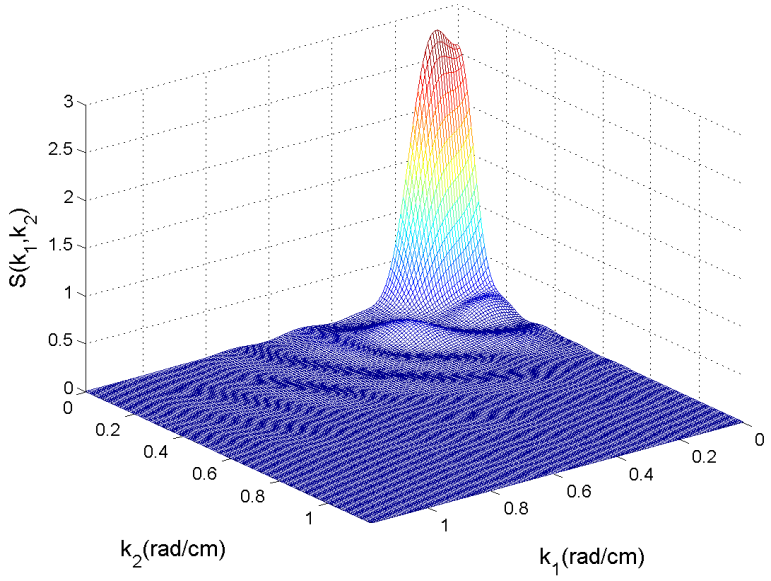

Figure 4.18: Spectral Density function S(κ_1, κ_2) of the cable's cross section on a 150 X 150 mesh.

predictions for the cable, including Steinman et. al [42], Matteo et. al [25], and Camo [11]. Shi et. al [54] treated the distribution as non-Gaussian to be rigurous from a theoretical point of view. Generating realizations using the SRM is relatively straightforward for Gaussian fields [38]. The simulation of a non-Gaussian field will

require a methodology to to approximate a non-Gaussian stationary stochastic process based on the SRM. For this study, a Gaussian distribution has been selected to facilitate the computations.

Shinozuka and Deodatis [40] have provided the simulation formula for a homogeneous stochastic field $f_o(x_1,x_2)$, with mean value equal to zero, autocorrelation function $R_{f_of_o}(\xi_1,\xi_2)$ and power spectral density function $S_{f_of_o}(\kappa_1,\kappa_2)$. The following relations hold for such field,

$$\varepsilon\left[f_o(x_1,x_2)\right]=0 \tag{4.28}$$

$$\varepsilon\left[f_o(x_1+\xi_1,x_2+\xi_2)f_o(x_1,x_2)\right]=R_{f_of_o}(\xi_1,\xi_2) \tag{4.29}$$

$$S_{f_of_o}(\kappa_1,\kappa_2)=\frac{1}{(2\pi)^2}\int_{-\infty}^{\infty}\int_{-\infty}^{\infty}R_{f_of_o}(\xi_1,\xi_2)e^{-i(\kappa_1\xi_1+\kappa_2\xi_2)}d\xi_1d\xi_2 \tag{4.30}$$

$$R_{f_of_o}(\xi_1,\xi_2)=\int_{-\infty}^{\infty}\int_{-\infty}^{\infty}S_{f_of_o}(\kappa_1,\kappa_2)e^{i(\kappa_1\xi_1+\kappa_2\xi_2)}d\kappa_1d\kappa_2 \tag{4.31}$$

The series that simulates the stochastic field $f_o(x_1,x_2)$ is the following,

$$\begin{aligned}f(x_1,x_2)=\sqrt{2}\sum_{n_1=0}^{N_1-1}\sum_{n_2=0}^{N_2-1}[&A_{n_1n_2}\cos\left(\kappa_{1_{n_1}}x_1+\kappa_{2_{n_2}}x_2+\Phi^{(1)}_{n_1n_2}\right)+\\&\tilde{A}_{n_1n_2}\cos\left(\kappa_{1_{n_1}}x_1-\kappa_{2_{n_2}}x_2+\Phi^{(2)}_{n_1n_2}\right)]\end{aligned} \tag{4.32}$$

Note $f_o(x_1,x_2)$ refers to the stochastic field and $f(x_1,x_2)$ to its simulation. The constants of Equation 4.32 are defined as follows:

$$A_{n_1n_2}=\sqrt{2S_{f_of_o}\left(\kappa_{1_{n_1}},\kappa_{2_{n_2}}\right)}\Delta\kappa_1\Delta\kappa_2 \tag{4.33}$$

$$\tilde{A}_{n_1 n_2} = \sqrt{2S_{f_o f_o}\left(\kappa_{1_{n_1}}, -\kappa_{2_{n_2}}\right)}\Delta\kappa_1\Delta\kappa_2 \tag{4.34}$$

$$\kappa_{1_{n_1}} = n_1\Delta\kappa_1; \;\; \kappa_{2_{n_2}} = n_2\Delta\kappa_2 \tag{4.35}$$

$$\Delta\kappa_1 = \frac{\kappa_{1_u}}{N_1}; \;\; \Delta\kappa_2 = \frac{\kappa_{2_u}}{N_2} \tag{4.36}$$

where κ_{1_u} and κ_{2_u} are the upper cut-off wave numbers corresponding to the x_1 and x_2 axes in the space domain. Moreover, the following criteria must be satisfied due to ergodic properties,

$$S_{f_o f_o}(\kappa_1, 0) = S_{f_o f_o}(0, \kappa_2) = 0 \tag{4.37}$$

It has been shown that the simulated stochastic field is periodic along the x_1 and x_2 axes with periods:

$$L_{x_{10}} = \frac{2\pi}{\Delta\kappa_1} \tag{4.38}$$

$$L_{x_{20}} = \frac{2\pi}{\Delta\kappa_2} \tag{4.39}$$

A sample function $f^{(i)}(x_1, x_2)$ of the simulated stochastic field $f(x_1, x_2)$ can be obtained by replacing the sequences of random phase angles $\Phi^{(1)}_{n_1 n_2}$ and $\Phi^{(2)}_{n_1 n_2}$ with their respective i-th realizations $\phi^{(1)(i)}_{n_1 n_2}$ and $\phi^{(2)(i)}_{n_1 n_2}$; n_1=0,1,...,N_1-1; n_2=0,1,...,N_2-1:

$$f^{(i)}(x_1,x_2)=\sqrt{2}\sum_{n_1=0}^{N_1-1}\sum_{n_2=0}^{N_2-1}[A_{n_1n_2}\cos\left(\kappa_{1_{n_1}}x_1+\kappa_{2_{n_2}}x_2+\phi_{n_1n_2}^{(1)(i)}\right)+\tilde{A}_{n_1n_2}\cos\left(\kappa_{1_{n_1}}x_1-\kappa_{2_{n_2}}x_2+\phi_{n_1n_2}^{(2)(i)}\right)] \tag{4.40}$$

The space increments separating the generated values of $f^{(i)}(x_1,x_2)$ have to obey the conditions;

$$\Delta x_1\leq\frac{2\pi}{2\kappa_{1u}};\ \ \Delta x_2\leq\frac{2\pi}{2\kappa_{2u}} \tag{4.41}$$

To perform generation of sample functions illustrating strength variation in the cross-section of a cable, the following parameters were chosen for N_1 and N_2

$$N_1=150\ \ and\ \ N_2=150 \tag{4.42}$$

$\Delta\kappa_1$, $\Delta\kappa_2$ and $L_{x_{10}}$, $L_{x_{20}}$ are calculated using Equations 4.27, 4.36, 4.38, and 4.39, respectively, as:

$$\Delta\kappa_1=0.0079\,rad/cm,\ \ \Delta\kappa_2=0.0079\,rad/cm \tag{4.43}$$

$$L_{x_{10}}=795.3\,cm,\ \ L_{x_{20}}=795.3\,cm \tag{4.44}$$

The conditions set on the space increments Δx_1 and $\Delta\ x_2$ by Equation 4.41 are

$$\Delta x_1\leq 2.66\,cm,\ \ \Delta x_2\leq 2.66\,cm \tag{4.45}$$

The selected space increments were chosen to be

$$\Delta x_1 = 1.27\,cm, \;\; \Delta x_2 = 1.27\,cm \tag{4.46}$$

Figures 4.19 to 4.21 illustrate three different sample functions of the field generated according to the SRM in a cable with a diameter of 24.35 cm. The sample functions show the variation from the mean plane. The simulated strength distribution in the cable's cross-section corresponding to the sample function is plotted right above the sample function and is compared to a strength distribution in one of the cross-section's of the Williamsburg bridge. It can be observed that the trends observed from the Williamsburg's data are kept; the upper section has a higher strength than the bottom section and the weaker points vary randomly in the lower portion of the cable. Small random higher strength areas are present at the lower section and the sides of the cable. Once a sample function of the simulated field is obtained for the cable's cross-section, the strength of the wires can be extracted from the generated grid as observed in Figure 4.22. The first step is to place the wires (e.g. 9000) within the generated grid, then a simple linear interpolation is performed to find the corresponding standardized value of the wires. Next, the actual strength of the wires can be recovered by referring to Equation 4.26.

The computational time required for the generation of the sample function was of about 6.5 seconds ; therefore, the fast fourier technique was not required for this simulation.

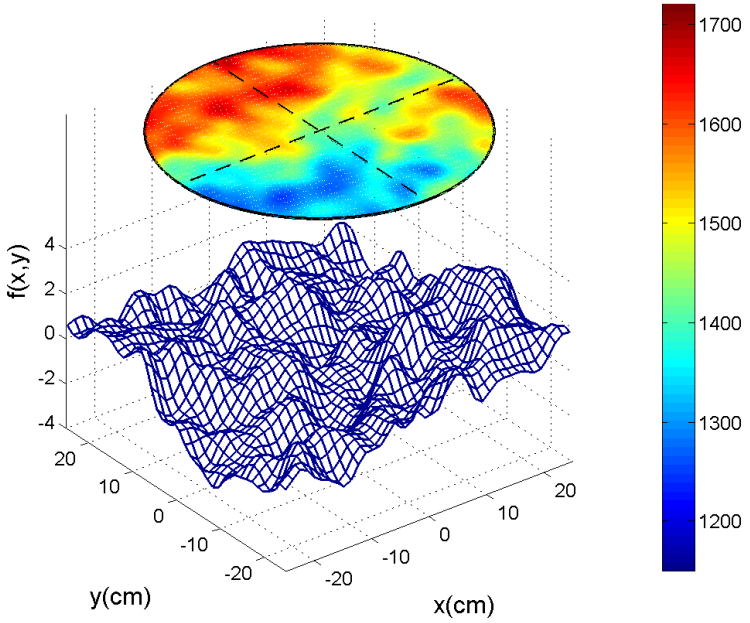

(a)

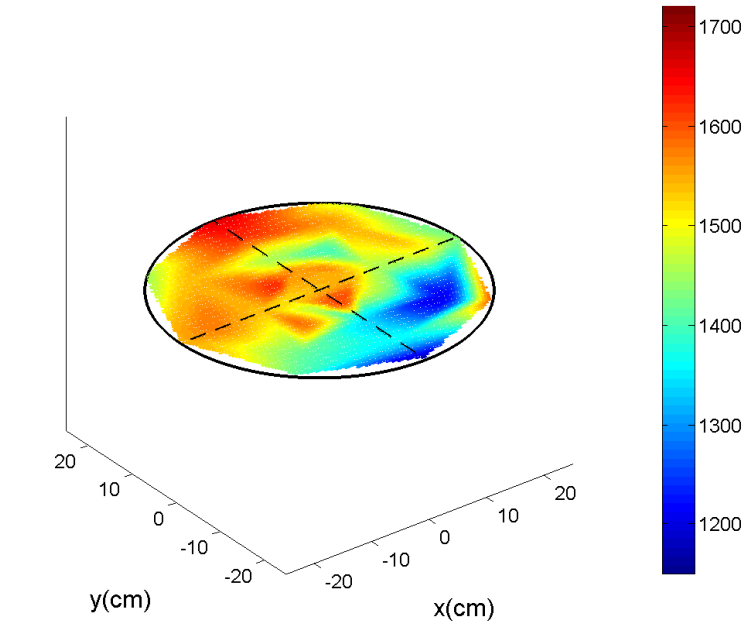

(b)

Figure 4.19: (a) A sample function showing the variation from the mean plane. The simulated strength distribution (MPa) in the cable's cross-section corresponding to the sample function is plotted right above the sample function and is compared to a (b) strength distribution in one of the cross-section's of the Williamsburg bridge.

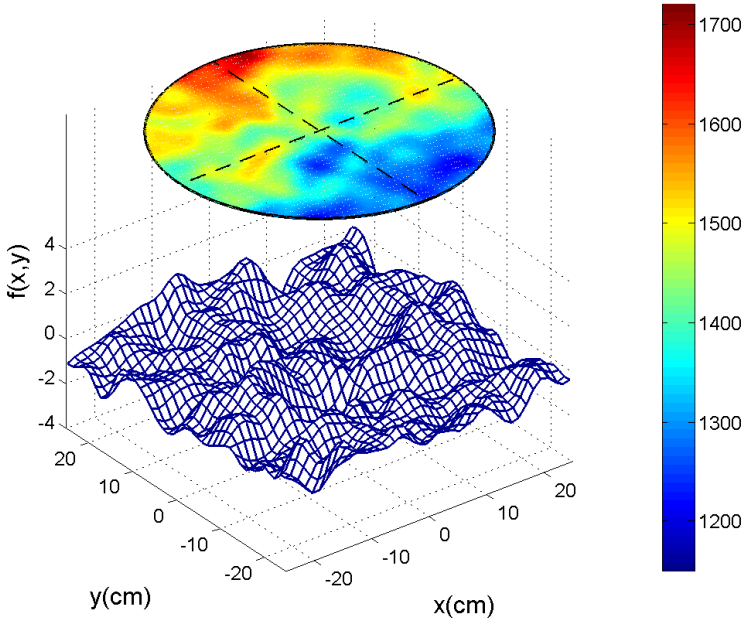

(a)

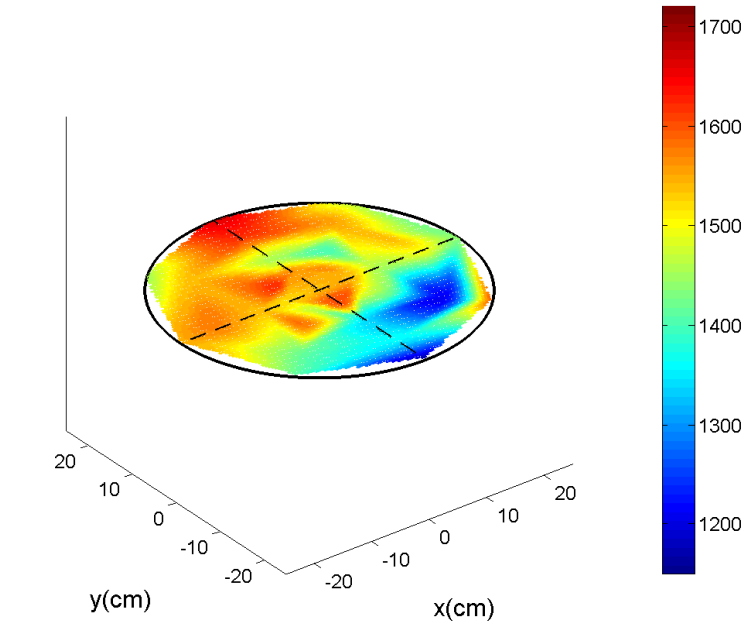

(b)

Figure 4.20: (a) A sample function showing the variation from the mean plane. The simulated strength distribution (MPa) in the cable's cross-section corresponding to the sample function is plotted right above the sample function and is compared to a (b) strength distribution in one of the cross-section's of the Williamsburg bridge.

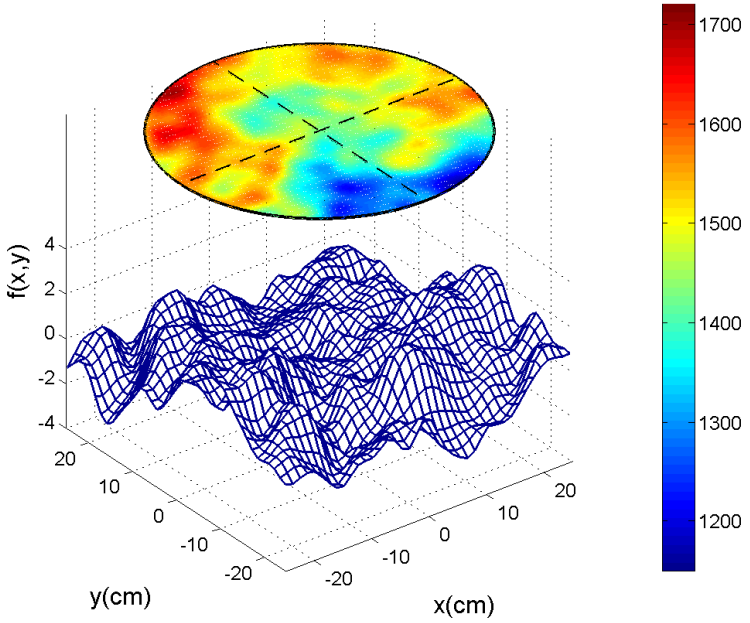

(a)

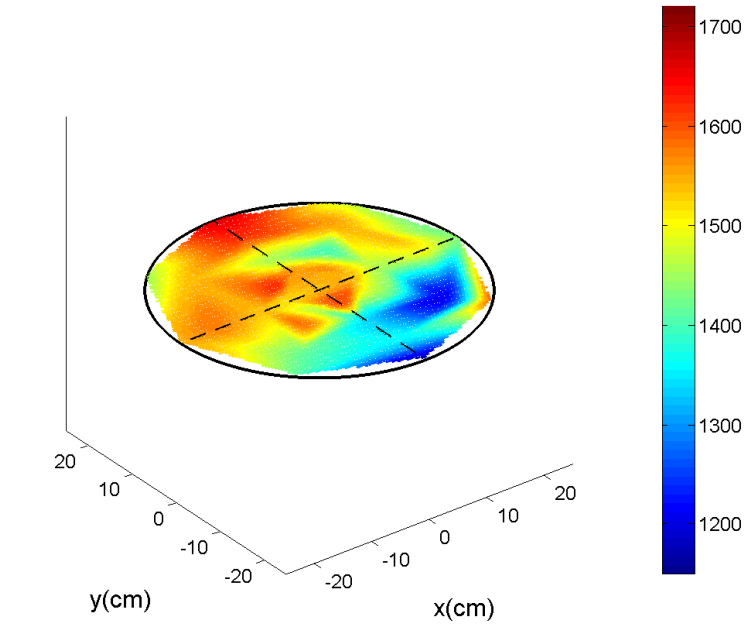

(b)

Figure 4.21: (a) A sample function showing the variation from the mean plane. The simulated strength distribution (MPa) in the cable's cross-section corresponding to the sample function is plotted right above the sample function and is compared to a (b) strength distribution in one of the cross-section's of the Williamsburg bridge.

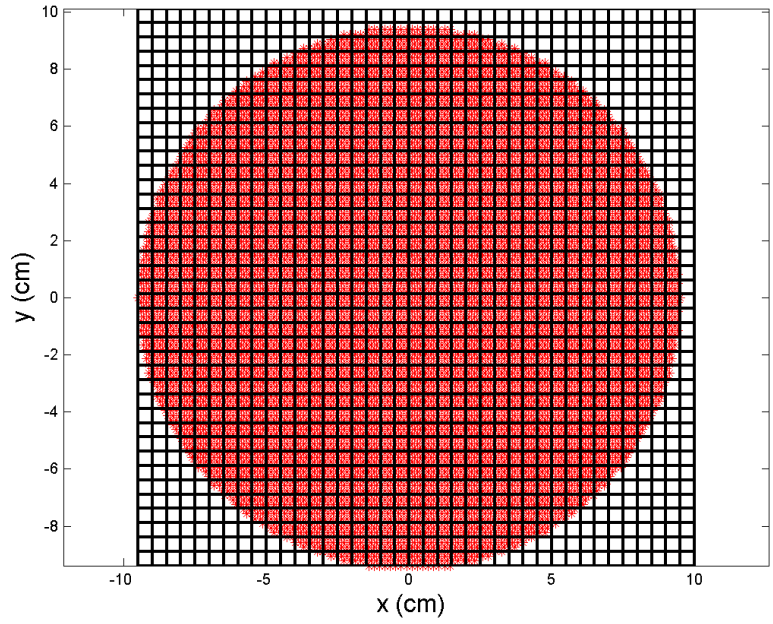

(a)

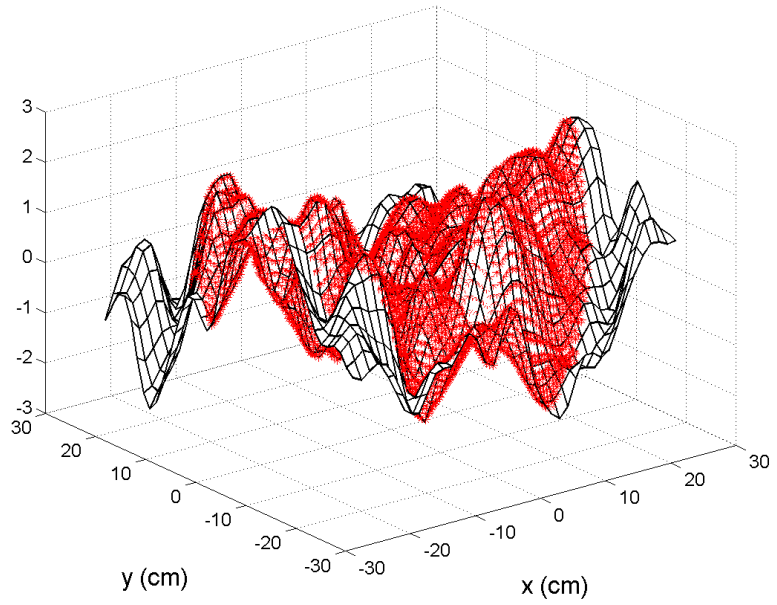

(b)

Figure 4.22: (a) Location of the 9000 wires as compared to the generated grid for the field. (b) Sample interpolation performed to extract the strength of the wires from the generated field for the cable's cross-section.

4.6 Proposed Three-Dimensional Random Field Approach for Strength Evaluation of Suspension Bridge Cables

The strength of the cable is proposed to be simulated as a three-dimensional stochastic field by the spectral representation method in order to account for the spatial correlation of the cable strength, which occurs both within the cross-section (over different wires) and along the length of the cable. The strength of each wire along a prescribed length can be extracted from the cable's strength field. The prescribed spectral density function in the three dimensional space can be obtained by combining the spectral density function that captures the behavior in the cross section as shown in Section 4.5 and the spectral density function that accounts for the spatial correlation along the length as predicted by Shi et. al [54]

$$Sxyz(k_1, k_2, k_3) = Sxy(k_1, k_2) * Sz(k_3) \tag{4.47}$$

Shinozuka and Deodatis [40] have provided the simulation formula for a homogeneous stochastic field in three dimensions f_o(x_1,x_2,x_3), with mean value equal to zero, autocorrelation function $R_{f_o f_o}$(ξ_1,ξ_2,,ξ_3) and power spectral density function $S_{f_o f_o}$(κ_1,κ_2,κ_3). The following relations hold for such field,

$$\varepsilon\left[f_o(x_1, x_2, , x_3)\right] = 0 \tag{4.48}$$

$$\varepsilon\left[f_o(x_1 + \xi_1, x_2 + \xi_2, x_3 + \xi_3) f_o(x_1, x_2, x_3)\right] = R_{f_o f_o}(\xi_1, \xi_2, \xi_3) \tag{4.49}$$

$$S_{f_o f_o}(\kappa_1, \kappa_2, , \kappa_3) = \frac{1}{(2\pi)^3} \int_{-\infty}^{\infty} \int_{-\infty}^{\infty} \int_{-\infty}^{\infty} R_{f_o f_o}(\xi_1, \xi_2, \xi_3) e^{-i(\kappa_1 \xi_1 + \kappa_2 \xi_2 + \kappa_3 \xi_3)} d\xi_1 d\xi_2 d\xi_3 \tag{4.50}$$

$$R_{f_o f_o}(\xi_1, \xi_2) = \int_{-\infty}^{\infty} \int_{-\infty}^{\infty} \int_{-\infty}^{\infty} S_{f_o f_o}(\kappa_1, \kappa_2, \kappa_3) e^{i(\kappa_1 \xi_1 + \kappa_2 \xi_2 + \kappa_3 \xi_3)} d\kappa_1 d\kappa_2 d\kappa_3 \tag{4.51}$$

The formulation used to simulate three-dimensional homogeneous stochastic field $f_o(x_1,x_2,,x_3)$ according to the spectral representation method is defined by the following series (a distinction is made between the stochastic field $f_o(x_1,x_2,,x_3)$ and its simulation $f(x_1,x_2,,x_3)$):

$$\begin{aligned} f(x_1, x_2, x_3) = \sqrt{2} \sum_{n_1=0}^{N_1-1} \sum_{n_2=0}^{N_2-1} \sum_{n_3=0}^{N_3-1} [& A^{(1)}_{n_1 n_2 n_3} \cos\left(\kappa_{1_{n_1}} x_1 + \kappa_{2_{n_2}} x_2 + \kappa_{3_{n_3}} x_3 + \Phi^{(1)}_{n_1 n_2 n_3}\right) \\ & + A^{(2)}_{n_1 n_2 n_3} \cos\left(\kappa_{1_{n_1}} x_1 + \kappa_{2_{n_2}} x_2 - \kappa_{3_{n_3}} x_3 + \Phi^{(2)}_{n_1 n_2 n_3}\right) \\ & + A^{(3)}_{n_1 n_2 n_3} \cos\left(\kappa_{1_{n_1}} x_1 - \kappa_{2_{n_2}} x_2 + \kappa_{3_{n_3}} x_3 + \Phi^{(3)}_{n_1 n_2 n_3}\right) \\ & + A^{(4)}_{n_1 n_2 n_3} \cos\left(\kappa_{1 n_1} x_1 - \kappa_{2 n_2} x_2 - \kappa_{3 n_3} x_3 + \Phi^{(4)}_{n_1 n_2 n_3}\right)] \end{aligned} \tag{4.52}$$

where,

$$A^{(1)}_{n_1 n_2 n_3} = \sqrt{2 S_{f_o f_o}\left(\kappa_{1_{n_1}}, \kappa_{2_{n_2}}, \kappa_{3_{n_3}}\right)} \Delta\kappa_1 \Delta\kappa_2 \Delta\kappa_3 \tag{4.53}$$

$$A^{(2)}_{n_1 n_2 n_3} = \sqrt{2 S_{f_o f_o}\left(\kappa_{1_{n_1}}, \kappa_{2_{n_2}}, -\kappa_{3_{n_3}}\right)} \Delta\kappa_1 \Delta\kappa_2 \Delta\kappa_3 \tag{4.54}$$

$$A^{(3)}_{n_1n_2n_3} = \sqrt{2S_{f_of_o}\left(\kappa_{1_{n_1}}, -\kappa_{2_{n_2}}, \kappa_{3_{n_3}}\right)}\Delta\kappa_1\Delta\kappa_2\Delta\kappa_3 \tag{4.55}$$

$$A^{(4)}_{n_1n_2n_3} = \sqrt{2S_{f_of_o}\left(\kappa_{1_{n_1}}, -\kappa_{2_{n_2}}, -\kappa_{3_{n_3}}\right)}\Delta\kappa_1\Delta\kappa_2\Delta\kappa_3 \tag{4.56}$$

$$\kappa_{1_{n_1}} = n_1\Delta\kappa_1;\;\; \kappa_{2_{n_2}} = n_1\Delta\kappa_2;\;\; \kappa_{3_{n_3}} = n_3\Delta\kappa_3 \tag{4.57}$$

$$\Delta\kappa_1 = \frac{\kappa_{1_u}}{N_1};\;\; \Delta\kappa_2 = \frac{\kappa_{2_u}}{N_2};\;\; \Delta\kappa_3 = \frac{\kappa_{3_u}}{N_3}; \tag{4.58}$$

where κ_{1_u}, κ_{2_u}, and $\kappa_{3_u}$are the upper cut-off wave numbers corresponding to the x_1, x_2, and x_3 axes in the space domain. Moreover, the following criteria must be satisfied due to ergodic properties,

$$S_{f_of_o}(\kappa_1, \kappa_2, 0) = S_{f_of_o}(\kappa_1, 0, \kappa_3) = S_{f_of_o}(0, \kappa_2, \kappa_3) = 0 \tag{4.59}$$

It has been shown that the simulated stochastic field is periodic along the x_1 ,x_2. x_3 axes with periods:

$$L_{x10} = \frac{2\pi}{\Delta\kappa_1} \tag{4.60}$$

$$L_{x20} = \frac{2\pi}{\Delta\kappa_2} \tag{4.61}$$

$$L_{x30} = \frac{2\pi}{\Delta\kappa_3} \tag{4.62}$$

A sample function $f^{(i)}(x_1, x_2, , x_3)$ of the simulated stochastic field $f(x_1, x_2, x_3)$ can be obtained by replacing the sequences of random phase angles $\Phi^{(1)}_{n_1 n_2 n_3}$, $\Phi^{(2)}_{n_1 n_2 n_3}$, $\Phi^{(3)}_{n_1 n_2 n_3}$, and $\Phi^{(4)}_{n_1 n_2 n_3}$, with their respective i-th realizations $\phi^{(1)(i)}_{n_1 n_2 n_3}$, $\phi^{(2)(i)}_{n_1 n_2 n_3}$,$\phi^{(3)(i)}_{n_1 n_2 n_3}$, and $\phi^{(4)(i)}_{n_1 n_2 n_3}$; n_1=0,1,...,N_1-1; n_2=0,1,...,N_2-1; n_3=0,1,...,N_3-1 :

$$
\begin{aligned}
f^{(i)}(x_1, x_2, x_3) = \sqrt{2} \sum_{n_1=0}^{N_1-1} \sum_{n_2=0}^{N_2-1} \sum_{n_3=0}^{N_3-1} [& A^{(1)}_{n_1 n_2 n_3} \cos\left(\kappa_{1_{n_1}} x_1 + \kappa_{2_{n_2}} x_2 + \kappa_{3_{n_3}} x_3 + \phi^{(1)(i)}_{n_1 n_2 n_3}\right) \\
& + A^{(2)}_{n_1 n_2 n_3} \cos\left(\kappa_{1_{n_1}} x_1 + \kappa_{2_{n_2}} x_2 - \kappa_{3_{n_3}} x_3 + \phi^{(2)(i)}_{n_1 n_2 n_3}\right) \\
& + A^{(3)}_{n_1 n_2 n_3} \cos\left(\kappa_{1_{n_1}} x_1 - \kappa_{2_{n_2}} x_2 + \kappa_{3_{n_3}} x_3 + \phi^{(3)(i)}_{n_1 n_2 n_3}\right) \\
& + A^{(4)}_{n_1 n_2 n_3} \cos\left(\kappa_{1 n_1} x_1 - \kappa_{2 n_2} x_2 - \kappa_{3 n_3} x_3 + \phi^{(4)(i)}_{n_1 n_2 n_3}\right)]
\end{aligned}
\tag{4.63}
$$

The space increments separating the generated values of $f^{(i)}(x_1,x_2,x_3)$ have to obey the conditions;

$$
\Delta x_1 \leq \frac{2\pi}{2\kappa_{1u}}; \;\; \Delta x_2 \leq \frac{2\pi}{2\kappa_{2u}}; \;\; \Delta x_3 \leq \frac{2\pi}{2\kappa_{3u}} \tag{4.64}
$$

The cost of generating sample functions of the simulated stochastic field can be drastically reduced by using the FFT technique [9]. Equation 4.63 is rewritten in the following form:

$$
\begin{aligned}
f^{(i)}(p_1x_1, p_2x_2, p_3x_3) = Re\Big[\sum_{n_1=0}^{M_1-1}\sum_{M_2=0}^{M_2-1}\sum_{n_3=0}^{N_3-1} \\
\big[B^{(1)}_{n_1n_2n_3} exp[i(n_1\Delta\kappa_1)(p_1\Delta x_1) + i(n_2\Delta\kappa_1)(p_2\Delta x_2) + i(n_3\Delta\kappa_3)(p_3\Delta x_3)] \\
+B^{(2)}_{n_1n_2n_3} exp[i(n_1\Delta\kappa_1)(p_1\Delta x_1) + i(n_2\Delta\kappa_1)(p_2\Delta x_2) - i(n_3\Delta\kappa_3)(p_3\Delta x_3)] \\
+B^{(3)}_{n_1n_2n_3} exp[i(n_1\Delta\kappa_1)(p_1\Delta x_1) - i(n_2\Delta\kappa_1)(p_2\Delta x_2) + i(n_3\Delta\kappa_3)(p_3\Delta x_3)] \\
+B^{(4)}_{n_1n_2n_3} exp[i(n_1\Delta\kappa_1)(p_1\Delta x_1) - i(n_2\Delta\kappa_1)(p_2\Delta x_2) - i(n_3\Delta\kappa_3)(p_3\Delta x_3)]\big]\Big]
\end{aligned}
\tag{4.65}
$$

where,

$$
p_1 = 0, 1, ..., M_1 - 1;\;\; p_2 = 0, 1, ..., M_2 - 1;\;\; p_3 = 0, 1, ..., M_3 - 1; \tag{4.66}
$$

and Re indicates the real part and $B^{(j)}_{n_1n_2n_3}$, j = 1,2,3,4 stand for:

$$
B^{(1)}_{n_1n_2n_3} = \sqrt{2}A^{(1)}_{n_1n_2n_3} exp[i\phi^{(1)(i)}_{n_1n_2n_3}] \tag{4.67}
$$

$$
B^{(2)}_{n_1n_2n_3} = \sqrt{2}A^{(2)}_{n_1n_2n_3} exp[i\phi^{(2)(i)}_{n_1n_2n_3}] \tag{4.68}
$$

$$
B^{(3)}_{n_1n_2n_3} = \sqrt{2}A^{(3)}_{n_1n_2n_3} exp[i\phi^{(3)(i)}_{n_1n_2n_3}] \tag{4.69}
$$

$$
B^{(4)}_{n_1n_2n_3} = \sqrt{2}A^{(4)}_{n_1n_2n_3} exp[i\phi^{(4)(i)}_{n_1n_2n_3}] \tag{4.70}
$$

$\Delta\ x_1$, $\Delta\ x_2$, $\Delta\ x_3$ and $\Delta\ \kappa_1$, $\Delta\ \kappa_2$, $\Delta\ \kappa_3$ are related in the following way:

$$M_1 \Delta x_1 = L_{x_{10}} = \frac{2\pi}{\Delta \kappa_1} \tag{4.71}$$

$$M_2 \Delta x_2 = L_{x_{20}} = \frac{2\pi}{\Delta \kappa_2} \tag{4.72}$$

$$M_3 \Delta x_3 = L_{x_{30}} = \frac{2\pi}{\Delta \kappa_3} \tag{4.73}$$

$$\tag{4.74}$$

The conditions of Equation 4.64 are equivalent to:

$$M_1 \geq 2N_1; \;\; M_2 \geq 2N_2; \;\; M_3 \geq 2N_3 \tag{4.75}$$

For optimum efficiency, M_1, M_2, and M_3 have to be powers of 2:

$$M_1 = 2^{\mu_1}; \;\; M_2 = 2^{\mu_2}; \;\; M_3 = 2^{\mu_3}; \tag{4.76}$$

4.6.1 Simulation of the Cable's Strength as a Three Dimensional Random Field

The computational time increases considerable when generating sample functions of a stochastic field $f_o(x_1,x_2,x_3)$ in three dimensions. Tables 4.1 and 4.2 show the compuational time when generating sample functions according to the cosine series, or Method of Cosines, (Equation 4.63) and the FFT technique (Equation 4.65), respectively. As expected, the FFT technique decreases the computational time dramatically , facilitating a stochastic analysis of the cable's strength. It is worthy to metion that the reported CPU times are for a fortran code since the iterations required by the method of cosines are solved more efficiently in fortran than Matlab.

The Method of Cosines allows that desired space increments be selected (meeting

the requirements of Equation 4.64); while there is less flexibility in specifying desired space increments with the FFT technique since the spacing is linked to other required parameters specified by Equations 4.74 and 4.75. A typical 9000 wire cable has a diameter of about 25 cm (9.625 in.) and should be modeled over a prescribed length of 18.3 m (60 ft). A grid with spacings of 2.54 cm (1 in) in the x and y direction and 30.48 cm (1 ft) in the z-direction was specified for the Method of Cosines. In order to get a better representation of the prescribed spectral density function in each direction, the divisions of the spectral density functions were increased; however, significantly increasing the CPU time as observed in Table 4.1. For the FFT technique, several combinations in the spacing of the spectral density function were performed by making use of Equation 4.76 for maximum efficiency, imposing the following conditions:

$$M_1 = 2N_1; \;\; M_2 = 2N_2; \;\; M_3 = 2N_3 \tag{4.77}$$

Furthermore, the CPU memory imposed the following condition in order to avoid memory overflow:

$$\mu_1 + \mu_2 + \mu_3 = 24; \tag{4.78}$$

Table 4.1: Computational time of the Simulation by the Method of Cosines

N_1	N_2	N_3	dx_1 (cm)	dx_2 (cm)	dx_3 (cm)	Time (s)
64	64	16	2.54	2.54	30.48	366
64	64	32	2.54	2.54	30.48	1162
64	64	64	2.54	2.54	30.48	17134
150	150	64	2.54	2.54	30.48	20850

For the FFT technique, the parameters outlined in row 1 of Table 4.2 are recommended since it captures the behavior in each direction of the Spectral Density Function evenly and provides a well distributed mesh. Under such parameters, the

Table 4.2: Computational time of the Simulation by the FFT technique

N_1	N_2	N_3	μ_1	μ_2	μ_3	M_1	M_2	M_3	dx_1 (cm)	dx_2 (cm)	dx_3 (cm)	Time (s)
64	64	64	7	7	10	128	128	1024	2.67	2.67	33.25	15.09
64	64	64	8	8	8	256	256	256	1.32	1.32	132.99	16.57
64	64	32	8	8	8	256	256	256	1.32	1.32	66.50	14.13
64	64	16	8	8	8	256	256	256	1.32	1.32	33.25	12.74
128	128	32	8	8	8	256	256	256	2.67	2.67	66.50	22.07
128	128	32	9	9	6	512	512	64	1.32	1.32	265.99	22.26
128	128	16	8	8	8	256	256	256	2.67	2.67	33.25	16.72

sample functions of the stochastic field will have periods of :

$$L_{x_{10}} = 341.76\,cm; \;\; L_{x_{20}} = 341.76\,cm; L_{x_{20}} = 340.48\,m \tag{4.79}$$

The dimensions of the sample function are greater than the dimensions of the prescribed cable; thus only the initial part of the sample functions is used to account for the strength variation in the cable. By making use of the three dimensional spectral density function specified in Equation 4.47, samples functions accounting for strength variation from the mean plane (Equation 4.24) along the length are generated. Figures 4.23 to 4.28 illustrate the sample function from 0-3.325 m (0-10.83) ft., spaced at 0.3325m (1.09 ft). It can be observed that the field varies randomly but smoothly in the cross-section and as moving along the length, accounting for both the correlation that occurs within the cross-section (over different wires) and along the length of the cable.

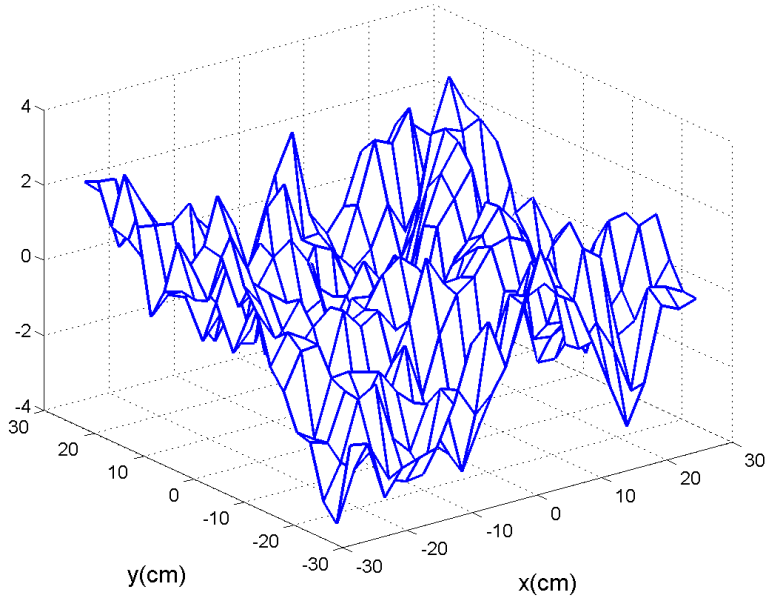

Figure 4.23: Sample function of stochastic field $f(x_1, x_2, x_3)$ representing the variation of the strength of the cable from the mean plane at 0 m.

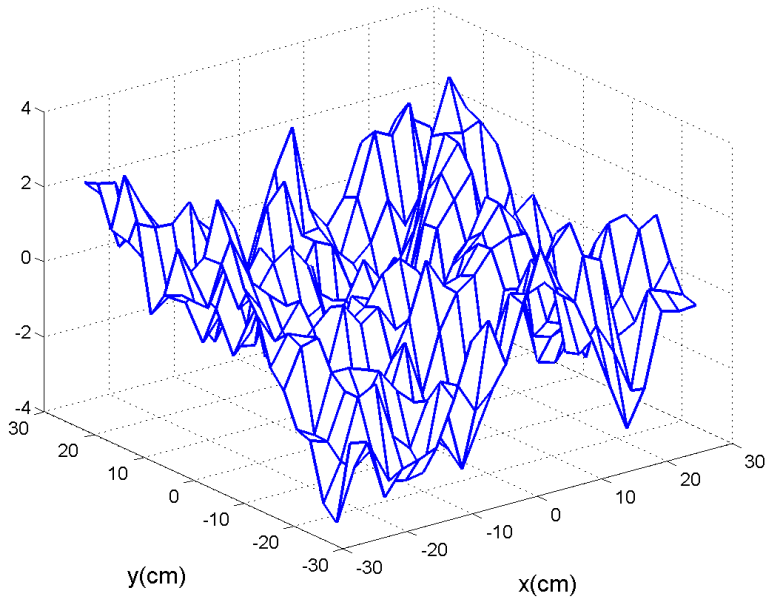

Figure 4.24: Sample function of stochastic field $f(x_1, x_2, x_3)$ representing the variation of the strength of the cable from the mean plane at 0.3325 m.

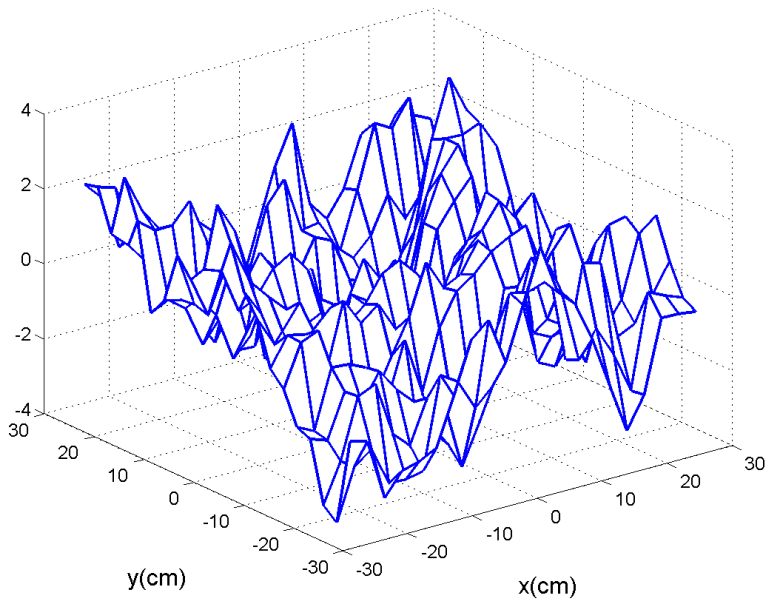

Figure 4.25: Sample function of stochastic field $f(x_1, x_2, x_3)$ representing the variation of the strength of the cable from the mean plane at 0.665 m.

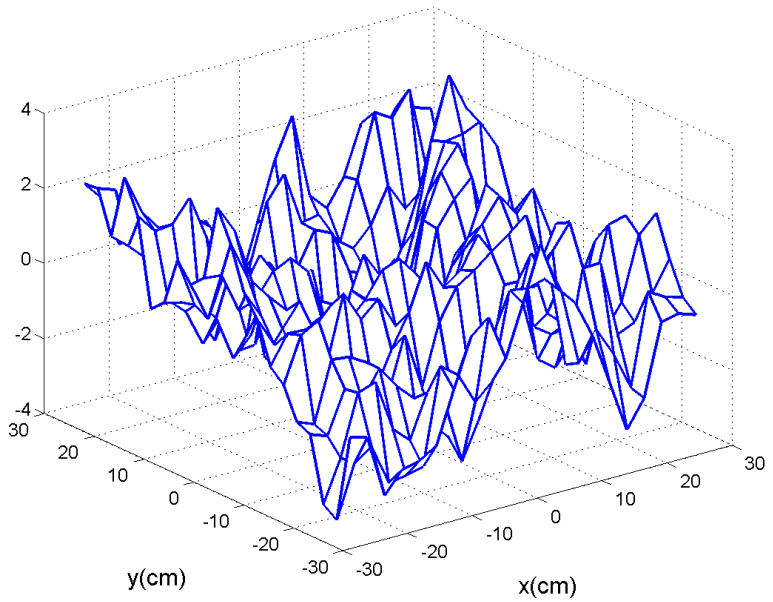

Figure 4.26: Sample function of stochastic field $f(x_1, x_2, x_3)$ representing the variation of the strength of the cable from the mean plane at 0.9975 m.

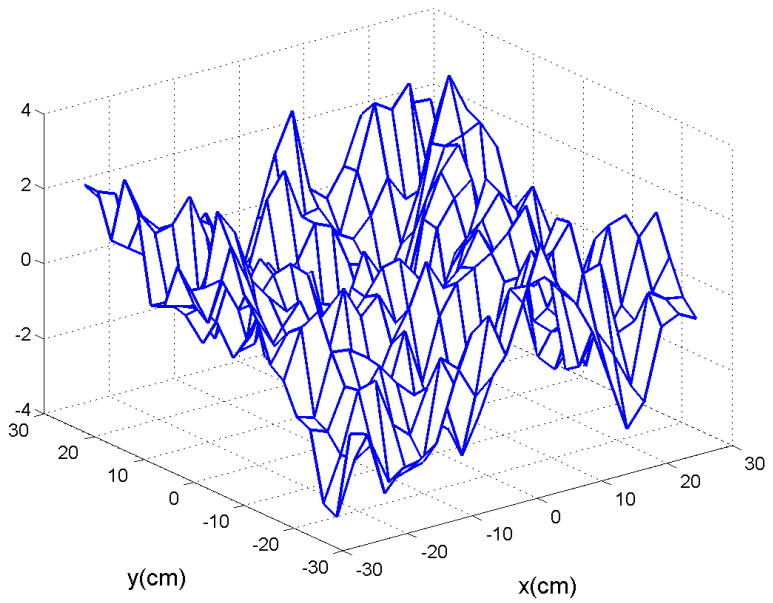

Figure 4.27: Sample function of stochastic field $f(x_1, x_2, x_3)$ representing the variation of the strength of the cable from the mean plane at 1.33 m.

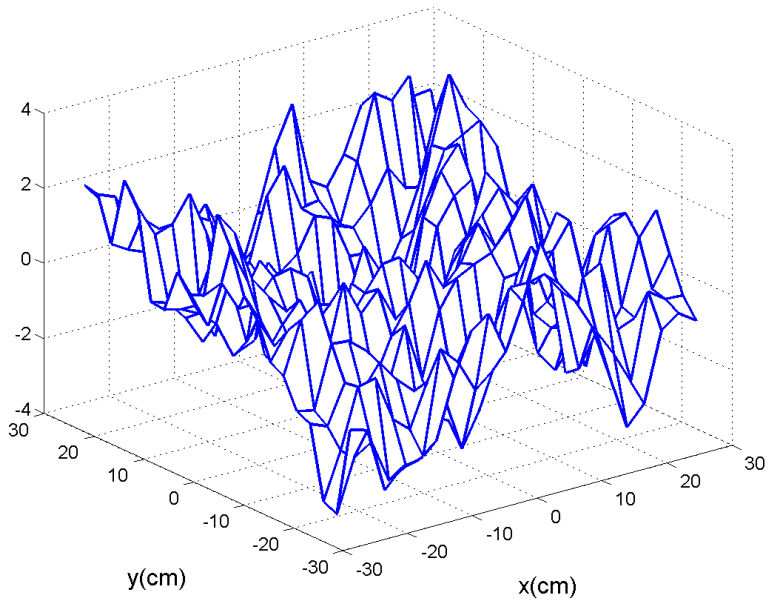

Figure 4.28: Sample function of stochastic field $f(x_1, x_2, x_3)$ representing the variation of the strength of the cable from the mean plane at 1.6625 m.

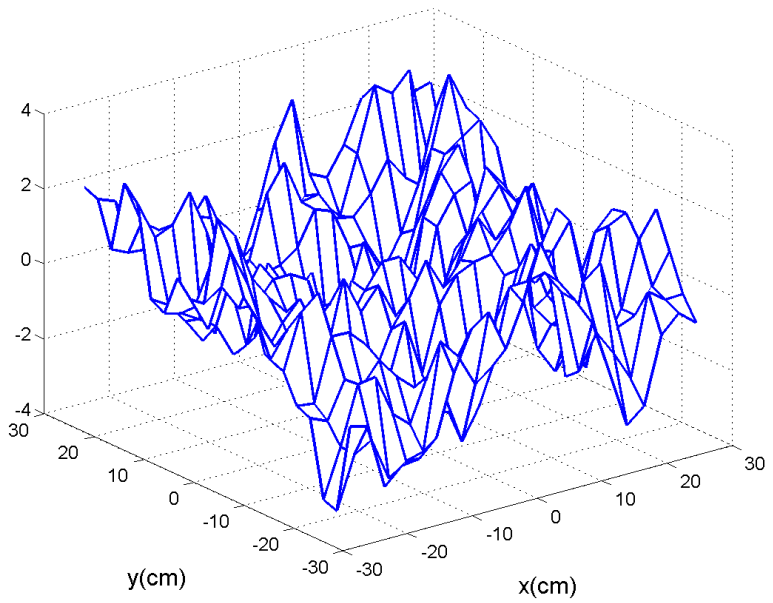

Figure 4.29: Sample function of stochastic field $f(x_1, x_2, x_3)$ representing the variation of the strength of the cable from the mean plane at 1.995 m.

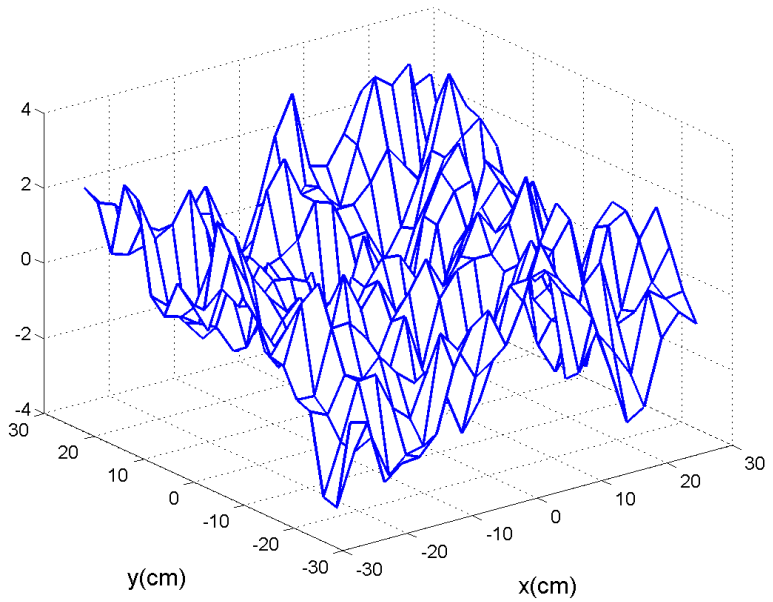

Figure 4.30: Sample function of stochastic field $f(x_1, x_2, x_3)$ representing the variation of the strength of the cable from the mean plane at 2.3275 m.

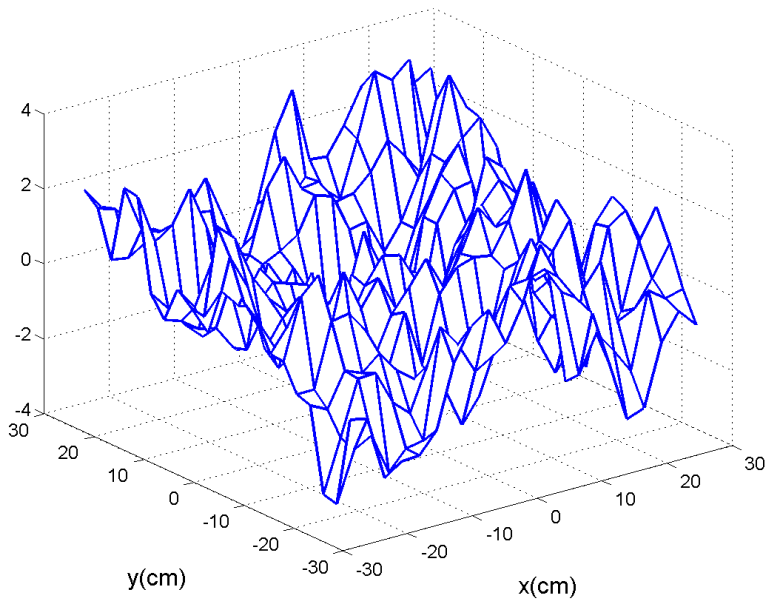

Figure 4.31: Sample function of stochastic field $f(x_1, x_2, x_3)$ representing the variation of the strength of the cable from the mean plane at 2.66 m.

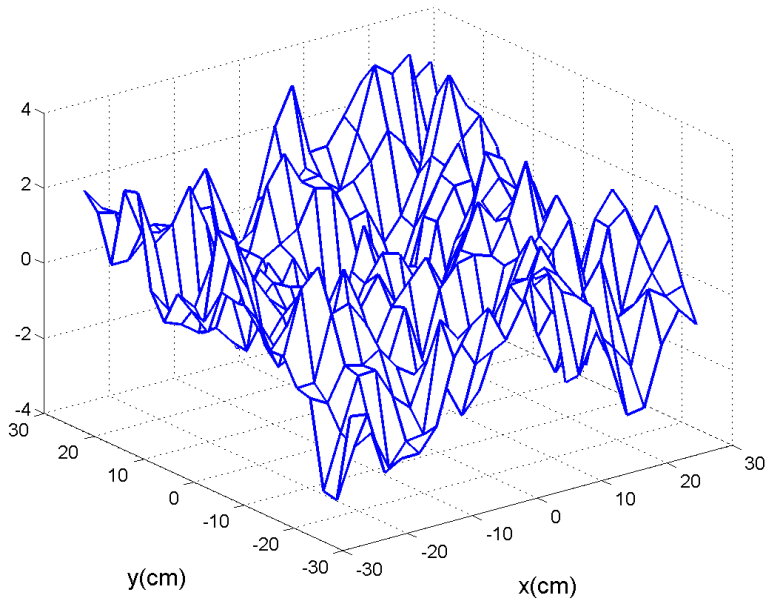

Figure 4.32: Sample function of stochastic field $f(x_1, x_2, x_3)$ representing the variation of the strength of the cable from the mean plane at 2.9925 m.

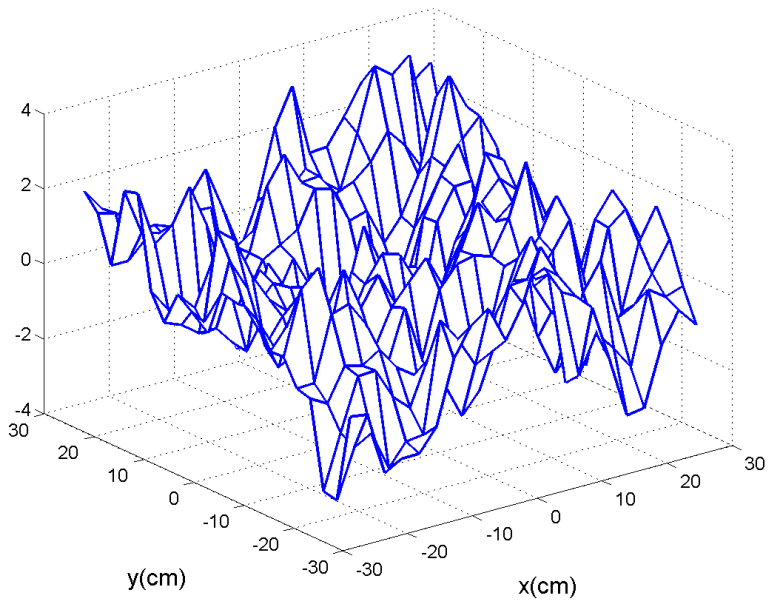

Figure 4.33: Sample function of stochastic field $f(x_1, x_2, x_3)$ representing the variation of the strength of the cable from the mean plane at 3.325 m.

Once the sample function of the field is obtained for the cable, the strength of the wires can be extracted from the generated grid by performing a three-dimensional linear interpolation. Then, the actual strength of the wires can be recovered by referring to Equation 4.26. The standardized and actual strength generated for three pairs of adjacent wires are illustrated in Figures 4.34 and 4.35, respectively. The wire pairs are taken from the bottom, center, and top sectors of the cable. It can be observed that we have obtained the behavior that most likely reflects the actual conditions inside a cable. The center wires have a higher strength than the lower wires as expected. Moreover, the two adjacent wires shown for the each sector have similar behavior and weak points at the same or nearby location along the length. The location of the weak spots between pairs does not match, since the field of the cable's strength is random along its three dimensions.

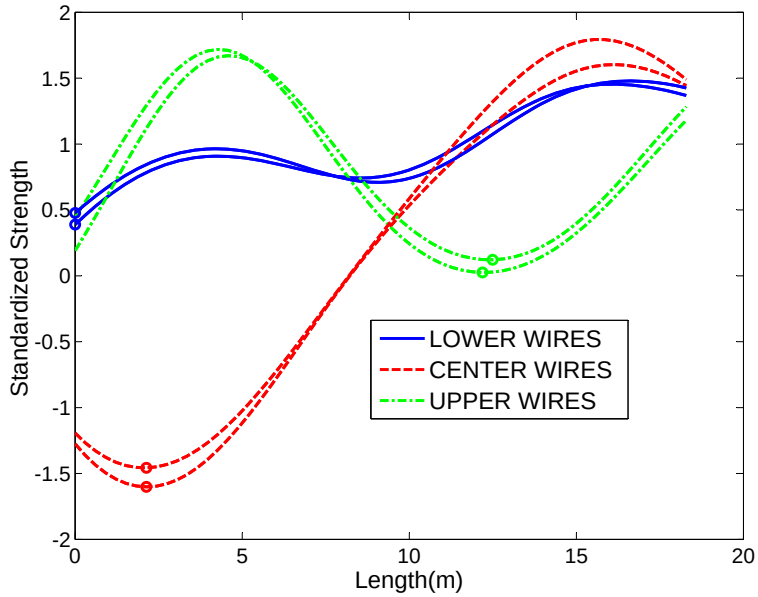

Figure 4.34: Generated standardized strength along the length of the 18.3 m cable for three pairs of adjacent wires in the cross section of the cable. The pairs come from the top, bottom, and lower sectors of the wires. The weak points are depicted by the symbol **o**.

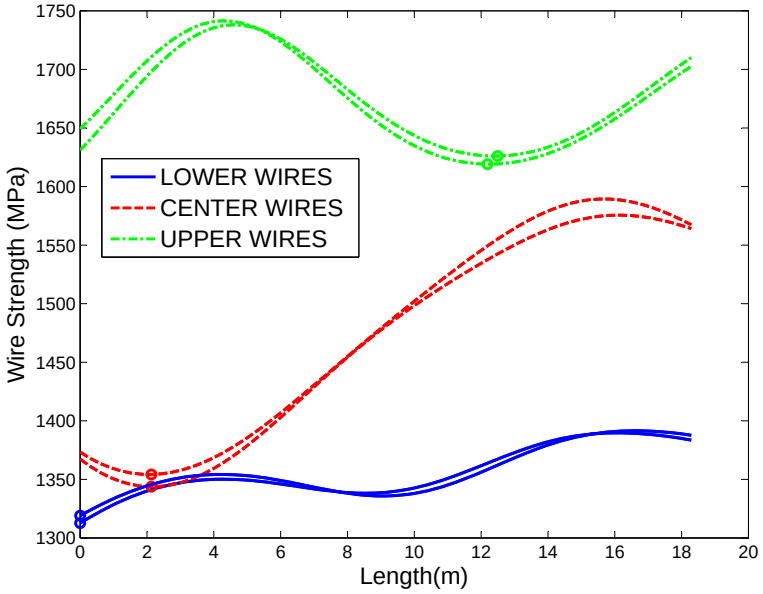

Figure 4.35: Actual strength along the length of the 18.3 m cable for three pairs of adjacent wires in the cross section of the cable. The pairs come from the top, bottom, and lower sectors of the wires. The weak points are depicted by the symbol **o**.

Chapter 5

Application of the Model to Suspension Bridges

5.1 Chapter Summary

In this chapter, the methodology to estimate the cable's failure load is completed by incorporating the strength variation of the wires in the finite element model that accounts for wire breaks and load recovery in broken wires. Monte Carlo simulations for different clamping cases are peformed by generating a number of realizations of the cable's strength within the FE model. The statistics of the failure load are estimated by ensemble averaging and fitting the best distribution to the data. The runs show that clusters of broken wires at the weaker sections of the cable are formed prior to full collapse of the cable. A comparison between the estimated cable's failure load and actual loads in suspension bridges is made in order to determine the current safety factor of the structure.

5.2 Model Description

The multi-scale model described in Section 3.7, representing wires as truss elements and placing spring elements between wires in the clamp region to account for the frictional interaction, was used to perform a stochastic analysis that predicts the load that will drive a suspension bridge cable to failure. We consider a cable with a diameter of 24.37 cm, composed of 9061 wires with a diameter of 0.4826 cm each. Two different clamping cases were considered, providing different levels of recovery for a broken wire. The first case provided almost full recovery in a broken wire after crossing a cable band, equivalent to a clamping length of 6 m (20 ft). The second case provided about 80 % recovery after one cable band and almost full recovery after crossing the second band, equivalent to a clamping length of 12 m (40 ft). The proposed three-dimensional random field described in Section 4.6 can be applied in a straightforward way to the cable being modeled. As described in Section 3.4, the reduced tensile strength of the wires is incorporated as a material parameter denoted

as the Critical Failure Stress (CFS) in the Finite Element Model. The formulation of the sample functions of the strength field is incorporated within the Finite Element Program.

The failure load of the cable is obtained through a Monte Carlo Simulation (MCS) with 1000 realizations for each case considered. The cable is loaded using the displacement controlled method for twenty steps. The load is kept constant for each realization. As wires start breaking as they exceed their CFS at different load levels, the first loading step was selected below the lowest CFS and then increasing the load in equal steps. The lowest recorded strength in the Williasmburg bridge for a wire was of 1,165 MPa; thus, the first load in the cable is taken as if each wire is carrying 1,000 MPa, which is equivalent to pulling the cable 4.5955 cm ($u = 4.5955$ cm) from each end. Then, the increments are defined as increasing the load in each wire with 12.5 MPa, which is equivalent to slowly pulling the cable 0.06 cm ($\Delta\ u = 0.06$ cm) from each end at every step. The cable fails at a different load in each realization.

The parallelization of the problem was essential to facilitate the stochastic analysis that determines the effect of corrosion uncertainity on the cable's failure load. The prallel machine used to solve the problem is known as the Hotfoot. The Hotfoot is a high-performance computing cluster owned by Columbia University Information Technology (CUIT) in partnership with the departments of statistics and astronomy. It contains two submit nodes, a Network File System server, and 62 execute servers with a total of 616 compute cores. There are 72 TB of raw storage set in a RAID (redundant array of independent disks) configuration that yields approximately 52 TB of working storage. Based on the 50 processors provided by the computer's administrators, the problem was partitioned into 25 processors. Two feap excutables, using 25 processors each and memory independent, were ran simultaneously. (The Sicortex machine described in Section 3.5.2 crashed and thus an alternative computer had to be considered to run the simulation).

5.2.1 Computational Details of the Simulation

The flowchart in Figure 5.1 illustrates how the finite element program FEAP [45] was used to run the realizations of the Monte Carlo simulation. The main routines that control the simulation are shown. FEAP, an opened source code, was modified in order to reduce memory storage and expedite the runs. The mesh, composed of truss and spring elements, is independent of the realization; while the material property that determines the wire breaks (CFS) in each wire is different for each run. The goal was to minimize calls to FEAP executable in order to take advantage of the unchanging mesh and generate the CFS within each run.

This approach avoids the reading of lengthy input files and reduces the total CPU time of the simulation. The FEAP executable is responsible for reading the input files, storing the nodes, elements, material properties, boundary conditions, and loading function. The program has two time variables, the step (STEP) which corresponds to the number of load increments during the quasi-static problem and the total time (TIME) which counts the number of times the program reaches a solution for an assigned load. For this simulation, the total number of steps was 20; each Monte Carlo realization has twenty loading steps. Thus, the total time is the number of realizations times 20. The routine dettime.f determines the step number according to the total time. Step 1 corresponds to the first step of a different realization of a Monte Carlo run. If dettime.f identifies step 1, it calls routine pzero.f, which sets the displacement and force vectors back to zero, but keeping the mesh information intact. The routine uprop.f assigns a proportional loading according to the step of the realization.

After the load is assigned, the element routines are called. For the one dimensional problem, there are two elements, the truss elements assigned to the wires and the spring elements that model the frictional interaction between wires. The elmlib.f routine calls the elements based on the stored information. For the truss elements (trussnd.f), there are two material property routines: the elas1d.f and the umatl1.f.

The former accounts for the constitutive equation for linear elastic trusses and the latter is a user routine in which a check is performed to determine if the current axial stress exceeds the critical failure stress. Once the program recognizes the first truss element with a user material property, it checks if step is equal to 1. If step is equal to one, it implies a new realization and a new simulation to determine the CFS along the wires is performed and stored for the current realization (20 steps). In order to alter the random numbers assigned for the strength variation formulation, the program changes the seed of the pseudo random number generator for each realization.

The spring elements memory storage had to be altered from the typical FEAP memory storage for material properties. In the model, each spring element has a different maximum tangential force based on its location within the cross-section and proximity to the clamping forces in the longitudinal direction. FEAP stores an array for each material of size of 401. Thus, the storage of 500,000 different material properties becomes too large, making the program significantly slower. Therefore, it was decided to store the springs' material properties in a Fortran module during the initial step of the simulation and reuse for the rest of the simulation.

Once the program has all the necessary information to solve the problem, it iterates until a solution is found using Newton's method for each step as illustrated in Figure 5.2, showing the solution commands assigned to FEAP. The outer loop (loop 1) initializes the FEAP executable. The middle loop (loop 2) assigns the realizations of the Monte Carlo simulation. Loop 3 provides the load increments for each realization (20 steps per realization). Loop 4 is the non-linear iterative process to reach a solution for each step, the number of iterations allowed are specified to 30. Loop 5 is where the linear solves are performed within the nonlinear process. The Conjugent Gradient (CG) solver is used in conjunction with a Block Jacobi Preconditioner. The command "ZERO, node" sets the displacement and force vectors equal to zero after each Monte Carlo realization. TIME counts the number of times the problem has been solved.

FEAP was called twenty times in order to obtain the 1,000 realizations. The average CPU time for each FEAP executable was of 3 hrs and the Monte Carlo simulation runs in 30 hours, since two FEAP executables were running simultaneously.

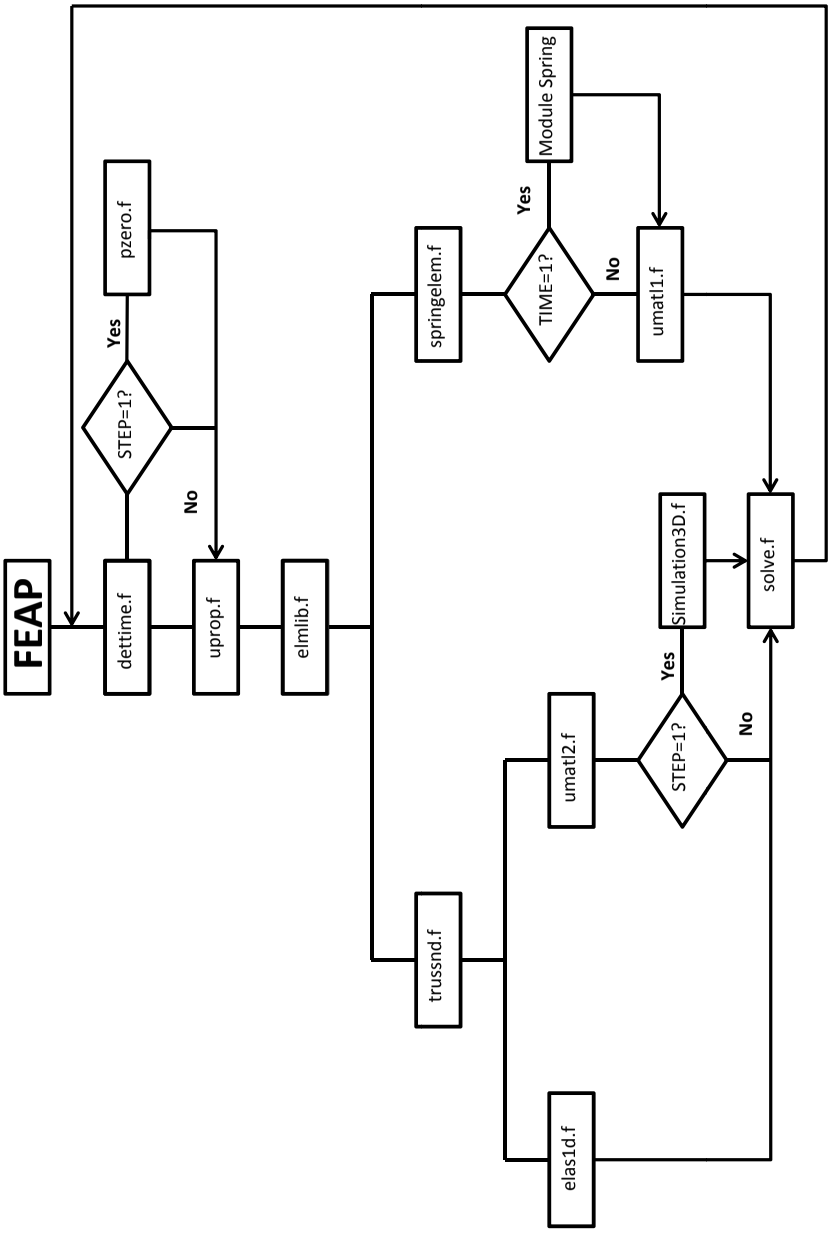

Figure 5.1: Flow chart illustrating the main routines used by FEAP to minimize memory storage and expedite the runs.

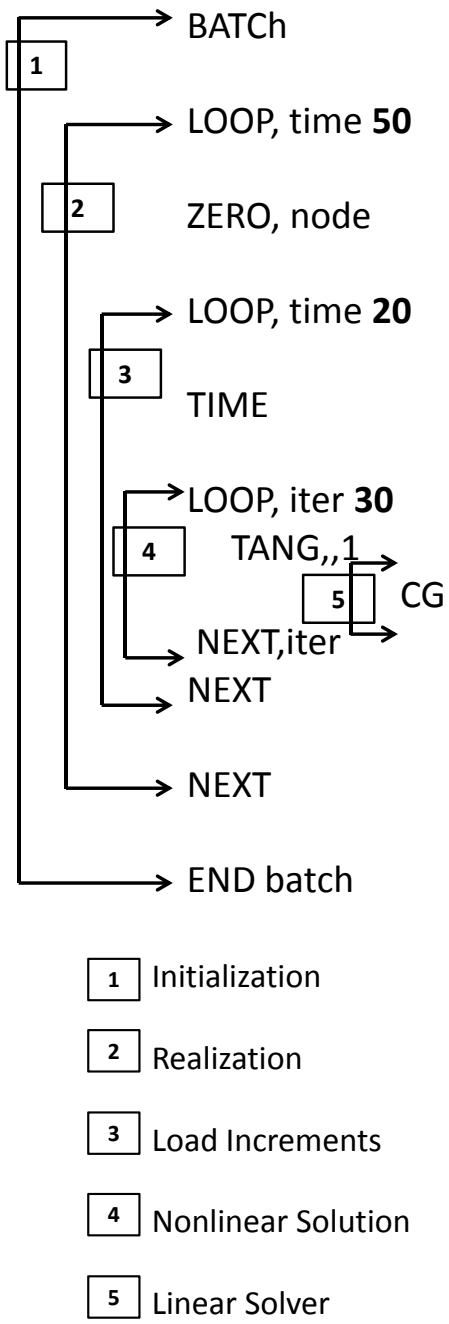

Figure 5.2: FEAP commands to perform the Monte Carlo Simulation to minimize calling the FEAP excutable.

5.3 Results

5.3.1 Sample Run

Figures 5.3 to 5.12 show a sample run of the model incorporating the strength variation within the cable due to corrosion. The force-displacement curve is zoomed in at the critical region before failure. The cross-sectional plots are at the critical section along the length where the greatest number of broken wires are found for this run. However, wires may start breaking at other spots along the length, especially as the load increases. At step 1 (Figure 5.3), none of the cases exhibit broken wires, showing a perfect elastic behavior. Until step 8, four (4) adjacent wires break at the bottom of the cable. At step 9, the number of broken wires in the same sector has increased to 14. A cluster composed of 27 broken wires has formed after loading step 10 is applied. Two cluster of broken wires appear at loading step 11; the orginal cluster has increased to 60 broken wires and a cluster of 38 broken wires appears near the bottom third of the cable. At loading step 12, the cable collapses and is no longer carrying any load.

In order to capture more broken wires before failure, smaller steps are required from the last surviving step. Thus, the run is repeated and the load increments are reduced from $\Delta = 0.06$ cm to $\Delta = 0.00013$ cm after step 11. At loading step 31 and 41, a total of 115 and 127 wires are broken, respectively. As the load is increased, the surrounding wires to the breaks are highly stressed as observed in Figure 5.8 and 5.9, where the wires in the region between clusters are carrying more load than the rest of the surviving wires. At step 53 (Figure 5.10), the wires between clusters have broken, forming one big cluster of broken wires. The number of broken wires increases to 574. At step 44, 2848 wires break at the lower half of the cable, increasing the stress in the surviving wires significantly as observed in Figure 5.11. After another small load increment, the cable collapses. The cable has failed in a domino like effect

in which the failure of weak wires causes other less weak wires to fail at their weakest spots at almost the same external load. The breaking of wires are expected to occur successively, but almost in an instantaneous manner. Steinman refers to such failure mechanism as the cascade effect [42].

By reducing the loading step, the response of the cable before failure is captured in more detail and the failure load is captured with more accuracy. However, it increases the CPU time excessively which is not appropriate for a stochastic analysis. As a conservative approach, the broken load is recorded as the last carried force usign load increments of $\Delta = 0.06$ cm. The margin of error for a run may vary between 0-2.16 MN, the maximum increment in the load of a cable between steps. The error is not too significant to justify the tremendous increment in the computational time required by taking tiny loading steps to capture the sequence of wire breaks.

It has been observed that the breakage of 100 to 200 wires is sufficient to trigger the domino effect under high loads, as exhibited in the example. The load in the cable is high and after these number of broken wires has been reached, the surrounding wires increment their load considerably. As a rough estimate, the load left by the broken wires can be distributed evenly to the surviving wires. If 100 wires are broken at 1165 MPa, it implies that each of the surviving wires will carry an extra 13 MPa. Likewise, if 200 wires break, the surviving wires will carry an extra 26 MPa. These load increments are enough to cause the collapse of the cable due to the small range in the strength variation exhibited in the wires extracted from the Williamsburg bridge (1,165 MPa to 1669 MPa). In fact, the load increment is higher than the slope of the mean plane variation, 7 MPa/cm. For instance, it is very likely that a wire at 1 cm above the cluster of broken wires will not have a sufficient higher strength to carry the load increment and will break.

The breakage of about 200 wires implies that approximately 2% of the wires in the cable have broken, which is too small to show a significant decrease in the overall

stiffness of the system before the cable's failure. The force-displacement curve is shown from zero loading to full collapse in Figure 5.13(a), showing that the first break occurs at a high load. A zoom at the small increments before failure is shown in Figure 5.13(b). A zig-zag behavior is observed before failure in a very small range and cannot be captured in a larger scale. This zig-zag behavior was also observed in the numerical simulations performed by Montoya et. al [26] on smaller strands. The zig-zag behavior implies that the wires are linear elastic and carry loads linearly until new breaks occur and reduce the stiffness of the cable.

Another relevant phenomenon is the formation of clusters with broken wires before full collapse of the cable. This behavior is attributed to the correlation of the strength in the cross-section of the cable as wires in close proximity in the cross section of the cable are highly correlated. The clusters are formed at random locations in the bottom sector of the cable as shown for two other runs in Figure 5.14. These clusters increase the stress in the surrounding surviving wires; this stress increment dissipates over a considerable area from the breaks as shown in Figure 5.14. The high stressed regions are most likely to fail after small load increments.

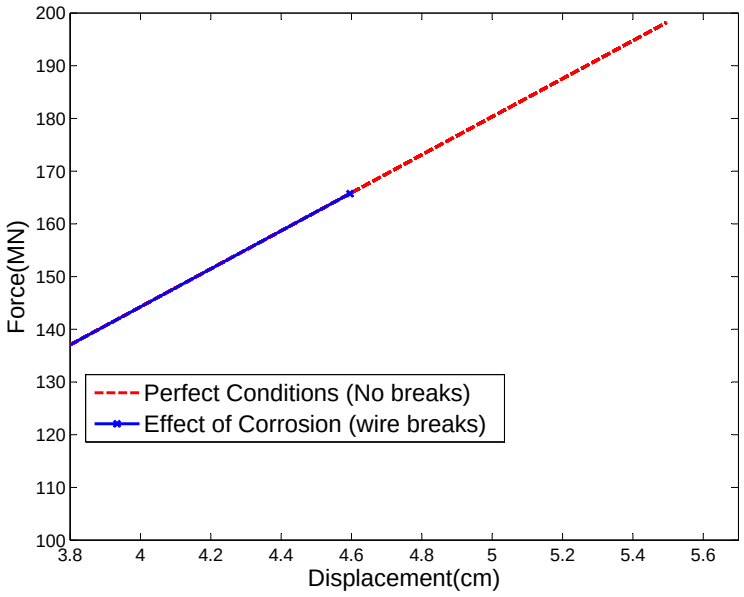

(a)

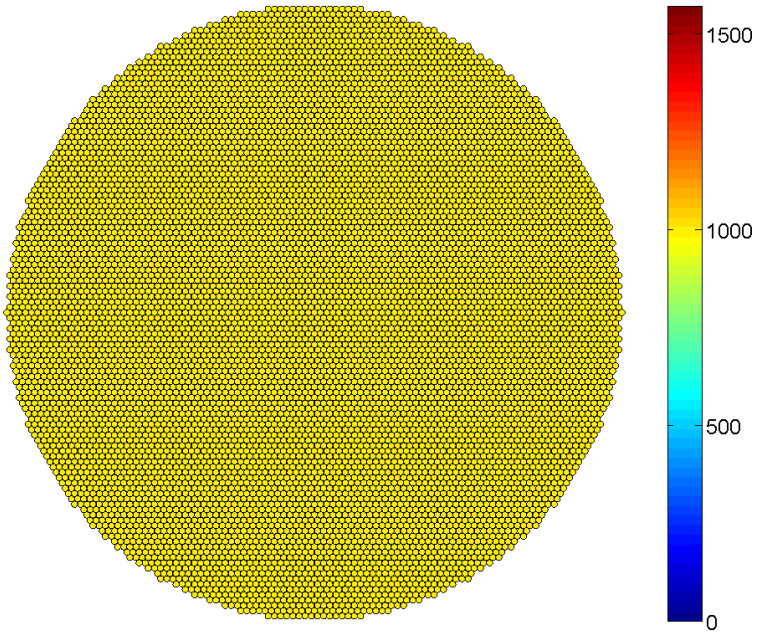

(b)

Figure 5.3: 9061 Wire Case behavior after Step 1. (a) Force-displacement curve of the corroded cable compared to the perfect condition case (no breaks) at u = 4.9555 cm. (b) Axial stress at the critical cross section. The blue circles denote broken wires.

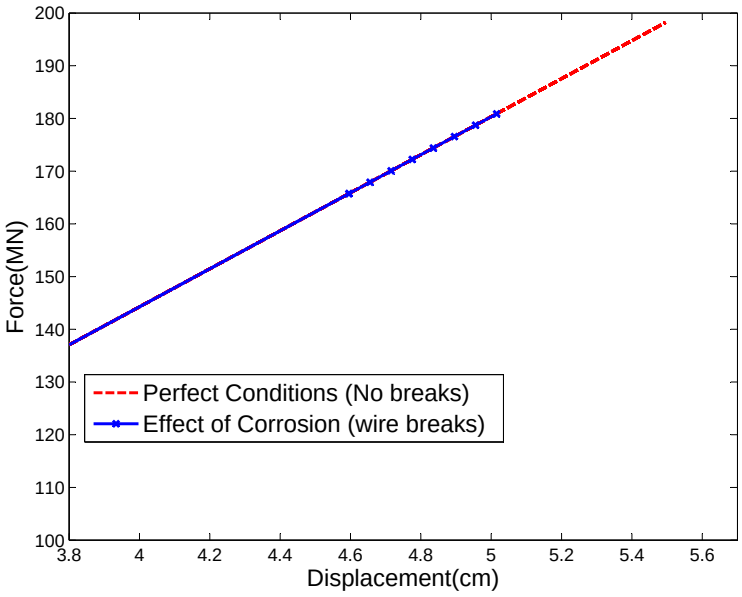

(a)

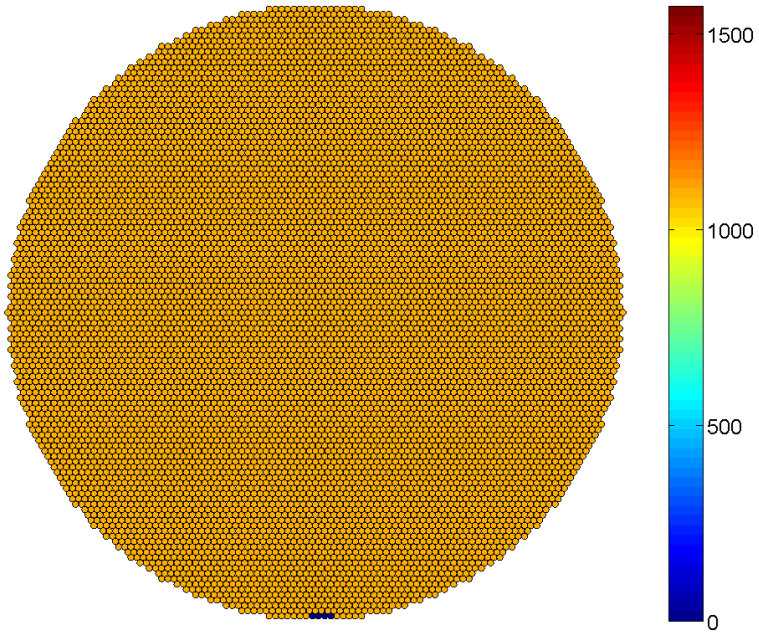

(b)

Figure 5.4: 9061 Wire Case behavior after Step 8. (a) Force-displacement curve of the corroded cable compared to the perfect condition case (no breaks) at u = 5.0155 cm. (b) Axial stress at the critical cross section. The blue circles denote broken wires.

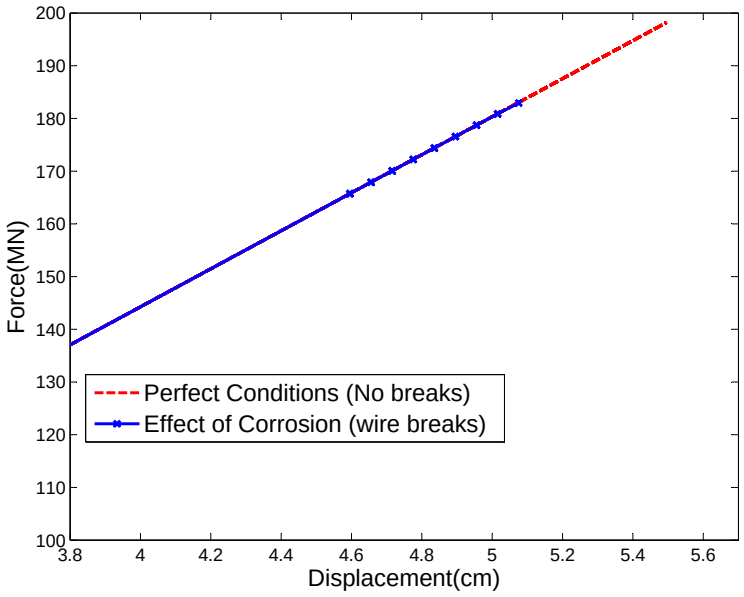

(a)

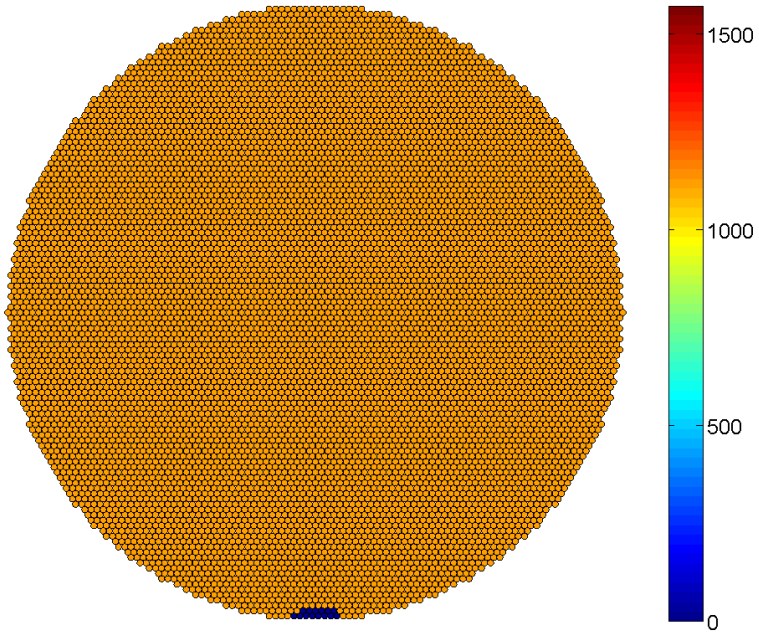

(b)

Figure 5.5: 9061 Wire Case behavior after Step 9. (a) Force-displacement curve of the corroded cable compared to the perfect condition case (no breaks) at u = 5.0755 cm. (b) Axial stress at the critical cross section. The blue circles denote broken wires.

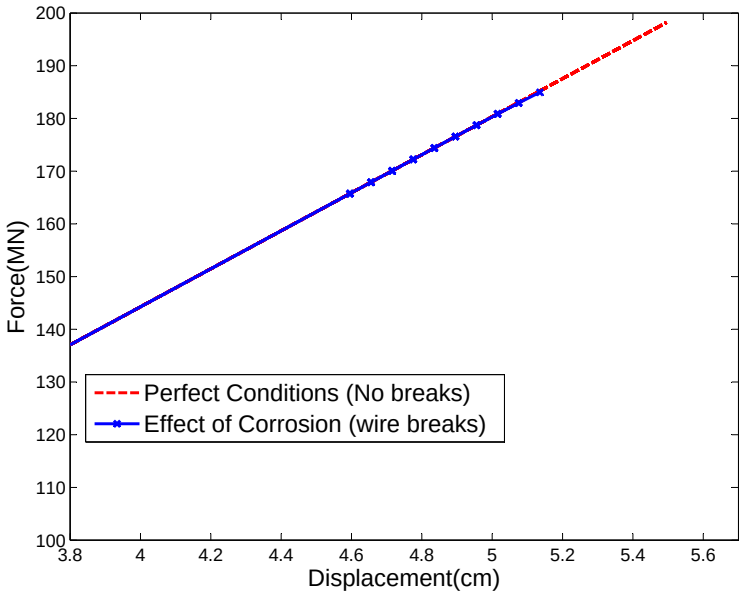

(a)

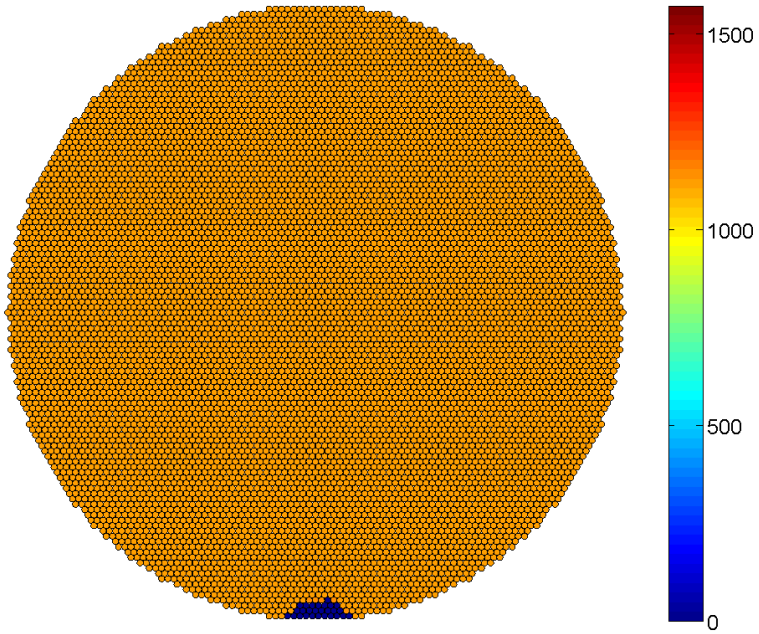

(b)

Figure 5.6: 9061 Wire Case behavior after Step 10. (a) Force-displacement curve of the corroded cable compared to the perfect condition case (no breaks) at u = 5.135 cm. (b) Axial stress at the critical cross section. The blue circles denote broken wires.

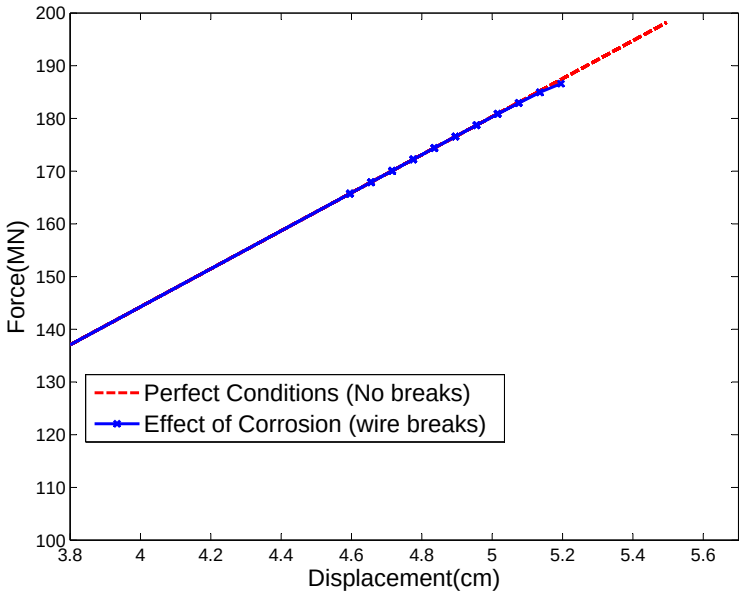

(a)

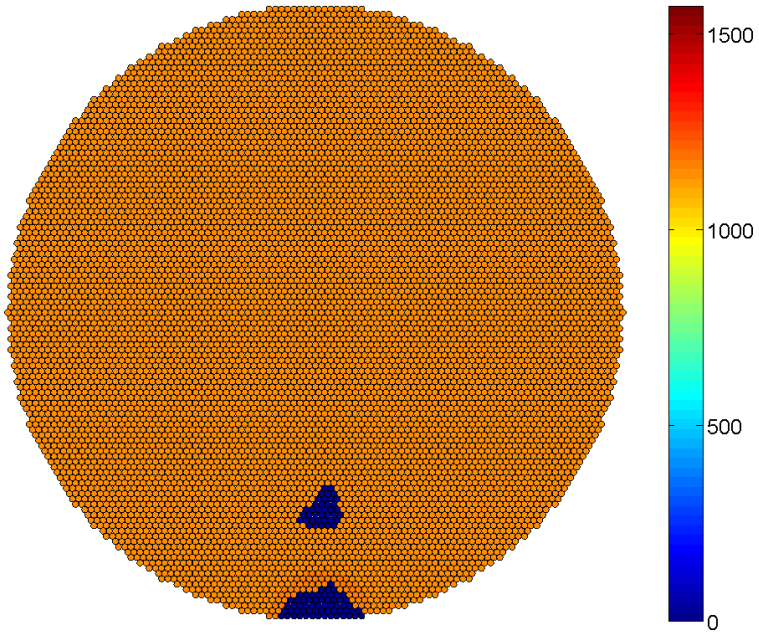

(b)

Figure 5.7: 9061 Wire Case behavior after Step 11. (a) Force-displacement curve of the corroded cable compared to the perfect condition case (no breaks) at u = 5.1955 cm. (b) Axial stress at the critical cross section. The blue circles denote broken wires.

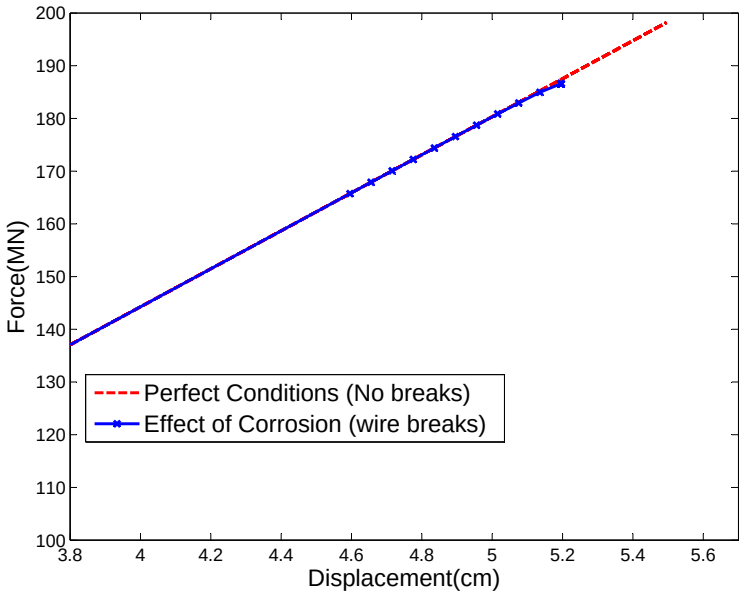

(a)

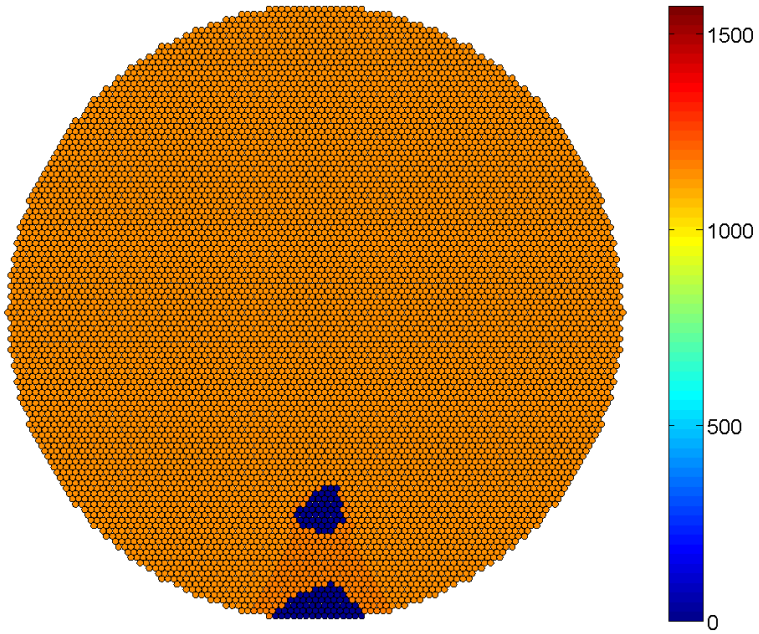

(b)

Figure 5.8: 9061 Wire Case behavior after Step 31. (a) Force-displacement curve of the corroded cable compared to the perfect condition case (no breaks) at u = 5.1957 cm.(b) Axial stress at the critical cross section. The blue circles denote broken wires.

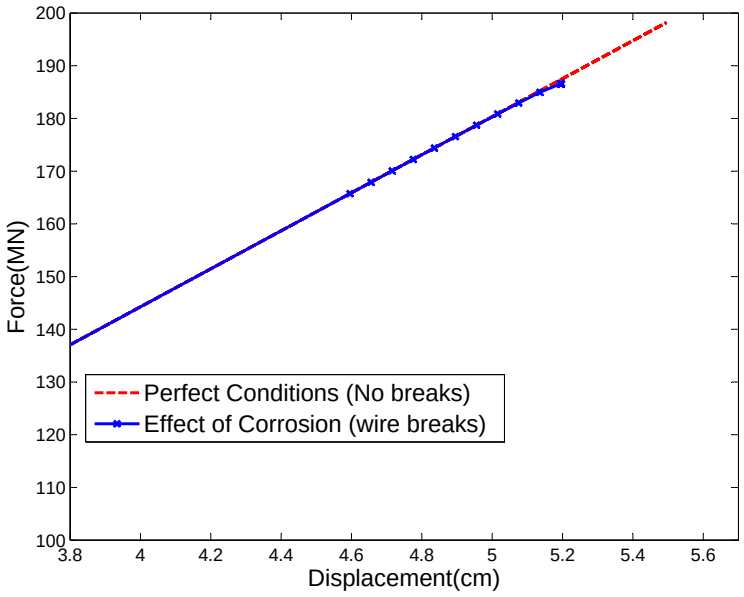

(a)

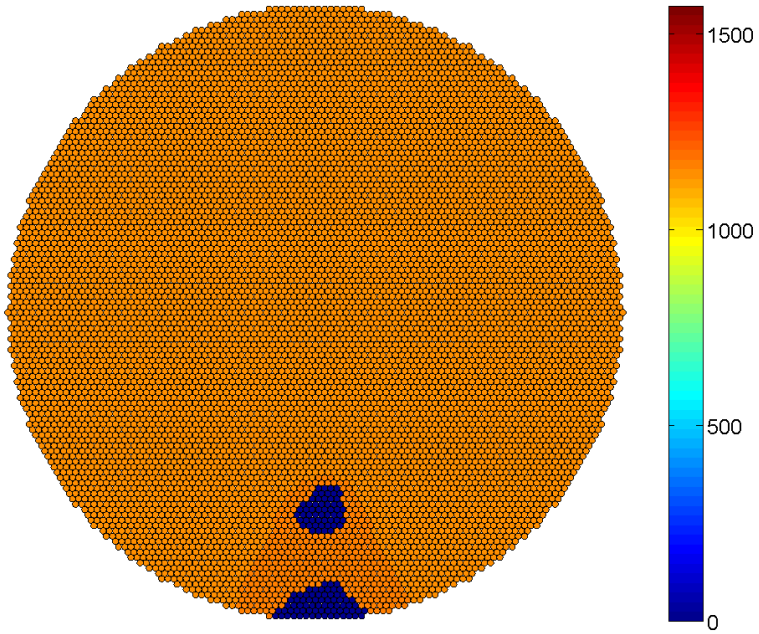

(b)

Figure 5.9: 9061 Wire Case behavior after Step 41. (a) Force-displacement curve of the corroded cable compared to the perfect condition case (no breaks) at u = 5.1959 cm. (b) Axial stress at the critical cross section. The blue circles denote broken wires.

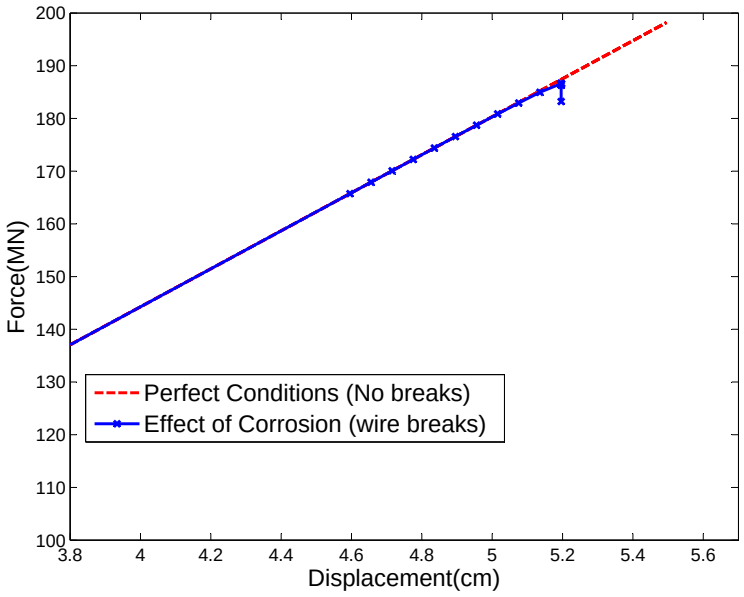

(a)

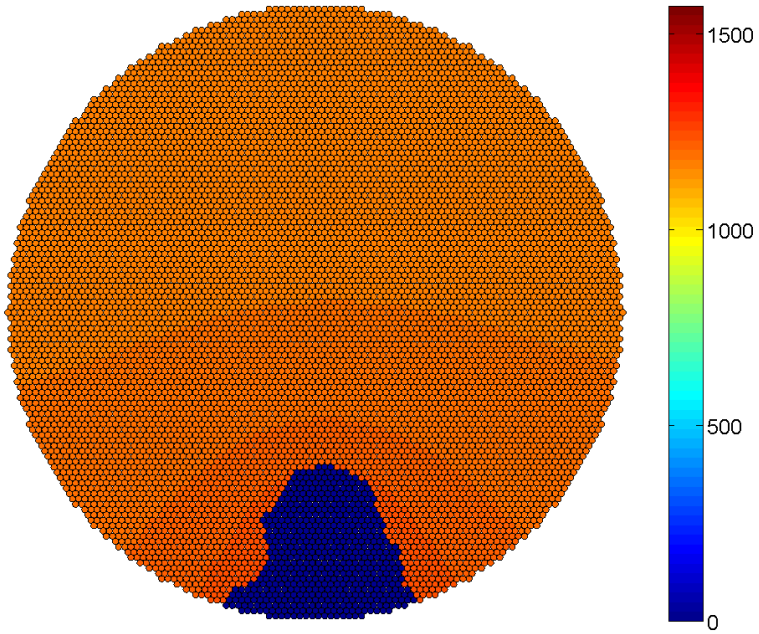

(b)

Figure 5.10: 9061 Wire Case behavior after Step 53. (a) Force-displacement curve of the corroded cable compared to the perfect condition case (no breaks) at u = 5.19605 cm. (b) Axial stress at the critical cross section. The blue circles denote broken wires.

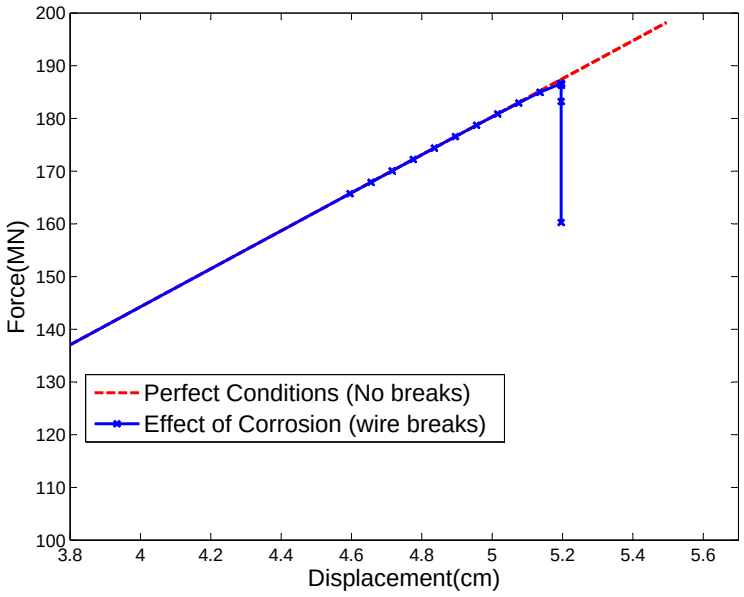

(a)

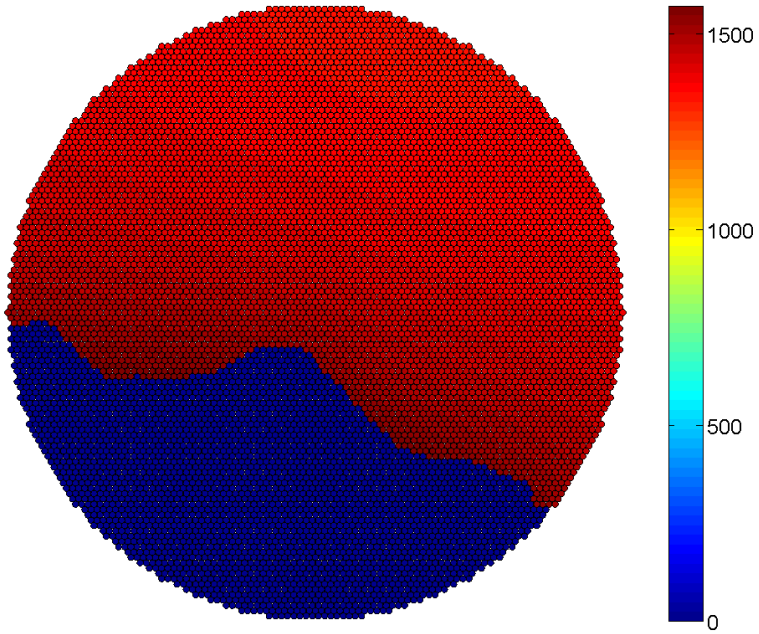

(b)

Figure 5.11: 9061 Wire Case behavior after Step 54. (a) Force-displacement curve of the corroded cable compared to the perfect condition case (no breaks) at u = 5.19606 cm. (b) Axial stress at the critical cross section. The blue circles denote broken wires.

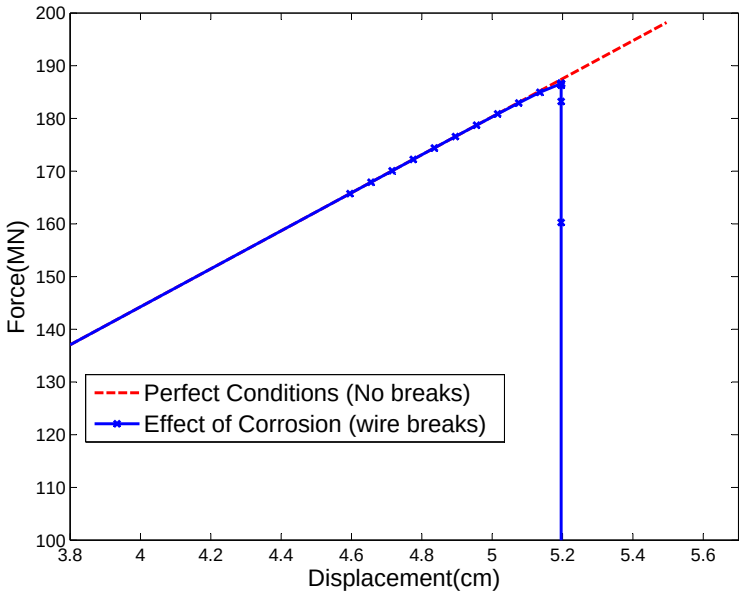

(a)

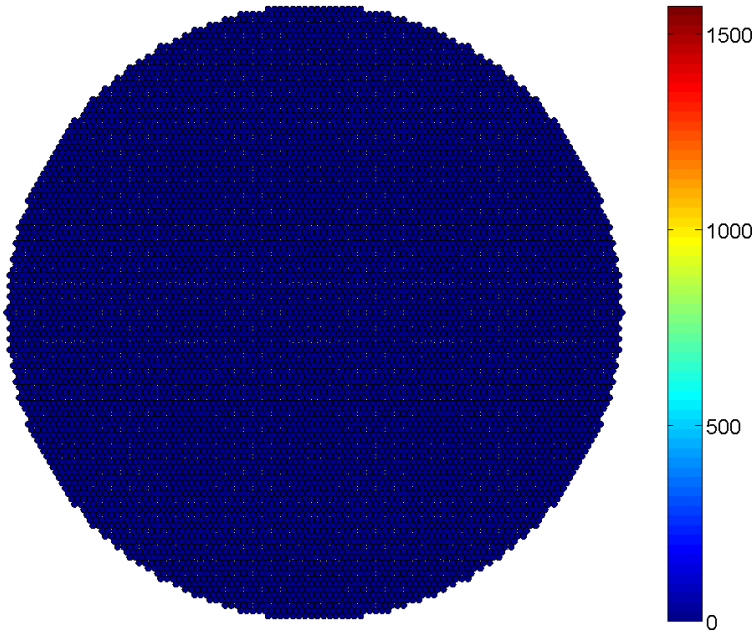

(b)

Figure 5.12: 9061 Wire Case behavior after Step 55. (a) Force-displacement curve of the corroded cable compared to the perfect condition case (no breaks) at u = 5.1961 cm. (b) Axial stress at the critical cross section. The blue circles denote broken wires.

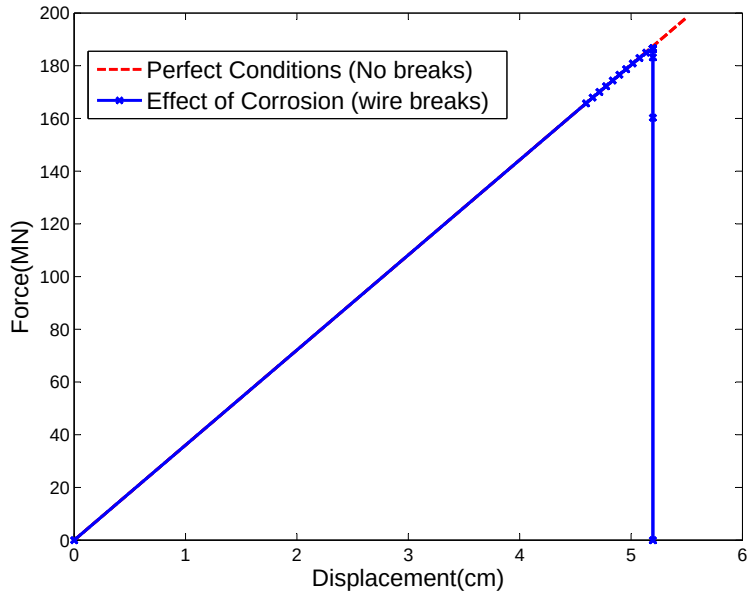

(a)

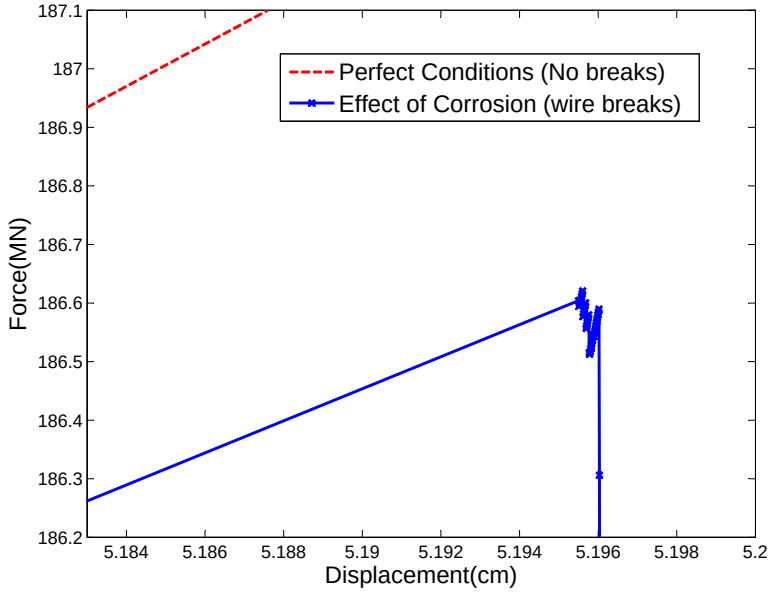

(b)

Figure 5.13: (a) Zoom out at the Force-displacement curve of the corroded cable compared to the perfect condition case showing the loading from 0 cm up to failure. (b) Force-displacement curve at the critical region before failure where the loading step increments are reduced.

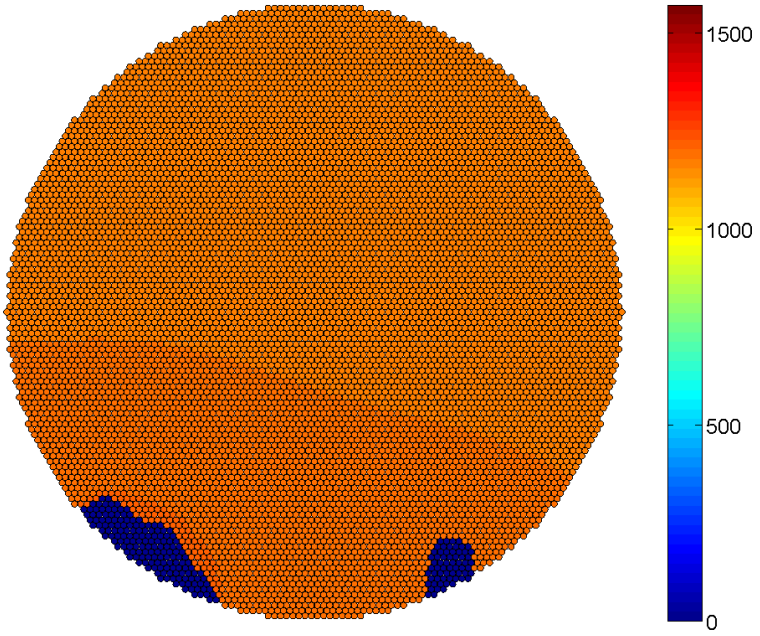

(a)

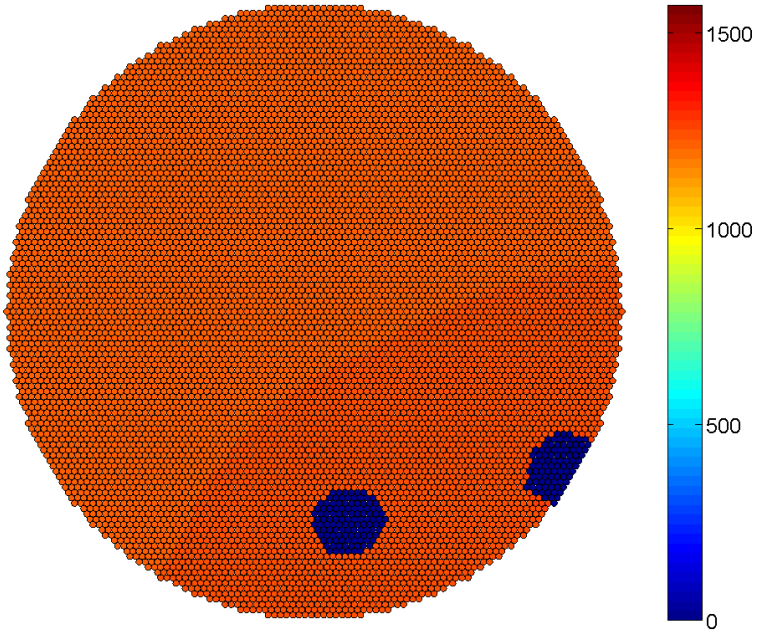

(b)

Figure 5.14: Sample runs showing the randomness of the location of the clusters.

5.3.2 Clamp Case A

The resulting force-displacement curves for the 1,0000 realizations are shown in Figure 5.15 for a clamping length of 6 m. The cable failure occurs at a different load for each case; this load is very high as it can be oberved that the effects of corrosion curves match the perfect conditions curve for an extensive loading. Figure 5.16 zooms in the region where the failure of the cable occurs. After the wires start breaking, the cable looses its stiffness and deviates from the perfect condtion case. Failure of the cable occurs a few steps, 3 to 5, after the first broken wires are observed; thus the nonlinear behavior in the cable takes place over a small range prior to the cable's failure. Although the cable's failure may occur at the same loading steps for different runs, the breaking load slightly deviates since the residual capacity of each particular realization varies according to the number of broken wires after each step. The histogram for the breaking load is illustrated in Figure 5.17.

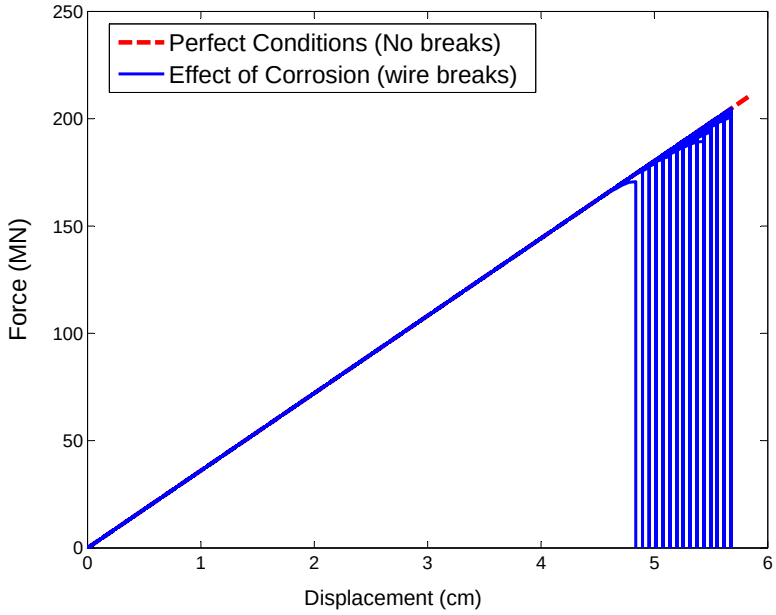

Figure 5.15: Force-displacement curves for the 9061-wires case for 1,000 realizations of strength variation due to corrosion compared to the perfect conditions (representing no breaks) for a clamping length of 6 m.

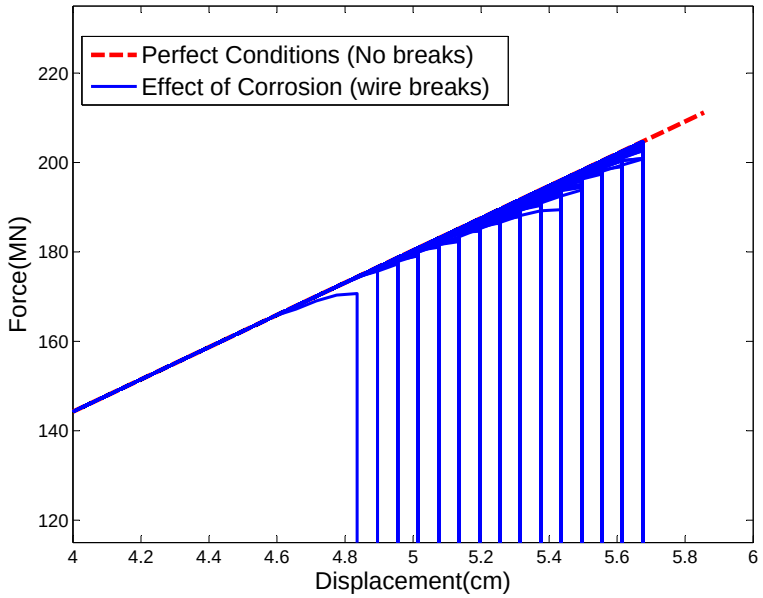

Figure 5.16: Force-displacement curves for the 9061-wires case for 1,000 realizations of strength variation due to corrosion compared to the perfect conditions (representing no breaks) for a clamping length of 6 m. This image zooms in the region where the failure of the cable occurs.

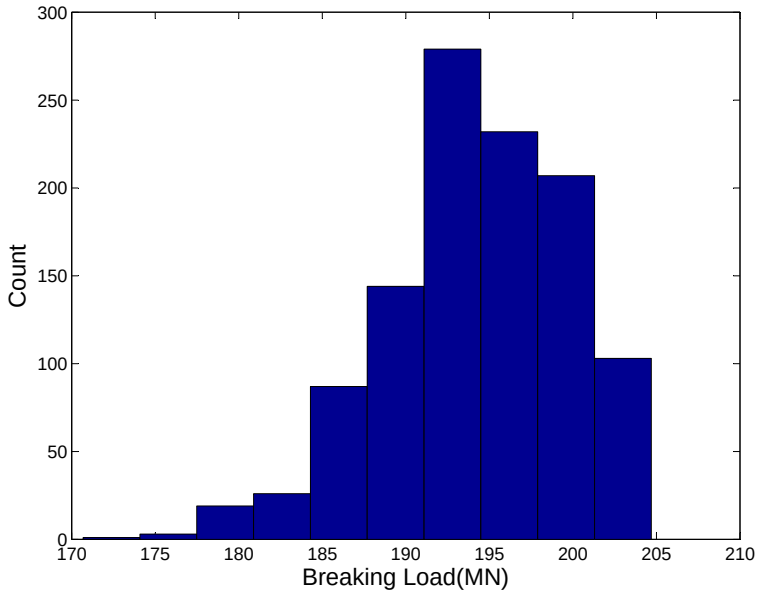

Figure 5.17: Histogram of the breaking load of the cable for a clamping length of 6 m.

The mean and standard deviation of the breaking load are:

$$\mu_{clampA} = 194.2\ MN \tag{5.1}$$

$$\sigma_{clampA} = 5.5\ MN \tag{5.2}$$

The breaking loads for each realization are standardized to zero mean and unit standard deviation. It was found that a beta probability distribution with CDF given by Equation 4.2 and corresponding PDF, Equation 4.3, provided the best fit. The parameters of the beta distribution were estimated as:

$$\bar{l_a} = -11.4,\ \bar{l_b} = 2.05,\ \alpha = 17,\ \beta = 3.5 \tag{5.3}$$

Figure 5.18 displays the standardized empirical CDF versus the fitted theoretical beta CDF. The corresponding standardized beta PDF is plotted in Figure 5.19. The coefficients of skewness and kurtosis for this beta distribution are -0.4501 and 3.26, respectively. The corresponding values for a standardized Gaussian distribution function are 0 and 3; thus, this distribution is mildly skewed from the Gaussian.

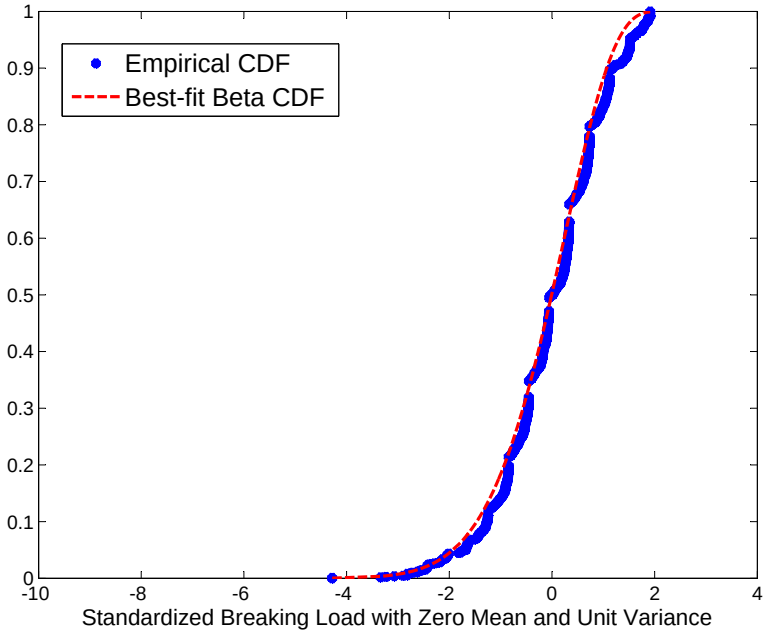

Figure 5.18: Empirical CDF obtained for the standardized breaking load versus best-fit beta CDF.

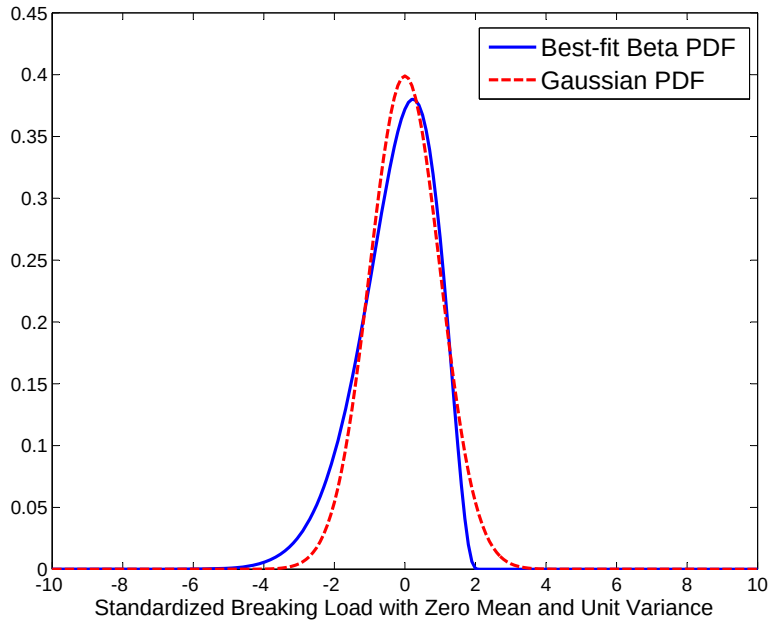

Figure 5.19: Best-fit beta PDF versus corresponding standardized Gaussian PDF.

5.3.3 Clamp Case B

The resulting force-displacement curves for the 1,0000 realizations are shown in Figure 5.20 for a clamping length of 12 m or two cable bands. Figure 5.21 zooms in the region where the failure of the cable occurs, which shows less non-linearity near the cable's failure load than for a clamping length of 6m. Failure of the cable occurs a few steps, 2 to 4, after the first broken wires are observed. A longer clamping length in broken wires imply that the surviving wires may fail prematurely since the carried load has a higher probability of exceeding the minimum carrying capacity at another spot along the length during the same loading step. The probability of this mechanism occuring prematurely is lowered with a smaller clamping length, since the broken wires recover the load at a shorter distance alleviating the surrounding wires. The histogram for the breaking load is illustrated in Figure 5.22.

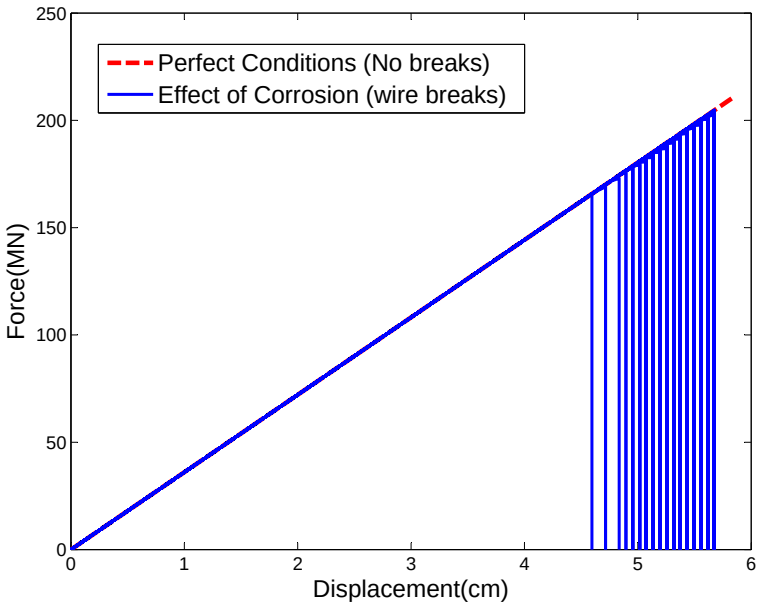

Figure 5.20: Force-displacement curves for the 9061-wires case for 1,000 realizations of strength variation due to corrosion compared to the perfect conditions (representing no breaks) for a clamping length of 12 m.

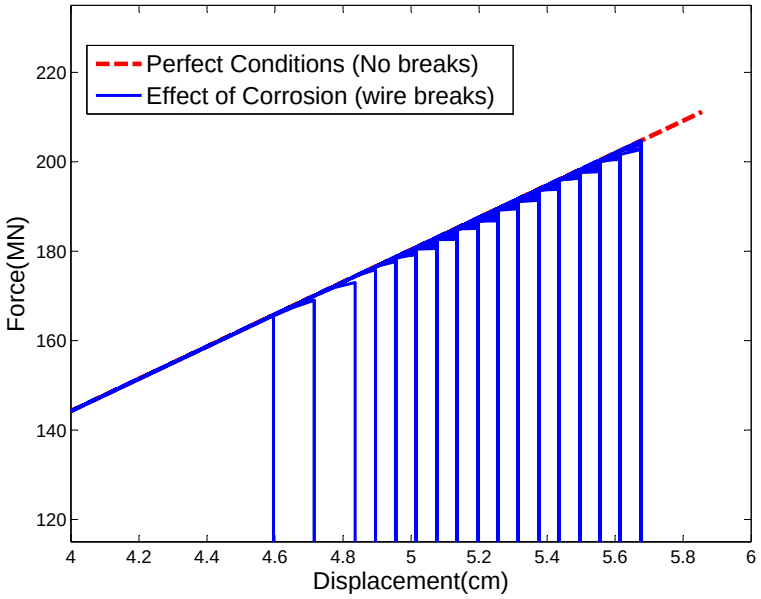

Figure 5.21: Force-displacement curves for the 9061-wires case for 1,000 realizations of strength variation due to corrosion compared to the perfect conditions (representing no breaks) for a clamping length of 12 m. This image zooms in the region where the failure of the cable occurs.

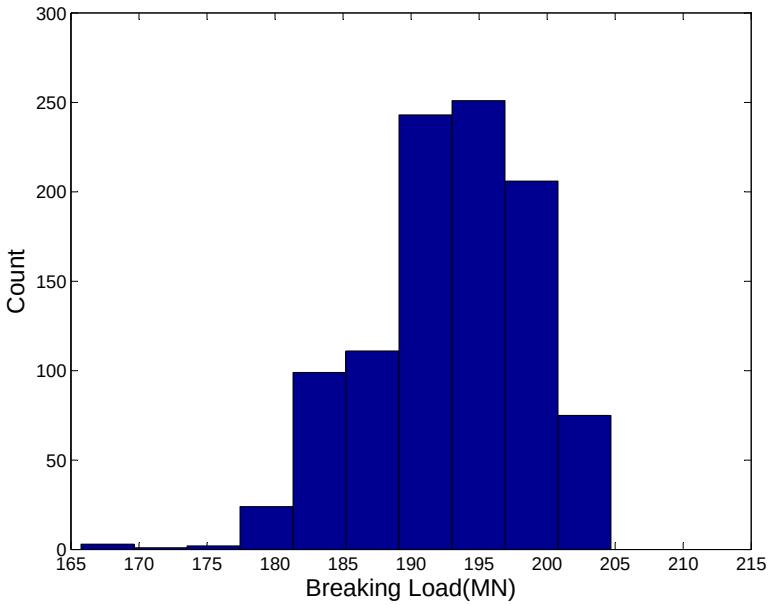

Figure 5.22: Histogram of the breaking load of the cable for a clamping length of 12 m.

The mean and standard deviation of the breaking load are:

$$\mu_{clampA} = 192.9\ MN \tag{5.4}$$

$$\sigma_{clampA} = 5.95\ MN \tag{5.5}$$

The breaking loads for each realization are standardized to zero mean and unit standard deviation. It was found that a beta probability distribution with CDF given by Equation 4.2 and corresponding PDF, Equation 4.3, provided the best fit. The parameters of the beta distribution were estimated as:

$$\bar{l_a} = -11.5,\ \bar{l_b} = 1.98,\ \alpha = 20,\ \beta = 3.8 \tag{5.6}$$

Figure 5.18 displays the standardized empirical CDF versus the fitted theoretical beta CDF. The corresponding standardized beta PDF is plotted in Figure 5.19. The coefficients of skewness and kurtosis for this beta distribution are -0.427 and 3.32, respectively. Similarly to case A, the distribution is mildly skewed from Gaussian; however having a slightly lower mean and more skewed to the left.

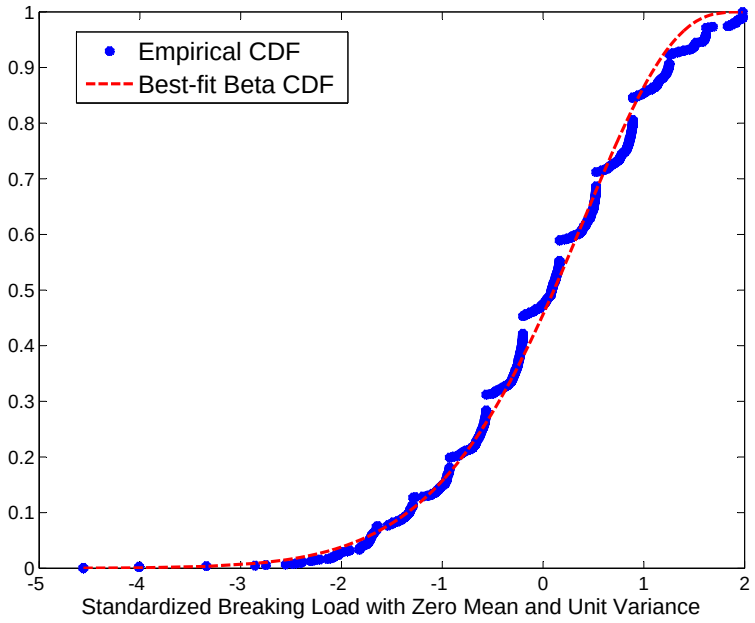

Figure 5.23: Empirical CDF obtained for the standardized breaking load versus best-fit beta CDF.

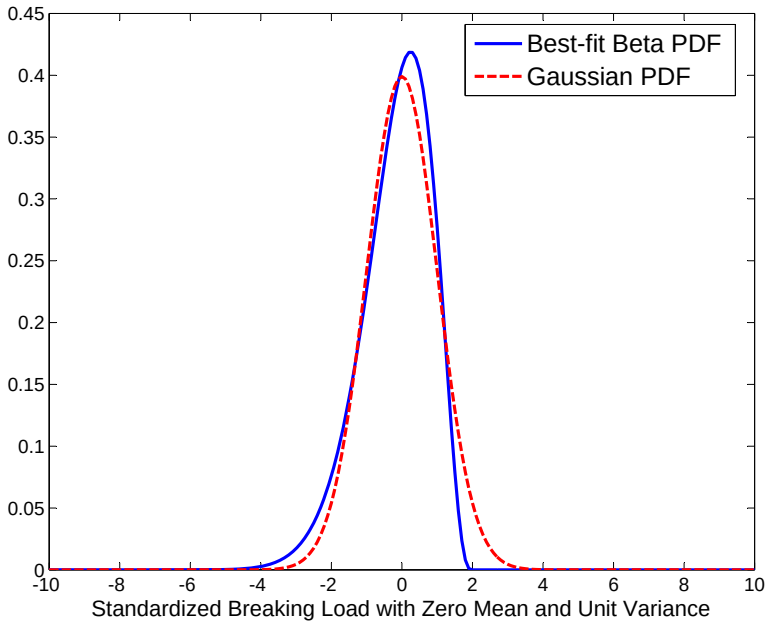

Figure 5.24: Best-fit beta PDF versus corresponding standardized Gaussian PDF.

5.3.4 Case C: Cable's Strength- No Load Redistribution

The results obtained in Sections 5.3.2 and 5.3.3 can be compared to the cable strength based solely on a random field approach as proposed by Shi et. al [54], but taking into account the spatial correlation of the strength of the cable along its three dimensions. This approach simulates the strength of the wire along a prescribed length and defines the weakspot along the length as the tensile strength of the generated wire segments. This approach does not account for load reddistribution after wire breaks and clamping length effects that can be obtained by inputting the wire strength in a finite element model. In units of force, the strength is denoted by $X_{(i)}$, which implies that the strength of the cable can be estimated by simply adding up the individual strength of the 9061 individual wires:

$$Y = \sum_{i=1}^{9061} X_{(i)} \tag{5.7}$$

The histogram for each of the 1,000 realizations is provided in Figure 5.25 and Figure 5.26 illustrates the empirical CDF obtained for the standardized breaking load versus corresponding standardized Gaussian PDF. Clearly, the cable strength distribution is Gaussian, as expected, since the field is generated according to a three diemnisonal Gaussian Stochastic field. The kurtosis and skewness parameters are 2.9 and 0.06, respectively.

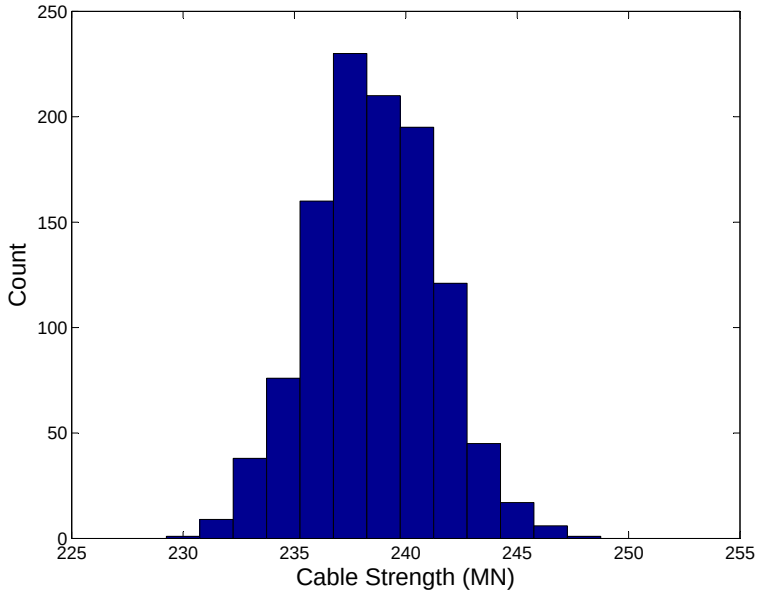

Figure 5.25: Histogram of the strength of the cable.

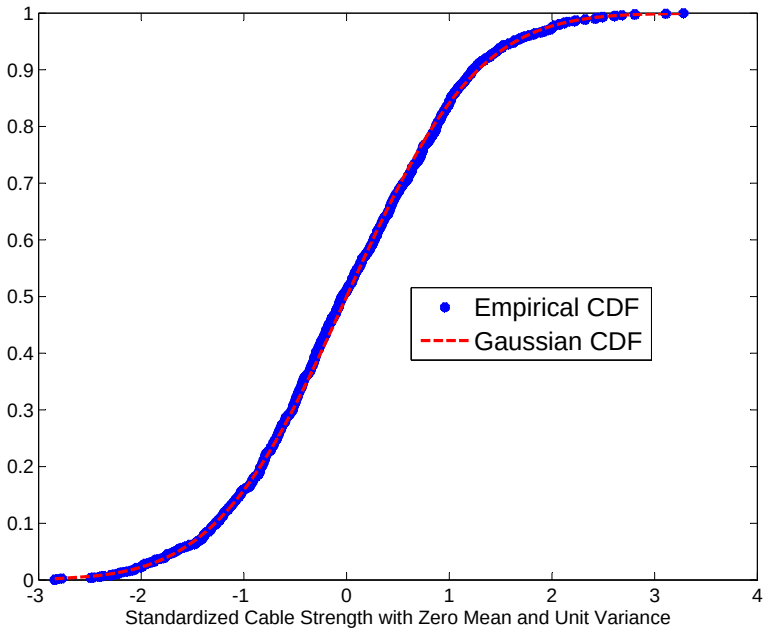

Figure 5.26: Empirical CDF obtained for the cable's strength versus corresponding standardized Gaussian PDF.

The mean and standard deviation of the cable strength are:

$$\mu_{clampA} = 238.6\ MN \tag{5.8}$$

$$\sigma_{clampA} = 2.76\ MN \tag{5.9}$$

The cable strength is significantly higher, about 18 %, than the breaking load obtained when inputting the wire's strength into the finite element model. The finite element model distributes the load left by the broken wires and consequently other weak wires may fail at their weakest spots at the same applied load. The cascade or domino effect cannot be captured by an approach based solely on a probabilistic analysis.

5.3.5 Hypothetical Case

The tested wires from the Williamsburg bridge indicated very little degradation in strength from the original quality of the wires. The minor deterioration in the wires determines the abrupt collapse of the cable at very high loads. In order to resemble a scenario in a different bridge with more degradated conditions, a hypothetical case was considered in which significant variations in the strength are observed at the cross section of the cable. Since the Williamsburg bridge wires' strength revealed a strong dependency with the y-coordinate (top-bottom in the cross-section of the cable), the hypothetical case followed the same trend having a strength mean plane of:

$$\mu(x, y) = 1039.4 + 23.62 * y\ (MPa) \tag{5.10}$$

Variations from the mean plane were generated according to the trends observed in

the Williamsburg bridge as observed in Figure 5.27. The spectral density function indicating the strength variation from the mean plane was calculated by Equation 4.23 in order to generate sample functions of the strength of the cable. The standard deviation ,σ_{grid}, of the hypothetical strength was taken as 238 MPa.

Figures 5.28 to 5.39 show a sample run of the model incorporating the strength variation generated by the hypothetical case. As wires start breaking at lower loads for this case, the loading step increment was selected as 0.2298 cm ($u = 0.2298$ cm) from each end. The cross-sectional plots are at the critical section along the length where the greatest number of broken wires are found for this run. The run indicates that the first wire breaks are found after applying the first loading step in the lower section of the cable. As the load increases, the number of broken wires gradually increases in the lower sector. Then, the breaks extend towards the center of the cable until full collapse occurs.

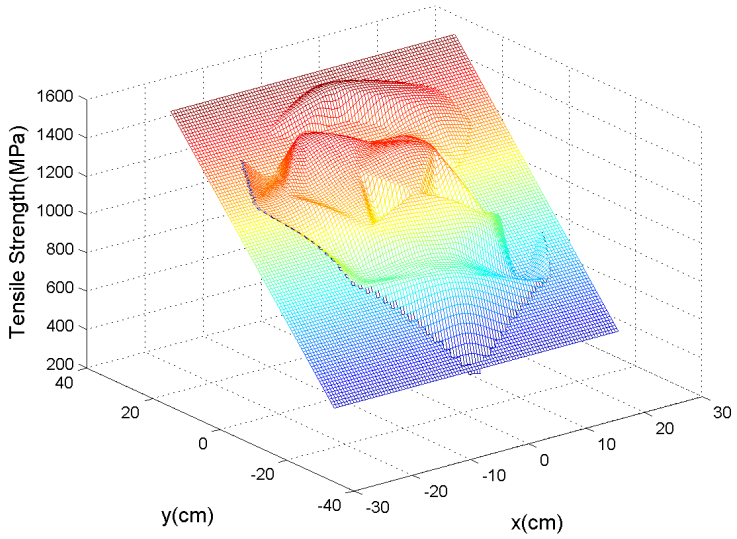

(a)

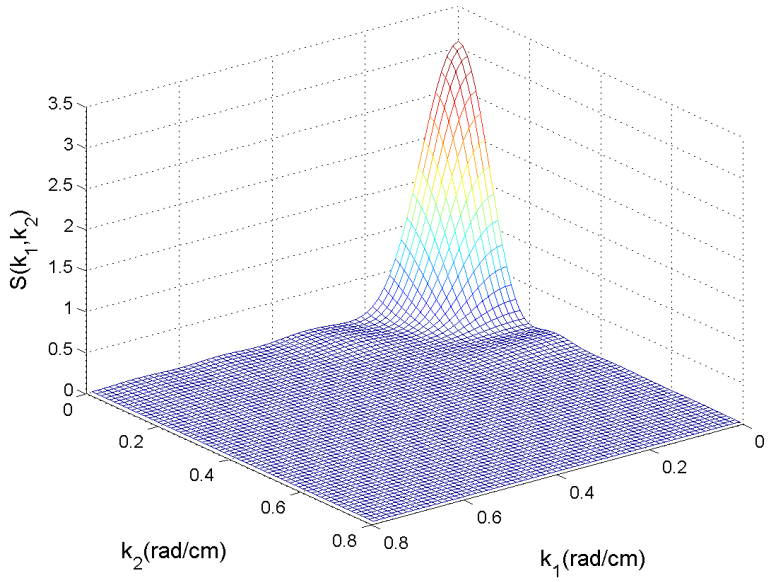

(b)

Figure 5.27: (a) Mesh plot indicating the hypothetical strength in the cross section of a cable and its variation from the hypothetical mean plane. (b) Corresponding spectral density function accounting for the variation of the strength data from the mean plane.

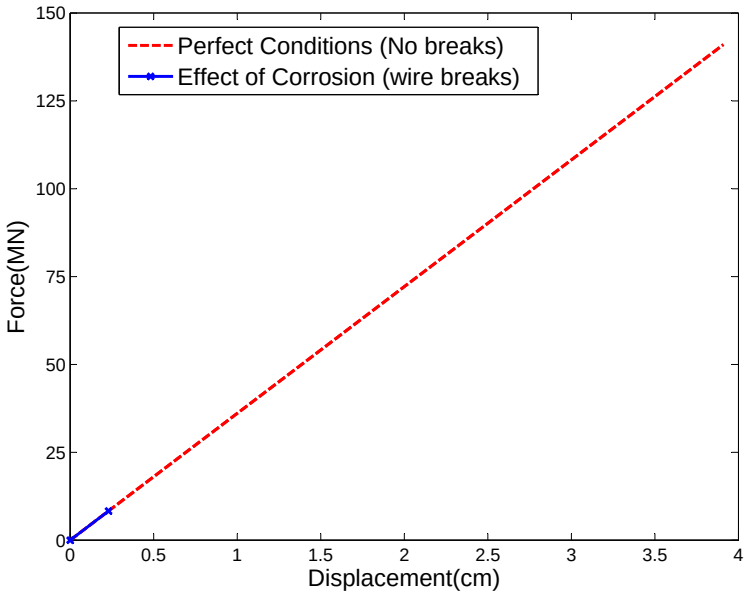

(a)

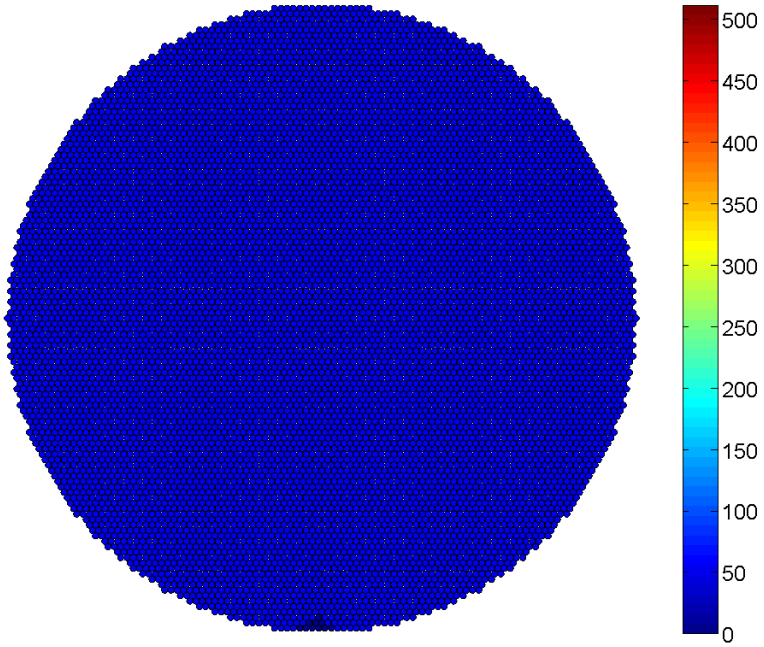

(b)

Figure 5.28: 9061 Wire Case behavior after Step 1. (a) Force-displacement curve of the corroded cable compared to the perfect condition case (no breaks) at u = 0.2298 cm. (b) Axial stress at the critical cross section. The blue circles denote broken wires.

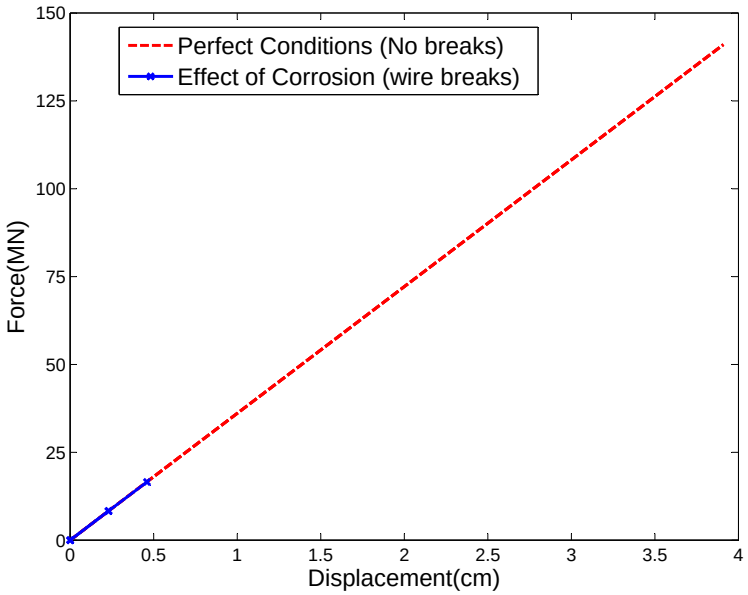

(a)

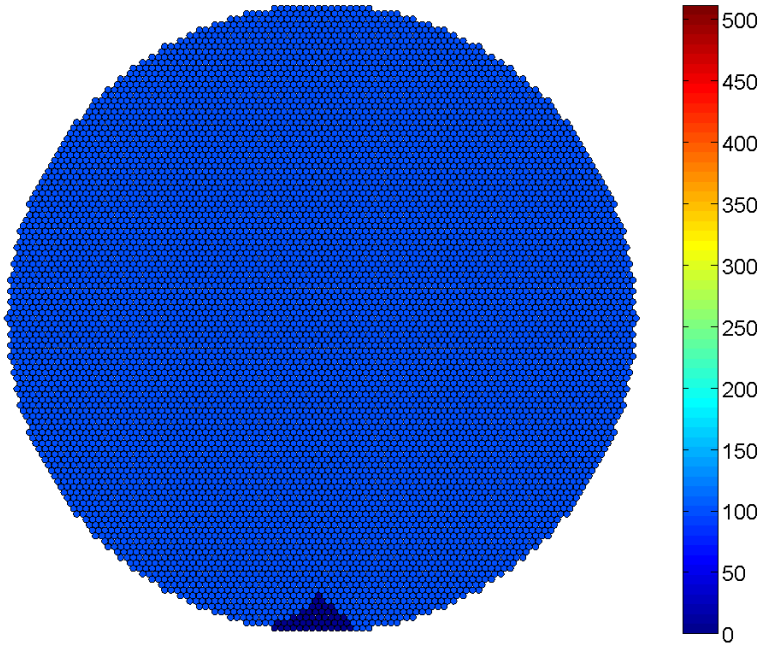

(b)

Figure 5.29: 9061 Wire Case behavior after Step 2. (a) Force-displacement curve of the corroded cable compared to the perfect condition case (no breaks) at u = 0.4598 cm. (b) Axial stress at the critical cross section. The blue circles denote broken wires.

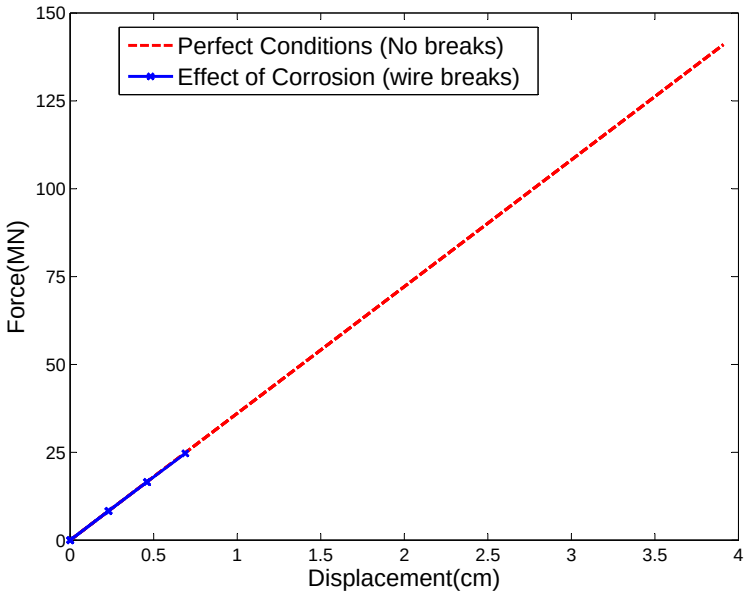

(a)

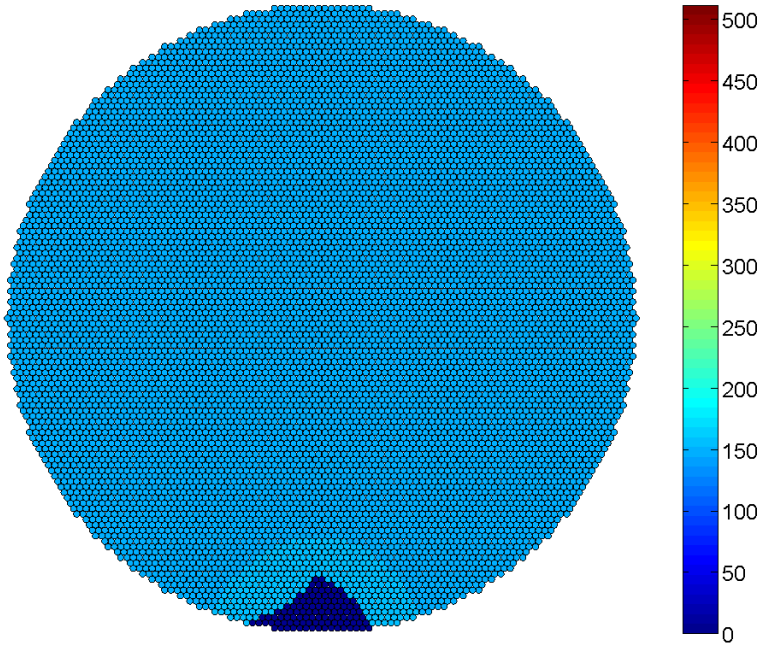

(b)

Figure 5.30: 9061 Wire Case behavior after Step 3. (a) Force-displacement curve of the corroded cable compared to the perfect condition case (no breaks) at u = 0.6898 cm. (b) Axial stress at the critical cross section. The blue circles denote broken wires.

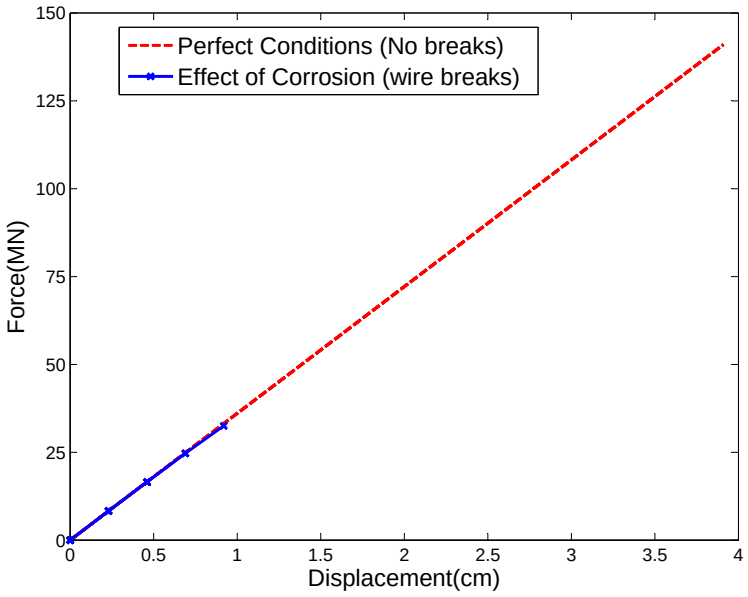

(a)

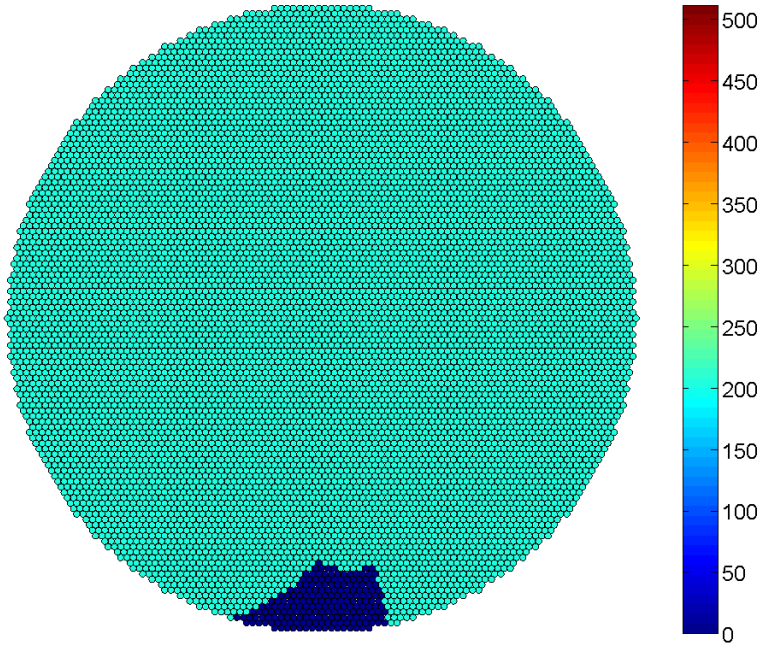

(b)

Figure 5.31: 9061 Wire Case behavior after Step 4. (a) Force-displacement curve of the corroded cable compared to the perfect condition case (no breaks) at u = 0.9198 cm. (b) Axial stress at the critical cross section. The blue circles denote broken wires.

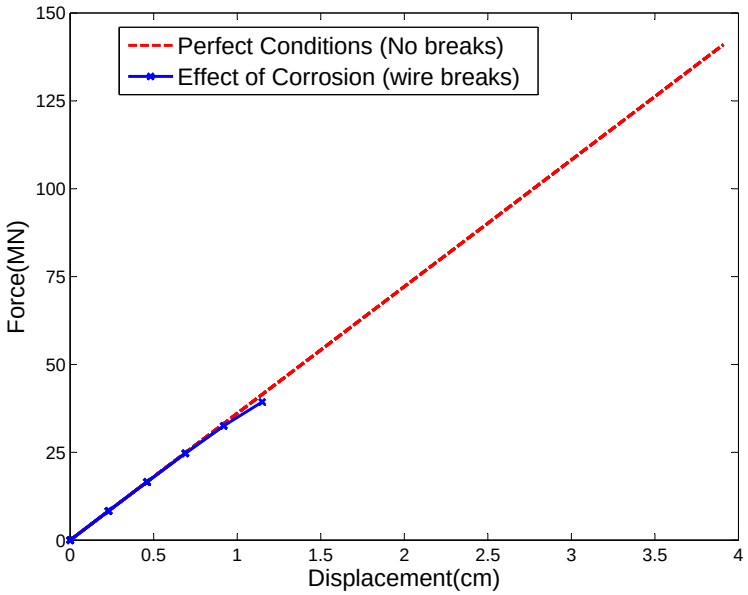

(a)

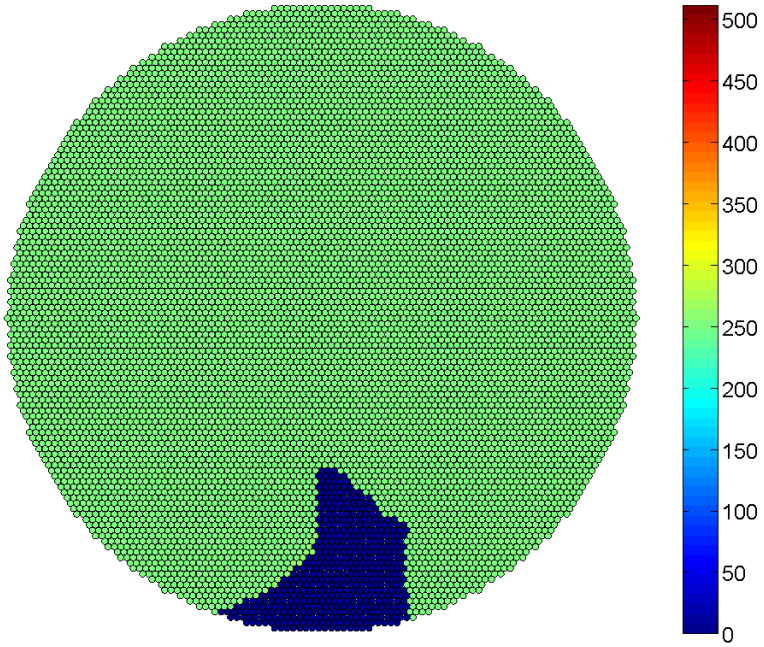

(b)

Figure 5.32: 9061 Wire Case behavior after Step 5. (a) Force-displacement curve of the corroded cable compared to the perfect condition case (no breaks) at u = 1.1498 cm. (b) Axial stress at the critical cross section. The blue circles denote broken wires.

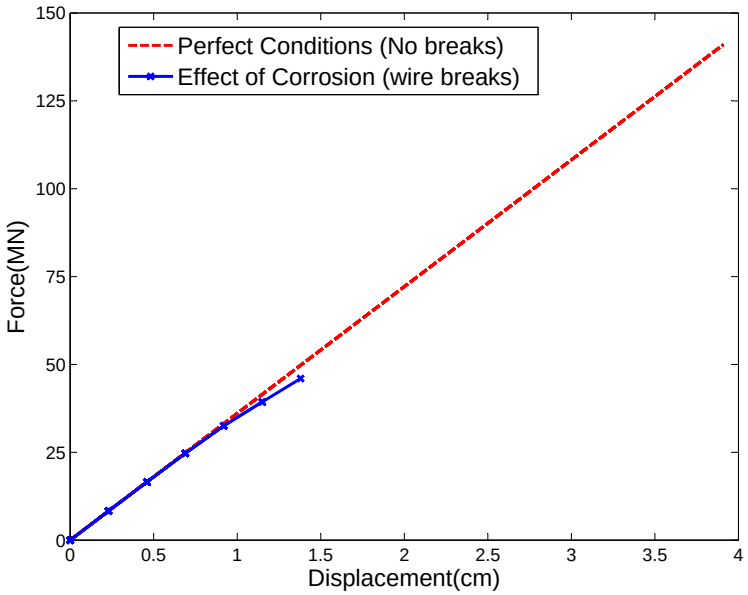

(a)

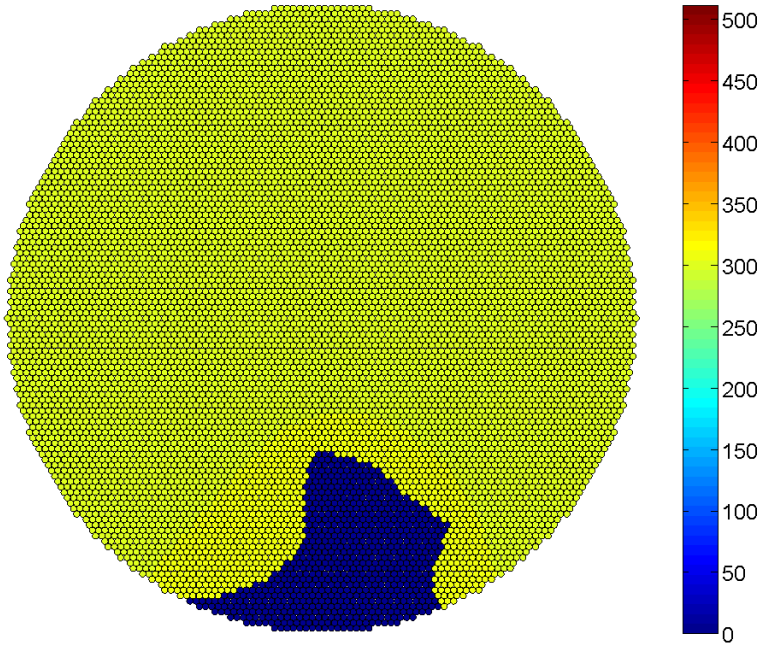

(b)

Figure 5.33: 9061 Wire Case behavior after Step 6. (a) Force-displacement curve of the corroded cable compared to the perfect condition case (no breaks) at u = 1.3798 cm.(b) Axial stress at the critical cross section. The blue circles denote broken wires.

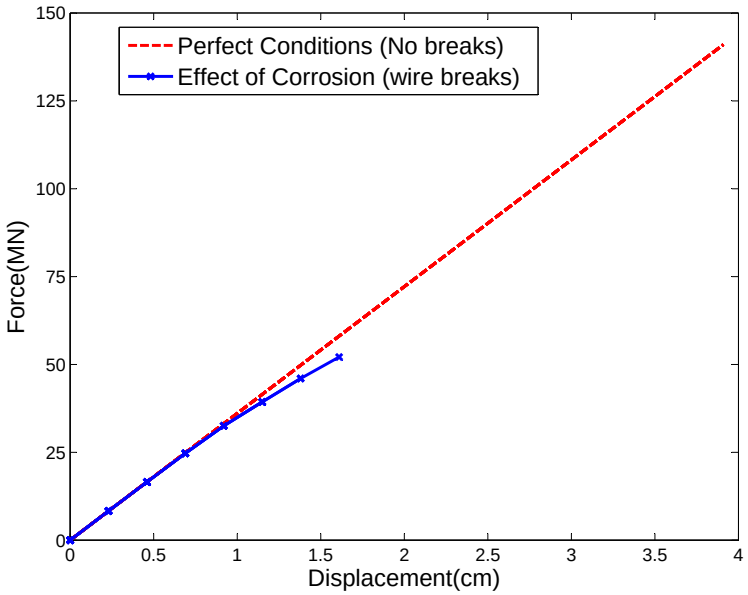

(a)

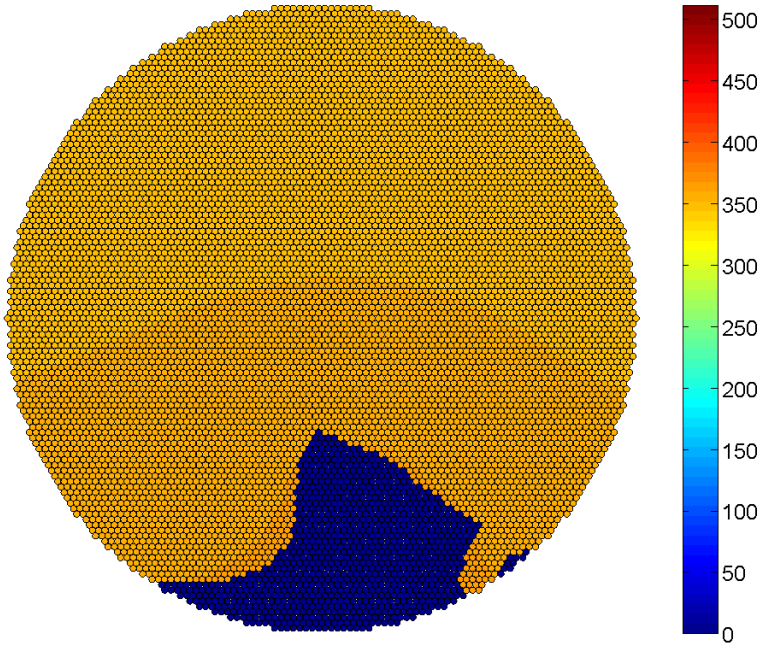

(b)

Figure 5.34: 9061 Wire Case behavior after Step 7. (a) Force-displacement curve of the corroded cable compared to the perfect condition case (no breaks) at u = 1.6098 cm. (b) Axial stress at the critical cross section. The blue circles denote broken wires.

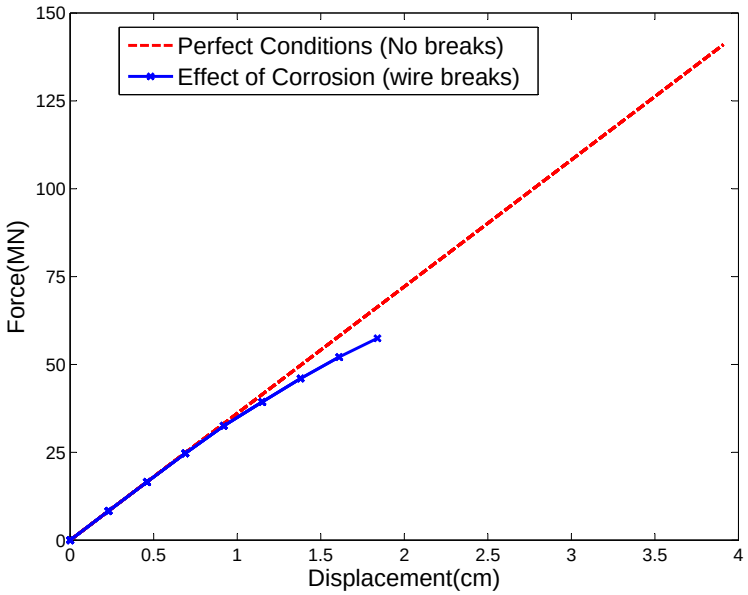

(a)

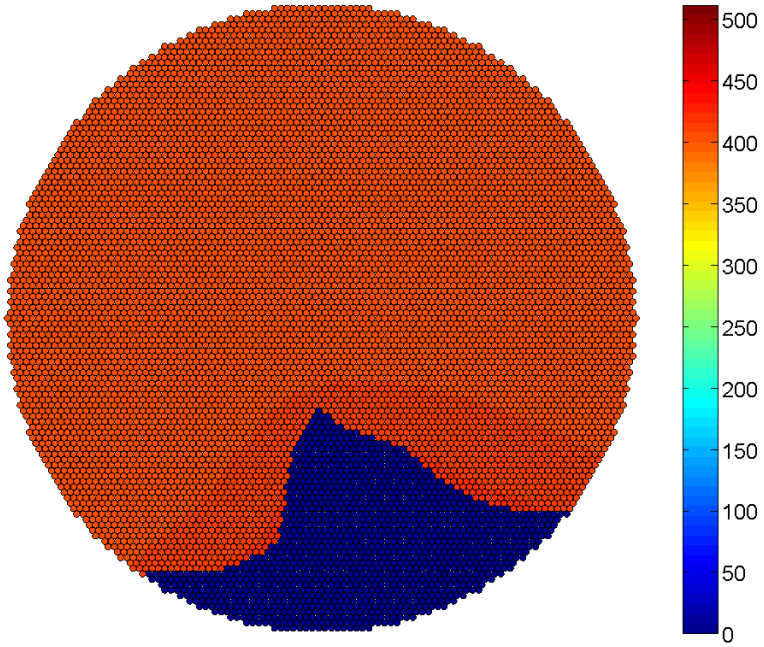

(b)

Figure 5.35: 9061 Wire Case behavior after Step 8. (a) Force-displacement curve of the corroded cable compared to the perfect condition case (no breaks) at u = 1.8398 cm. (b) Axial stress at the critical cross section. The blue circles denote broken wires.

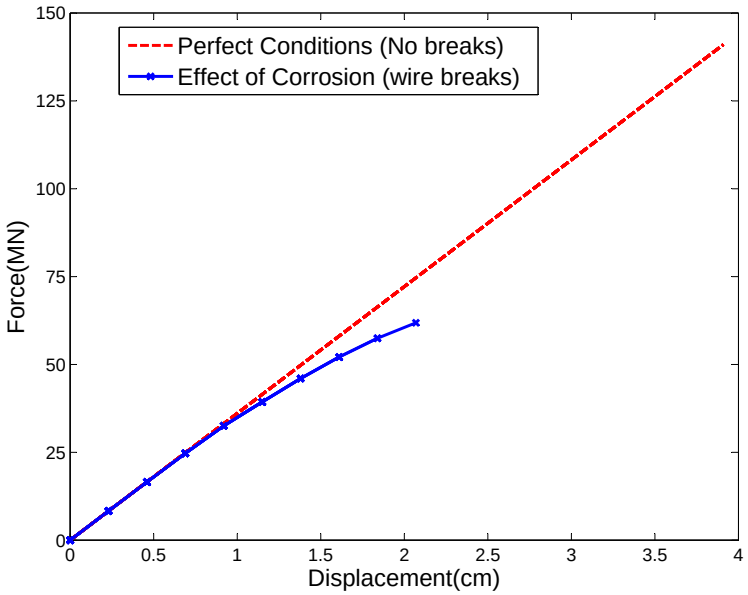

(a)

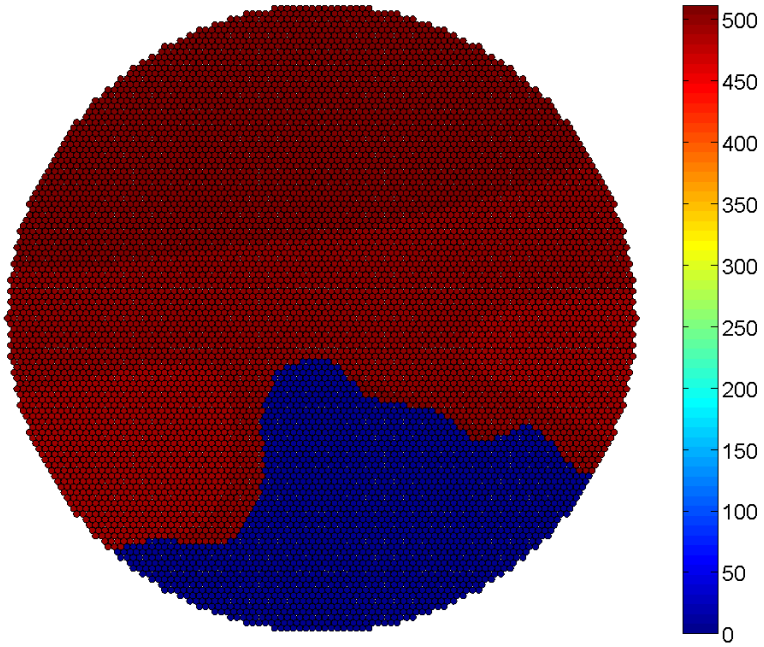

(b)

Figure 5.36: 9061 Wire Case behavior after Step 9. (a) Force-displacement curve of the corroded cable compared to the perfect condition case (no breaks) at u = 2.0698 cm. (b) Axial stress at the critical cross section. The blue circles denote broken wires.

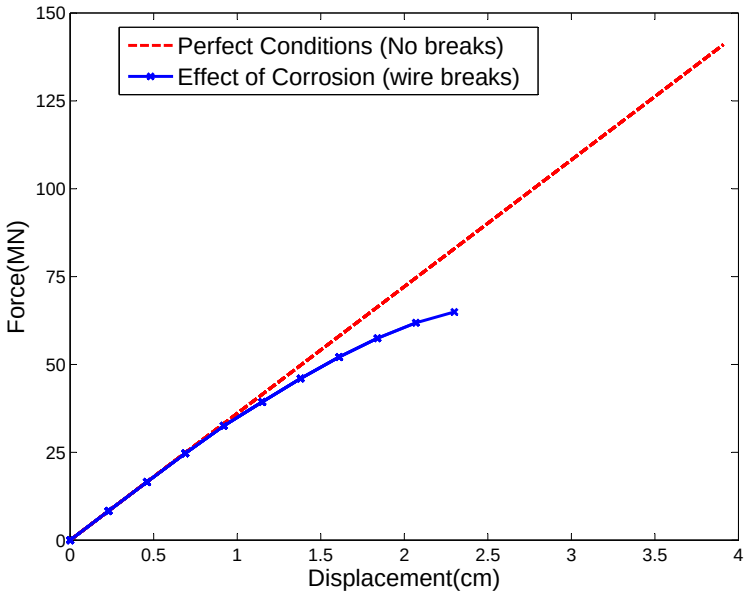

(a)

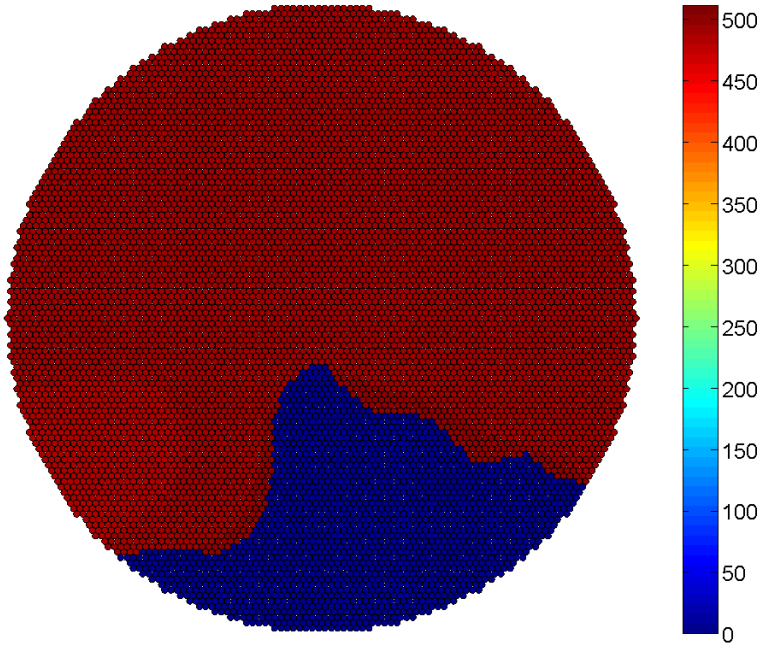

(b)

Figure 5.37: 9061 Wire Case behavior after Step 10. (a) Force-displacement curve of the corroded cable compared to the perfect condition case (no breaks) at u = 2.2998 cm. (b) Axial stress at the critical cross section. The blue circles denote broken wires.

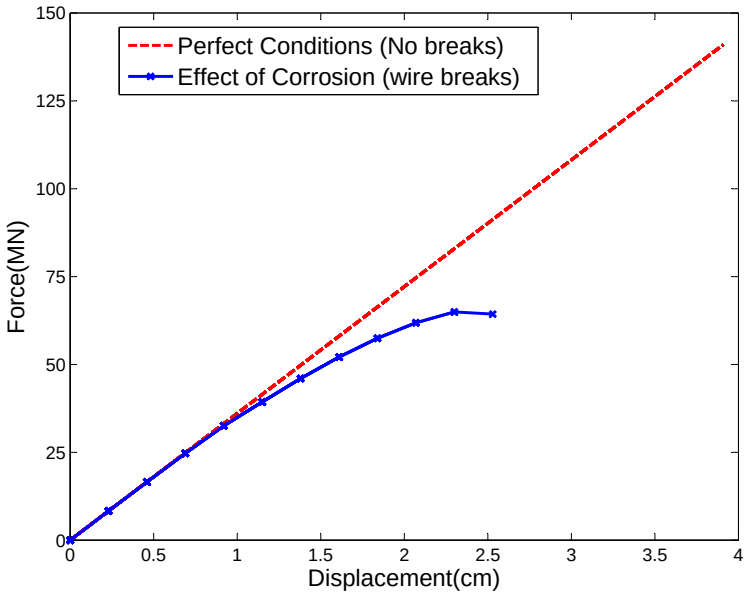

(a)

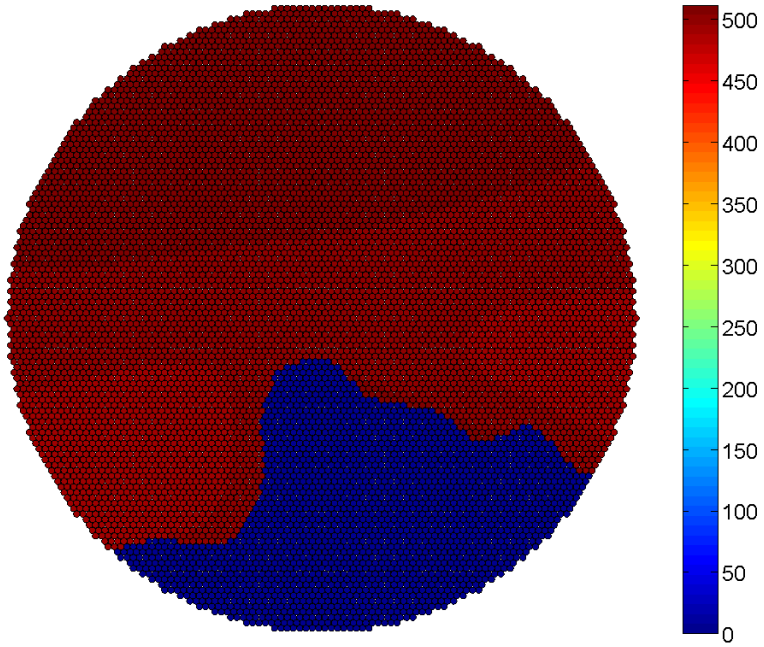

(b)

Figure 5.38: 9061 Wire Case behavior after Step 11. (a) Force-displacement curve of the corroded cable compared to the perfect condition case (no breaks) at u = 2.5928 cm. (b) Axial stress at the critical cross section. The blue circles denote broken wires.

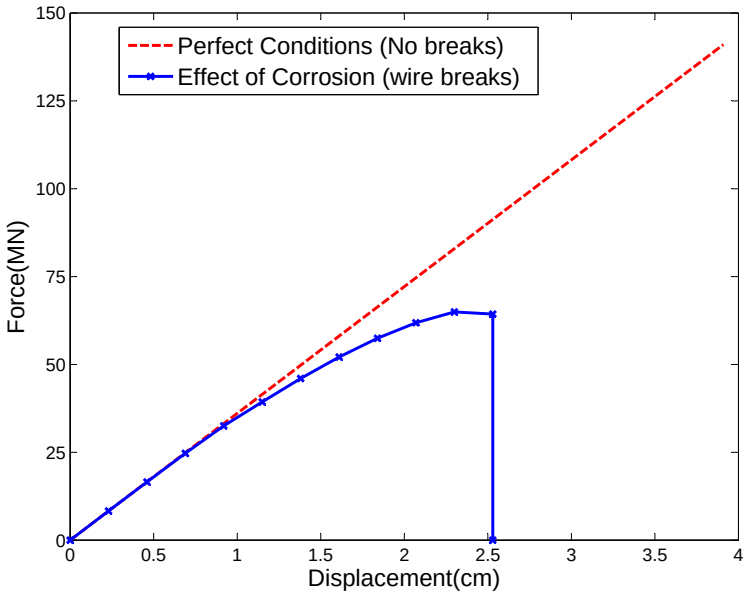

(a)

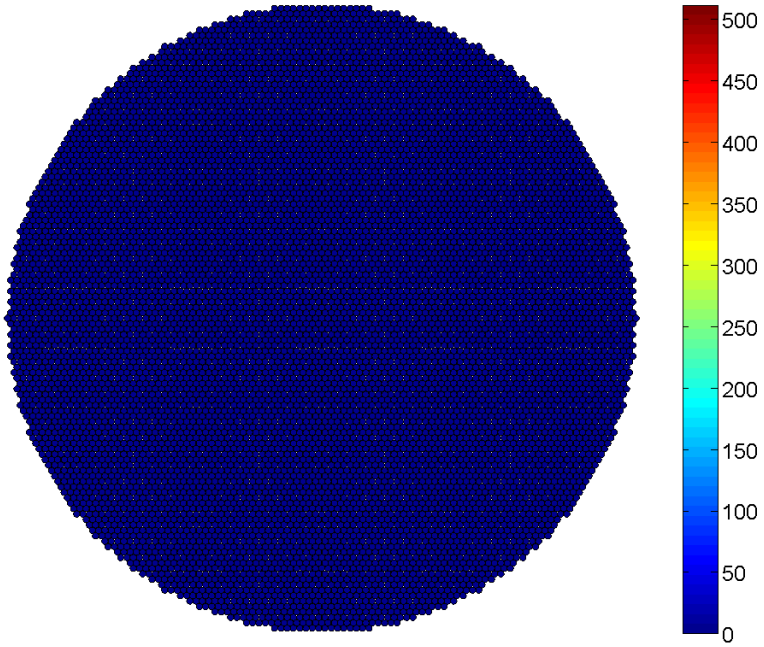

(b)

Figure 5.39: 9061 Wire Case behavior after Step 12. (a) Force-displacement curve of the corroded cable compared to the perfect condition case (no breaks) at failure. (b) Axial stress at the critical cross section. The blue circles denote broken wires.

The resulting force-displacement curves for the 1,0000 realizations are shown in Figure 5.40 for a clamping length of 6 m or one cable band. The mechanism of failure

of the cable has a more stable behavior than the Williamsburg bridge cable; the surviving wires are able to carry more load despite the presence of a significant number of broken wires. Thus, a more apparent nonlinear behavior in the cable is observed in the response of the cable. The stiffness of the overall cable has significantly decreased after the breaks. The histogram for the breaking load is illustrated in Figure 5.41.

The mean and standard deviation of the breaking load for the hypothetical case are:

$$\mu_{hyp} = 79.06\ MN \tag{5.11}$$

$$\sigma_{hyp} = 10.82\ MN \tag{5.12}$$

The breaking loads for each realization are standardized to zero mean and unit standard deviation. It was found that the gaussian distribution fitted well the distribution of the breaking load as observed in Figure 5.42. The coefficients of skewness and kurtosis for the distribution are 0.23 and 2.9669, respectively. These values are very similar to the corresponding values for a standardized Gaussian distribution function, which are 0 and 3.

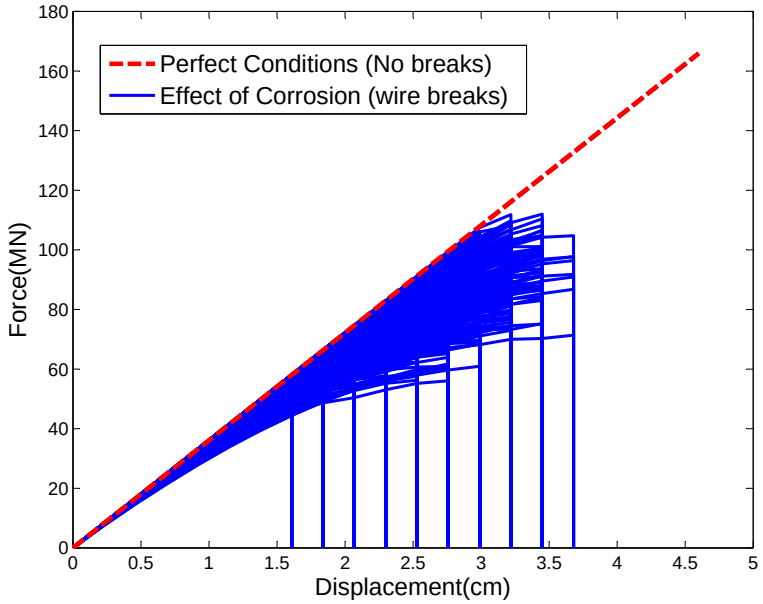

Figure 5.40: Force-displacement curves for the 9061-wires case for 1,000 realizations of strength variation due to corrosion compared to the perfect conditions (representing no breaks) for a clamping length of 6 m.

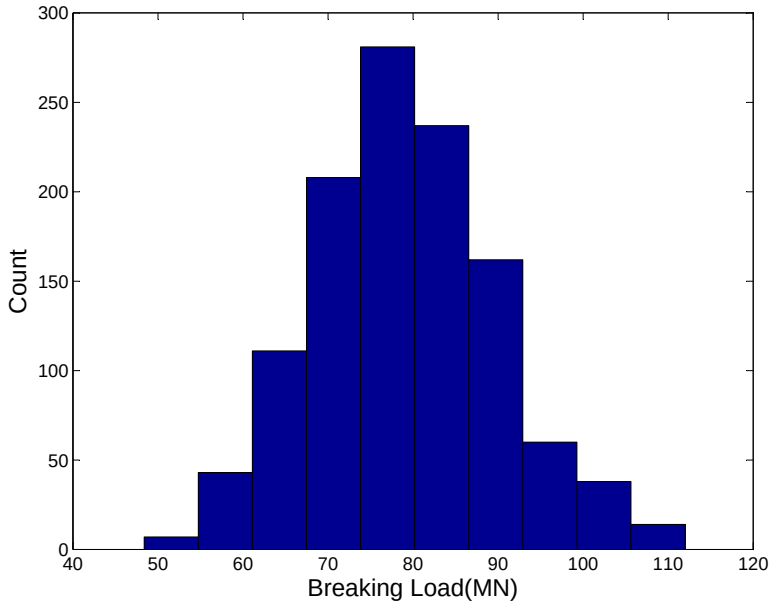

Figure 5.41: Histogram of the breaking load of the hypothetical cable for a clamping length of 6 m.

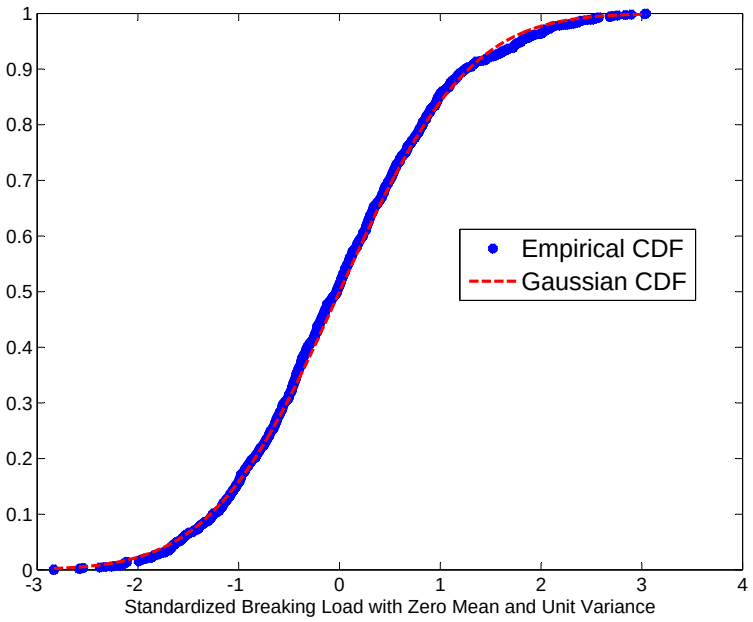

Figure 5.42: Empirical CDF obtained for the cable's strength versus corresponding standardized Gaussian PDF.

5.4 Discussion of the Monte Carlo Simulations

The failure mechanism for a suspension bridge cable has been illustrated in this chapter. The failure load of the cable is obtained through a Monte Carlo Simulation (MCS) with 1000 realizations. The clamping effects are illustrated for two cases, the former considering full recovery after one cable band and the latter is for full recovery after two cable bands. The case with a longer clamping length fails prematurely; although no substantial difference is observed since it has been observed that the failure mechanism can occur fairly quickly after entering the critical region of consecutive wire breaks. The applied load was based on the the wire segment that provided the minimum tensile strength from the Williamsburg Bridge investigation, which was of 1,165 MPa. In fact, the load applied in the cable during the simulation is much higher than those carried by actual bridge cables. For example, the Williamsburg Bridge carries about 45-55 MN of load daily in each cable [42], about 305-375 MPa per wire. The safety

factor can be obtained as the ratio of the mean breaking load over the ultimate load as shown in Table 5.1. The breaking load captured in the model is about 3.5-4.4 times higher than the mean breaking strengths of 194.2 MN and 192.9 MN for clamp cases A and B, respectively. This indicates that the simulated cable is far from collapsing under current deterioration conditions and typical applied loads.

Table 5.1: Safety Factor

Case	**Ultimate Load (MN)**	**Mean Breaking Load (MN)**	**Safety Factor**
A	45	194.2	4.41
A	55	194.2	3.53
B	45	192.9	4.29
B	55	192.9	3.51
C	45	238.6	5.30
C	55	238.6	4.34

The incorporation of the the proposed approach to simulate the strength variation as three dimensional field causes the formation of clusters of broken wires before full collapse of the cable. The exhibited nonlinear behavior of the cable before failure for the simulations is not as evident as the nonlinear behavior observed in Chapter 3 for the smaller strands cases and the main cable with uncorrelated strength between the wires. For smaller strands, a small number of wire breaks cause significant reductions in the strand's stiffness. Likewise, if the strength of the cable is not correlated in the cross-sectional direction, more evident nonlinear effects are observed. For the hypothetical case considered, the strength variation occurs over a larger range resulting in a progressive failure mechanism rather than instantaneous. However the Williamsburg inspection data indicated that the wires were not severly corroded and will break at high loads. As the load in the surviving wires is adjusted, the surrounding wires to the breaks are highly stressed and most likely will fail after small load increments. More wires extracted within the cross-section or extraction of wires after several years may be used to refine the cross-sectional strength variation observed in suspension bridges.

Finally, the advantages of incorporating the finite element method within the Monte Carlo simulation are apparent. The FEM model accounts for load distribution and clamping length effects which are undertaken by previous probabilistic approaches and can overestimate the structural capacity of suspension bridge cables.

Chapter 6

Conclusions and Outlook

6.1 Contributions and Limitations of this Research

A new methodology that provides more reliable results when estimating the remaining strength capacity of main cables of suspension bridges is proposed, which may help prevent an abrupt collapse of suspension bridges. Reliable assessment of the cable's remaining capacity is needed by bridge authorities in order to make important decisions regarding maintenance and rehabilitation or even replacement of such structures. The proposed approach is the first one incorporating experimental testing, probability concepts, and finite element analysis to evaluate the performance of main cables. This method is a significant improvement compared to visual inspections and other methods currently in use which do not account for the correlation of the cable's strength along its length and within the cross section.

In fact, previous methods disregarded the load recovery induced by friction within the prescribed length that was simulated. The assumption made was that after three successive clamps the broken wires were able to recover load. However, due to the high compaction stresses provided by the cable bands, broken wires can quickly recover a significant portion of the load even after crossing one clamp. In this research work, the load transfer mechanism and the recovery length in parallel bridge wires have been studied by finite element models that account for the frictional contact between the wires. A hexagonal seven wire strand, with six outer wires and one inner wire, has been subjected to several experimental tests. The outer wires have been loaded in axial tension while the central wire has carried a part of the load due to friction in the wires imposed by radial bands that were tightened at three different levels: tightly clamped, loosely clamped and unclamped. The results from these tests were used to validate the contact friction model. Three numerical models that employ springs at contact points have been studied: (i) linear springs, which correspond to a shear lag model (ii) elasto-perfectly plastic springs with varying elastic constants and (iii) elasto-perfectly plastic springs with varying yielding. These models have

been first verified on a 2D benchmark problem of two plates in contact where both elasto-perfectly plastic spring models have shown that they are capable of recovering the Coulomb's friction law. The model alleviates the computatiaional difficulties and cost that characterize full contact models. The models have been validated on a seven wire strands for the tightly, loosely and unclamped cases and the results were shown to be in excellent agreement with available experimental results.

The model is extended to study the reduction of the load carrying capacity of multiple wire strands with corrosion-induced wire breaks. Corrosion usually occurs randomly along the length of the wires, causing wire breaks and consequently an overall reduction in the load carrying capacity of strands. The contact-friction mechanism was extended to the many wire case. This approach is found very efficient (for these types of problems where many contact points are encountered). To study the contact mechanics and load transfer due to friction, we considered 7, 19, 37, 91 and 127 wire-strands under axial tensile loading, applied incrementally via a displacement controlled loading. If a wire breaks, its immediate neighbors will take over most of the load carried by that wire. However, due to friction induced by the clamp, the broken wire partially regains some of the load, relieving the neighboring wires. While each wire is assumed linear and elastic, from a system perspective, the behavior is nonlinear due to the multiple wire breaks which reduce the capacity of the strand to carry loads.

The method has been implemented on a parallel computer alleviating the limitations of speed and memory requirement of serial machines. Modeling 9000 or more wires represents a computational challenge; however simplifying the model to one dimensional truss elements and making use of parallel computers, enables a full stochastic analysis to determine the effect of corrosion uncertainty on the cable's failure load. The proposed friction approach represented a significant computational breakthrough when modeling thousands of wires, all under contact-friction.

In addition, a new method is proposed to account for the spatial correlation of the cable's strength, which occurs both within the cross section (over different wires) and along the length of the cable. The probabilistic characteristics of the field are obtained from data available from a Williamsburg bridge investigation program. The strength of the cable is simulated by the Spectral Representation Method in three dimensions. The strength of each wire is obtained from the field simulation and incorporated to the Finite Element Model that drives a main cable to failure by increasing the load gradually. The sample run was able to capture the breakage of wires in clusters, which is a more realistic scenario than what previous methods were able to simulate. A Monte Carlo Simulation allows that the breaking load of the cable be predicted with sufficient accuracy. Taking into account that the proposed random field-based methodology does not require additional testing, is general enough to be applied in a straightforward way to another suspension bridges. The FFT technique makes its computational cost very reasonable and it should be used for estimating the strength of suspension bridge cables.

Up to this point we have treated the stochastic process as Gaussian. However, the field data mildly deviated from a Gaussian distribution. Methodologies to simulate non-Gaussian processes should be incorporated to check any effects in the results (although no significant variations are expected). By treating the 3D field as Gaussian, the simulation of the random field is simplified and the computational cost is reduced. The other limitation comes from the pool of data that is available; ideally more tested wires within the cross-section would give a more accurate approximation of the tensile strength of the cable. Also, other solver packages for solving nonlinear problems may be used to solve the problem more efficiently.

6.2 Future Research Outlook

An integrated sensor network has been developed using a variety of sensors that measure either directly the corrosion rate of bridge wires (direct sensing) or indirectly the environmental parameters (temperature, relative humidity, etc.) related to the corrosion rate of the wires (indirect sensing). Sensors were tested in the Carleton Laboratory at Columbia University in a cyclic corrosion chamber to assess their reliability and to correlate their readings with corrosion rate in wires. Experimental results show that the sensor network provides reliable readings of the variation of conditions inside the main cable. Strong correlations were found between the temperature sensor readings and the corrosion rate sensor readings. Incorporating the sensor readings to the proposed methodology will provide authorities with very accurate means to determine the safety and maintenace of cable supension bridges. For this analysis, a dynamic finite element model could be employed, in which the load is kept constant with time, but the material parameters of the wires change according to readings provided by the sensors in real time.

In addition a new pool of the data will be acquired by examining the conditions of the full scale mock-up tested. The cable was placed inside an accelerated corrosion chamber that created cyclic aggressive environments for a period of two years which are equivalent to several years of outdoor exposure. The work completed up to this date, includes dismantling of the cable specimen and visual inspection of the corroded state of the wires. Furthermore, 200 wires have been selected to get a representative pool from each sector within the cable's cross section. These wires have been extracted and will be cut into 18-in. segments to be tested in tension for breaking strength. The sequence of these segments will be recorded in order to approximate the correlation structure of the tensile strength both within the cross-section (over different wires) and along the length of the cable.

Chapter 7

Bibliography

[1] 2008. Suspension Bridges. ICE Manual of Bridge Engineering. Institution of Civil Engineers.

[2] A.H. Ang adn W.H. Tang. *Probability concepts in engineering planning and design, decision, risk, and reliability*, volume 2. Wiley, 1984.

[3] A. Aktan, F.Catbas, K. Grimmelsman, and M. Pervizpour, 2003. Development of a model health monitoring guide for major bridges. Submitted to the Federal Highway Administration Research and Development, Drexel Intelligent Infrastructure and Transportation Safety Institute, Philadelphia, PA.

[4] S.C Barton, G.W Vermaas, P.F Duby, A.C West, and R. Betti. Accelerated corrosion and embrittlement of high-strength bridge wire. *Journal of Mechanics in Civil Engineering*, 12(1):33–38, 2000.

[5] J.R. Benjamin and C.A. Cornell. *Probability, statistics, and decision for civil engineers*. McGraw-Hill, 1970.

[6] R. Betti, A.C. West, G. Vermaas, and Y. Cao. Corrosion and embrittlement in high-strength wires of suspension bridge cable. *ASCE-Journal of Bridge Engineering*, 10(2):151–162, 2005.

[7] P. Bocchini and G. Deodatis. Critical review and latest developments of a class of simulation algorithms for strongly non-gaussian ranodm fields. *Probabilistic Engineering Mechanics*, 23:393–407, 2008.

[8] J. Boussinesq. *É*quilibre d'*é*lasticit*é* d'un solide isotrope sans pesanteur, supportant diff*é*rents poids. *C. Rendus Acad. Sci. Paris*, 86:1260–1263, 1878.

[9] E.O Brigham. *The Fast Fourier Transform and its Applications*. Prentice Hall, 1988.

[10] D. Brown. *Bridges: Three Thousand Years of Defying Nature*. MBI Publishing Company, first edition, 2001.

[11] S. Camo. Probabilistic strength estimates and reliability of damaged parallel wire cable. *J. Bridge Eng.*, 8(5):297–311, 2003.

[12] C.H. Chien and G. A. Costello. Effective length of a fractured wire in wire rope. *Journal of Engineering Mechanics*, 111(7):952–961, 1985.

[13] G. Costello. *Theory of wire rope*. Springer, 1990.

[14] H. L. Cox. The elasticity and strength of paper and other fibrous materials. *Journal of Applied Physics*, 3:72–79, 1952.

[15] B. Das. *Principles of Foundation Engineering*. CL-Engineering, 7^{th} edition, 2011.

[16] R.O. Davis and A.P.S Selvadurai. *Elasticity and Geomechanics*. Cambridge University Press, 1 edition, 1996.

[17] R. Fan and J. Fish. The rs-method for material failure simulations. *International Journal for Numerical Methods in Engineering*, 73(11):1607–1623, 2008.

[18] A.A. Flamant. Sur la repartition des pressions dans un solide rectangulaire charg*é* transversalement. *Compte Rendu à l'Académie des Sciences*, 114:1465–1468, 1892.

[19] A. Gjelsvik. Development length for single wire in suspension bridge cable. *Journal of Structural Engineering*, 117(4):1189–1200, 1991.

[20] M. Goland and E. Reissner. The stresses in cemented joints. *Journal of Applied Mechanics*, 11:A17–A27, 1944.

[21] Hibbitt, Karlson, and Inc. Sorensen, 2009. ABAQUS/Standard Users Manual, Vol. II, Pawtucket, RI, Version 6.8.

[22] X. L. Huang and O. G. Vinogradov. Dry friction losses in axially loaded cables. *Structural Engineering and Mechanics*, 4(3):330–344, 1996.

[23] X. L. Huang and O. G. Vinogradov. Extension of a cable in the presence of dry friction. *Structural Engineering and Mechanics*, 4(3):313–329, 1996.

[24] M. Labrosse, A. Nawrocki, and T. Conway. Frictional dissipation in axially loaded simple straight strands. *Journal of Engineering Mechanics*, 126(6):641–646, 2000.

[25] J. Mateo, G. Deodatis, and D. Billington. Safety analysis of suspesion bridge cables: Williamsburg bridge. *ASCE-Journal of Structural Engineering*, 120(11):3197–3211, 1994.

[26] A. Montoya, H. Waisman, and R. Betti. A simplified contact-friction methodology for modeling wire breaks in parallel wire strands. *Computers and Structures*, page http://dx.doi.org/10.1016/j.compstruc.2012.03.003, 2012.

[27] C. E. Murray, H. F. Yan, I. C. Noyan, Z. Cai, and B. Lai. Finite-size effects in thin-film composites. *Philosophical Magazine A*, 82(16):3087–3117, 2002.

[28] C. E. Murray, H. F. Yan, I. C. Noyan, Z. Cai, and B. Lai. High-resolution strain mapping in heteroepitaxial thin-film features. *Journal of Applied Physics*, 98(1):013504, 2005.

[29] A. Nawrocki and M. Labrosse. A finite element model for simple straight wire rope strands. *Computers and Structures*, 77(4):345–349, 2000.

[30] Adrzej S. Nowak. Live load model for highway bridges. *Structural Safety*, 13(1-2):53–66, 1993.

[31] I. C. Noyan, A. Brügger, R. Betti, and B. Clausen. Measurement of strain/load transfer in parallel seven-wire strands with neutron diffraction. *Experimental Mechanics*, 265(275), 2010.

[32] R.J. Perry. Estimating strength of williamsburg bridge suspension cables. *Am.Stat*, 52(3):211–217, 1998.

[33] M. Raoof. Wire recovery length in helical strand under axial-fatigue loading. *International journal of fatigue*, 13(2):127–132, 1991.

[34] M. Raoof and Y. Ping Huang. Wire recovery length in suspension bridge cable. *Journal of Structural Engineering*, 118(12):3255–3267, 1992.

[35] M. Raoof and I. Kraincanic. Determination of wire recovery length in steel cables. *Computers and Structures*, 68(5):445–459, 1998.

[36] and D.Khazem R.Q. Haight, Billington D.P. Safety analysis of suspension bridge cables: Williamsburg bridge. *J. Struct. Eng.*, 120(11):3197–3211, 1997.

[37] Martin H. Sadd. *Elasticity: Theory, Applications, and Numerics*. Elsevier, Inc., first edition, 2005.

[38] M. Shields, P. Bocchini, and G. Deodatis. A simple and efficient methodology to approximate a general non-gaussian stationary stochastic process by a translation process. *Probabilistic Engineering Mechanics*, 23:393–407, 2008.

[39] M. Shinozuka and G. Deodatis. Simulation of stochastic processes by spectral representation. *Applied Mechanics Rev.*, 44(4):191–204, 1991.

[40] M. Shinozuka and G. Deodatis. Simulation of multi-dimensional gaussian stochastic fields by spectral representation. *Applied Mechanics Rev.*, 49(1):29–52, 1996.

[41] J.P. Singh, J.L. Hennessy, and A. Gupta. Scaling parallel programs for multiprocessors: Methodology and examples. *IEEE Computer*, 26(7):42–50, 1993.

[42] Gronquist Bridsall Steinman, Boynton and Columbia University, 1998. Williamsburg Bridge cable investigation program: Final report. Submitted to the New York State Dept of Transp. and New York City Dept. of Transp., New York, NY.

[43] K. Suzumura and S. Nakamura. Environmental factors affecting corrosion of galvanized steel wires. *ASCE-Journal of Materials in Civil Engineering*, 16(1):1–7, 2004.

[44] M. Taya and R. J. Arsenault. A comparison between a shear lag type model and an eshelby type model in predicting the mechanical properties of a short fiber composite. *Scripta Metallurgica*, 21:349–354, 1987.

[45] R.L Taylor, 2008. FEAP- A Finite Element Program, Version 8.2 Users Manual, University of California, Berkeley.

[46] R.L Taylor, 2008. FEAP- A Finite Element Program, Version 8.2 Parallel Users Manual, University of California, Berkeley.

[47] Timoshenko and J.N. Goodier. *Theory of Elasticity*. McGraw-Hill,New York, 2 edition, 1970.

[48] S. Timoshenko and S. W. Krieger. *Theory of Plates and Shells*. McGraw-Hill,New York, 2 edition, 1959.

[49] W. S. Utting and N. Jones. The response of wire rope strands to axial tensile loads: Part i. *International Journal of Mechanical Science*, 29(9):605–619, 1987.

[50] W. S. Utting and N. Jones. The response of wire rope strands to axial tensile loads: Part ii. *International Journal of Mechanical Science*, 29(9):621–636, 1987.

[51] O. Volkersen. Luftfahrtforschung. 15:41–47, 1938.

[52] H. Waisman, A. Montoya, R. Betti, and I.C Noyan. Load transfer and recovery length in parallel wires of suspension bridge cables. *ASCE-Journal of Engineering Mechanics*, 137(227), 2011.

[53] P. Wriggers. *Computational contact mechanics*. Springer, 2 edition, 2006.

[54] S. Yuwei, G. Deodatis, and R. Betti. Random field-based approach for strength evaluation of suspension bridge cables. *ASCE-Journal of Structural Engineering*, 133(12):1690–1699, 2007.